Title
ATOMIC MECHANISMS OF Y' PRECIPITATE PLATE GROWTH IN THE Al-Ag SYSTEM

Author
Howe, J.M.

Publication Date
1985-03-01

Lawrence Berkeley Laboratory
UNIVERSITY OF CALIFORNIA

Materials & Molecular Research Division

ATOMIC MECHANISMS OF γ' PRECIPITATE PLATE GROWTH IN THE Al-Ag SYSTEM

J.M. Howe
(Ph.D. Thesis)

March 1985

Prepared for the U.S. Department of Energy under Contract DE-AC03-76SF00098

DISCLAIMER

LBL-19286

ATOMIC MECHANISMS OF γ' PRECIPITATE PLATE GROWTH IN THE AL-AG SYSTEM

James Maxwell Howe

Materials and Molecular Research Division
Lawrence Berkeley Laboratory
and Department of Materials Science and Mineral Engineering
University of California
Berkeley, CA 94720

This work was supported by the Director, Office of Energy Research, Office of Basic Energy Sciences, Materials Science Division of the U.S. Department of Energy under Contract No. DE-AC03-76SF00098.

TABLE OF CONTENTS

ABSTRACT vii

1. INTRODUCTION 1

2. THE AL-AG SYSTEM 7

2.1. α Supersaturated Solid Solution 7

2.2. G.P. Zones 7

2.3. γ' Precipitates 9

2.4. γ Precipitates 12

3. THEORIES OF PRECIPITATE PLATE GROWTH 15

3.1. Interface Structure 15

3.1.1. Coherent Interfaces 15

3.1.2. Semicoherent (Misfit Dislocation) Interfaces 16

3.1.3. Incoherent Interfaces 19

3.2. Interface Migration 19

3.3. Precipitate Shape Due to Interfacial Energy Effects 21

3.3.1. Coherent Precipitates 21

3.3.2. Semicoherent Precipitates 22

3.3.3. Incoherent Precipitates 23

3.4. Precipitate Shape Due to Strain Energy Effects 24

3.4.1. Coherent Precipitates 24

3.4.2. Semicoherent Precipitates 26

3.4.3. Incoherent Precipitates 27

3.5. Precipitate Shape Due to Atomic Mechanisms of Growth 28

3.5.1. General Theory of Precipitate Morphology 27

4. TRANSMISSION ELECTRON MICROSCOPY TECHNIQUES 30

4.1. Conventional TEM (Amplitude Contrast Imaging) 30

4.2. High-Resolution TEM (Phase Contrast Imaging) and Image Simulations 32

4.3. Optical Diffraction 37

4.4. Energy-Dispersive X-ray Spectroscopy 38

4.5. Convergent-Beam Electron Diffraction 41

5. EXPERIMENTAL PROCEDURES 48

5.1. Materials and Heat-Treatments 48

5.1.1. Al-Ag Alloys 48

5.1.2. Ag_2Al 48

5.1.3. 99.99% Ti 49

5.2. Electropolishing and Ion-Beam Milling 49

5.3. Precipitate Extractions 50

5.4. High-Resolution TEM 51

5.5. Image Simulations 52

5.5.1. FCO128 53

5.5.2. DEF128 54

5.5.3. IM128 55

5.6. Energy-Dispersive X-ray Spectroscopy 56

5.7. Convergent-Beam Electron Diffraction 58

6. EXPERIMENTAL RESULTS AND DISCUSSION 59

6.1. Plan of Attack 59

6.2. High-Resolution Transmission Electron Microscopy 61

6.2.1. The Structure of γ' Precipitate Plate Faces 61

6.2.2. The Structure of γ' Precipitate Edges 69

6.2.3. Nucleation of Ledges at Precipitate Intersections . 76

6.2.4. The Structure of Precipitate Edges in a <111> Orientation 79

6.3. Energy-Dispersive X-ray Spectroscopy 92

6.3.1. Quantitative Analyses of Extracted γ' Precipitates 92

6.3.2. Quantitative Analysis of Matrix 94

6.4. Analysis of Electron Diffraction Patterns and Construction of Atomic Model for γ' Precipitates 96

6.5. Image Simulations 100

6.5.1. Determination of Optimum Defocus Conditions 100

6.5.2. Image Simulations for HCP γ' Structure 103

6.5.3. Image Simulations of Precipitate/Matrix Interface 108

6.6. Comparison of Experimental HREM Images of γ' Precipitates with Simulated Images Based on Model γ' Crystal Structure 110

6.7. HREM Images of Ag_2Al $\langle 1\bar{1}20\rangle$ Single Crystal 114

6.8. Atomic Mechanism of Precipitate Plate Growth 116

6.9. Convergent-Beam Electron Diffraction 119

6.9.1. Space Group and Lattice Parameter Determinations for α-Titanium 120

6.9.2. Effect of Specimen Thickness on Symmetry Determinations by CBED 127

6.9.3. Space Group and Lattice Parameter Determinations for γ' Precipitates 134

7. CONCLUSIONS 143a

8. FUTURE WORK 146

9. ACKNOWLEDGEMENTS 148

10. APPENDICES 150

10.1. Computer Program for Calculating the Atomic Positions of a 90° Shockley Partial Dislocation Ledge Using Isotropic Elastic Theory 150

10.2. Simulated Images for HCP Crystals Containing 33 to 66 a/o Ag 155

10.3. Anomalous Order in γ' Precipitates 156

10.4. Influence of Surface and Elastic Strain Energies on the Aspect Ratios of γ' Precipitate Plates 159

11. REFERENCES 164

12. TABLES 179

13. FIGURE CAPTIONS 191

FIGURES 213

ATOMIC MECHANISMS OF γ' PRECIPITATE PLATE GROWTH IN THE AL-AG SYSTEM

J.M. Howe

Materials and Molecular Research Division
Lawrence Berkeley Laboratory
and Department of Materials Science and Mineral Engineering
University of California
Berkeley, CA 94720

ABSTRACT

Recent advances in both electron microscopy instrumentation and technique now make it possible to study the shape-evolution of precipitate particles on an atomic level. In this investigation, the techniques of high-resolution electron microscopy, image simulation, energy-dispersive x-ray spectroscopy, electron diffraction and convergent-beam electron diffraction are used to characterize the atomic structure, chemistry and growth mechanisms of γ' precipitate plates in an Al-Ag alloy. The γ' precipitates were formed by aging a solid-solution Al-15 w/o Ag alloy for times of 10 to 120 min. at 350°C.

Energy-dispersive x-ray spectroscopy results reveal that the precipitates contain about 66 a/o Ag for the range of aging times examined and therefore, have the composition Ag_2Al. In addition, high-resolution electron microscopy of γ' precipitates in both <110>//<11$\bar{2}$0> and <111>//<0001> orientations shows that all interfaces of the precipitate are largely coherent with the matrix and are faceted along low-energy {111} and {110} matrix planes, due to the influence of surface and elastic strain energies on the transformation. Further comparison between experimental and calculated high-resolution images of the precipitate/matrix interface and of Shockley partial dislocation ledges on the precipitate faces demonstrates that both thickening and lengthen-

ing of γ' precipitate plates occurs by the passage of the Shockley partial dislocations along alternate {111} matrix planes by a terrace-ledge-kink mechanism. These images and electron diffraction information also indicate that the γ' precipitates are ordered, where the A-planes in the precipitate contain nearly pure Ag and the B-planes have the composition Al_2Ag, and that the limiting reaction in the growth process is the substitutional diffusion of Ag across kinks in the Shockley partial dislocations, which terminate in the Ag-rich A-planes. In addition, the terraces between ledges are atomically flat and ledges are uniformly stepped-down from the centers to the edges of isolated precipitates, leading to the overall shape predicted by the general theory of precipitate morphology.

Lastly, CBED analyses of γ' precipitates indicate that they have the space group $P6_3/mmc$, even though these results disagree with the ordered arrangement of atoms suggested by both the conventional diffraction patterns and high-resolution images. This difference may be due to the limited thickness of the extracted precipitates, which fails to reveal the true 3-dimensional crystal symmetry in the CBED analyses, or to the fact that the precipitates are disordering at the aging times and temperature examined. The effect of specimen thickness on symmetry determinations by CBED was also examined for an α-titanium sample. The results from this study show that the symmetries observed in CBED patterns from thin specimens may be due to the limited thickness of the specimen, rather than to the actual space group of the material.

1. INTRODUCTION

The concept of growth of an interface normal to itself by a ledge mechanism was originally proposed by Gibbs (1) for the growth of close-packed crystal faces into a vapor or liquid. By the early 1960's a large volume of theoretical and experimental evidence had established the existence and the importance of the ledge mechanism of growth at both solid/liquid (2-7) and solid/vapor (8-12) interfaces. Comparatively, the theory of solid/solid interfaces was considerably less developed at this time. Even in 1962, when Aaronson (13) proposed a general theory of precipitate morphology based on the migration of partially or fully coherent interphase boundaries by a ledge mechanism, there was almost no direct experimental evidence of ledges. With the advent of improved transmission electron microscopy (TEM) techniques, however, observations of growth ledges at interfaces in many metals (14-16) and ceramics (17-19) now indicates that it is a fairly universal growth mechanism and is considerably more common than was originally anticipated. In fact, the rather wide variety of experimental evidence for growth ledges at solid/solid interfaces by 1971 led Weatherly (20) to remark that, "there is no reason to doubt that the ledge mechanism is the universal one for the growth or dissolution of all faceted precipitates." Since the properties of a wide variety of engineering materials depend on the state of such precipitates, an understanding of their structure and growth behavior is of considerable practical importance as well as of theoretical interest to the materials scientist.

According to the general theory of precipitate morphology just mentioned, when the composition and crystal structure of a precipitate

differ from the matrix, the precipitate morphology is determined by the mechanism of atomic attachment across the interphase boundary. In the case of precipitate plates, the edges or fast-growing interfaces were originally thought to have high-energy disordered structures and hence, grow at a rate limited only by nonstructural factors such as long-range volume diffusion. Unlike the edges, the broad faces or slow-growing interfaces were thought to have lower-energy coherent or semicoherent dislocation interfacial structures which could grow only by the formation and passage of ledges laterally across the interphase boundary. Although the edges of the ledges could have a disordered structure and therefore also be controlled by volume diffusion, the nucleation and growth of ledges was considered to be overall a much slower process than the migration of a disordered interphase boundary, thus causing the large aspect ratios of precipitate plates.

Within about the last 15 years, the growth behavior of the edges and faces of plate-shaped precipitates in a variety of alloy systems, i.e. Al-Cu (21-27), Fe-C (28-31), Cu-Zn (32), Ti-Cr (33), Mo_2C in ferrite (34) and Al-Ag (35-39) have been compared to growth kinetics predicted for partially or fully coherent and disordered interfaces (40-58). While these studies have mostly confirmed the predictions of the general theory of precipitate morphology, several contrary results have been obtained (36). For instance, in the Al-Ag system chosen for this study, hot-stage TEM and kinetic analyses indicated that both the faces and edges of $\gamma(Ag_2Al)$ precipitates may grow by a ledge mechanism and therefore, that the precipitates may be fully or partially coherent in a number of different boundary orientations, not just at their faces.

These same analyses also showed that the heights and growth behavior of ledges or "superledges" on the plate edges were considerably different from those on the faces of the precipitates. In addition, the growth rates of individual ledges on the faces were sometimes much slower than allowed by volume diffusion, suggesting that they were either several ledges high or alternatively, that a kink-on-ledge mechanism of growth was necessary to effect movement. This new information questioned the validity of disordered interphase boundaries as previously envisioned; however, the resolution limitations of conventional TEM had prevented previous investigators from elucidating the atomic-scale mechanisms of growth involved (59).

In order to resolve many remaining problems concerning ledge growth and the coherency of precipitate/matrix interphase boundaries, Howe et al. (60-62) studied the interfacial structure of γ' precipitates using both conventional and high-resolution TEM. Their results showed that: 1) all ledges on the faces of γ' precipitates are multiples of two {111} planes high, supporting the theory and conventional TEM observations (35,36) that plate thickening occurs by passage of Shockley partial dislocations on alternate {111} planes, 2) most ledges are more than just two {111} planes high, indicating a strong tendency toward diffusional and/or elastic interactions and thus explaining why a range of migration rates was observed for ledges on the faces of similar precipitates in a previous study (36), 3) the terraces between ledges are atomically flat and ledges are uniformly stepped-down from the centers to the edges of isolated precipitates as predicted by the general theory of precipitate morphology (13), 4) the {111} planes are continuous across

the edges of ledges, indicating that they are largely coherent and not disordered as treated in most kinetic analyses (40,53), and 5) the edges of precipitate plates and "superledges" on the edges appear to be composed of similar two-plane ledges arranged vertically above one another and hence, may grow by the same mechanism of atomic attachment as ledges on the broad faces. These authors further proposed that both the edges of γ' precipitates and ledges on the faces grow by similar kink mechanisms.

The purpose of the present research is to perform highly detailed analyses of both the structural and chemical components required for growth of γ' precipitates, so that the mechanism of growth can be modeled on an atomic level. In order to accomplish this, the techniques of high-resolution electron microscopy (HREM), image simulations, electron diffraction, convergent-beam electron diffraction (CBED) and energy-dispersive x-ray spectroscopy (EDS) are used. Each of these techniques provides unique information about the structure and chemistry of a material, and this combination of techniques was chosen to corroborate the results.

The Al-Ag system is ideally suited for this type of study because:

1. the α(fcc) $\rightarrow$ γ'(hcp) transformation is one of the simpler diffusional transformations involving a distinct change in crystal structure,

2. detailed studies have been done on the interfacial structure of γ' plates by conventional (35,60,63) and high-resolution TEM (61,62), and on the growth kinetics and structure of both the faces and edges of γ plates by conventional TEM (35,36),

3. Al and Ag atoms have considerably different atomic scattering factors and therefore, might be distinguishable by atomic-resolution microscopy,

4. Al and Ag atoms are similar in size, i.e. 1.42 Å versus 1.43 Å, respectively, and therefore, there is a minimum amount of strain associated with the transformation,

5. both phases may be disordered solid solutions, thereby simplifying the transformation mechanism, and

6. diffusion and thermodynamic data are available for the matrix and the precipitate.

Although Al-Ag alloys are not used commercially, primarily due to the high cost of Ag, the basic precipitation process is analogous to those of important commercial alloys such as the high-strength, corrosion and fracture resistant Al-Cu-Mg and Al-Mg-Zn alloys (64), and similar growth mechanisms might be expected to occur.

Since many different aspects of precipitation in the Al-Ag system are considered in this study, a summary of previous work on this system is given in the next section (Sect. 2.). This summary is followed by brief reviews of several aspects of phase transformations (Sect. 3.) and electron microscopy (Sect. 4.) which are relevant to this investigation. These reviews are included in order to provide an unfamiliar reader with most of the background necessary to understand and interpret the experimental procedures and results which are presented in the next sections (Sects. 5. and 6.). The experimental results are organized into a progression which considers the information obtained from each TEM tech-

nique, and then subsequently combines this information to arrive at the final results. The main conclusions from these results are then summarized (Sect. 7.) and suggestions are made for future work in this area (Sect. 8.).

2. THE AL-AG SYSTEM

The Al-Ag equilibrium phase diagram and an enlargement of the Al-rich side, including the metastable G.P. zone solvus (65,66), are shown in Figs. 1(a) and (b) (67). Although the basic aging sequence for an alloy quenched from the solid solution α-phase and aged within the metastable solvus is generally accepted as:

α supersaturated solid solution → G.P. zones → γ' → γ(Ag_2Al)

there is still some disagreement as to the exact structures and nucleation mechanisms of each of these phases. The results of a number of studies, mostly performed during the 1950's and 1960's are summarized below, according to the particular stage of precipitation. Several very recent studies on this system are also included. For more complete discussions of the Al-Ag system than is presented here, see references 68 and 69.

2.1. α Supersaturated Solid Solution

The solid solubility of Ag in Al increases regularly with temperature up to 558°C, as shown in Fig. 1. In addition, Hren and Thomas (35) observed the presence of clusters 20 to 100 Å in diameter at temperatures above 500°C in an Al-20 w/o Ag alloy using hot-stage TEM. They interpreted this as evidence that the alloy never exists as a homogeneous solid solution. Clustering in the solid solution has also been reported by other investigators (69).

2.2. G.P. Zones

G.P. zones were first detected in Al-Ag alloys by x-ray small angle scattering experiments. From these investigations, two models were

developed for the structure of an alloy containing zones: 1) Guinier and Walker (70) and Freise et al. (71) proposed that less than half of the total Ag was contained in spherical, Ag-rich G.P. zones, which were surrounded by Ag-depleted halos, and 2) Baur and Gerold (72) interpreted their results as meaning that all of the Ag was contained within the zones, and that the matrix was at a uniformly low Ag concentration, i.e. that there is a miscibility gap in the Al-Ag system. While this latter interpretation is generally accepted as correct, Howe and Gronsky (73) have shown that the model proposed by Guinier and Walker (70) and Freise et al. (71) can occur for certain heat-treatments.

Subsequent TEM investigations by Nicholson and Nutting (74) of an Al-16 w/o Ag alloy confirmed the presence of spherical G.P. zones. While the volume fraction and radii of the zones differed from those obtained by x-ray small angle scattering, the difference was attributed to difficulties in making accurate measurements of zone sizes and numbers from the TEM micrographs (71).

Baur and Gerold (72) also found that a change in temperature from 140 to 190°C resulted in a change in Ag concentration inside the G.P. zones from 54 to 37 a/o Ag. These changes were taken as indirect evidence of a low-temperature ordered phase, and a high-temperature disordered state. Gragg and Cohen (75), however, proposed that a change in the shape of the zones from spherical to octahedral, accompanied by an increase in the Ag content when aging above or below 170°C, respectively, was responsible for the observed diffuse x-ray scattering.

More recently, Gronsky (76) has shown by HREM that: 1) Ag-rich G.P. zones formed at room temperature are sharply faceted along {111}

interfaces yielding an octahedral shape, and 2) there is no ordering within the zones. These results agree with the model of Gragg and Cohen (75). Gronsky also observed unit-cell high ledges at the G.P. zone/matrix interface.

In addition, Alexander et al. (77) and Hono and Hirano (78) have now studied the degree of faceting of G.P. zones along {111} and {100} interfaces as a function of aging temperature in the range of 110 to 350°C using TEM and field-ion microscopy, respectively. Their results both show that the zones are highly faceted at low aging temperatures, in agreement with Gronsky (76), and that the amount of faceting decreases with increasing aging temperature, such that large zones formed at higher aging temperatures approach a spherical shape. Alexander et al. (77) further use a discrete lattice plane model modified by the incorporation of thermodynamic functions appropriate to the fcc Al-Ag solid solution to calculate the orientation dependence of the chemical interfacial energy as a function of reaction temperature and thereby, account for the faceting and its temperature dependence.

No further work has been performed regarding the composition or degree of ordering within the zones.

2.3. γ' Precipitates

The transition phase γ' has a hcp crystal structure with lattice parameters a = 2.858-2.87 Å and c = 4.607 Å (69,79,80). Its orientation relationship with the matrix is:

$$(111)_\alpha // (0001)_{\gamma'} \quad ; \quad [110]_\alpha // [11\bar{2}0]_{\gamma'},$$

which is the best fit of the hexagonal lattice with the cubic matrix (Fig. 2).

Although some investigators (81) contend that γ' results from growth of the G.P. zones and Howe and Gronsky (73) have shown that under certain circumstances that can occur, Nicholson and Nutting (74) found that γ' usually nucleated heterogeneously, mainly on helical dislocations, and these bands of precipitates gradually expanded to form a uniform distribution of γ'. They suggested that nucleation occurred by Ag enrichment of the helical dislocations which lowered the stacking fault energy (82), followed by climb of the dislocations onto a {111} plane, and formation of two partial dislocations separated by a ribbon of stacking fault (γ' precipitate) according to the reaction:

$$a/2[\bar{1}10] \rightarrow a/3[\bar{1}11] + a/6[\bar{1}1\bar{2}].$$

Nicholson and Nutting also showed that the γ' precipitates were faulted during the initial stages of growth due to missing a/6<112> shears on alternate {111} planes. This result was deduced from the lengths of streaks through the <000> reciprocal lattice point, compared to the thicknesses of γ' plates measured from electron micrographs. Once the plates were 200Å or thicker, the precipitates were found to be nearly perfect. These investigators also showed that the removal of stacking faults with increasing thickness was accompanied by long-range ordering in the c-direction, since <0001> reflections were observed in the <110> diffraction patterns. They suggested that the ordering might be due to alternate basal planes with compositions of Al_2Ag and pure Ag.

Hren and Thomas (35) also studied the growth and dissolution of γ' precipitates in an Al-20 w/o Ag alloy "in-situ" by hot-stage TEM. All dislocations were found to be effective nucleation sites for γ' precipitates within the temperature range of 100 to 400°C, and either produced

a single orientation of γ' by a reaction of the type:

$$a/2[\bar{1}10] \rightarrow a/6[\bar{1}2\bar{1}] + a/6[\bar{2}11], \text{ fault on } (111)$$

or two orientations of γ' by reactions such as:

$$a/2[110] \rightarrow a/3[\bar{1}11] + a/6[\bar{1}1\bar{2}], \text{ fault on } (\bar{1}11)$$

$$a/3[111] \rightarrow a/6[011] + a/6[\bar{2}11], \text{ fault on } (111).$$

Growth parallel to the γ' basal planes occurred rapidly and appeared to be controlled by the creation of additional faults on alternate {111} planes. In this same work, ordering was detected in the earliest stages of growth suggesting that in thin foils, the precipitates are always nearly perfect. These same precipitates subsequently became disordered during the later stages of growth above about 350°C, as evidenced by the disappearance of the <0001> reflections.

Howe et al. (60-62) also studied the structure of γ' precipitates in an Al-14.92 w/o alloy aged at 350°C using both conventional and high-resolution TEM. These investigators showed that plate thickening occurs by the passage of Shockley partial dislocations on alternate {111} planes and that there is a strong tendency for diffusional and/or elastic interactions among the ledges, giving rise to multiple-unit ledges which display the diffraction contrast behavior of 1/2<110> dislocations. They also showed that the {111} matrix planes are continuous across the edges of ledges indicating that the ledges are largely coherent, and that the terraces between ledges are atomically flat and ledges are uniformly stepped-down from the centers to the edges of isolated precipitates, as predicted by the general theory of precipitate morphology. Observations of precipitate edges also indicated that they are composed of similar two-plane ledges arranged vertically above one

another and thus, that they may grow by the same mechanism of atomic attachment as ledges on the faces. In addition, the aspect ratios of early-stage γ' precipitates were observed to be much larger than calculated equilibrium values, probably due to the ledge mechanism of growth, and all interfaces of the precipitates displayed a strong preference for low-energy <110> configurations within the resolution limits of the techniques employed. Lastly, all three variants of Shockley partial dislocations were seen on the same {111} planes of precipitates, and these authors proposed that this may be due to a reduction in strain energy associated with growth of γ' precipitates.

Aaronson et al. (83) also showed that in an Al-15 w/o Ag alloy, the splitting of $a/2[\bar{1}10]$ dislocations into partials occurs at temperatures below 375°C. They proposed that the volume free energy change accompanying formation of γ' must be greater than the sum of the interfacial free energies of the faces and edges for nucleation to occur.

It is interesting to note that no explanation for the decrease in the c/a ratio during growth of γ' from 1.63 (for perfect close packing) to 1.59 (γ' prior to γ), i.e. 2.5%, has been offered, and no quantitative chemical microanalyses have been reported for this phase.

2.4. γ Precipitates

The equilibrium γ phase has a composition near Ag_2Al and is hexagonal, with a = 2.885 Å and c = 4.582 Å at the Al end, to a = 2.870 Å and c = 4.662 Å at the Ag side (Figs. 1 and 2) (84-87). Its space group is $P6_3/mmc$, two atoms to the unit-cell, randomly occupied by Ag or Al, although ordering within the phase has been observed (68,88). For example, Neumann (88) found that single crystals of Ag_2Al aged for 10 days

at 180°C displayed short-range ordering within the basal planes, where each Al atom was surrounded by six Ag atoms, and that some undetermined long-range order occurred on alternate basal planes in the c-direction of the crystal.

The formation of γ occurs either by discontinuous precipitation in which a favorably oriented grain boundary migrates through the G.P. zones and γ' precipitates, or by the transformation of γ' directly into γ by the acquisition of misfit dislocations (63,67). Since the stable γ phase is thought to differ from the transition phase γ' only by its dimensions a and c, it has been suggested (87) that γ' is merely a stressed form of γ, the stresses arising from coherency strains prior to the formation of misfit dislocations.

Laird and Aaronson (63) studied the interfacial structure of the faces of γ precipitate plates in an Al-15 w/o Ag alloy and found them to be decorated with three types of dislocation arrays: 1) parallel arrays, 2) grids consisting of two sets of parallel arrays, and 3) hexagonal nets of dislocations. All dislocations had a/6<112> edge-type Burgers vectors parallel to the broad faces of the γ precipitates; however, their sometimes uneven spacings indicated that they were often not in equilibrium arrangements. Laird and Aaronson (36) also studied the lengthening and thickening of the precipitates "in-situ" by hot-stage TEM. Thickening occurred by the migration of ledges in the form of dislocations or ordered arrays of dislocations across the semicoherent faces. Lengthening also occurred by the movement of ledges or "super-ledges" a few hundred Angstroms in height. The measured thickening rates were found to be much slower than those predicted by volume diffusion

control, a result which was consistent with growth rates controlled by interfacial ledges.

Abbott and Hawarth (37) used microprobe analyses to monitor the solute distribution around isolated γ plates during dissolution. In all cases, they found that the solute concentration at the precipitate/matrix interface was less than the equilibrium value, a result which they interpreted as evidence for interface controlled dissolution.

Sagoe-Crentsil and Brown (38) also studied the dissolution of $\gamma(Ag_2Al)$ plates in an Al-15.3 w/o Ag alloy between temperatures of 466 and 494°C, using a combination of SEM and electron probe studies. They found that growth at the tips of precipitates varied linearly with time while growth of the faces was parabolic with time. The broadface kinetics were slower than expected for volume diffusion control. Composition profiles adjacent to the faces and tips of precipitates were found to be similar, indicating that the tips of precipitates should grow slower than was observed experimentally while the edges should grow faster than was observed experimentally. They proposed that this discrepancy can be explained by an extra flow of solute from the tips to the faces of precipitates by an interfacial dislocation network which acts as a short circuit for solute.

3. THEORIES OF PRECIPITATE PLATE GROWTH

Several theories of precipitate plate growth are outlined in the following sections, with specific reference to the Al-Ag system whenever possible. These sections were included because there is currently considerable debate as to whether interfacial energy effects (39), strain energy effects (89), or the atomic mechanisms of growth (13) are responsible for the morphologies and aspect ratios of plate-shaped precipitates, such as the γ' precipitates examined in this study, as discussed in more detail in Appendix 10.4. Thus, the following summary serves as a theoretical base to which the experimental results of subsequent sections may be compared.

3.1. Interface Structure

3.1.1. Coherent Interfaces

A fully coherent interface results when when two different crystals match across an interface plane such that the lattice is continuous across this plane (90,91). This can only occur when the two crystals are oriented so that they have the same atomic configuration at the interface. For the particular case of an hcp precipitate in an fcc matrix, the $\{111\}_{fcc}$ and $\{0001\}_{hcp}$ planes are hexagonally close-packed, with the same interatomic distances for identical atom species. When these two crystals are joined across their close-packed planes, the resultant interface is completely coherent with the following orientation relationship:

$$(111)_{fcc}//(0001)_{hcp} \quad ; \quad [110]_{fcc}//[11\bar{2}0]_{hcp}.$$

If more than one atomic species is present in the system, such as with Al-Ag, then there will also be a particular arrangement of atoms

which produces the lowest energy in each phase. It is likely that a change in chemical composition will occur across the interface resulting in a chemical contribution to the interfacial energy, because some atoms will be bonded to less favorable neighbors across the interface. In general, coherent interfacial energies can vary from a few up to around 200 ergs/cm^2. Aaronson et al. (92) have estimated the chemical interfacial energy ($\Delta F_{\alpha\gamma}^{chem}$) along coherent regions of γ precipitates in an Al-18 w/o Ag alloy as about 40 ergs/cm^2 using the relationship of Servi and Turnbull (93) below:

$$\Delta F_{\alpha\gamma}^{chem} = \frac{nz_\gamma(x_\gamma - x_\alpha)^2 \Delta H^\circ}{Nz_\alpha} \qquad (1)$$

where n = number of atoms per unit area in the plane of the interface, z_γ = number of bonds between an atom at the boundary in the precipitate and the nearest neighboring atoms across the boundary, x_γ = mole fraction of Ag in γ at the boundary, x_α = mole fraction of Ag in the alloy, z_α = coordination number in the matrix, and ΔH° = enthalpy of solution of γ in an infinitely dilute solution of α.

3.1.2. Semicoherent (Misfit Dislocation) Interfaces

When the distance between atoms is different across an interface, it is still possible to maintain coherency by straining both of the lattices. The strain, however, increases the energy of the system roughly proportional to the square-root of the misfit and for sufficiently large misfits, it then becomes more favorable energetically to replace the coherent interface with a semicoherent interface, where the disregistry is accommodated by misfit dislocations. This appears to be the case for the transition of a γ' to a γ precipitate. The disregistry (δ) between

two lattices may be defined as:

$$\delta = \frac{a_\beta - a_\alpha}{a_\alpha} \tag{2}$$

where a_β and a_α are the lattice parameters of the unstrained α and β lattices, and $a_\beta > a_\alpha$. It has been shown (94-96) that in one dimension, the misfit can be accommodated without any long-range strain fields by a set of edge dislocations of equilibrium spacing (D) given by:

$$D = \frac{a_\alpha}{\delta} \tag{3}$$

and that for small misfits:

$$D \sim \frac{b}{\delta} \tag{4}$$

where b is the Burgers vector of the dislocations, given as:

$$\mathbf{b} = \frac{a_\alpha + a_\beta}{2} \tag{5}$$

These equations indicate that as the misfit increases, the dislocation spacing decreases. There may also be misfit in two or three directions of an interface as in the basal planes of hexagonal γ' precipitates, and in this case, the coherency strains can be relieved by introducing a second and third set of dislocations of spacing $D_2 \sim b_2/\delta_2$ and $D_3 \sim b_3/\delta_3$.

Once strain has been accommodated by misfit dislocations, the matching in a semicoherent interface is then nearly perfect except for highly distorted regions around the misfit dislocations, which terminate at the interface. Accordingly, the interfacial energy of a semicoherent interface can be considered to consist of two parts (97): 1) a chemical contribution (ΔF^{chem}) as for the fully coherent interface, and 2) a

structural contribution (ΔF^{str}) due to the structural distortions caused by the misfit dislocations. This structural contribution increases roughly proportional to $\delta^{1/2}$, but levels off as δ approaches 0.25, because the dislocation strain fields begin to overlap and cancel each other. The energies of semicoherent interfaces generally range from about 200 to 500 ergs/cm^2.

Frank and van der Merwe (94-96) derived the following expression for the total interfacial energy of an α/β boundary ($\Delta F^{tot}_{\alpha\beta}$) using elastic continuum mechanics:

$$\Delta F^{tot}_{\alpha\beta} = \frac{\mu \mathbf{b}}{4\pi^2} \{1 + \beta - (1 + \beta^2)^{1/2} - \beta \ln [2\beta(1 + \beta^2)^{1/2} - 2\beta^2]\} \quad (6)$$

where

$$\beta = 2\pi\delta(\Omega/\mu) \quad (7)$$

$$1/\Omega = [(1 - \sigma_\alpha)/\mu_\alpha] + [(1 - \sigma_\beta)/\mu_\beta] \quad (8)$$

and μ = shear modulus at the boundary, μ_α and μ_β = shear modulus within α and β, σ_α and σ_β = Poisson's ratio within α and β, and $\mathbf{b}$ is given by Eq. (5). The term Ω accounts for elastic interactions within each crystal, while μ recognizes such interactions across the α/β boundary. Aaronson et al. (92) have estimated the structural contribution ($\Delta F^{str}_{\alpha\gamma}$) to the total interfacial energy ($\Delta F^{tot}_{\alpha\gamma}$) of a γ precipitate to be about 115 ergs/cm^2 using this relationship. When added to the chemical energy ($\Delta F^{chem}_{\alpha\gamma}$) and multiplied by a scaling factor (0.75) to account for slight variations in data (98), this yielded a total interfacial energy of 130 ergs/cm^2.

3.1.3. Incoherent Interfaces

When δ exceeds 0.25, or one dislocation every four interplanar spacings, the regions of distortion around the dislocations overlap to the extent that the interface can be considered as incoherent (99). An incoherent interface can also result when two adjacent crystals have very different atomic configurations across an interface, with very little possibility of good atomic matching. Very little is known about the actual atomic structure of incoherent interfaces although in the past, they have often been considered to have a disordered structure. More recent studies, however, indicate that there is probably some long-range matching across most interfaces (100,101). Incoherent interfaces have energies which range from about 500 to 1000 ergs/cm^2. The energy of a disordered γ precipitate interphase boundary ($\Delta F_{\alpha\gamma}^{dis}$), i.e. possibly at a plate edge, has been estimated as 350 to 465 ergs/cm^2 (36,92).

The previous sections were included to summarize several aspects of interfacial structure which are relevant to this study. Considerably more detailed and eloquent treatments of boundary structure may be found in a number of references (90,91,100,102-106).

3.2. Interface Migration

In the previous treatment of semicoherent interfaces, the misfit dislocations were assumed to epitaxial, i.e. their Burgers vectors were contained within the interface plane and connected corresponding lattice sites. Glide of this type of dislocation cannot cause the interface to advance and therefore, the interface is sessile. It is possible to have glissile interfaces, however, where glide of the interfacial dislocations results in a change in the stacking sequence of the matrix to that

of the precipitate. The α_{fcc} to γ'_{hcp} transformation is an example of this mechanism. As shown in Fig. 3, glide of a Shockley partial dislocation with Burgers vector $\mathbf{b} = a/6[11\bar{2}]$ on (111) locally changes the stacking sequence from fcc to hcp. If additional Shockley partial dislocations pass along every other (111) plane, the region of hcp stacking is extended two layers at a time in a direction normal to the dislocation glide plane (107,108). Therefore, these dislocations serve the dual purpose of accommodating misfit at the interface as well as providing the necessary structural change for the fcc to hcp transformation. The same structural change can also be accomplished by the expansion of an $a/3[111]$ vacancy-type loop on a (111) plane; however, unlike the previous case involving a Shockley partial dislocation, this is a nonconservative process requiring the addition of vacancies for dislocation climb (102).

An important characteristic of glissile dislocation interfaces is that they can produce a macroscopic shape change within the crystal. For example, Fig. 4 shows two different ways of transforming cubic close-packed planes into a hexagonal lattice (107). As shown in Fig. 4 (a), if the fcc to hcp transformation is accomplished by passage of identically oriented Shockley partials of the same type on every other (111) plane, then an overall shape change occurs. This distortion must be accommodated within the matrix, resulting in a very high strain energy at precipitate edges. However, if the transformation is accomplished by using equal numbers of all three Shockley partials on (111), as illustrated in Fig. 4 (b), then a large shape change does not occur. Such an arrangement would be highly favored from a strain energy viewpoint and

consequently, the Shockley partial dislocations might be stacked vertically rather than at an angle as in the previous case. The appearance of all three types of Shockley partials on the same faces of precipitates and the residual contrast associated with the edges of γ' plates led Howe et al. (60,61) to suggest that the latter situation might exist for these precipitates.

3.3. Precipitate Shape Due to Interfacial Energy Effects

3.3.1. Coherent Precipitates

As discussed in Sec. 3.1., there are two main contributions to the energy of an interphase interface: 1) structural and 2) chemical. Therefore, from an interfacial energy viewpoint, it is favorable for a precipitate to be completely surrounded by low-energy coherent interfaces, thus minimizing the structural contribution to the interfacial energy. Accordingly, the major contribution to the interfacial energy is the chemical one, and the boundary will align along low-index precipitate/matrix planes in order to minimize the number of unlike bonds across the interphase boundary. This theory thus predicts that coherent precipitates will assume a shape which minimizes their interfacial energy; that is, they will be faceted along low-index planes. This can only occur, however, if the precipitate has the same crystal structure and similar lattice parameter as the matrix. An example of this occurs in the Al-Ag system, where Ag-rich G.P. zones form in the Al matrix. Since the atomic diameters of Al and Ag differ by only 0.7%, coherency strains contribute a negligible amount to the total energy of the alloy, and the equilibrium shape can be predicted from a γ-plot of the interfacial energy (109), as shown by LeGoues and Aaronson (110),

and experimentally confirmed by Gronsky (76) and Alexander et al. (77).

3.3.2. Semicoherent Precipitates

When the crystal structure of a precipitate differs from that of the matrix, it may be difficult to find a lattice plane that is common to both phases. However, for certain combinations, such as an hcp precipitate in an fcc matrix, good matching occurs across the close-packed planes and the precipitate is able to form a low-energy coherent or semicoherent interface. Good matching does not usually occur across other planes, however, and the precipitate edges may be bounded by high-energy incoherent interfaces. Such a situation was thought to occur when the general theory of precipitate morphology was first proposed, and was originally envisioned for the growth of $\gamma(Ag_2Al)$ precipitates (13). A γ-plot of the interfacial energy (111) in this case resembles a sphere with two cusps normal to the coherent interface, as shown in Fig. 5. Subsequently, the Wulff theorem (112) predicts a disc-shaped equilibrium precipitate with an aspect ratio of γ_i/γ_c, where γ_i and γ_c are the energies of the incoherent and (semi)coherent interfaces, respectively. Additionally, angular, plate-shaped precipitates are predicted if the γ-plot also contains smaller cusps arranged symmetrically in the plane of the plate. This appears to be the case for γ' and γ hexagonal precipitates in Al-Ag alloys, which are faceted along low-index <110> directions in the {111} matrix planes (60,63).

Aaronson et al. (92) have roughly estimated the interfacial free-energies of coherent, semicoherent and disordered Al/Ag_2Al interfaces in an Al-18 w/o Ag alloy as about 40, 130 and 350 ergs/cm^2, respectively, as mentioned in Sect. 3.1. Based on these estimates, the equilibrium

aspect ratios of coherent and semicoherent precipitates should be about 9:1 and 3:1. However, Howe et al. (61) have shown that γ' precipitates can have aspect ratios significantly larger than these at the earliest stages of growth, i.e. as large as 35:1, indicating that some other mechanism is responsible for the large aspect ratios of these precipitates. Subsequent results of the present study will show that although the chemical contribution to the interfacial energy does play a significant role in the growth process and in determining the structure at the precipitate/matrix interface, it is not the limiting reaction which ultimately controls the morphologies and aspect ratios of these precipitates.

It should be noted that the above Wulff construction only predicts the equilibrium shape when misfit strain energy effects are negligible. Otherwise, one must utilize models which incorporate elastic strain effects, as discussed in Sect. 3.4.

3.3.3. Incoherent Precipitates

When two phases have two completely different crystal structures or their lattices are in a random orientation, it is unlikely that coherent or semicoherent interfaces form, and the precipitate is said to be incoherent. In this case, a γ-plot and the precipitate shape are roughly spherical, since the interfacial energy is high for all interface planes. Some faceting may occur, however, if particular crystal planes lie at cusps in the γ-plot.

3.4. Precipitate Shape Due to Strain Energy Effects

3.4.1. Coherent Precipitates

It is now well-established that the elastic strain energy exerts a large influence in determining both the shape and habit plane of a coherent precipitate (12,89,113-122). The stresses and strains created in both a precipitate and the surrounding matrix were shown by Eshelby (115,116) to be proportional to the shape change that would have occurred in the precipitate, had the surrounding matrix not constrained the transformation process. This shape change is denoted by the stress-free transformation strain tensor (ε^T_{ij}). Eshelby also showed that the energy stored in an elastic strain field caused by the transformation of an ellipsoidal precipitate could be expressed as:

$$E = -1/2 \int \sigma^P_{ij} \varepsilon^T_{ij} \, dV = -1/2 \int C_{ijkl} \varepsilon^P_{kl} \varepsilon^T_{ij} dV \qquad (9)$$

where E = the total strain energy of the transformation, σ^P_{ij} and ε^P_{kl} = the stresses and strains within the coherent precipitate, C_{ijkl} = the elastic constants, and the integral is over the volume of the precipitate. Thus, the most important factors in determining the shape and habit plane of a precipitate are the magnitudes and directions of the stress-free transformation strains and the elastic constants of the precipitate and matrix.

While analytic solutions for Eqn. (9) exist for a variety of possibilities (113,114,123-126), the particular case of a plate-shaped precipitate which undergoes a tetragonal transformation strain, such as the γ' precipitates in this study, where $\varepsilon^T_{ij} = \begin{pmatrix} \varepsilon_{11} & & \\ & \varepsilon_{22} & \\ & & \varepsilon_{33} \end{pmatrix}$ and $\varepsilon_{11} = \varepsilon_{22} \ll \varepsilon_{33}$, can be easily visualized using simple physical insight. As

illustrated in Fig. 6, the elastic strain energy can be minimized by making a given volume of precipitate as large as possible in the small strain direction parallel to the faces, and as small as possible in the large strain direction perpendicular to the plate faces. Thus, the minimum energy configuration is an infinitely thin precipitate plate. In addition, if the matrix is elastically anisotropic, it is easier for the matrix to accommodate misfit perpendicular to the plane of the precipitate if this maximum strain direction lies parallel to elastically "soft" directions in the matrix. Hence, these two factors predict that a precipitate which undergoes a tetragonal transformation strain will form as a thin plate which lies along elastically soft planes in the matrix. In this case, the strain components are $\varepsilon_{11} = \varepsilon_{22} = \Delta/3$ and $\varepsilon_{33} = \xi + \Delta/3$, and the solution for the elastic strain energy per unit volume of precipitate (E_V) is given as (127):

$$E_V = \frac{\mu}{(1 - \nu)} \{2/9(1 + \nu)\Delta^2 + \pi/4\xi^2(c/a) + \pi/3(1 + \nu)\Delta\xi(c/a)\} \quad (10)$$

where μ = shear modulus, ν = Poisson's ratio, ε_{11}, ε_{22} and ε_{33} = principal stress-free transformation strains, Δ = uniform dilation $\Delta V/V$, ξ = extra strain normal to the habit plane, c/a = inverse precipitate aspect ratio, i.e. c = the precipitate thickness and a = the precipitate diameter, and assuming isotropic elasticity and that the matrix and precipitate have the same elastic constants. The first term represents the shape independent energy due to a dilation alone, the second term is the energy due to the uniaxial strain alone, and the third term is regarded as an interaction energy. Since $\Delta + \xi = \delta V$, the fixed volume change of the transformation, E_V is a function of only Δ and c/a.

If a simple shear (s) along the habit plane is also associated with the transformation, $\varepsilon_{13} = \varepsilon_{31} = s/2$ and the additional strain energy per unit volume of precipitate due to this shear (E_s) is (127):

$$E_s = \frac{\mu}{(1 - \nu)} [\pi/8(2 - \nu)s^2(c/a)] \qquad (11)$$

where the amount of shear is fixed by the crystallography of the transformation and the value of Δ. Thus, the total strain energy per unit volume of precipitate is equal to $E_v + E_s$, and both the normal and shear components of the strain can best be accommodated by minimizing c/a.

3.4.2. Semicoherent Precipitates

The treatment of semicoherent precipitates is similar to that of coherent precipitates. Again, in the case of tetragonal strains, strain energy considerations predict that precipitates should form as thin plates, where the thin direction is parallel to the direction of maximum strain. However, unlike the case of coherent precipitates, semicoherent precipitates must lie along plastically soft directions within the matrix. The reason for this is that they must lie parallel to appropriate slip systems within the matrix, in order to accommodate the slip dislocations necessary for growth. Such precipitates thus have an invariant plane (118) and often grow by the movement of glissile dislocation interfaces, as described in Sect. 3.2. For the case of γ' precipitates in an Al matrix, these plates lie along the four {111}<110> slip systems in the matrix, thus accommodating the Shockley partial dislocations needed to achieve the fcc → hcp structural transformation. This feature is illustrated by Fig. 7, which shows an early-stage γ' precipitate that is only two {111} planes high, i.e. 4.6 Å thick, and has an

aspect ratio of about 20:1. Notice the stacking change across the precipitate, indicating its hcp structure. Such precipitates were commonly observed in thin foils in this investigation, and the effects of surface and elastic strain energies on their aspect ratios are discussed in future detail in Appendix 10.4.

3.4.3. Incoherent Precipitates

When a precipitate is incoherent with the matrix there are no coherency strains; however, misfit strains still arise if the precipitate is the wrong size for the space it occupies in the matrix. Elastic strain fields result when the matrix and precipitate are constrained to occupy the same volume, where the elastic strain energy now increases as the square of the volume misfit (δ), and $\delta = \Delta V/V$. In addition, Nabarro (128) has shown that the aspect ratio also contributes to the strain energy of an incoherent inclusion, being highest for a sphere ($c/a = 1$), intermediate for a needle ($c/a = \infty$) and lowest for a thin oblate spheroid where $c/a \sim 0$.

3.5. Precipitate Shape Due to Atomic Mechanisms of Growth

3.5.1. General Theory of Precipitate Morphology

As mentioned in the Introduction, in 1962 Aaronson (13) proposed a general theory of precipitate morphology based on the migration of coherent or partially coherent interfaces by a ledge mechanism. Essentially this theory states that when the composition and crystal structure of a precipitate differ from that of the matrix, the precipitate shape is determined by the mechanisms of atomic attachment across the interphase boundary. In the particular case of precipitate plates, this theory further predicts that the precipitates should have the overall

shape sketched in Fig. 8., when viewed edge-on. Here, it was envisioned that a plate-shaped precipitate should possess at least one orientation in which there was good atomic matching with the matrix, and that this interface would thus constitute the habit plane or faces of the precipitate. Because of the coherency of these faces, they would not be able to move normal to themselves and were thus constrained to grow by a ledge mechanism, where ledges nucleated near the center of the precipitate and migrated laterally across the faces, as indicated by arrows in Fig. 8. The edges of the ledges, as well as the edges of the precipitate, were not expected to be in a favorable orientation with the matrix and were therefore thought to possess a disordered structure (similar to a high-angle grain boundary), which could grow at a rate limited only by nonstructural factors such as long-range volume diffusion. Because the nucleation and passage of ledges along the faces of precipitates was considered to be overall a much slower process than the normal migration of the disordered edges, this was thought to cause the large aspect ratios of these precipitate plates. Subsequent observations (36) that precipitates may be fully or partially coherent in a number of different boundary orientations and not just at their faces led to a further revision of the theory that the morphology might also depend on factors such as interledge spacing versus boundary orientation (14).

Because the general theory of precipitate morphology is concerned with diffusional nucleation and growth, it is important that the kinetic aspects of the migration of coherent and disordered interphase boundaries be considered. A detailed summary of these kinetic analyses was recently given by Howe (129) and will not be repeated here, since this

study is primarily concerned with the structural aspects of the general theory of precipitate morphology.

In the case of γ' precipitates in Al-Ag alloys, two processes have to occur for the precipitates to grow. First, there has to be a structural change in order to transform the fcc matrix into the hcp precipitate. This structural transformation has been proposed to occur by the passage of Shockley partial dislocations on every other {111} matrix plane, as illustrated in Fig. 3, and there has been ample experimental evidence to show that this does occur (35,60-63). In Fig. 8, the transformation can be described as occurring in the C-plane of matrix atoms, where passage of a Shockley partial dislocation changes the stacking sequence of the matrix (ABC) to that of the precipitate (ABA), thus causing the precipitate to thicken by two atomic planes. This implies that single ledges should be two {111} matrix planes high. The second change which must occur, is that Ag atoms must diffuse to the precipitate, cross the interphase boundary (presumably at the ledges), and become incorporated into the hcp structure, since the equilibrium composition of γ' and γ precipitates is usually assumed to be Ag_2Al, or 66 a/o Ag. The questions that remain to be answered are exactly how the chemical and structural changes occur, and how they are related; that is, whether one precedes the other, or whether they occur concurrently.

4. TRANSMISSION ELECTRON MICROSCOPY TECHNIQUES

4.1. Conventional TEM (Amplitude Contrast Imaging)

The formation of an image in the TEM can be described by the Abbe theory of image formation for an objective lens (130,132). Abbe's theory says that for plane parallel incident illumination, all radiation which is scattered by the object at the same angle will be focussed to a single point in the backfocal plane of the objective lens. The amplitude distribution in the back-focal plane is therefore the Fraunhofer diffraction pattern of the object. The formation of such a pattern is described mathematically by the Fourier transform. If the object is a crystalline specimen, then not only will there be sharp diffraction maxima in addition to a central spot, but there will also be a scattering distribution around each spot due to the size, shape and thickness variations of the portion of the crystal giving that spot. If the amplitude distribution at the exit face of the crystal is given by a transmission function, say $q(x,y)$, then the amplitude distribution in the back-focal plane of the objective lens $Q(u,v)$ is calculated by taking the Fourier transform (F) of $q(x,y)$, or:

$$Q(u,v) = F[q(x,y)] = \iint q(x,y)\exp[2\pi i(ux + vy)]dxdy. \qquad (12)$$

Furthermore, the diffracted intensities $I(u,v)$ at position (u,v) in reciprocal space can be computed from the square of the amplitude distribution multiplied by a transfer function $S(u,v)$ which accounts for the aperture and aberrations limitations of the objective lens, as:

$$I(u,v) = |Q(u,v)S(u,v)|^2. \qquad (13)$$

The second function of the objective lens is to take all radiation scattered from each point in the object and recombine it in the image plane with the correct relative phases to form a wave function $\psi(x,y)$, where:

$$\psi(x,y) = q\left(\frac{-x}{M}, \frac{-y}{M}\right) . \tag{14}$$

Thus, it recreates the transmission function of the object, inverted and magnified by a factor (M). The recombination of diffraction spectra during image formation is again described mathematically by the Fourier transform and therefore, the amplitude distribution in the image plane is given by:

$$F[Q(u,v)S(u,v)] = q(x,y) * s(x,y) = \iint [q(X,Y)s(x - X, y - Y)]dXdY \tag{15}$$

where $s(x,y)$ now represents a smearing or spread function. This is accounted for mathematically by a convolution integral, since the Fourier transform of a product of two functions is the convolution of their Fourier transforms. The intensity distribution in the image plane may be similarly computed from the square of the amplitude distribution as:

$$I(x,y) = \psi\psi^* = |q(x,y) * s(x,y)|^2. \tag{16}$$

If an aperture is used to select one particular diffraction spot and its surrounding scattering from the amplitude distribution in the back-focal plane, the image will show intensity only for those regions of the crystal giving that diffracted spot. Changes in the image intensity will result from corresponding variations in the diffracted intensity due to variations in thickness, orientation, composition or degree of imperfection of tne crystal region. Conventional bright-field (BF)

imaging allows only the forward scattered beam to pass through the objective aperture and therefore, contribute to image formation. A bright-field image is thus a map of the intensity variation I(x,y) of the forward scattered beam. Similarly, a dark-field (DF) image constitutes a map of the intensity variation of one of the Bragg scattered beams, or of a particular region of diffuse scattering from the specimen. It is apparent that the resolution of this type of image is dependent on how localized the scattering event is in the specimen.

4.2. High-Resolution TEM (Phase Contrast Imaging) and Image Simulations

In the previous section, image contrast resulted from the intensity variation of a single scattered beam. This section discusses contrast which results when two or more scattered beams are allowed to pass through the objective aperture. This method relies on phase differences which are induced in the electron beam as it passes through the specimen and down the microscope column and hence, it is referred to as phase contrast imaging. Unlike amplitude contrast imaging where the resolution is limited by how localized scattering is within the specimen, this type of imaging is capable of resolving single atoms, provided aberrations within the microscope are low enough to recreate the transmission function of the specimen. Hence, it is the quality of the microscope which limits the resolution of this type of imaging process.

In order to obtain an image which is directly interpretable in terms of the actual atomic arrangement in a crystal, special experimental conditions must be satisfied. First, the wave function at the exit face of the specimen should have a direct relationship with the structure of the crystal. Since the wave function is necessarily two-

dimensional, interpretation of an image in terms of the projected atom positions requires that the specimen be oriented very precisely (130). Experimentally, this can be achieved by obtaining the highest order of symmetry between corresponding diffraction spots, or by maximizing the symmetry of higher-order Laue zone lines using convergent-beam electron diffraction. Secondly, the combined influence of aberrations, defocus and aperture limitations of the objective lens must be such as to turn the wave function into an image intensity which has some direct relationship with a projection of the specimen structure. This requires knowledge of the microscope and specimen parameters: C_s = spherical aberration coefficient of the objective lens, C_c = chromatic aberration coefficient, Δz = defocus value of objective lens, λ = the electron wavelength, α_i = beam convergence angle, r = aperture radius and t = specimen thickness. In addition, the microscope must be precisely aligned (131). Many of the parameters above can be determined experimentally, as outlined by Spence (132) and Gronsky (133), particularly with the aid of an optical bench.

In very thin specimens, i.e. less than 100 Å, of low atomic number, the lateral spread of the electron wave due to Fresnel diffraction may be neglected and the wave may be considered to travel straight through the specimen, experiencing only a phase change which is proportional to the electrostatic potential it has encountered along a straight line path. The specimen is thus a phase object with a transmission function $q(x,y) = \psi_e(x,y)$ at the exit face of the crystal, given by the complex wave amplitude (134-139):

$$\psi_e(x,y) = \exp[-i\sigma\phi_p(x,y)] \tag{17}$$

where the interaction constant $\sigma = 2\pi me\lambda/h^2$, m = mass of the electron, e = charge of the electron, h = Plank's constant, and $\phi_p(x,y) = \int_{-t/2}^{t/2} \phi(x,y,z)dz$ = the projected specimen potential along the beam direction, defined as the z-axis. This phase object assumes the Ewald sphere to be a plane normal to the incident beam direction. A further approximation, known as the weak-phase object approximation, assumes kinematic scattering within the specimen and therefore, that the phase change $\sigma\phi_p(x,y)$ is much less than $\pi/2$. Under these conditions:

$$\psi_e(x,y) \sim 1 - i\sigma\phi_p(x,y) \tag{18}$$

and the complex amplitude distribution in the back-focal plane of the objective lens is given as:

$$\psi_d(u,v) = \delta(u,v) - i\sigma F[\phi_p(x,y)] \tag{19}$$

where $\delta(u,v)$ = a sharp delta-function peak and $F[\phi_p(x,y)]$ = a scattered amplitude. In addition, the corresponding intensity in the back-focal plane is then given by:

$$I(u,v) = \delta(u,v) + \sigma^2[\phi_p(u,v)]^2 \tag{20}$$

where $\phi_p(u,v) = F[\phi_p(x,y)]$. In practice, however, complete reconstruction is not achieved in the back-focal plane due to lens aberrations, apertures and microscope instabilities. These factors introduce perturbations in the phase of the scattered wavefront and in HREM, are represented by a contract transfer function (CTF) (140). This is done mathematically by multiplying the wave function $\psi_d(u,v)$ in the back-focal plane by a phase factor $\exp[i\chi(u,v)]$ and an aperture function

A(u,v), to produce the actual wavefront transferred by the objective lens as:

$$\psi_d'(u,v) = \delta(u,v) - i\sigma F[\phi_p(x,y)]A(u,v)\exp[i\chi(u,v)] \qquad (21)$$

Here, $\chi(u,v)$ is the phase distortion function, given as (132,141):

$$\chi(u,v) = \frac{2\pi}{\lambda}\left[C_s\frac{\lambda^4 g^4}{4} + \Delta z\frac{\lambda^2 g^2}{2}\right] \qquad (22)$$

which accounts for the effects of spherical aberration through C_s, and the condition of focus by the defocus value (Δz). From Eqn. (22), it is apparent that greater distortions occur for beams lying further from the optic axis. The detrimental effects of spherical aberration, however, can be lessened by under-focussing the objective lens, i.e. Δz is negative. This was first recognized by Scherzer (142), who defined the optimum degree of underfocus (Δz_{Sch}) for maximum resolution (d_{Sch}), where $\sin\chi = -1$ over the maximum range of spatial frequencies as:

$$\Delta z_{Sch} = -1.2(C_s\lambda)^{1/2} \qquad (23)$$

where

$$d_{Sch} = 0.7\ C_s^{1/4}\lambda^{3/4}. \qquad (24)$$

It is apparent that the resolution improves with both decreasing C_s and λ, through improved lens designs and higher accelerating voltages, respectively. Similarly, the aperture function A(u,v) is taken to include the presence of a physical aperture in the back-focal plane and/or envelope functions (E_α), which reflect the influence of a finite illumination angle α_i and (E_c), which accounts for phase effects due to chromatic aberrations, i.e. voltage and current instabilities in the electron source and lenses (132,143). Since these envelope functions

act as a virtual aperture in the back-focal plane, it is desirable to maximize both the spatial and temporal coherence of the source and minimize microscope instabilities, so that maximum recombination of the wave function can occur.

A further Fourier transform of Eqn. (21) then gives the complex image amplitude as:

$$\psi_i(x,y) = 1 - i\sigma\phi_p(x,y) * F\{A(u,v)\exp[i\chi(u,v)]\}. \qquad (25)$$

Since the transforms of the sine and cosine of $\chi(u,v)$ are both real and the cosine term is small within the domain of the weak-phase object approximation, the image intensity can then be expressed as:

$$I(x,y) = \psi_i(x,y)\psi_i^*(x,y) \sim 1 + 2\sigma\phi_p\left|\frac{-x}{M}, \frac{-y}{M}\right| * F[A(x,y)\sin\chi(u,v)]. \qquad (26)$$

The function $F[A(u,v)\sin\chi(u,v)]$ is negative and sharply peaked (132), so the bright-field image of a weak-phase objective consists of dark detail on a bright background at Δz_{Sch} and for correctly chosen $A(u,v)$. On this simplest theory of image contrast, the image intensity is linearly proportional to the projected potential of the specimen. Thus, the process of high-resolution image formation can be simply illustrated, as shown in Fig. 9.

In the presence of atoms of medium or high atomic number, and for crystalline specimens such as those often encountered in materials science, the value of $\sigma\phi_p(x,y)$ may exceed $\pi/2$ within the thickness range for which the phase object approximations, i.e. Eqns. (17) and (18), are valid. There are other approximations which are useful; however, for more reliable interpretations of the images of crystals, the more sophisticated theory of n-beam dynamical diffraction of electrons and

the methods of computation developed on this basis should be used. These are detailed in a number of references (132,138,144-153), and will not be explored further here.

4.3. Optical Diffraction

The use of an optical bench has become popular in HREM (132,133). This device utilizes a coherent laser light source to illuminate a TEM negative. When the negative contains certain periodicities, such as in a lattice image, the laser beam is diffracted into corresponding pairs of "Bragg" spots, each at a distance (D) from the center of the screen, given by:

$$D = \lambda L/d \tag{27}$$

where λ = wavelength of the light, L = diffraction camera length and d = spacing of the periodic modulation. Therefore, the periodicities revealed by optical diffraction are essentially identical to the periodicities in the specimen. When the optical diffraction pattern is further recorded on photographic film, the amplitude of the diffraction pattern is thus given by the Fourier transform of Eqn. (26) as:

$$Q(U,V) = \delta(U,V) - 2\sigma\phi_p(U,V)\sin\chi(U,V)A(U,V) \tag{28}$$

where U and V represent coordinates in the plane of the optical diffraction pattern, i.e. given by Eqn. (27). The intensity of the optical diffraction pattern is then given from Eqn. (28) as:

$$I(U,V) = \delta(U,V) + 4\sigma^2[\phi_p(U,V)]^2\sin^2\chi(U,V)A(U,V). \tag{29}$$

Comparing Eqns. (29) and (20) indicates that they are identical if σ in Eqn. (20) is replaced by 2σ, and the second term in Eqn. (20) is multiplied by $\sin^2\chi(U,V)A(U,V)$. Therefore, provided that the sample

satisfies Eqn. (17) and the electron micrograph is recorded at the optimum focus condition, where $\sin\chi(u,v)$ is nearly equal to -1 over the maximum range of spatial frequencies, the intensity in the optical diffraction pattern should be identical to that of the electron diffraction pattern.

Optical selected area diffraction patterns can also be obtained from high-resolution electron micrographs simply by placing an aperture in the path of the laser. This technique allows diffraction information to be obtained from areas as small as 10 Å, thereby revealing detail which may otherwise be obscured during conventional SAD in the microscope (154-156). In addition, an optical diffraction pattern from a thin amorphous film, such as at the edge of most metallic specimens, allows determination of the CTF and therefore, the conditions of most of the important microscope parameters during imaging (132,157). It is therefore desirable to have part of this amorphous film present in any high-resolution negative.

4.4. Energy-Dispersive X-ray Spectroscopy

Since the technique of EDS is now firmly established and commonly used throughout the biological and materials science communities (158-160), only a brief account of the physics of the process of x-ray generation and the Cliff-Lorimer ratio method of quantitative chemical analysis is given here. The process of x-ray emission is shown schematically in Fig. 10(a). An energetic electron from the incident beam interacts inelastically with the inner shell electrons of an atom, and ejects one of these electrons from a shell of low energy (E_1). Because the inner shell vacancy leaves the atom in an ionized state, an electron

from a higher energy shell (E_2) gives up energy in the form of electromagnetic radiation in order to fill the vacancy and return the atom to its ground state. The energy of the emitted radiation is then exactly equal to the energy difference between the energy levels involved ($E_2 - E_1$). Since this energy difference is fairly large for inner shells, the radiation appears as x-rays. Because each element contains unique discrete energy levels, the energies of the emitted x-rays indicate the element from which it came and hence, the name characteristic x-ray emission. Characteristic x-ray lines are usually named according to the shell in which the initial vacancy occurs and the shell from which an electron drops to fill that vacancy. As shown in Fig. 10 (b), if the initial vacancy occurs in the K shell and the vacancy-filling electron drops from the adjacent L shell, a $K\alpha$ x-ray is emitted. If the electron drops from the M shell (two shells away), the emitted x-ray is a $K\beta$ x-ray, and so on.

The most useful property of characteristic x-rays is the variation of their energy with atomic number. This relationship is described by Moseley's law (161,162):

$$E = c_1(Z - c_2)^2 \qquad (30)$$

where E = energy of the characteristic x-ray, Z = the atomic number, and c_1 and c_2 = constants for a given line type. For a given line type, the x-ray energy increases with atomic number. Thus, the atomic number of an emitting atom can be determined from the energy of an x-ray emission if the line type is known.

The detected intensities of characteristic x-rays are primarily influenced by three factors: 1) the atomic number of the emitting atom

and the average atomic number of the surrounding atoms, 2) absorption, and 3) flourescence. Two parameters characterize the atomic number dependency of the emitting atom. The first is the ionization cross section, which expresses the probability that an initial vacancy will occur under the given operating conditions. The second is the flourescence yield, which is the probability that once a vacancy is created it will produce a characteristic x-ray. The average atomic number of the surrounding atoms affects the amount of energy lost to other scattering processes and thus, unavailable to produce an ionization event. The second major influence on the emitted intensity is absorption, or the probability that emitted characteristic x-rays will be absorbed before they emerge from the sample. The third factor is secondary flourescence, which is one result of such absorption. For example, a high-energy characteristic x-ray of one element (A) may be absorbed by a second element (B). The presence of both elements A and B in a sample will then lead to an increased intensity of characteristic x-rays from element B and a decreased intensity from element A.

In the analyses of thin foils in the TEM, the effects of absorption and flourescence can often be neglected (163), with the result that the x-ray intensities leaving the sample are identical to those generated by single ionization events within the sample. This is known as the thin film criterion. As a result, quantitative analyses of thin foils can be performed using the ratio method (164,165), where the x-ray intensities (I_A and I_B) of two elements (A and B) in a foil are measured simultaneously, and related directly to the mass concentrations of these elements (C_A and C_B) present in the sample by the equation:

$$\frac{C_A}{C_B} = k_{AB} \frac{I_A}{I_B} \tag{31}$$

where k_{AB} = a proportionality factor, often known as the Cliff-Lorimer factor since they were first measured experimentally by Cliff and Lorimer (166). The term k_{AB} varies with operating voltage but is independent of sample thickness and composition as long as the two intensities are measured simultaneously and the thin film criterion is satisfied. Hence, if k_{AB} is determined experimentally for an arbitrary set of operating conditions, the atomic concentrations of atoms A and B in an unknown specimen can be determined under the same set of operating conditions from the measured x-ray intensities using the experimental value for k_{AB} and the additional relation that:

$$C_A + C_B = 1. \tag{32}$$

Similar expressions may also be used to determine the atomic concentrations for more than just two elements in a sample.

4.5. Convergent-Beam Electron Diffraction

Unlike the situation in HREM where a small 2nd condenser aperture and a defocussed beam of plane parallel electrons are desired for maximum coherence, CBED relies on using a large 2nd condenser aperture and strongly excited objective and condenser lenses to form a highly-convergent, incoherent electron probe on the specimen. The effects of having such a convergent-beam of electrons incident on the specimen can be conveniently illustrated using the Ewald sphere construction shown in Fig. 11 (a). Because of the short wavelengths of high-energy electrons, the radius of the Ewald sphere ($1/\lambda$) is generally much larger than the spacing of lattice points in reciprocal space. Thus, when a defocussed

beam of electrons is incident on a thin foil, the diffraction spots in the zero-order Laue zone (ZOLZ) are excited when they are intersected by the Ewald sphere. However, the separation between the Ewald sphere and the reciprocal lattice points in the ZOLZ increases with distance from the origin until reflections in this plane are no longer excited to an appreciable extent. If the electron beam is now focussed to a form a convergent probe on the thin foil, the electrons are incident over a range of angles ($2\alpha_i$), which leads to a similar angular range of Ewald spheres in the reciprocal lattice. Thus, the electron beam samples the third-dimension of reciprocal space and because the effective radius of the resulting Ewald sphere is less than for plane parallel illumination, a significant amount of large-angle electron scattering occurs in the higher-order Laue zones (HOLZs), as illustrated in Figs. 11 (a) through (c). These effects cause 3-dimensional dynamical diffraction to occur and hence, the CBED pattern now contains 3-dimensional information about the crystallography of the sample. Large-angle scattering is greatly enhanced if the specimen is cooled to liquid nitrogen or helium temperatures, thereby reducing the amount of thermal diffuse scattering in the specimen.

The spacing of the reciprocal lattice parallel to the electron beam (H) can be found by measuring the radius (G) of a HOLZ ring. As shown in Fig. 11 (a), the value of G depends on the intersection of the Ewald sphere with the reciprocal lattice and therefore, it is a function of the electron wavelength (λ). Using simple geometry, Steeds (167) has shown that the radius of the first-order Laue zone (FOLZ) is given approximately by:

$$G = (2KH)^{1/2} \tag{33}$$

where $K = 1/\lambda$. Thus, by measuring G, the reciprocal lattice spacing (H) and hence, the crystal lattice spacing parallel to the electron beam can be determined. Lattice parameter determinations by this method are accurate up to about 2% if performed carefully.

Having an angular range of electrons incident on the sample also causes the Bragg spots in the diffraction pattern to expand into discs, the diameter of which is related to the convergence angle of the incident beam according to the expression:

$$\frac{\alpha_i}{\theta_B} = \frac{Y}{X} \tag{34}$$

where X = the distance from the center of the forward scattered beam to the center of the Bragg disc, i.e. any reciprocal lattice vector g, Y = the diameter of the Bragg disc, θ_B = the Bragg angle of the reflection and α_i = the semi-angle of convergence of the electron beam. These discs also contain 2-dimensional maps of the diffracted intensity as a function of the inclination between the incident electron beam and a particular crystal direction. This diffracted intensity can be used to precisely determine the specimen thickness (168-171) and orientation, and because it relates to the 3-dimensional structure of the crystal, it can also be used to determine the point and/or space group of the sample, as discussed in more detail below.

The determination of crystal point groups by CBED was originally introduced by Buxton et al. (172), who used group theory and graphical construction to determine the pattern symmetries of the 31 diffraction groups and relate these to the 32 crystal point groups. Later refine-

ments by Steeds and Vincent (173,174) and Tanaka et al. (175) now make point group determination by CBED a relatively straightforward procedure. The most common procedure for determining the point group of a sample requires a detailed examination of the intensity distributions within the convergent-beam discs, and the use of Tables 2 and 3 in Buxton et al. (172). These are reproduced as Tables 1 and 2 herein. In Table 1, the 31 diffraction groups are listed, along with detailed information about the symmetries observed in the CBED patterns. These 31 diffraction groups consist of the 10 2-dimensional point groups (1, 2, m, 2mm, 4, 4mm, 3, 3mm, 6 and 6mm), plus an additional 21 groups which arise when these are combined with the 3-dimensional symmetry elements consisting of a horizontal mirror plane (1_R), an inversion center (2_R), a horizontal rotation axis (m_R) and a four-fold rotary inversion (4_R). For each of the diffraction groups, Table 1 lists the symmetries present in the bright-field disc (000 disc) and the whole pattern (hkl discs in ZOLZ + hkl discs in HOLZs if visible). The dark-field columns in Table 1 describe the symmetries present in the intensity distribution within an hkl disc. The "general" column refers to any general hkl disc which is not positioned on one of the major symmetry elements of the crystal, while the "special" column refers to the symmetries observed in an hkl disc which is positioned for example, at the Bragg position on one of the mirror planes in the diffraction group. The ±G columns refer to the symmetries observed when opposite reflections of a particular hkl pair are set at the Bragg position. Depending on the point group of the crystal and whether or not it is centrosymmetric, the +g and -g discs may display identical or different internal symmetries. One of the main advantages that CBED has over x-ray diffraction for determining the

point group of a crystal, is the ability to readily distinguish between centrosymmetric and noncentrosymmetric crystals simply by comparing the intensity distributions between pairs of hkl discs, due the breakdown of Friedel's law for a noncentrosymmetric crystal in electron diffraction (176,177). Having determined the diffraction group of a crystal by comparing the symmetries of the hkl discs with the symmetries given in Table 1, it is then possible to further determine the crystal point group by referring to Table 2. In Table 2, each diffraction group is related to a particular point group (by an X) according to the zone axis in which the diffraction group was identified. Thus, having determined the diffraction group and knowing the zone axis of analysis, the crystal point group can be found by moving across Table 2 to the X, and then tracing down to the bottom row in the table.

Tanaka et al. (175) have recently introduced a slightly different method for determining the diffraction group of a crystal. Essentially, by obtaining a symmetric many-beam (SMB) CBED pattern from a crystal, it is possible to determine the diffraction group of the crystal from the single SMB pattern, simply by observing the symmetries contained within each of the excited discs. Having done this, Table 2 can then used exactly as described above to determine the crystal point group. Examples of some of the many-beam patterns derived by Tanaka et al. are given in Fig. 12. These will be used later in this study.

The 230 3-dimensional space groups arise from the application of translational symmetry elements such as glide planes and screw axes to the 32 crystal point groups. Once the point group of a crystal has been identified, determination of the space group can be accomplished by

observing the presence of so-called "lines of dynamical absence" or Gjonnes-Moodie lines (178,179), which occur in kinematically forbidden reflections due to dynamical interactions. These Gjonnes-Moodie lines appear as bands of negligible intensity in the CBED discs due to screw axes or glide planes which lie either parallel or perpendicular to the incident electron beam, as shown in Fig. 1 of Gjonnes and Moodie (178). Thus, by identifying kinematically forbidden reflections, the space group of the crystal can be determined either from the conditions limiting possible reflections given in Volume I of the "International Tables for X-ray Crystallography" (180), or from Tables 1-17 in Tanaka et al. (181). The tables given by Tanaka et al. are particularly useful, since they list the zone axes that can be used to distinguish between Gjonnes-Moodie lines which are due to screw axes and those which are due to glide planes, for 191 of the 230 possible space groups.

The last useful property of CBED to be discussed, is lattice parameter determinations from HOLZ lines. Since HOLZ lines in CBED patterns arise from elastic interactions, they are the electron diffraction equivalent to Kossel lines in x-ray diffraction (87), and they possess the same symmetries as Kossel patterns in x-ray diffraction; that is, they contain 3-dimensional crystallographic information. These HOLZ lines appear as sharp lines super imposed upon the broader intensity distributions within the convergent-beam discs. Since the HOLZ line arrangement is very sensitive to small changes in lattice parameters in a material, lattice parameter determinations with an accuracy of 0.02% can be accomplished by comparison with a known standard (167,182-185), provided that the HOLZ lines can be indexed. Fortunately, computer pro-

grams which generate the positions of HOLZ lines for specified accelerating voltages, lattice parameters, crystal symmetries and zone axes are now available (160,183). Because the positions of the HOLZ lines vary with all of these factors, it is important that the standard to be used for a lattice parameter determination has similar lattice parameters, a similar space group and a similar atomic scattering factor as the unknown sample, and that the CBED patterns for the standard and unknown are recorded at the same accelerating voltage.

5. EXPERIMENTAL PROCEDURES

5.1. Materials and Heat-Treatments

5.1.1. Al-Ag Alloys

Two Al alloys containing 14.92 w/o Ag (4.2 a/o Ag) and 3.76 w/o Ag (1.0 a/o Ag) were received from H.I. Aaronson in the form of 7 mil (178 μm) sheet. The alloys had been vacuum melted and cast using Al and Ag of 99.99% purity. Both ingots were then homogenized at 535°C for about 40 hrs. to reduce segregation, and hot and cold rolled to final thickness. Discs of 2.3 mm diameter were punched from the sheets. These were solution-annealed for 30 min. at 550°C to form an Al-Ag solid solution, and then immediately quenched in cold water. All of the 3.76 w/o Ag discs and several of the 14.92 w/o Ag discs were retained in this state for use as EDS standards. The remaining 14.92 w/o Ag discs were subsequently aged for either 10, 30 or 120 min. at 350°C, followed by another cold-water quench. The 350°C aging temperature was chosen because it lies above the G.P. zone solvus for this alloy composition (Fig. 1) and thus, a dense dispersion of γ' precipitates could be produced directly from the supersaturated solid solution, without the influence of a previous G.P. zone distribution. All HREM was performed on the samples aged for 30 min.

5.1.2. Ag_2Al

Single crystal bars having the composition Ag_2Al (Ag-33 a/o Al) and oriented such that the $\{11\bar{2}0\}$ and {0001} planes were normal to the long axis were grown under Argon from seed crystals, as described by Thomas and Okamoto (186) and Mote et al. (187). Approximately 10 mil (255 μm) thick sheets were cut from the bars parallel to the $\{11\bar{2}0\}$ planes, using

an Isomet diamond saw. These were further ground to about 5 mil (125 μm) thickness on water-cooled 600 grit SiC paper. Discs 2.3 mm diameter were then punched and given the same solutionizing and aging treatments described for the 30 min. Al-Ag alloy above. These samples were used mainly as standards for quantitative EDS analyses of γ' precipitates, although some HREM and diffraction was also performed on them.

5.1.3. 99.99% Ti

Hot-rolled 32 mil (0.8 mm) thick, 99.99% Ti sheet was ground to 5 mil (125 μm) thickness on water-cooled SiC papers down to 600 grit. Discs 3.0 mm in diameter were punched, vacuum encapsulated and annealed for 1 hr. at 600°C to produce a completely recrystallized α-phase microstructure. These samples were used as standards for CBED analyses of γ' precipitates.

5.2. Electropolishing and Ion-Beam Milling

Discs from the two Al-Ag alloys and the pure Ti were polished in a twin-jet Fischione apparatus using a 25% HNO_3 / 75% CH_3OH electrolyte at around -30 to -40°C. The voltage and current conditions were generally about 14-20 V and 15-35 mA for the Al-Ag alloys, and around 50-52 V and 45-55 mA for the Ti. After perforation, the thin foils were rinsed in three separate CH_3OH baths and immediately dried and stored under vacuum.

Ion-beam milling of thin foils was found to facilitate high-resolution imaging by removing a thin oxide which inevitably formed on the surfaces of the foils during polishing. However, significant heating of thin foils while milling at room temperature can occur and if not avoided, this heating can be sufficient to alter the microstructure of

the sample (73). In order to minimize such heating, thin foils were either milled at liquid nitrogen temperature (~ -190°C) using a Gatan cold-stage assembly, or alternately milled and cooled in 30 sec. intervals, using an accelerating voltage of 4 keV, a maximum of 0.3 mA total gun current (0.15 mA each gun) and a 12° tilt.

Thin foils of Ag_2Al were also polished in a twin-jet Fishione apparatus using an aqueous electrolyte containing about 3% KCN, 1.5% NaOH, 0.5% AgCN and 0.3% KCO_3 (186). These foils were difficult to polish, but the best results were obtained by cooling the bath to about 5°C, and using an applied potential of 15-20 V and a current of 15-20 mA. After perforation, these foils were immediately rinsed in distilled water, followed by CH_3OH and finally CH_5OH, and then dried and stored under vacuum.

5.3. Precipitate Extractions

Additional 1/2 in. × 1/2 in. (12 mm × 12 mm) sheets of the Al-14.92 w/o Ag alloy were solution annealed and aged for 10, 30 and 120 min. at 350°C, identically to the discs described in Sect. 5.1.1. The γ' precipitates were then extracted from each of these sheets as follows. A sheet was placed in a beaker containing 5% NaOH in water. After about 1 hr., a substantial portion of the matrix had dissolved and a black residue filled with precipitates was left on the sheet surface. The sheet was then transferred to a beaker containing CH_3OH and ultrasonically cleaned for about 1 hr. This frees the precipitates from the surface and disperses them throughout the CH_3OH. A small amount of the CH_3OH was then collected in an eyedropper and a drop or two deposited on a lacy carbon film supported on a Cu grid. This left the γ' plate-shaped pre-

cipitates face-down on the carbon film, readily accessible for CBED and quantitative EDS analyses.

5.4. High-resolution TEM

High-resolution micrographs were obtained according to the optimum conditions outlined in Sect. 4.2. All lattice images were taken on a JEOL 200CX microscope, equipped with a pointed LaB_6 filament and operating at 200 keV. Either the central spot or outer quadrant of an undersaturated filament was used in order to maximize beam coherence. Specimens were tilted into exact <110>//<11$\bar{2}$0> or <111>//<0001> orientations using the top-entry, high-resolution goniometer. Objective apertures with radii of either 0.64 $Å^{-1}$ or 0.74 $Å^{-1}$ were usually used to filter out higher-order spatial frequencies and thus, improve image contrast. After determining the voltage center, astigmatism was corrected by first maximizing the symmetry of Fresnel fringes around protrusions along the edges of the foils, and then by maximizing the symmetry of phase contrast in the amorphous layer while slightly over and underfocussing the objective lens at magnifications of up to 800 kX. Final correction of astigmatism was then made by minimizing the phase contrast in the amorphous layer. This establishes the minimum contrast condition (Δz_{mc}), where the image shift due to spherical aberration has been offset by a weak objective lens at under-focus from the Gaussian image plane (Δz_G = 0) given by:

$$\Delta z_{mc} = 0.044(C_s\lambda)^{1/2} \qquad (35)$$

which occurs for $\sin\chi = 0.3$. Since this is easily observable and can be calculated for known C_s and λ, it serves as a reference point from which the objective lens can be defocussed in set increments to reach Scherzer

defocus (Eqn. (23)), or some other desired focus condition. For the JEOL 200CX at 200 keV, C_s = 1.2 mm, C_c = 1.4 mm and therefore, Δz_{mc} = -240 Å, Δz_{Sch} = -660 Å, Δz_{2nd} = -1290 Å and Δz_{3rd} = -1690 Å. In addition, a defocus value of about -1460 Å was found to be optimum for including all of the first-order matrix and precipitate reflections in the imaging process and thus, was often used in this study as described in more detail later. After correction of astigmatism the desired magnification was selected (usually 270 or 350 kX), and a through-focus series was taken in either 120 or 340 Å increments, starting near the minimum contrast condition, and continuing to at least the third pass-band interval. The illumination intensity was such that the beam could usually be defocussed to convergence angles of > 2 mrad to improve coherence, while still maintaining sufficient intensity to allow exposure times of about 4 sec. Amorphous edges were almost always included in the images for subsequent optical diffraction analyses of the imaging conditions.

Optical diffraction was performed on high-resolution micrographs to determine the CTF and spatial frequencies recorded in the image. A He-Ne laser light source (λ = 6328 Å) was used, and the diffraction patterns were recorded on Type 52 Polaroid film, usually at exposures of about 1/125 sec.

5.5. Image Simulations

Simulated high-resolution electron microscope lattice images were calculated on the LBL CDC 7600 computer using the A.S.U. Multislice Programs developed by O'Keefe and Skarnulis (188), and later modified into the ZOLZPROG series of programs by Spence (189). The ZOLZPROG consists of three programs, FCO128, DEF128 and IM128, which are run in succession

and use a 128 × 128 array to compute a simulated electron image. Each of these programs except FCO128 uses the output from the previous program, together with new input containing additional operating parameters, to calculate the final image. In summary, FCO128 calculates the Fourier coefficients of the model crystal, DEF128 then calculates the diffracted amplitudes and phases of the electron wave after interaction with the model crystal (Eqns. (17)-(20)) and IM128 subsequently imposes the effects of microscope aberrations on the perfect wave from DEF128 before synthesizing the final image (Eqns. (21),(22),(25),(26)). Each of these programs, and the values commonly used as input parameters in this study are described briefly below.

5.5.1. FCO128

FCO128 calculates the kinematic structure factors, or the Fourier coefficients of the crystal potential for the ZOLZ nearest the electron beam direction. Typical parameters which must be input for this initial program are the unit cell dimensions, the number of atoms and their fractional positions within the unit cell, the space group symmetry operators, the atomic numbers, isotropic temperature factors and occupancies of each type of atom in the unit cell, the projection direction, any special reflections and the maximum number of reflections (DSMAX) to be considered in the calculations. In this investigation, all images were simulated with the electron beam incident along $\langle 110 \rangle // \langle 11\bar{2}0 \rangle$ matrix/precipitate directions, since these orientations gave the most information and were often used for HREM. The unit-cells and lattice parameters used in the calculations of images of perfect hcp crystals and fcc/hcp interphase interfaces were similar to those shown in Fig. 2,

and described in Sects. 2.3 and 2.4. The concentrations of Ag (atomic number 47, isotropic temperature factor 0.25) and Al (atomic number 13, isotropic temperature factor 0.30) atoms in columns of disordered atoms along the projection direction were varied among the basal planes of the precipitate to achieve an ordered lattice which matched experimental images. The <0001> hcp reflections were included in all of the calculations.

Short computer programs were often written to construct initial input files for FCO128, an example of which is given in Appendix 10.1., where a somewhat larger than usual program was used to calculate the atomic positions of a Shockley partial dislocation ledge using isotropic elastic theory, and assign the atomic concentrations of Ag and Al for input into FCO128. The number of atoms per unit cell and values of DSMAX varied from 2 and 4.0 for a perfect hcp unit cell, to 162 and 2.15 for the dislocation ledge just described, where the unit-cell dimensions (a and b) in the projected plane (x and y) were about 30 and 26 Å, respectively. The unit-cell dimension (c) along the electron beam direction (z) was always 2.864 Å, which was the value then used for the slice thickness (Δz) in subsequent phase-grating calculations.

5.5.2. DEF128

DEF128 then calculates the single-slice dynamical electron scattering (phase-grating) amplitudes from the output of FCO128, and stacks up to 50 of these outputs to produce the multi-slice scattered wave from a thick crystal, i.e. solves the time-independent Schrödinger equation by the Cowley-Moodie (134) multislice method. The most important values input for this part of the program are the accelerating voltage of the

microscope (200 keV for the JEOL 200CX), which is used to determine the electron wavelength and interaction parameter (Eqn. (17)), the phase-grating slice thickness (Δz = 2.864 Å), the number of beams to be used in the multislice calculations (~ DSMAX/2) and the coordinates (h,k) of the Laue circle center, i.e. if the electron beam is tilted with respect to the crystal, or vise-versa. In addition, as outlined in Sect. 4.2., use of Eqns. (17) and (18) requires that the phase change due to the phase-grating should be everywhere less than $\pi/2$, or $\sigma\phi_p(x,y) < \pi/2$. A further restriction on the phase-grating is that the sampling interval should be sufficiently fine so that changes in phase between adjacent points are very much less than $\pi/2$, i.e. $\sigma\phi_p(x,y) << \pi/2$. DEF128 checks these two criteria and prints a warning if they are exceeded. Also, a convolution test is performed to ensure that all important reflections are included in the phase-grating calculations. The number of phase-grating coefficients to be checked is specified (~ number of Fourier coefficients/4) and the indices (h,k) of any reflection which exceeds the set convolution limit is printed. Finally, the crystal thicknesses at which the exit wave (Eqn. (18)) is to be saved for later imaging are specified according to the number of phase-grating slice thicknesses.

5.5.3. IM128

IM128 then synthesizes the beams from DEF128 in a Fourier series to form the electron lattice image, taking instrumental aberrations into account. It is here that effects such as spherical aberration and extent of focus of the objective lens (Eqn. (22)) on the actual wave used to form the image are taken into account. The important instrumental parameters and typical values for the JEOL 200CX that were used as

input for this part of the simulations are: slice numbers to be imaged (1-50), h,k coordinates of the optic axis and objective aperture center (0,0), radius of objective aperture (0.64 $Å^{-1}$), spherical aberration coefficient (1.2 mm), semi-angle of illumination (1.0 mrad), half-width of Gaussian spread of defocus (50 Å), halfwidth of Gaussian distribution of vibration (0 Å) and the focus values to be imaged (-240 to -2295 Å).

5.6. Energy-Dispersive X-Ray Spectroscopy

Energy-Dispersive X-Ray Spectroscopy (EDS) analyses were performed on a Philips EM400 operating at 100 keV, and equipped with a Kevex System 7000 Si(Li) x-ray detector. Spectra were acquired in the TEM mode with a probe diameter of about 400 Å. All x-ray spectra were obtained using a low-background Be specimen holder with the specimen tilted 30° toward the Si(Li) detector. The Kevex analytical spectrometer (multichannel analyzer) was set to the 40 keV range for spectra acquisition since Al and Ag $K\alpha$ peaks lie at 1.487 and 22.162 keV, respectively. Since the γ' precipitates examined in this study were generally < 400 Å thick, absorption and flourescence were neglected, and the Cliff-Lorimer relation (Eqn. (31)) was used for all quantitative analyses. Cliff-Lorimer proportionality constants ($k_{\alpha AgAl}$) were determined using Ag_2Al and Al-Ag solid solution alloy standards under the same microscope operating conditions as used for the precipitate spectra acquisitions. Care was always taken to work in the thinnest areas of these specimens to assure that absorption of Al by Ag was negligible. The Al and Ag peak intensities were measured using 210 and 410 eV windows, centered at 1.50 and 22.18 keV, respectively. The background intensity was measured on either side of these peaks using the same size windows, averaged, and

then manually subtracted to obtain the final number of counts in each peak.

Because the generation of x-rays is random with time, the standard deviation (σ) per unit time is the square root of the number of counts (N) so that:

$$1\sigma = N^{1/2}. \tag{36}$$

Various confidence levels can also be ascribed to the standard deviation, i.e. 1σ = 68%, 2σ = 95% and 3σ = 99.7%. The precision of measurement, or the reliability limits which can be assigned to a value are found by determining what fraction σ is of N (158):

$$\text{C.V.}(\%) = (\sigma/N)100 = \frac{N^{1/2}}{N}\ 100 = \frac{100}{N^{1/2}} \tag{37}$$

where C.V. = the coefficient of variation. In this investigation, a minimum of 10^4 counts were obtained in each of the Al and Ag peaks such that the coefficient of variation was < 1%. About ten extracted precipitates were analyzed in each of the Al-14.92 w/o Ag samples aged for 10, 30 and 120 min. at 350°C. In these cases, the average composition $\bar{x} = \frac{x_i}{n}$, where $x_i = C_{Ag}/C_{Al}$ in each precipitate and n = the number of precipitates analyzed. The standard deviation (s) is then given as (190).

$$s = \left[\frac{\Sigma(x_i - \bar{x})^2}{n - 1}\right]^{1/2} \tag{38}$$

and the coefficient of variation becomes:

$$\text{C.V.}(\%) = (s/\bar{x})100. \tag{39}$$

5.7. Convergent-Beam Electron Diffraction

Convergent-Beam Electron Diffraction (CBED) was performed at 100 keV on a Philips EM400, modified such that the objective and 2nd condenser lens currents could be separately varied to achieve a wide range of convergence angles on the specimens. For space group analyses, convergence angles of about 15 mrad were obtained in the TEM mode by using a 300 μm 2nd condenser aperture, an 0.2 μm 1st condenser spot size (probe diameter ~ 400 Å), and then increasing the objective lens current so that the diffraction discs in the ZOLZ just touched without overlapping, while focussing the probe independently on the sample with the 2nd condenser lens control. Tilting experiments were performed by translating the 2nd condenser aperture (equivalent to a gun tilt), after having obtained a zone axis pattern. A 450 mm camera length was typically used to photograph the intensity distributions within the ZOLZ discs. Use of a double-tilt, liquid-nitrogen cooled specimen holder (Temp. = -188°C) was absolutely necessary in order to eliminate contamination of the extracted precipitates on the carbon films, and in order to reduce thermal vibrations and diffuse scattering so that the FOLZs were clearly visible. Thus, the cold-stage holder was used for almost all CBED experiments. In order to photograph FOLZs, a camera length of 280 mm and a 100 μm 2nd condenser aperture were used.

6. EXPERIMENTAL RESULTS AND DISCUSSION

6.1. Plan of Attack

The objective of this research is to characterize the atomic mechanisms of growth of γ' plate-shaped precipitates in an Al-15 w/o Ag alloy. In order to accomplish this, several different TEM techniques were employed. Each of these techniques yields particular information about the structural or chemical aspects of the growth process, such that when the information from each of these complimentary techniques is combined, a complete picture of the growth process at the atomic level is achieved. Thus, the following experimental results have been organized into a progression which considers the information obtained from each TEM technique, and then subsequently combines this information to arrive at the final results. This "plan of attack" is outlined schematically in Fig. 13. Essentially, HREM is first used to determine the interfacial structures of both the faces and edges of γ' precipitates, in order to obtain an understanding of the structural aspects of the transformation. Next, EDS is used to characterize the compositions of both the matrix and precipitates, so that the chemical aspects of the transformation can be considered. By combining the structural and chemical information from these two techniques with electron diffraction information from the structural studies, a model for the γ' precipitate is then constructed. In order to verify the proposed model, a variety of image simulations are compared with HREM images of the precipitates and precipitate/matrix interface. Further examination of these structures subsequently elucidates the relation between the structural and chemical aspects of the growth process, allowing the mechanisms of growth to be

modeled at the atomic level. Finally, CBED is used to try to determine whether any symmetry or lattice parameter changes occur during growth of the precipitates, and to further verify the model crystal structure. Unfortunately, difficulties were encountered in the CBED studies which prevented complete analyses of some of these factors.

One question that often arises when talking about electron microscopy is whether or not the information obtained from the small volume of material that is typically examined is representative of processes which occur in the bulk sample. This is particularly of concern in HREM, where many experimental variables need to be satisfied in order to be able to interpret a micrograph correctly, and the area examined is often on the order of hundreds or thousands of square Angstroms. In order to attempt to address these problems in this study, the same experiment was usually repeated several times on different samples and precipitates, to try to get some statistical evidence that the observed precipitate structures were representative of the majority of the transformation processes which had occurred in the sample. Thus, when more than one micrograph of a similar aspect of the transformation process is presented, it was not included as "just another pretty picture" but rather, because it either shows some additional information about the process in question, or because a number of such observations helps show that the results obtained are reproducible and therefore, representative of the whole sample.

6.2. High-Resolution Transmission Electron Microscopy

6.2.1. The Structure of γ' Precipitate Plate Faces

As shown by Fig. 14, the 30 min. aging treatment at 350°C was designed to produce a relatively dense dispersion of well-developed γ' precipitates without the influence of a prior G.P. zone structure, and this was accomplished. Since the γ' plates precipitate on all four of the {111} matrix planes, two variants of the precipitates are edge-on in the <110> orientation shown in Fig. 14, while the other two variants are inclined to the electron beam. Strain contrast from dislocation ledges on the faces of these inclined precipitates is visible in the upper right corner of Fig. 14 (arrows). As indicated by the micron marker in this figure, the γ' precipitates are on the order of one to several μm in diameter and about 100 to 300 Å thick.

Figure 15 (a) shows a low magnification lattice image of two γ' precipitates, again edge-on in a <110> orientation. The isolated precipitate is about 150 Å thick at its center, while the larger intersected precipitate is about 200 Å thick. For this image, an objective aperture of radius 0.74 Å was used to eliminate higher-order spatial frequencies, as shown in the corresponding electron diffraction pattern in Fig. 15 (b). The heights of a number of ledges are indicated in Fig. 15 (a), according to the number of {111} matrix planes that cross the edges of the ledges to become {0001} basal planes in the precipitate. The structural character of these ledges is shown in greater detail in the enlargements in Figs. 16 (a)-(d). From these enlargements, it is readily apparent that ledges are present on both faces of both precipitates, and that all of these ledges are multiples of two {111} matrix planes in

height, indicating that thickening of the precipitates is occurring by passage of Shockley partial dislocations along alternate matrix planes as proposed by previous investigators (35,36,63,74). In addition, four and six-plane ledges are most common on the faces and are present in relatively large numbers. The presence of these multiple-unit ledges explains why both 1/6<112> and 1/2<110> contrast behavior was observed for ledges on the faces of these precipitates in a previous investigation (60). The 1/6<112> Shockley partial dislocations associated with each two-plane ledge are so close together that their strain fields overlap, leading to the contrast behavior exhibited by a 1/2<110> dislocation. This interpretation can be easily visualized by referring to the (111) face of the Thompson tetrahedra reproduced in Fig. 17. Here it can be seen that the displacements associated with two Shockley partial dislocations can add to produce the strain field of a perfect dislocation by a reaction such as:

$$a/6[2\bar{1}\bar{1}] + a/6[1\bar{2}1] \rightarrow a/2[1\bar{1}0].$$

The presence of these multiple-unit ledges also indicates that there is a strong tendency for single ledges to interact. One reason for these attractive interactions may be due to the elastic strain fields associated with the Shockley partial dislocations just mentioned. Again, reference to Fig. 17 shows that if all three different types of Shockley partials interact, their strain fields will exactly cancel to produce a six-plane ledge which has no long-range strain field in the (111) plane. Hence, this type of dislocation configuration would be highly favored from a strain energy viewpoint. Such a situation was outlined previously in Fig. 4, and has been proposed to occur for γ' precipitates (61). A

second reason which may also contribute to the multiple nature of these ledges is the overlap of diffusion fields experienced by ledges which are migrating on the same faces of precipitates. This overlap causes ledges to merge and migrate together, as treated theoretically by Jones and Trivedi (43).

Also notice that in Figs. 15 (a) and 16 (d), ledges on opposite faces of the thin precipitate tend to lie across from one another. In addition, the terraces between the ledges are atomically flat and ledges on both faces are uniformly stepped-down as they approach the plate edge from its center, located in the lower right corner of Fig. 15 (a). These characteristics lead exactly to the overall shape predicted by the general theory of precipitate morphology (13) for growth by ledges, as sketched in Fig. 8.

Another important feature apparent from the micrographs in Fig. 16 is that the {111} planes are continuous as they cross the edges of the ledges into the precipitates. This implies that if atomic attachment occurs at the edges as thought, then attachment takes place across a largely coherent interface, at least in this orientation and direction, and not across a disordered interphase boundary as is usually considered in most kinetic analyses (42,43). The fact that attachment is occurring at the edges of the ledges is supported by the observation that the edges of the ledges are often indistinct, while the terraces between them are generally sharply defined. Particularly good examples of this are given by the four and six {111} plane ledges in Fig. 16, where opposite edges of corresponding ledges are labelled (a) and (b). While the edges of the ledges give variable contrast, the terraces between them

appear atomically flat.

Part of the variable contrast at the edges of these ledges may be due to the fact that the dislocations associated with them are not exactly parallel to the <110> electron beam direction through the thickness of the foil. A linear Shockley partial dislocation lying along a <110> direction should have sufficiently few kinks in a thin foil so that its true projection is seen (191). However, as a ledge bends away from a low-index <110> orientation, the density of kinks increases rapidly (60), thereby complicating image interpretation. Hence, the variable contrast at the edges of these ledges is most likely due to kinks in the dislocations at the edges.

Although the heights and structures of the previous lattice images have enabled a variety of factors to be deduced about the growth process, the images do not show atomic detail at the edges of the ledges. Hence, an effort was made to obtain better images which might resolve atomic detail at the ledges. However, in order to be able to interpret detail which might be present, an atomic model of a Shockley partial dislocation ledge was first constructed, and a number of simulated images were calculated from this model. The model ledge contains a Shockley partial dislocation with a Burgers vector that is 90° to the <110> electron beam direction, i.e. the Burgers vector is in pure edge orientation. This type of ledge can be pictured from the Thompson tetrahedron in Fig. 17, if the electron beam is assumed to lie along the $[1\bar{1}0]$ direction, and the Shockley partial dislocation has an $a/6[\bar{1}\bar{1}2]$ Burgers vector. The atomic positions around the dislocation core centered at the edge of the ledge were calculated using isotropic elastic

theory, as given by Hirth and Lothe (191a). The computer program which was developed to perform these calculations as well as output the atomic positions and concentrations of the atoms in the proper format for input into the image simulations, is included as Appendix 10.1.

Figure 18 shows a through-focus series of computed images for a crystal thickness of 37.2 Å, based on the model described above. The actual atomic positions from the model are shown in the projected potential in the top left corner of this figure, where the extra half-plane of atoms associated with the Shockley partial is indicated by an arrow, and the dislocation core which terminates at the edge of the ledge is circled. The stacking change caused by the passage of the Shockley partial dislocation is also indicated on either side of the ledge in the projected potential. Similar through-focus series of images were calculated for a variety of crystal thicknesses, and one image which was found to be useful for comparison with actual electron lattice images is shown in Fig. 19.

Figure 19 (a) again shows the projected potential for the model ledge with the dislocation and its core indicated as before. Also notice from this model that the atom positions in the A-planes in the hcp γ' precipitate have a much larger projected potential than those in the B-planes, although the projected potentials of atoms in the B-planes are still slightly larger than the projected potentials of atoms in the fcc matrix. This is due to the fact that the precipitate has been constructed such that the A-planes are comprised of essentially pure Ag, while the B-planes contain only 33 a/o Ag with a balance of Al, and the matrix contains nearly pure Al. While the rationale behind such ordering

of Ag on the basal planes of the precipitate will be discussed in detail in a later section, it is sufficient to note at this time that the projected potentials of the atoms increases with the Ag concentration due to the high electron density of Ag atoms as compared to Al, leading to the different sizes of the projected atom positions in the model. The result of having Ag-rich layers in the precipitate often leads to the effect that these atomic columns are indistinguishable above a dark background in the calculated and experimental images, while the Al-rich atomic columns appear white above the black background, as illustrated by Fig. 19 (b). This effect makes it nearly impossible to locate the exact position of the dislocation core, which is circled in the figure, and even makes it difficult to locate the relative position of the extra half-plane of atoms, as apparent from Fig. 19 (b). However, the presence of the extra half-plane of atoms due to the Shockley partial dislocation can be readily verified by drawing an appropriate Burgers circuit around the ledge (see Fig. 25 for example).

Figure 20 shows the best experimental image of a ledge on a precipitate face that was obtained in this study. This particular ledge is a multiple-unit ledge, again emphasizing the strong propensity for interactions among ledges. When the Burgers circuit shown is constructed for this approximately ten-plane ledge (the exact height of the ledge is somewhat uncertain because the image at the precipitate/matrix interface is slightly confused, probably due to a slight specimen tilt from an exact <110> zone axis orientation) a closure failure of four lattice planes occurs, as indicated in the figure. Strictly speaking, the separation between each lattice plane in the circuit leads to a clo-

sure failure of a/6<112> + a/12<112>, or a/4<112>. However, this closure failure actually represents the presence of four a/6<112> partial dislocations located at the edge of the ledge, rather than the true atomic displacements associated with each dislocation ledge. Because of the dark contrast which occurs on the Ag-rich planes in the precipitate, in addition to an anomalous reduction in contrast in the precipitate around the ledge, it is difficult to distinguish the exact atomic arrangement at the edge of the ledge, i.e. to distinguish the individual dislocations. Despite these limitations, by sighting along the {111} matrix planes parallel to the top face, it is possible to conclude that these planes are completely continuous as they cross the edge of the ledge and become the {0001} basal planes of the precipitate. Also, slight displacements of these planes normal to the Burgers vectors of the ledge dislocations is evident, i.e. perpendicular to the precipitate face, just as in the atomic model in Fig. 19 (a). This type of displacement leads to the g b×u contrast which is typically seen in conventional amplitude contrast images of such dislocations. Thus, from the matching between the calculated and experimental images of Shockley partial dislocation ledges in Figs. 19 and 20, it is possible to ascertain with considerable confidence that single Shockley partial dislocations on every other {111} matrix are responsible for the structural transformation needed for growth of these γ' precipitates, and that the growth interface is essentially coherent in this orientation. In addition, the atomic positions at the edge of the ledge can be easily visualized by reference to Fig. 19 (a).

Ideally, one would like to compute a simulated image for a multiple-unit ledge, which could be compared directly with the experimental image in Fig. 20. Unfortunately, while it is relatively simple to construct the projected potential for a single ledge as in the previous simulations, calculating an an image for a ten-plane ledge becomes a formidable task, not just from an elastic mechanics standpoint, but also because the large unit cell that is required for such a model increases the sampling interval in the phase-grating calculations beyond allowable limits, as discussed in Sects. 4.2. and 5.5.2. Thus, the combining of ledges hinders interpretation of their precise atomic structure. It is clear that further work in this area could concentrate on obtaining good HREM images of a single (or possibly a double) ledge, which could be compared directly with image simulations. This is certainly possible, but will require considerable searching to find a ledge in a part of a foil which meets all of the experimental requirements (mainly thickness) needed for atomic interpretation.

Several questions which arose during the initial stages of this work were whether it might be possible to actually determine the atomic concentration of Ag in the column of atoms corresponding to the Shockley dislocation core, or if there was a single kink the dislocation ledge, whether it might be possible to image such a kink in a thin foil. Both of these questions are important with regard to this study because they would allow the concentration of Ag to be directly correlated with the structural component of the transformation. While such correlations may be possible, particularly with the use of a high-resolution, high-voltage microscope such as the Berkeley JEOL ARM1000, the image calcula-

tions which have been performed for the JEOL 200CX used in this study indicate that it is unlikely that an image can be obtained which can distinguish such subtle effects, particularly given the limitations imposed by the fact that real TEM samples are not always ideal. For further discussion of this point refer to Appendix 10.2.

6.2.2. The Structure of γ' Precipitate Edges

The edges of γ' precipitates were also examined in a <110> orientation by HREM. Fig. 21 shows one such edge, for a precipitate which is about 160 Å thick at its center. Notice that the stepped-down shape of the edge indicates that it is composed of Shockley partial dislocations which have migrated across the precipitate faces and assumed a staggered configuration at the edge. Again, by sighting along the {111} planes parallel to the precipitate faces, it is possible to conclude that the precipitate edge is largely coherent, just as for the ledges on the faces in the previous section. This should be the case if it is indeed composed of the same Shockley partial dislocations as seen in Figs. 19 and 20. In addition, there appears to be a larger misfit at this interface than along the precipitate faces, as evidenced by the substantial bending of some matrix planes as they cross the edge into the precipitate. In fact, close examination of Fig. 21 indicates that there may be several terminating {111} planes at the precipitate edge. Such 1/3<111> dislocation loops around the precipitate periphery, with Burgers vectors normal to the faces, may be necessary in order to accommodate the slight contraction which occurs in the c-direction of the precipitate during transformation, as shown in Fig. 2. These image characteristics agree reasonably well with a precipitate edge that is modelled as being com-

posed of Shockley partial dislocations which are stacked vertically, and for a precipitate which experiences a slight contraction in the c-direction during growth.

Also notice that the precipitate edge is essentially flat, rather than having a semi-circular or parabolic-cylinder shape as assumed in most kinetic analyses (40,107,192). This planar shape is much clearer in the enlargement of the precipitate edge in Fig. 22, which was taken with a slightly different objective lens defocus. Several crystallographic planes in the matrix are also indicated in the top-left corner of this figure. Comparing these planes with the precipitate edge shows that the edge parallels a {112} matrix plane overall. However, closer inspection reveals that this roughly planar interface is further faceted along {111} matrix planes, which are also indicated in the top-left corner. In addition, these {111} facets have a six-plane repeating pattern, which is indicated in the figure. This six-plane repeating pattern is particularly interesting because it appears to directly relate to the way in which the structural transformation from the fcc matrix to the hcp precipitate occurs. As discussed in Sect. 3.2., a hcp precipitate could thicken either by the nucleation and propagation of the same Shockley partial dislocation on alternate {111} matrix planes, or by the incorporation of equal numbers of all three different types of Shockley partial dislocations on alternate {111} planes. However, the latter situation is highly favored from a strain energy viewpoint, since the strain fields of the three variants of Shockley partial dislocations would tend to cancel one another and eliminate long-range strains parallel to the habit plane of the precipitate. This effect can be easily

visualized by considering Fig. 4 (b), which shows that when all three variants of Shockley partials on alternate {111} planes are used to accomplish the fcc → hcp transformation, the partial dislocations may be stacked vertically at the precipitate edge. There is a negligible strain energy associated with this configuration at the edge since an overall shape change does not occur. Also note that in this figure, the same six-plane repeating pattern is observed as for the precipitate edge shown in Fig. 22. That is, if each block in Fig. 4 (b) represents two (111) planes, examination shows that if the second block is translated to the right by $a/6[\bar{1}\bar{1}2]$, the third block is translated to the left by $a/6[2\bar{1}\bar{1}]$, or what amounts to the edge component of an $a/6[2\bar{1}\bar{1}]$ translation seen in a $[1\bar{1}0]$ projection (see Fig. 17), and the fourth block is similarly translated to the left by $a/6[\bar{1}2\bar{1}]$, a six-plane repeating pattern results. This six-plane pattern is identical to the six-plane pattern indicated in Fig. 22, demonstrating that all three variants of Shockley partial dislocations are participating in the transformation and growth of these precipitates. Thus, it appears than when new Shockley partial dislocations are nucleated on the faces of these precipitates, the influence of the elastic strain energy is sufficient to ensure that each of the three variants is nucleated in roughly equal numbers.

Although the six-plane repeating pattern is clear in Fig. 22, it is not possible to resolve individual dislocations at the precipitate edge, or to construct Burgers circuits to reveal their presence. This is due to the fact that there is some overlapping matrix at the precipitate edge, which confuses the image and leads to light/dark Moiré fringes

through the thickness of the precipitate, parallel to the faces. The Moiré fringes also have a repeating pattern which occurs about every sixth {0001} plane. However, this effect does not appear to be responsible for the staggered appearance at the precipitate edge, as can be seen by comparing the irregular positions of the Moiré fringes in Fig. 22 with the highly regular, staggered configuration at the edge. The presence of this overlapping matrix is due to the fact that the precipitate edge is not in an exact <110> orientation through the thickness of the foil, causing an overlap of matrix at the edge.

In order to gain more information about the structure of precipitate edges, additional attempts were made to find a precipitate whose edge was in a thin region near the edge of a hole, thereby increasing the possibility for the edge to lie along an exact <110> orientation through the thickness of the foil. Fig. 23 shows a low-magnification lattice image of one such precipitate, where the edge of the foil is located in the lower-right corner. A through-focus series of the precipitate edge is shown in Fig. 24. Again, sighting along the {111} planes parallel to the faces in Fig. 24 shows that the edges are largely coherent with the matrix over a range of defocus values, as was observed for the previous precipitate. There also appears to be evidence of one terminating fringe near the lower face of this precipitate and the {111} planes bend substantially in this area, indicating that there is more strain along this interface than parallel to the faces of the precipitate, which always appear to be perfectly coherent. These structural observations agree with the lattice parameter changes given in Fig. 2, which show a negligible (~ 0.5%) expansion along the a-axis of γ' pre-

cipitates and a 2.5% contraction along the c-axis perpendicular to the faces. Given the transformation strain along the c-axis, the presence of one or two a/3<111> dislocations at the edges of a 50 Å thick precipitate should fully accommodate the misfit strain along this direction. These Frank dislocation loops should further possess an interstitial character and reside within the precipitates, if the contraction along the basal planes is to be accommodated in the manner suggested by Dahmen et al. (193). While this appears to be the case in this through-focus series, the character of the terminating fringe varies with defocus, as can be seen by comparing the four images in Fig. 24. Hence, while both the magnitude of the strains and the number of possible dislocations observed at the precipitate edges in the lattice images agree with those predicted by elasticity considerations, it is difficult to determine the exact atomic structure of these defects from the images, due to the complexity of the interfacial structure and the change in contrast which occurs at the precipitate edges. Unlike the glissile Shockley partial dislocations which are stacked at the edges, the presence of these Frank-type loops implies that part of the precipitate edges must grow by a nonconservative process (102,194), requiring the addition of interstitial atoms for movement. This factor needs to be taken into account in order to accurately describe the atomistics of the growth process in current kinetic analysis of γ' precipitate plate edges. At the 350°C aging temperature used in this study, there should be an abundance of vacancies available for atomic transport to the edges.

The precipitate edges at defocus values of -1460 and -1690 Å were enlarged in Figs. 26 and 27, so that Burgers circuits could be used to

identify the types of dislocations present at the edges. However, before analyzing the dislocations in these images, the different types of Burgers circuits that can be used to distinguish between Shockley partial dislocations which are pure edge (a 90° Shockley partial) or largely screw (a 30° Shockley partial) in character will be discussed with reference to Figs. 17 and 25 (129). As illustrated by Fig. 17, if the two Shockley partial dislocations that bound a ledge are of the type $a/6[\bar{1}\bar{1}2]$ and $a/6[\bar{1}2\bar{1}]$, and the ledge is viewed along a $[1\bar{1}0]$ electron beam direction, the Burgers vector of the $a/6[\bar{1}\bar{1}2]$ partial lies perpendicular to the viewing direction and its full edge character is seen. However, the $a/6[\bar{1}2\bar{1}]$ partial lies at an angle of 30° to the viewing direction and thus, it contains only a small edge component in the plane perpendicular to the electron beam while having an large screw component out of this plane. Because of this screw component, two different types of Burgers circuits can be drawn to distinguish between the 30° and 90° Shockley partial dislocations ledges. These two different Burgers circuits are shown in Figs. 25 (a) and (b), where it is apparent that the circuits differ only in the projected atomic positions which they follow in the hcp precipitate. All of the atom positions shown in these models are not coplanar, that is, every other atom actually lies in a plane which is slightly above or below the plane of the diagram. What these diagrams actually represent then, are the projected atom positions which are seen when a lattice image is taken in a <110> orientation. The fact that the atom positions are not coplanar, however, allows the screw component of the 30° dislocation to be identified, by constructing Burgers circuits which account for the translation out of the plane of the diagram. The Burgers circuit in Fig. 25 (a) translates out of the plane

of the diagram as it traverses across every other basal plane. Thus, it does not reveal the presence of the 30° Shockley partial associated with the ledge in Fig. 25 (a). If the circuit is now constructed such that it remains coplanar, the presence of the 30° dislocation is indicated by a closure failure as shown in Fig. 25 (b). The reverse situation occurs for the pure edge dislocation shown in Figs. 25 (c) and (d), i.e. the opposite Burgers circuit leads to a closure failure. Hence, by constructing both types of Burgers circuits around a ledge, or around a number of ledges such as at a precipitate edge, the quantities of different types of Shockley partials can be determined.

Figure 26 shows both types of Burgers circuits constructed around the precipitate edge taken at -1460 Å defocus. At this defocus the precipitate is 48 {111} matrix planes thick, as indicated in the figure. Notice that a Burgers circuit such as the one in Fig. 25 (b) produces a closure failure of 16 lattice planes, indicating the presence of 16 Shockley partial dislocations with Burgers vectors that lie at an angle of 30° to the beam direction. Similarly, when a Burgers circuit such as the one in Fig. 25 (c) is drawn, 8 additional closure failures occur, indicating the presence of 8 partial dislocations containing Burgers vectors which lie at right angles to the electron beam. Thus, a total of 24 dislocations are associated with this precipitate, which is 48 planes thick, giving excellent experimental evidence that growth is occurring by the passage of Shockley partial dislocations across alternate {111} matrix planes (35,60-62). Furthermore, the ratio of two 30° Shockley partials to every one 90° partial proves that all three types of Shockley partial dislocations are participating in the transformation from

the fcc matrix to γ' precipitates, as illustrated by Fig. 4 (b) and suggested by the staggered appearance and six-plane repeating pattern at the edge of the precipitate in Fig. 22.

Figure 27 shows the same Burgers circuits drawn around the precipitate edge taken at -1690 Å defocus. At this defocus two atomic layers along the upper face of the precipitate are not revealed and hence, the precipitate appears to be only 46 {111} planes thick. However, a 2:1 ratio of screw to edge dislocations is again revealed, as for Fig. 26. Since the quality of this image is particularly good, an attempt was made to try to resolve the atomic positions of the dislocations at the edge. Figure 28 shows a further enlargement of the top-half of the edge in Fig. 27. At this defocus and thickness, all of the atomic columns in the precipitate do not appear as separate spots but rather, join in pairs, similar to the simulated images at -1185 and -1290 Å defocus in Fig. 18. This effect makes it more difficult to distinguish the atom positions at the interface. However, a six-plane repeating pattern is apparent at the edge, and the atomic positions of four possible 90° Shockley partial dislocations are indicated on the figure, based on their similar image characteristics when compared with the simulated images for the 90° partial dislocation shown in Figs. 18 and 19. The 30° Shockley partials are more difficult to identify in this image due their small edge component in this projection.

6.2.3. Nucleation of Ledges at Precipitate Intersections

Previous studies (26,60,61,194,195) have shown that rapid nucleation of ledges often occurs when precipitates intersect. An example of this effect in the Al-Ag system is illustrated by the series of

conventional TEM micrographs in Fig. 29., where the impinging precipitate on the left has nucleated a profusion of ledges on the face of the nearly vertical precipitate. Notice that in the densely ledged region, the displacement fringes on the face of the intersected precipitate bend almost 90° (white arrow) in the weak-beam dark-field (WBDF) micrograph in Fig. 29 (c), indicating a substantial change in the precipitate thickness. However, the ledges are so closely spaced in this area that there is no possibility of resolving them by conventional TEM methods, even when WBDF is used.

Figure 30 shows a low-magnification lattice image of a similar precipitate intersection, again taken in a <110> orientation, as indicated by the inset electron and optical diffraction patterns. In this case, a thin (~ 90 Å) γ' precipitate has impinged upon a much thicker (~ 260 Å) precipitate, nucleating a large number of ledges on the intersected face. An enlargement of the intersected region is shown in Fig. 31. In this image, the edge of the impinging precipitate clearly indicates the position of the face of the intersected precipitate prior to the impingement event. Thus, it is possible to estimate the number of ledges which have been nucleated from this interface out into the matrix by counting the number of planes which show evidence of transformation. In this case, about twenty {111} matrix planes display such evidence on the right side of the intersection, indicating that about ten ledges have been nucleated. However, the precipitate structure in this area is not regular like the structure in the thick precipitate. This may be due to the fact that the ledges do not extend completely through the thickness of the foil, thereby confusing the image as in Fig. 22, or it may also

indicate that there is such a strong driving force for nucleation of new ledges at precipitate intersections that nucleation occurs extremely rapidly and in a disordered manner. The presence of true hcp crystalline structure at this location can be verified by taking a dark-field image using a $\langle 1\bar{1}01 \rangle$ precipitate reflection, as shown by the image in the upper-right corner in Fig. 31. Thus, HREM reveals much more information about intersection events than is available from CTEM images.

Also notice the inset simulated image of the precipitate structure in the lower-right corner of Fig. 31, and its agreement with the contrast of the surrounding precipitate. In addition, notice how there is a variation in intensity between the atoms on alternate basal planes in the precipitate, and how the relative intensities between these planes changes with position in the precipitate, probably due to slight thickness changes across this area. These contrast features will be discussed in detail later; however, these general precipitate image characteristics should be noted at this time.

Lastly, an enlargement of the edge of the thick precipitate is shown in Fig. 32. This edge displays the same characteristics as the edge in Fig. 22, being relatively flat and having a staggered, six-plane repeating pattern, as indicated in the figure. Thus, this type of edge structure appears to occur for both thick and thin precipitates, indicating that it is a fairly universal characteristic of growth, i.e. that all three variants of Shockley partial dislocations participate in the transformation throughout the growth process.

6.2.4. The Structure of Precipitate Edges in a <111> Orientation

All of the previous lattice images were taken with a <110> electron beam direction. While this allowed the structure of both ledges on the faces and the edges of precipitates to be determined, it is very difficult to obtain information about structural phenomena which occur along the <110> direction, either because they are hidden in the projection of atomic columns along this direction, or because they occur in limited numbers and are not present in the thin foils used for interpretable lattice images. Thus, the structure of precipitate edges was examined in a <111> orientation to search for important structural characteristics along the third dimension of the precipitates. Particular features that were examined included the atomic structure and coherency of the precipitate edges as well as the structure of kinks. However, before presenting the experimental results from these studies, possible atomic structures which have been proposed for kinks, the edges of ledges and the edges of precipitates are briefly reviewed (60,61).

Figure 33 shows an atomic model of a γ' hcp precipitate in a $[\bar{1}01]$ matrix orientation, as indicated in the accompanying legend. In this model, the first layer of hcp precipitate was formed by introducing a pair of 30° and 90° Shockley partial dislocation ledges on a (111) plane, i.e. to represent the splitting of a perfect dislocation into two Shockley partials as outlined in Sect. 2.3. For the sake of simplicity, subsequent hcp layers on the top face were created by introducing additional Shockley partials of the same type on every other (111) plane. The bottom face of the precipitate was thickened by adding opposite Shockley partials on $(\bar{1}\bar{1}\bar{1})$ planes. Strictly speaking, this model is

inaccurate in that previous lattice images have shown that all three types of Shockley partial dislocations participate in the transformation; however, this fact does not affect the present analyses. In addition, this model also assumes that the precipitate is disordered, that no relaxations have occurred around the Shockley partial dislocations and that there are no lattice parameter changes associated with the transformation. Again, these simplifications do not destroy the integrity of the model, and are not important for the present analyses.

The present analyses are aimed at determining how the structure at the edge of a precipitate (or at the edge of a ledge) might appear in a <111> projection. First, consider the two planes of atoms enclosed in the box at the precipitate edge in Fig. 33. The bottom plane contains B-sites and is continuous across the edge/matrix interface. The top plane is also continuous across this interface, although it contains atoms which are in A-sites within the precipitate and in C-sites in the matrix, the interface between these two types of sites being separated by a Shockley partial dislocation. Now imagine that the two planes of material enclosed in the box are removed from the model and viewed perpendicular to the precipitate face, in the <111> direction indicated by the arrow in Fig. 33. This slab of material appears as shown in Fig. 34, where atoms in A,B and C-sites and those which are associated with the Shockley partial dislocation are all distinguished. In addition, a single-atom kink has been introduced into the Shockley partial dislocation.

Examination of the model in Fig. 34 shows that the {110} matrix planes are continuous across the precipitate/matrix interface in all

directions, even at the kink, although some local bending of these planes occurs due to the mismatch between A and C-sites across the interface. Also notice that the introduction of this kink produces a distortion which leads to an open space at the precipitate/matrix interface. Both ledges on the faces and at the edges of precipitates are thought to migrate by the movement of such kinks parallel to the <110> dislocation line direction (36,59,60), rather than by overall forward propagation of the dislocation ledge. Further consideration of some of the structural aspects of the kink indicate why this may occur. First, the excess volume introduced by the kink should reduce the activation energy needed for the migration of a solute atom (ΔG_m) across the interface (12,99). This can be envisioned as being similar to the reduced activation energy associated with migration along a grain boundary or a dislocation core. Second, Dahmen (196) has suggested that atoms which cross the interface at a Shockley partial dislocation only have to perform partial jumps and therefore, should have an activation energy which is different than that of a diffusional jump in the matrix or precipitate. In this case, the jump distance (α) is reduced from that of regular substitutional diffusion, which should lead to preferred migration toward the direction of the interface as well as rapid transfer across the interface. Thirdly, if an atom is incorporated into the hcp precipitate by the sideways movement of a kink, both the dislocation line length and number of "unlike" bonds across the interface remains constant while the interface advances. On the other hand, if single atoms were to add randomly along the Shockley partial dislocation, incorporation of each new atom would cause a corresponding increase in the dislocation line length and number of "unlike" bonds, which is an

energetically unfavorable situation. Finally, it must be remembered that once an atom crosses the interface into the precipitate, it is highly unlikely that it will jump back into the matrix due to the favorable bonding situation and reduction in free energy that it experiences in the precipitate. Thus, all of the factors above indicate that advancement of the precipitate/matrix interface should occur by atomic attachment at kinks, and that the edges of precipitate plates and hence, the edges of ledges should be fully coherent in a <111> matrix orientation. All that remains, is to test these models by HREM. However, before doing this, it is necessary to consider some of the more macroscopic information that can be obtained from CTEM images of such interfaces and to explain the imaging conditions that must be used in order to obtain the HREM images.

Figure 35 shows a γ' precipitate orientated such that its face is perpendicular to the electron beam, i.e. the zone axis (**B**) = $[111]_{Al}//[0001]_{\gamma'}$. Several major crystallographic directions are superimposed on the precipitate and six of its edges are numbered. These numbered edges are all parallel to <110> directions within the (111) matrix plane. Also notice that the segments between the numbered edges appear macroscopically to follow <112> directions; however, ledges are apparent on all of these segments (arrows). Laird and Aaronson (36) have shown by in-situ TEM studies that similar γ precipitates do not lengthen by the overall movement of the <110> edges of the precipitates but rather, by the lateral movement of these ledges on the edges. Thus, the structure of such ledges is a particularly important factor in determining the atomistics of the growth process.

The nature of the ledges becomes more apparent in the pair of BF-WBDF micrographs in Fig. 36, taken between edges numbered 5 and 6 in Fig. 35. From these enlargements, it is clear that both the terraces and ledges into which the <112> edge is resolved are also parallel to <110> directions, in this particular case, to $[0\bar{1}1]$ and $[\bar{1}01]$. Since many of the ledges are only about 25 Å high, there is obviously a strong preference for all interfaces to lie along close-packed <110> directions even on a very fine scale. Thus, interfacial energy effects (Sect. 3.3.) appear to be exerting a rather large influence in determining the overall shape of the precipitate. However, it is not possible to obtain more detailed structural information about these interfaces without employing higher-resolution imaging techniques.

In order to obtain HREM images of the precipitate edges in a <111> orientation, it was necessary to employ the following tilted-illumination conditions. Fig. 37 (a) shows a $[111]_{Al}//[0001]_{\gamma'}$ diffraction pattern taken from the precipitate and surrounding matrix shown in Fig. 38. In this orientation, the six high-intensity spots immediately surrounding the forward scattered beam are the first-order $<01\bar{1}0>$ precipitate reflections, representing a lattice spacing of about 2.5 Å. If a 0.64 $Å^{-1}$ objective aperture is placed around these spots as shown in Fig. 37 (b), an axial lattice image of the precipitate is obtained. However, the first-order matrix reflections in this orientation are the <220> spots (the <110> spots are kinematically forbidden), which are also coincident with the $<11\bar{2}0>$ precipitate reflections as indicated in Fig. 37 (a). These <220> spots correspond to a 1.4 Å lattice spacing. Thus, there is no possibility of resolving these planes unless the

incident electron beam is tilted so that the <220> matrix reflections are symmetrically positioned inside the objective aperture, which has a diameter that is slightly greater than the resolution limit of the JEOL 200CX, as shown in Fig. 37 (c). With these tilted-illumination conditions, both the $\{01\bar{1}0\}$ and $\{11\bar{2}0\}$ spacings are resolved in the precipitate, and the {220} planes are resolved in the matrix. Thus, it is possible to determine the coherency of the precipitate edges in this orientation by examining the continuity of the {220} planes as they cross the interface to become the $\{11\bar{2}0\}$ precipitate planes. In addition, information about the atomic structure of the edges can be obtained from the axial lattice images, since the precipitate structure is seen as a true projection under these conditions. Hence, many of the following figures show both axial and tilted-illumination images in order to reveal as much information about the interface as possible, and also to compare the reliability of the tilted-illumination images for revealing the true structure of the interface. Both sets of images were obtained by first taking a through focus series of micrographs under axial conditions, and then by tilting the illumination and taking a second through-focus series without changing any of the microscope parameters other than the objective lens defocus.

Also notice the diffuse spots indicated by arrows in Fig. 37 (a), located at the 1/3 and 2/3 positions of the $<11\bar{2}0>$ precipitate reflections. These spots were present in many of the <111> diffraction patterns in this study, and will be considered in detail in establishing a model for the structure of the γ' precipitates in Sect. 6.4.

The first set of ledges at the edge of a precipitate to be examined, is shown enclosed by the box in Fig. 38 (a). A dark-field image of the precipitate, in which portions of the precipitate/matrix interface are defined more clearly, is also shown in Fig. 38 (b). A low-magnification axial lattice image of these ledges is shown in Fig. 39, where it can be seen that both the terraces and edges of the ledges into which the precipitate edge is resolved are about 150 Å long. Several important crystallographic directions in the matrix are also shown in this figure. Comparison with these directions shows that this interface parallels a <112> direction overall, in this particular case $[\bar{1}\bar{1}2]$, just as the ledged edges of the precipitate shown in Figs. 35 and 36. However, it is also apparent from Fig. 39 that the edges of the ledges which comprise this interface further parallel <110> directions within the matrix on a nearly atomic level. Several of these ledges are shown in greater detail in Figs. 40 through 43.

Figure 40 shows both axial and tilted-illumination images of the base of the ledge on the far-left in Fig. 39. The <110> directions in the matrix are again indicated in Fig. 40 (a), and from these directions it is clear that the edges of these ledges parallel <110> directions on an atomic level. Also, examination of the {220} matrix planes in Fig. 40 (b) shows that they are continuous as they cross the edge of the precipitate to become the $\{11\bar{2}0\}$ precipitate planes. However, much clearer images of this effect are shown in subsequent micrographs.

The corner of the first ledge on the left in Fig. 39 is shown enlarged in Figs. 41 (a) and (b). Notice that in Fig. 41 (a), the corner of this ledge is not sharp but nearly flat, and that this nearly planar

interface also parallels a <112> direction within the matrix on an atomic level. Thus, the precipitate edges which lie along <112> directions on a macroscopic level not only possess ledges which are resolved into <110> facets on the order of hundreds of Angstroms high, but they also possess small regions along the edges which parallel <112> directions on a microscopic level. Such microscopic ledges are not revealed by CTEM methods. In addition, these regions are further faceted along <110> directions down to the single-atom level, as indicated by the small black dots in Fig. 41 (a), which delineate the exact atom positions at the precipitate edge since they are difficult to see without the original print. This faceting at the atomic-level demonstrates that these precipitates are highly crystallographic on both macroscopic and microscopic levels and therefore, that interfacial energy effects (Sect. 3.3.) exert a strong influence in determining their overall shape. That is, there is an extreme tendency for all interfaces of the precipitate to lie along the low-energy close-packed directions, presumably because this minimizes both the chemical and structural contributions to the interfacial energy, as discussed in Sect. 3.3. Since the precipitate edges were also faceted along <112> directions in the <110> lattice images (see Fig. 20), there is a strong tendency for the precipitate/matrix interface to lie along low-energy directions in the perpendicular direction (third dimension) as well. While this configuration at the edges may be mainly due to strain energy considerations as discussed in Sect. 6.3., it also minimizes the interfacial energy at the edges in much the same way as described above.

Figure 42 shows the next ledge to the right, which displays the same characteristics as the previous ledges. In addition, note that in Fig. 42 (b), both sets of {220} matrix planes are clearly visible, and that they are continuous as they cross into the precipitate. This indicates that the edges of the precipitate are completely coherent, as predicted by the model in Fig. 34. Lastly, Fig. 43 shows an enlargement of the ledge on the far-right in Fig. 39. Notice that the base at the bottom of this ledge (arrow) in Fig. 43 (a) is slightly rounded, rather than forming a sharp corner. This may be due to the fact that such a corner should be a favorable site for atomic attachment and therefore, for nucleation of new ledges at the edge, since the number of "unlike" bonds for an atom which attaches at this location is less than for an atom which tries to add to the interface at some arbitrary location along a linear <110> segment (6,12,129).

Figure 44 shows both axial and tilted-illumination images of the corner of a second precipitate which was examined in this orientation. The electron diffraction patterns corresponding to these images are shown in Fig. 45. Notice that several ledges on the order of 50 Å or less are present along the edge of this precipitate, near the corner. These edges are enlarged in Figs. 47 through 51. Also notice that the spots at 1/3 and 2/3 of the $\langle 11\bar{2}0 \rangle$ positions are present in the optical diffraction patterns from both of the images, indicating that these periodicities were recorded in the lattice images. However, it is difficult to see these periodicities in subsequent enlargements from different areas of the precipitate. What is revealed in enlargements such as the one in Fig. 46, is individual or small clusters of bright atom

positions spaced at $2n\langle 11\bar{2}0\rangle$, n = integral distances in the precipitate, such as the ones indicated by arrows in the figure. Later analyses will show that these diffraction spots are most likely due to short-range ordering on alternate basal planes of the precipitates, thus explaining why it is difficult to see any contrast effects other than the slightly regular arrangement of bright atom positions in these <111>//<0001> lattice images.

The enlargements in Fig. 47 show the corner at the edge of the precipitate, in addition to several ledges with heights of about ten $\{01\bar{1}0\}$ planes or less. Again, sighting along the {220} matrix planes in Fig. 47 (b) reveals that they are continuous across all of these features, showing that the edges are totally coherent in this orientation. This effect is clearly seen in the further enlargement of the corner at the edge, shown in Fig. 48. Since ledges have often been observed to nucleate at the corners of precipitate plates and propagate across their faces in in-situ TEM studies of γ' and V plates (35,36), as well as in other alloy systems (20,26,197), these corners have been proposed to act as large stress concentrators, which aid in the nucleation of new dislocations for ledge growth. However, lattice images such as the one in Fig. 48 indicate that the corners of γ' precipitates are also entirely coherent, and that the strain of the lattice planes at the corner of the edge is nearly the same as at other locations along the edge. Thus, an alternative explanation must be proposed to explain this phenomenon, at least for these γ' plates. One possibility might be that the corner of the precipitate contains a greater degree of disorder than the linear <110> edges, due to the fact that the Shockley partial dislocations

which comprise the edge must bend in order to change their orientation at the corner. Such bending would introduce kinks at the corner, similar to the kink illustrated in Fig. 34. These kinks can then act as nuclei for ledges at the edges, leading to the observed behavior. While these kinks would increase the lattice distortion and hence, the stresses at the corners, the increase is considerably more localized and much smaller in magnitude than is usually assumed to occur from more macroscopic considerations.

Figure 49 shows another approximately 50 Å high ledge at the edge. In addition, a number of single-plane ledges (arrows) are present on the terraces to either side of this larger ledge, suggesting that it is composed of similar single-plane ledges which have merged and are now migrating together. Such merging of ledges on the faces of precipitates has been predicted by Jones and Trivedi (43) from analyses of the diffusion fields around the ledges, and was discussed with regard to ledges on the faces in Sect. 6.2. Additionally, since the edge of the precipitate is bounded by Shockley partial dislocations, each single-plane ledge in this <111>//<0001> projection should contain a kink at the edge, as shown in Fig. 34. Thus, the merging of these single ledges into "superledges" at the edges may also be partly due to elastic interactions between kinks, similar to the type of elastic interaction displayed by the Shockley partial dislocation ledges in Figs. 4 (b) and 26.

Thus, it appears that ledges at the precipitate edges in <111> projections may behave similarly to those observed in <110> projections. That is, both ledges on the faces of the precipitates and ledges at the

edges are composed of the same Shockley partial dislocations, which grow by the movement of kinks parallel to the dislocation line direction, as illustrated by Fig. 34. Because the character of both types of ledges is inherently related to the elastic character of the ledge dislocations, all of the features of the ledges will try to arrange in such a way as to minimize the elastic strain energy associated with the transformation process. Thus, strain energy effects also appear to exert a large influence in determining how these precipitates grow. However, these strain energy effects do not appear to limit how fast growth can occur but rather, only the form in which the structural aspect of the transformation takes place.

Also note that it is the type of superledges which have been shown in Fig. 49 and many of the previous figures, which contributed to the lengthening rate of the γ precipitate plotted in Fig. 10 of Laird and Aaronson (36). However, HREM images such as those in Fig. 49 show that precipitate edges also lengthen by the movement of ledges which are only one atomic plane high. While the movement of such ledges obviously does not contribute to the macroscopic lengthening rate of these precipitates as significantly as does the larger superledges, they are responsible for some movement of the edges and can only be observed by high-resolution TEM techniques.

That growth of the edges of precipitates is occurring by the lateral migration of these ledges along the edges is clearly illustrated by the HREM images shown in Figs. 50 and 51. Fig. 50 again shows both axial and tilted-illumination lattice images of a series of single-atom ledges at the edge of a γ' plate. Notice the one-to-one correspondence

between the ledges shown in these two images, indicating that atomic detail is being faithfully reproduced by the tilted-illumination technique. The single-atom ledges are spaced an average of about 35 Å apart along the edge. An enlargement of the three ledges on the far right in Fig. 50 is shown in Fig. 51. Notice from the enlargement that the terraces between each of these ledges is atomically flat while the edges of the ledges (arrows) are indistinct, indicating that atomic attachment is occurring at these locations. Again, since each of these ledges is actually a kink in a Shockley partial dislocation, this image demonstrates conclusively that atomic attachment and hence, growth of the γ' precipitates, is occurring by the motion of kinks in Shockley partial dislocations parallel to the dislocation line direction, as proposed by the model in Fig. 34. Also notice that the {220} matrix planes are continuous across both terraces and ledges at the precipitate edge in this figure, as in all of the previous figures, showing that the edges are coherent in this orientation as predicted by the model in Fig. 34. Sighting along the {220} planes in the plane of the figure also shows that they bend slightly as they cross the interface to become the $\{11\bar{2}0\}$ precipitate planes, again conforming to the predictions of the model in Fig. 34.

The results of all the previous HREM studies can thus be summarized at this point as showing that the growth of both the faces and edges of γ' precipitate plates does not occur by the attachment of individual atoms randomly on these interfaces as illustrated in Fig. 52 (a) but instead, by the attachment of atoms at kinks in the Shockley partial dislocations which constitute the ledges on both the faces and edges of

these precipitate plates, as illustrated in Fig. 52 (b). Thus, the standard terrace-ledge-kink mechanism of growth which was originally proposed for the growth of close-packed interfaces of a solid into a vapor or liquid (1-12), also appears to be equally valid for describing the growth of a close-packed solid of one crystal structure into that of another.

6.3. Energy-Dispersive X-ray Spectroscopy

6.3.1. Quantitative Analyses of Extracted γ' Precipitates

As mentioned in Sect. 5.3., γ' precipitates were extracted from the Al matrix so that accurate quantitative analyses of their chemical composition could be obtained. Precipitates were extracted from samples of the 14.92 w/o Ag (4.2 a/o Ag) alloy which had been aged for 10, 30 and 120 min. at 350°C, in order to determine whether the chemistry of the γ' precipitates changes during the early stages of growth at this temperature. Fig. 53 shows scanning electron microscope (SEM) secondary electron images of the surface of the 30 min. sample after etching for about 1 hr. The γ' precipitates are visible protruding above the Al matrix in these micrographs, although a high atomic number residue appears to be covering part of the surfaces of many of these precipitates.

Figure 54 (a) shows a BF TEM image of two γ' precipitates lying face-down on a lacy carbon film, typical of the type of extracted precipitates which were chosen for analyses in this study. Notice that these precipitates are relatively clean, although some black particles are present on their surfaces and at the edges. EDS analyses of these particles (198) showed that they are nearly pure Ag, indicating that precipitation of Ag on the γ' precipitates occurs during the extraction

process. This Ag presumably is put into solution as the matrix dissolves in the NaOH etch. It did not cause any problems in the EDS analyses of these precipitates, however, because it was possible to position the electron probe on large clean areas between the particles. Figure 54 (b) shows the x-ray spectrum obtained from this precipitate, and enlargements of the Al Kα and Ag Kα peaks which were used for quantification are shown in Figs. 54 (c) and (d). The large Cu peak apparent in Fig. 54 (b) is due to fluorescence from the Cu grid supporting the carbon film.

Figure 55 further shows these same spectra ((a), (c) and (e)) compared to similar spectra ((b), (d) and (f)) from the Ag_2Al standard used to obtain the k-factors in this study. Although nearly twice the number of counts were obtained for the Ag_2Al standard and thus, the peaks in these spectra are roughly twice as high as those for the precipitate, visual inspection shows that the ratio of the heights of the Al Kα to the Ag Kα peaks is about the same for both the precipitate and Ag_2Al standard, i.e. about 2.5:1.

Table 3 shows the integrated intensities of the K_α x-ray peaks and background obtained from three separate spectra of the Ag_2Al standard. The concentrations of Ag to Al (C_{Ag}/C_{Al}) determined from these intensities are shown in Table 4, where the average composition ($\bar{x}$) and the $\Sigma (x_i - \bar{x})$ are also given. From this information, $k_{\alpha AgAl}$ was determined to be 2.233 ± 0.180 by using Eqns. (31) and (38). The coefficient of variance (C.V.) is about 8%.

Table 5 similarly lists the integrated intensities obtained from the x-ray spectra of precipitates which had been aged for 10, 30 and 120 min. at 350°C. The concentrations of Ag to Al determined from these

intensities by using Eqn. (31) and $k_{\alpha AgAl}$ given above, are shown in Table 6. A summary of the results from these analyses are presented in Table 7, where the final percentages of Ag and Al in the precipitates were determined by using Eqn. (32). As shown by the last column in Table 7, the γ' precipitates contained about 66 a/o Ag with a balance of Al at each of the aging times examined. Thus, it appears that these metastable precipitates contain the same concentration of Ag as the congruently melting compound Ag_2Al, as shown by the equilibrium phase diagram in Fig. 1 (a). This composition lies near the left side of the equilibrium γ phase field at 350°C, and is the composition usually assigned to equilibrium γ precipitates which form in Al-Ag solid-solution alloys after extended high-temperature aging treatments (Sect. 2.4.). Also notice that the composition of the γ' precipitates does not appear to vary over the range of aging times investigated, i.e. from 10 to 120 min. at 350°C.

6.3.2. Quantitative Analysis of Matrix

The Ag content of the matrix was also determined in a thin foil of the sample which had been aged for 30 min. at 350°C. This was done in order to estimate whether there was still a driving force for precipitation after 30 min. at this aging temperature, or whether the matrix had already obtained its equilibrium Ag concentration and thus, the precipitates were entering the coarsening regime. This was important to ensure that most of the ledges and interfacial structures that were observed by HREM in this study were due to the influence of precipitation rather than to coarsening, or in the case of smaller precipitates, dissolution.

Figure 56 (a) shows an x-ray spectrum obtained from the Al-14.92 w/o Ag alloy which had been solution annealed and quenched, i.e. all of the Ag is in solution. The Ag $K\alpha$ peak from this spectrum is shown enlarged in Fig. 56 (b). Similar spectra obtained from the same alloy after aging for 30 min. at 350°C are shown in Figs. 56 (c) and (d) for comparison. Notice from Figs. 56 (b) and (d), that the Ag $K\alpha$ peak decreased to slightly less than half of its initial size after the 350°C aging treatment. It was possible to obtain the matrix spectrum from the aged sample without fluorescence from the Ag-rich precipitates by tilting the sample to a <110> orientation, where the precipitates were edge-on and the probe could be located between them, as shown in Fig. 57.

Two standards were used to determine the k-factor for quantitative chemical analyses of the matrix composition: 1) the solid-solution 14.92 w/o Ag (4.2 a/o Ag) alloy, and 2) a solid-solution 3.76 w/o Ag (1.0 a/o Ag) alloy. The integrated x-ray peak intensities obtained from these two alloys are shown in Table 8, and the resulting concentrations of Ag to Al are given in Table 9. From this information, $k_{\alpha AgAl}$ was determined to be 1.251 ± 0.030, with C.V. = 2.4%. The integrated peak intensities obtained from the matrix after aging for 30 min. at 350°C are similarly shown in Table 10, and by substituting these intensities into Eqns. (31) and (32) and using the value for $k_{\alpha AgAl}$ given above, the matrix was found to contain 7.08 w/o Ag (1.87 a/o Ag) with the balance Al, and C.V. = 1.8% from Eqn. (37). Table 11 from Mondolfo (69) shows the equilibrium concentrations of Ag in Al over a range of temperatures. At 350°C, 6.61 w/o Ag (1.74 a/o Ag) is soluble in Al. Thus, the present

analyses indicate that the matrix is still slightly supersaturated with Ag (~ 0.4 w/o) after aging for 30 min. at 350°C and therefore, that a driving force for precipitation remains, albeit ever so slight. This confirms that the atomic features observed in the previous HREM images are due to the effects of precipitation and not to coarsening or dissolution. The one exception to this might occur when two different sized precipitates intersect, where contact between the precipitates leads to a high driving force for nucleation of new ledges and a local flux of Ag occurs from the smaller precipitate to the larger one.

6.4. Analysis of Electron Diffraction Patterns and Construction of Atomic Model for γ' Precipitates

Evidence has appeared in many of the previous sections which suggests that γ' precipitates might be ordered. For example, the matching between the calculated and experimental HREM images in Figs. 19, 20 and 31 was obtained by ordering of Ag on alternate basal planes, a point which was mentioned only briefly when these figures were presented. In addition, most of the $\langle 110\rangle//\langle 11\bar{2}0\rangle$ and $\langle 111\rangle//\langle 0001\rangle$ matrix/precipitate SAD patterns contained extra spots which were only briefly noted during the previous analyses. However, now that the chemical composition of the γ' precipitates is known to be 66 a/o Ag or Ag_2Al, it is possible to combine this knowledge of the chemistry with the extra information contained in the SAD patterns and HREM images to construct an atomic model of the γ' precipitate structure. That is the purpose of this section.

The $\langle 111\rangle_\alpha//\langle 0001\rangle_{\gamma'}$ matrix/precipitate SAD pattern in Fig. 37 (a) was reproduced in Fig 58 (a), and may be compared directly with the completely-indexed schematic diffraction pattern shown in Fig. 58 (b).

By comparing these two patterns, it is clear that the two diffuse reflections indicated by arrows in Fig. 58 (a) lie at 1/3 and 2/3 of the distance from the forward-scattered beam to the $\langle\bar{1}\bar{1}20\rangle$ precipitate spot, as indicated by the x's in Fig. 58 (b). Since the electron diffraction pattern has six-fold symmetry, these diffuse spots are symmetrically disposed throughout the pattern, and their diffuse character indicates that they may be due to short-range order within the basal planes. Neumann (88) observed similar diffuse spots at the 1/3 and 2/3 positions of $\langle 11\bar{2}0\rangle$ reflections in <0001> x-ray diffraction patterns taken from single crystals of Ag_2Al which had been aged for 10 days at 180°C, as shown in Fig. 59. Based upon this data, he proposed a possible model for short-range order within the basal planes of the Ag_2Al crystal, which is shown in Fig. 61. In this model, each Al atom in the basal plane is surrounded by six Ag atoms, giving an overall composition of 66 a/o Ag. A similar arrangement of atoms will be used in constructing an atomic model for the γ' precipitates in this study. However, the ordered basal planes in these precipitates contain only about 33 a/o Ag and hence, each Ag atom is surrounded by six Al atoms, i.e. the same atomic arrangement as in Fig. 60 with the atom types reversed.

Neumann (88) also reported the presence of long-range order among alternate basal planes of the Ag_2Al crystal, as evidenced by the appearance of sharp <0001> peaks where l=2n+1, in $\langle 11\bar{2}0\rangle$ single crystal x-ray diffraction patterns (Fig. 60). However, he further concluded that these peaks were due to a variation in Al content of less 2% among alternate basal planes because of their weak intensities. Similar <0001> l=2n+1 reflections were observed in $\langle 110\rangle//\langle 11\bar{2}0\rangle$ SAD patterns from γ' precipi-

tates in TEM studies by Nicholson and Nutting (74). Unlike Neumann, however, the strong intensities of the reflections in these studies led Nicholson and Nutting to suggest that there must be a large difference in composition among alternate basal planes in the precipitates, possibly as large as having alternate basal planes of pure Ag and Al_2Ag. The same <0001>, l=2n+1 reflections were seen in all of the <110>//<11$\bar{2}$0> SAD patterns in this study, as shown by the electron diffraction pattern in Fig. 62 (a), which was taken from a single γ' precipitate. The strong precipitate reflections indicated by arrows in this figure are kinematically forbidden but can arise due to double diffraction, as illustrated by the indexed diffraction pattern in Fig. 62 (b). For example, diffracted intensity can occur in the [0001] position by double diffraction from the [01$\bar{1}$1] and [0$\bar{1}$10] spots, i.e. [01$\bar{1}$1] + [0$\bar{1}$10] = [0001].

It is often possible to determine whether or not certain forbidden reflections are present due to double diffraction, by tilting the crystal about the axis containing the forbidden reflections. If the forbidden spots remain after the crystal has been tilted to the extent that intensity from reflections outside of the forbidden row can no longer contribute toward double diffraction, then it may be concluded that the spots are due to some other phenomena such as ordering. This test was applied to determine whether or not the <0001>, l=2n+1 reflections associated with γ' precipitates are due to double diffraction. Fig. 63 (a) shows the γ' precipitates contained within the selected-area aperture used for the tilting experiment. For simplicity, only a single variant of precipitate was examined. The resulting <110>//<11$\bar{2}$0> symmetric SAD pattern from precipitates is shown in Fig. 63 (b), where the <0001> spot

is indicated, i.e. compare with Fig. 62 (b). Notice that the <0001> spot retains considerable intensity as the sample is tilted about the horizontal axis, even when reflections on only the top side of the forbidden row are excited, as in Fig. 63 (d). This effect persists up to about an 11° tilt, where the Ewald sphere starts to intersect the FOLZ, as shown in Fig. 62 (f). Thus, it may be concluded that these spots are mainly due to ordering on alternate basal planes, rather than to double diffraction. Also, notice that additional spots appear every 1/6 of the distance between all of the matrix reflections in the symmetric SAD pattern in Fig. 63 (b), but that these spots readily disappear as the crystal is tilted slightly off the zone axis orientation. The origin of these spots is discussed further in Appendix 10.3.

Thus, based on the chemistry and ordering within the γ' precipitates described above, a possible atomic model for the γ' precipitate structure was constructed, as shown in Fig. 64. Notice that in this model, alternate basal planes are composed of pure Ag and Al_2Ag, in order to account for the <0001>, l=2n+1 long-range order reflections present in the <110>//<11$\bar{2}$0> diffraction patterns, and that the A-type basal planes are pure Ag. In addition, each Ag atom is surrounded by six Al atoms within the B-type basal planes in order to account for the 1/3 and 2/3<11$\bar{2}$0> short-range order reflections present in the <111>//<0001> diffraction patterns. However, two major assumptions were made in constructing this model structure. First, although the strong <0001> spots in the electron diffraction patterns indicate that there is a significant compositional difference among alternate basal planes in the precipitates, the choice of alternate planes of pure Ag and Al_2Ag cannot be

made solely from the presence of these spots in the diffraction patterns. The choice of a 66 a/o Ag difference among alternate planes was not totally arbitrary, however, since the difference in contrast between these planes in experimental HREM images such as Figs. 20 and 31 suggests that the difference in concentration of Ag between these planes is large. In addition, one of the only ways in which the short-range order within the basal planes could be accounted for was by letting one of the planes contain 33 a/o Ag, with each Ag atom surrounded by six Al atoms as described above. The second major assumption included in the model was that the A-planes of the precipitate are pure Ag, rather than the B-planes. However, this choice was again not an arbitrary one, since in experimental HREM images such as Fig. 31 where the atom positions are represented by white spots, the A-planes in the precipitate are generally darker than the B-planes. This is most likely due to the higher concentration of Ag in the A-planes, which causes greater electron scattering. However, both of these assumptions can be verified by comparing experimental HREM images of the γ' precipitates and the precipitate/matrix interface which are interpretable in terms of both the types and positions of atomic species, with calculated images of these structures under comparable specimen and microscope conditions. Many image simulations were performed in order to accomplish this and the results of these simulations are discussed in the following section.

6.5. Simulated Images of γ' Precipitates and Precipitate/Matrix Interface

6.5.1. Determination of Optimum Defocus Conditions

As discussed in Sect. 4.2., special experimental conditions must be satisfied in order to obtain a HREM image which is directly

interpretable in terms of the projected specimen potential. In particular, the influence of microscope instabilities and lens aberrations on the wave function at the exit face of the specimen must be taken into account. These factors introduce perturbations in the phase of the scattered wave and in HREM, are represented by the contrast transfer function (CTF) of the microscope. Thus, interpretation of a HREM image in terms of the atomic structure of the specimen requires a detailed knowledge of the CTF and its relationship with the spatial frequencies of the specimen. In this study, the CTF for the JEOL 200CX was determined over a range of defocus values using the program developed by Kilaas (200) and the typical microscope conditions: Acc. Voltage = 200 keV, C_s = 1.2 mm, Δ = 50 mrad and α_i = 0.4 mrad. Notice that a smaller value for α_i was used in computing these CTF's than for the simulated images which follow. This was done in order to slightly reduce damping of the CTF at the higher spatial frequencies and thereby, observe the behavior of the CTF under the best possible conditions.

Figure 65 shows the CTF for the JEOL 200CX over a range of objective lens defocus values starting from the minimum contrast condition Δz_{mc} = -240 Å and continuing through Scherzer defocus Δz_{Sch} = -660 Å, the second pass band Δz_{2nd} = -1290 Å, the third pass band Δz_{3rd} = -1690 Å and out to the fourth pass band at Δz_{4th} = -2295 Å. The locations of the spatial frequencies of the first-order reflections for both the precipitate and matrix are also indicated by small markers in these graphs, along the horizontal axes where the CTF = 0. These frequencies include the position of the <0001> precipitate reflection at about 0.21 $Å^{-1}$, and the positions of the <0002>, <$0\bar{1}10$>, <$0\bar{1}11$> precipitate reflections and

the <111> and <020> matrix reflections which lie between about 0.40 to 0.50 $Å^{-1}$.

The CTF at defocus values of -660 and -1460 Å are again shown in Figs. 66 (a) and (b), respectively, along with their original undamped form and graphs of the damping functions due to the energy spread (Δ) and convergence (α_i) of the electron beam. Notice that at Scherzer defocus in Fig. 66 (a), only spatial frequencies out to about 0.40 $Å^{-1}$ are transferred with $\sin\chi = -1$ by the objective lens, while spatial frequencies greater than this are either truncated as the CTF goes to zero at about 0.42 $Å^{-1}$, or are transferred with the opposite phase, i.e. $\sin\chi = 1$. Thus, Scherzer defocus does not represent the optimum objective lens setting for the spatial frequencies in this specimen. However, when $\Delta z = -1460$ Å as in Fig. 66 (b), all of the spatial frequencies of the specimen are imaged by the objective lens with roughly the same phase and amplitude. Thus, this objective lens setting represents an optimum imaging condition for the specimen although, because $\sin\chi = 1$ at this defocus, the bright-field image of a true weak-phase object will consist of bright atoms on a dark background, where the brightness of the atoms is related to the projected specimen potential.

Figure 67 shows one additional series of CTF's, in -20 Å defocus increments from -1400 to -1500 Å. Notice that the CTF is optimized at defocus values of about -1460 to -1500 Å. At defocus values less than about -1460 Å, the higher spatial frequencies around 0.50 $Å^{-1}$ are truncated, and for defocus values greater than -1500 Å, the flat part of the CTF between 0.40 $Å^{-1}$ and 0.50 $Å^{-1}$ starts to degenerate and thus, can no longer be used to transfer these frequencies in phase. In the simulated

images which follow, images at -1460 Å defocus are always shown since they represent the optimum imaging condition and correspond with experimental HREM images which are shown in subsequent sections.

6.5.2. Image Calculations for HCP γ' Structure

The main objective of this section is to examine simulated HREM images of the γ' crystal structure in order to determine how variations in Ag between alternate basal planes in the precipitate affect the appearance of these images. This information will then indicate if HREM can be used to determine whether the compositions of the alternate A and B basal planes in the precipitate contain essentially 100 and 33 a/o Ag, respectively, as assumed by the model in Fig. 64. Fig. 68 shows how the simulated HREM images of a γ' precipitate vary as a function of objective lens defocus for alternate basal planes which vary in composition from 66 a/o Ag each (Fig. 68 (a)), to 99 a/o Ag on the A-planes and 33 a/o Ag on the B-planes (Fig. 68 (d)). Notice that the precipitate structure which contains equal amounts of Ag on both types of basal planes (Fig. 68 (a)) can be readily distinguished from those that do not (Figs. 68 (b)-(d)) by the difference in image contrast at Gaussian defocus (Δz_G = 0 Å) and the minimum contrast condition (Δz_{mc} = -240 Å). In addition, examination of the remaining images shows that the contrast is the same for both A and B-planes when they contain the same amount of Ag, regardless of the defocus value employed. However, when the A and B-planes contain different concentrations of Ag, such as in Figs. 68 (b)-(d), the image contrast is different for these two planes at all of the defocus values shown. Further, the difference in contrast between the A and B-planes often increases as the difference in Ag concentration between

these planes is increased, as can be seen by comparing Figs. 68 (b), (c) and (d) at -1290 Å defocus. This effect does not always occur, however, as seen by comparing Figs. 68 (b), (c) and (d) at -1690 Å defocus, where only subtle changes in contrast accompany the large changes in Ag concentration between these two planes. Thus, these image simulations indicate that for a correctly chosen defocus value it is certainly possible to distinguish between a precipitate which contains the same amount of Ag on alternate basal planes from one which does not, and that it may also be possible to estimate the difference in Ag concentration between alternate basal planes in the precipitate by observing the image contrast between these two planes and/or the change in image contrast as a function of objective lens defocus for a given sample thickness.

Figure 69 is a similar series of calculated images which shows how the image contrast between alternate basal planes changes as a function of specimen thickness for a defocus value of -1460 Å. Again, notice that the contrast between alternate basal planes does not change as a function of specimen thickness when the A and B-planes contain the same Ag concentration (Fig. 69 (a)), but that it does change when the concentrations on these two planes differ (Figs. 69 (b)-(d)). Also notice that there is a similar progression in the appearance of the images with thickness for the three structures which contain different amounts of Ag on alternate basal planes. (Figs. 69 (b)-(d)). For example, at 37.2 Å thickness the Ag-rich A-planes are darker than the Ag-poor B-planes for all three models, while at 71.6 Å thickness the Ag-rich A-planes are brighter than the Ag-poor B-planes. In fact, this reversal in contrast between the A and B-planes can make it impossible to distinguish between

them by examining the hcp precipitate structure alone, i.e. it is virtually impossible to distinguish Fig. 69 (c) at 71.6 Å thickness from Fig. 69 (d) at 37.2 Å thickness without previous knowledge of the positions of the A and B-planes. However, note that in both Figs. 69 (c) and (d) at 54.4 Å thickness and in Fig. 69 (b) at 37.2 Å thickness, moving from an atom position in the A-plane to an atom position in the B-plane involves moving from a relatively dark atom position to a much brighter one. That is, atoms in the Ag-poor B-plane lie 1/3 of the lattice spacing to the right of the A atom positions, and are brighter in the images at -1460 Å defocus. Unfortunately, also note that if any of these images are rotated by 180° such that the tops and bottoms of the images are inverted, the exact opposite effect occurs, i.e. moving from what appears to be an atom in an A-plane to a B-plane is accompanied by a decrease in the brightness of the atom positions. Thus, the exact structure of the precipitate cannot be determined by examination of its image intensity alone. However, as will be shown in the following section, it can be uniquely determined if the relationship between the ABA stacking in the precipitate can be compared with the ABC stacking sequence in the matrix, provided that part of the precipitate image is at a thickness where some of the atom positions on both A and B-planes are visible.

The reversal in contrast which occurs between the A and B-planes as the specimen thickness increases can be explained by examination of the behavior of the amplitude and phase of the <0001> beam as a function of specimen thickness, as shown in Figs. 70 through 72. First, Fig. 70 shows how the amplitude of the <0001> beam changes as the specimen thickness increases, as a function of the difference in Ag concentration

between the A and B-planes. Notice that the amplitude of the <0001> beam is always zero when the A and B-planes contain equal amounts of Ag, thus explaining why the contrast of these planes is always the same regardless of specimen thickness or objective lens defocus. However, when the concentrations between these planes is different, the amplitude of the <0001> beam steadily increases with thickness up to 75 Å and in addition, the magnitude of the increase is roughly proportional to the difference in Ag concentration between the two planes, i.e. the amplitude of the <0001> beam increases more rapidly when the A and B-planes contain 99 and 33 a/o Ag, respectively, than when they contain 77 and 55 a/o Ag. Since the amplitude of the <0001> beam increases with specimen thickness up to 75 Å, its effect on the character of the image should also increase up to this thickness. This is indeed the case, as can be seen by comparing Figs. 69 (b)-(d) at 17.2 Å thickness where there is almost no evidence of the <0001> periodicity, with the images at greater thicknesses where the contrast between alternate basal planes is always different. Fig. 71 further shows the change in amplitude of the <0001> beam for a precipitate which contains 99 a/o Ag on the A-planes and 33 a/o Ag on the B-planes up to a specimen thickness of 200 Å and also, the amplitudes of all of the first-order precipitate reflections which are used to form the HREM images in this study up to this same thickness. Notice that the periodicity of the <0001> forbidden reflection is about twice that of the allowed <0002> reflection.

Figure 72 also shows the variations in the phases of the first-order beams as a function of specimen thickness up to 200 Å. Because of the high scattering power of Ag, the phases of most of the beams vary

significantly from $-\pi/2$ at thicknesses of up to only 50 Å, indicating that the weak-phase object approximation (Eqn. (17)) is only valid for γ' specimens which are on the order of 20 Å or less. In addition, notice that the phase of the <0001> beam changes by almost 2π by the time the specimen has reached a thickness of only about 70 Å, while the phase of the <0002> beam is roughly constant up to this thickness. This explains the contrast reversal which occurs between the A and B-planes up to this thickness, i.e. the phase of the <0001> beam changes from about $\pi/2$ at 35 Å to $-\pi/2$ at 70 Å, while the relative amplitudes of the <0001> and <0002> beams and the phase of the <0002> beam remain nearly constant at these thicknesses.

Thus, the results from the simulated images examined in Figs. 68 and 69 indicate that it may be possible to determine whether the A and B-planes in the γ' precipitates contain about 100 and 33 a/o Ag, respectively, as proposed for the model in Fig. 64, but only for certain combinations of objective lens defocus and specimen thickness, and provided that the correspondence between the atomic stacking in the matrix and precipitate can be determined. While it is possible to determine the objective lens defocus from a HREM negative to the accuracy needed for correct image interpretation by using an optical bench, it is extremely difficult to measure the specimen thickness in the very thin areas where HREM images are most interpretable. As was shown in Fig. 69, this can represent a serious problem for distinguishing between the A and B-planes in the precipitate when one of the planes is dark. In this case, the only way to make this distinction is to examine the precipitate image over a gradation in specimen thickness near the edge of the hole,

which either causes the atom positions in both planes of the precipitate to appear at some point, or causes sufficient detail in the image at the precipitate/matrix interface such that the A and B-planes can be distinguished by their relation with the matrix. This latter point is discussed in greater detail in the next section.

6.5.3. Image Simulations of the Precipitate/Matrix Interface

Figure 73 shows a series of simulated images of a γ' precipitate/matrix interface for a γ' precipitate which contains 100 a/o Ag on the A-planes and 33 a/o Ag on the B-planes as shown by the projected potential in the upper-left corner, as a function of both objective lens defocus and specimen thickness. The contrast from the precipitate in these images is usually the same as that in the previous simulations except that in images of thicker crystals, such as in the lower-right corner of Fig. 73, the uneven matching of the projected potential at the top and bottom of the unit cell creates an additional interface which sometimes destroys the true symmetry in the precipitate. This effect is not important in images of thinner crystals.

Two points in Fig. 73 are particularly worth considering. First, notice that in the simulated image at -1460 Å defocus and 37.2 Å thickness, the exact structure of the precipitate can be determined, since there is just enough contrast in the dark precipitate planes to define the atom positions. For example, by examining the structure of the precipitate it is possible to see that moving from an atom position in the dark plane to a bright atom position in the plane above requires a translation of 1/3 of the lattice spacing to the right. Since this translation is needed to move from an atom position in an A-plane to one

in a B-plane, it can be tentatively decided that the A-plane is Ag-rich. However, as mentioned in the previous section, positive confirmation of this fact requires that the ABA stacking sequence in the precipitate progress in the same direction as the ABC stacking in the matrix. Further examination of the matrix in this image shows that the stacking of the A,B and C-planes occurs by translation of the atoms by 1/3 of the lattice spacing to the right, thus verifying that the A and B-planes in the precipitate were correctly chosen, and that the A-planes are therefore Ag-rich. If a contrast reversal had occurred between the A and B-planes in the precipitate, moving from a dark atom position to a bright one would have required a translation of 1/3 of the lattice spacing to the left, which is the opposite of the translation in the matrix. Secondly, notice that the image contrast between the A and B-planes does not change when Δz_{mc} = -240 Å. Therefore, although the atomic positions of neither the precipitate nor the matrix are visible at this defocus value, it can conceivably be used to distinguish between Ag-rich and Ag-poor planes in the image and then compared with images taken at other defocus values where the atom positions are visible, in order to make a positive determination of the precipitate structure.

One additional series of simulated images of the precipitate/matrix interface as a function of specimen thickness is shown in Fig. 74, for objective lens defocus increments of -20 Å, from -1400 to -1500 Å. These images were included for comparison with the experimental HREM images which follow in Sect. 6.6. Notice from these images, that the brightness of the atoms corresponds directly with the projected potential for crystal thicknesses less than 20 Å, and that the matrix

displays a strong double periodicity along the <200> direction for thicknesses greater than about 100 Å. Also notice that the precipitate structure is distorted in the thicker simulations due to the boundary effect mentioned above.

Lastly, it should be mentioned that a number of additional image simulations were performed that are not shown herein. These simulations explored the effects of both crystal tilt and beam tilt on the projected potential of the precipitate structure and also, the variation of the contrast between alternate basal planes up to crystal thicknesses of 500 Å. However, since these did not have a profound effect on the images or yield much additional information which might be useful for subsequent analyses, they were not included in this section.

6.6. Comparison of Experimental HREM Images of γ' Precipitates with Simulated Images Based on Model γ' Precipitate Structure

A possible atomic model for γ' precipitates was constructed in Fig. 64, and a number of different image simulations were performed on this model in Sect. 6.5. in order to investigate whether HREM could be used to determine the atomic structure of γ' precipitates. The results of these simulations showed that it is possible to identify the atomic structure of γ' precipitates, provided the following conditions are satisfied for the HREM images: 1) atom positions in both the A and B-planes of the precipitate are visible at some point in the image, 2) there is a difference in contrast between atoms in the A and B-planes, 3) the atom positions in the matrix are visible so that the atomic stacking in the precipitate and matrix can be compared, 4) the objective lens is in the range of -1400 to -1500 Å underfocus, and preferably (5)

either a through-focus series of images or a gradation in sample thickness in a single image is available for comparison with simulated images of the precipitate/matrix interface. The purpose of this section is to match experimental HREM images of γ' precipitates with simulated images according to the conditions outlined above, in order to determine the atomic structure of the γ' precipitates.

Figure 75 shows an experimental HREM image of a γ' precipitate/matrix interface in the sample which was aged for 30 min. at 350°C. The edge of the foil is located at the left, as evidenced by the amorphous layer which is just visible in the micrograph. The electron and optical diffraction patterns corresponding to this image are also shown in the top corners of the figure. Comparing the positions of the halos in the optical diffraction pattern with the CTF's shown in Figs. 65 and 67 indicates that this image was taken at about -1440 Å underfocus. In addition, notice that the brightness of the atoms in the darker planes of the precipitate slowly decreases from the left to the right side of the micrograph. Comparison of this contrast change with the simulated images in Fig. 74 shows that good agreement is obtained for a sample thickness which varies from about 20 Å at the edge of the foil to about 40 Å on the right side of the micrograph. This fact is clearly illustrated by the inset simulated image of the interface at -1440 Å defocus and 37.2 Å thickness, shown in Fig. 75. Thus, because all of the conditions needed for correct interpretation of an experimental image outlined above are satisfied for this micrograph, it is possible to conclude that the model for the interface shown by the projected potentials in Figs. 73 and 74 is correct. This further implies that the

model for γ' precipitates constructed in Fig. 64 is also correct, since this model was used to construct the hcp part of the interface. This fact can be confirmed by comparing the brightness of the atoms on alternate basal planes in the precipitate with the stacking sequence in both the precipitate and matrix. Notice that moving from an A-plane to a B-plane involves a translation of 1/3 of the lattice spacing to the right, and is accompanied by in increase in the brightness of the atoms in the B-plane. As shown in Sect. 6.5.3., this information is sufficient to conclude that the A-planes in the precipitate are Ag-rich while the B-planes are Ag-poor.

The only factor in the model in Fig. 64 that cannot be completely determined from this micrograph, is the exact concentrations of Ag in the A and B-planes of the precipitate. However, it is possible to conclude that the A and B-planes contain a difference in concentration of at least 40 a/o Ag, since the atoms in the A-planes become almost invisible at about 40 Å thickness in Fig. 75, which only occurs for precipitate structures that contain at least 88 a/o Ag on the A-planes, as seen by comparing Figs. 69 (b)-(d) at 37.2 Å thickness. Thus, it is very likely that the A and B-planes in the γ' precipitates contain essentially pure Ag and 33 a/o Ag, respectively, when the additional condition of short range order within the Ag-poor basal planes is also considered.

Figure 76 (a) shows another HREM image of a precipitate/matrix interface obtained from a second sample. The corresponding electron diffraction pattern is shown in Fig. 76 (b), and an optical diffraction pattern which included the area contained within the box in Fig. 76 (a),

plus some additional area surrounding the box, is shown in Fig. 76 (c). Notice that all of the first-order precipitate and matrix periodicities are present in the optical diffraction pattern from the interface. This image was taken at about -1460 Å defocus, as determined by an optical diffraction pattern from the amorphous edge of the sample, which is off to the left side of the micrograph, i.e. the sample thickness is increasing from left to right in the micrograph. Although one set of basal planes is almost completely out-of-contrast in this micrograph, there are a few atoms which are visible in these planes, as indicated by the arrows in Fig. 76 (a). By comparing these atomic positions with those in the bright planes, it is possible to determine that the ABA stacking sequence in the precipitate proceeds by a 1/3 lattice translation to the right, from an atom in a dark A-plane to an atom in a bright B-plane, and that this same translation is observed in the matrix. Thus, it is again possible to conclude that the A-planes in the precipitate are Ag-rich. This fact is further demonstrated in Fig. 77, where the area enclosed in the box in Fig. 76 (a) is shown enlarged in Fig. 77 (c), and compared with the projected potential for a γ' precipitate which contains pure Ag on the A-planes and 33 a/o Ag on the B-planes (Fig. 77 (a)) and a calculated image from this projected potential for a sample thickness of 40.1 Å at -1460 Å defocus (Fig. 77 (b)). Notice the excellent agreement between the calculated and experimental images in this figure. Also, judging from the low contrast of the atoms in the A-planes of the precipitate in Fig. 77 (c), it is possible to conclude that these planes contain nearly pure Ag, further supporting the model in Fig. 64.

Finally, now that the conditions for interpretation of the atomic structure of γ' precipitates has been outlined and several examples have also been given, it is possible to further examine atomic detail which was present in some of the previous HREM images, but which was only casually mentioned up to this point. For example, referring back to the lattice image in Fig. 31 shows that in the simulated image superimposed on the precipitate, the change in the brightness of the A-atoms from left to right across the figure and the relation between the stacking in the precipitate and matrix all agree with the model precipitate structure proposed in Fig. 64. In addition, further examination of the through-focus series of micrographs of the precipitate edge in Figs. 24 again shows the same difference in contrast between the A and B basal planes as a function of objective lens defocus, again substantiating the precipitate model. Thus, examples can be found throughout the images in this thesis, which agree with model precipitate structure and image simulations.

6.7. HREM Images of Ag_2Al $\langle 11\bar{2}0 \rangle$ Single Crystal

Lattice imaging was also performed on the same $\langle 11\bar{2}0 \rangle$ Ag_2Al single crystal specimen that was used as a standard in the previous EDS analyses. This was done in order to determine how both the simulated and experimental HREM images which had been obtained for the γ' precipitates compared with a known Ag_2Al specimen. Recall that this sample had been given the same solutionizing and aging treatments as the Al-Ag alloy containing γ' precipitates examined in this study. Figure 78 shows the Ag_2Al thin foil and the corresponding electron diffraction condition that was used for the high-resolution image. This image was again taken

at about -1460 Å defocus. Notice that the Ag_2Al specimen contains a number of faults, although there are relatively large areas of perfect crystalline Ag_2Al in between these faults.

The area of the specimen that is contained within the box in Fig. 78 is shown enlarged in Fig. 79 (a), where both calculated and experimental HREM images of γ' precipitates which were obtained under similar imaging conditions are also shown superimposed on the top-left and right corners of this image, respectively. Notice the excellent agreement among all three images, further substantiating the validity of the model in Fig. 64, i.e. that the precipitate contains an overall composition of Ag_2Al and is ordered on alternate basal planes. It is also interesting to note that the Ag_2Al specimen appears to be ordered after the solutionizing and aging treatments, even though the 550°C solutionizing treatment is above the 350°C order-disorder temperature reported for γ' precipitates by Hren and Thomas (35), and the 30 min. aging treatment was given at this temperature. One possible explanation for this effect might be that the order-disorder temperature for Ag_2Al is higher than 350°C, and that the single crystal ordered during the aging treatment. However, further time-temperature relationships need to be examined to confirm this possibility. Also notice that all of the major periodicities present in electron diffraction patterns which contain γ' precipitates in this study are present in the optical diffraction pattern in Fig. 79 (b), which was taken from the HREM image of the Ag_2Al crystal in Fig. 79 (a).

Lastly, the same tilting experiment which was performed on the γ' precipitates in Fig. 63, was also performed on this $\langle 11\bar{2}0 \rangle$ Ag_2Al single

crystal. As shown in Fig. 80 (b), the <0001>, l=2n+1 spots also remained for this crystal after tilting to the same degree as in Fig. 63 (f), indicating that the presence of these reflections is due to long-range order on alternate basal planes in the Ag_2Al crystal as was observed for the γ' precipitates, and not to double diffraction.

6.8. Atomic Mechanisms of Precipitate Plate Growth

Now that the structure and chemistry of γ' precipitates and the precipitate/matrix interface have been determined at the atomic level, it possible to further establish the relationship between the structural and chemical components of the transformation, thus enabling the growth of these γ' precipitates to be described at the single-atom level. As illustrated in Fig. 81, there are two possible ways in which a γ' precipitate can thicken by the passage of a Shockley partial dislocation along an alternate matrix plane. Figure 81 (a) shows a γ' precipitate which is composed of B-planes that are pure Ag and A-planes that contain 33 a/o Ag. The stacking sequence in both the precipitate and matrix are also labelled, and the interface between the precipitate and matrix is indicated by a solid line. Notice that in order for the precipitate in Fig. 81 (a) to thicken, two things must happen: 1) a Shockley partial dislocation must propagate along the C-plane in the matrix and shift these atoms into A positions, thus accomplishing the structural change needed for advancement of the γ' interface, and 2) there must be a corresponding chemical change which allows the B-planes in the precipitate to become pure Ag and the A-planes to contain 33 a/o Ag. Notice that in this case, where the B-planes in the precipitate contain most of the Ag, the structural and chemical aspects of the transformation occur

independently. That is, the structural change is accomplished by the passage of the Shockley partial dislocation along the C-plane of matrix atoms while the major chemical change occurs in the B-plane below. However, the calculated and experimental HREM images of the precipitate/matrix interface previously analyzed in Sect. 6.6. showed that the A-planes in the precipitate are nearly pure Ag therefore, that the correct model for the precipitate/matrix interface is illustrated by Fig. 81 (b), rather than by Fig. 81 (a). Similar analyses of the chemical and structural aspects of the transformation for the model in Fig. 81 (b) now indicate that both changes occur in the same atomic plane. That is, the structural transformation is accomplished by the passage of the Shockley partial dislocation along the C-plane in the matrix, and the major chemical change also occurs by this plane attaining a composition of nearly pure Ag. Further, since it was previously shown in Sect. 6.2.4. that both thickening and lengthening of γ' precipitates occurs by the movement of kinks in the Shockley partial dislocations parallel to their line direction, it is also possible to conclude that growth of these precipitates occurs by the substitutional diffusion of Ag atoms across kinks in the Shockley partial dislocation ledges and thus, that this step is the limiting reaction in the growth process. Thus, by combining the information available from high-resolution microscopy, chemical analyses and image simulations, it is possible to describe the mechanisms of the transformation at the single-atom level.

In addition, notice that the B-plane in the two-plane ledge does not undergo a structural transformation as the Shockley partial dislocation propagates along the interface, since the dislocation terminates in

the C/A-plane above. Thus, the B-plane is structurally similar to the matrix in all directions, except for strains introduced by the terminating partial dislocation in the C/A-plane above. Consequently, substitutional diffusion of Ag along this plane at the edge of the ledge should be essentially independent of ledge structure and therefore, similar to volume diffusion of Ag in the matrix. This implies that consideration of the structural aspects of the transformation such as the disorder associated with kinks and their density along the ledges only needs to be considered for the top atom plane in a single two-plane ledge. In addition, because the B-plane possesses the required structural arrangement for the hcp precipitate before the Shockley partial dislocation has passed, significant compositional changes may occur in this layer prior to its incorporation into the precipitate, further indicating that the transfer of Ag across kinks in the Shockley partial dislocation ledges limits the growth of these precipitates. Thus, while previous kinetic analyses have been successful in predicting the growth rates of both the edges of precipitate plates and ledges on the faces by assuming that they are disordered interfaces (21-58), the observations above indicate that a number of subtle but important aspects of such transformations need to be taken into account in order to accurately understand and model the growth process on an atomic level.

Knowledge of the growth mechanism of these precipitates also provides an explaination the for their large aspect ratios. Since thickening of the precipitates requires the nucleation of new ledges on the faces, it is overall a much slower process than the diffusion-controlled growth of the edges, thus leading to the large aspect ratios. Therefore,

the atomic mechanism of growth of these γ' precipitates agrees with the overall predictions of the general theory of precipitate morphology proposed by Aaronson (13), although as shown in this study, both the edges of the precipitates and ledges on the faces grow as coherent interfaces, rather than as disordered interphase boundaries as was originally envisioned. While this study does not address the problem of nucleation of ledges on the precipitate faces directly, it intuitively seems that the nucleation of these ledges must initially relate to the driving force for precipitation when there is a large supersaturation of Ag in the matrix, i.e. two-dimensional nucleation of ledges on the faces is quite probable, but as the supersaturation of Ag decreases during the later stages of growth and the precipitates grow to the size that elastic misfit at the interphase boundary can be accommodated by the generation of misfit dislocations, a new source of ledges arises. After this misfit is accommodated, however, there are few opportunities for nucleation of subsequent ledges and thickening of the precipitates slows dramatically. Such a picture for the evolution of these precipitates agrees with experimental observations of the thickening rates of γ precipitates measured by Laird and Aaronson (36).

6.9. Convergent-Beam Electron Diffraction

Extracted γ' precipitates from the Al-14.92 w/o Ag alloy which had been aged for 10, 30 and 120 min. at 350°C were examined by CBED. Since these plates require both chemical and structural changes for growth, it was hoped that CBED could be used to follow any symmetry or lattice parameter changes which might occur during the early stages of the growth process, thus allowing further characterization of the atomic

mechanisms of growth. It was also hoped that determination of the space group of the precipitates would further confirm the model for their structure shown in Fig. 64, and discussed in detail in several previous sections. Unfortunately, difficulties were encountered in the CBED studies which prevented complete determination of some of these factors. Most of the problems which arose were due to the limited thickness of the γ' precipitates, as discussed in the following sections. Because of the difficulties encountered in analyzing the extracted precipitates, both space group and lattice parameter determinations were performed on the pure Ti standard for comparison. α-titanium was chosen as a standard material because it has similar lattice parameters, average atomic scattering factor and space group anticipated for the γ' precipitates. In addition, because the thinness of the γ' precipitates was thought to be responsible for some of the anomalous results from their space group analyses, a separate experiment was performed on the Ti standard to examine the effect of specimen thickness on center of symmetry determinations. This experiment is included as Sect. 6.9.2. Thus, in order to clarify the presentation of the CBED results, the complete space group and lattice parameter determinations for the α-titanium are shown first, followed by the results from the extracted precipitates.

6.9.1. Space Group and Lattice Parameter Determinations for α-Titanium

In its α-phase form, Ti has a hexagonal close-packed structure with $a = 2.95030$ Å and $c = 4.68312$ Å (201). Alternatively stated, it has a two atom unit-cell basis and is centrosymmetric, with the space group $P6_3/mmc$. All of the CBED pattern symmetry elements for this space group

have been derived by Goodman (179), and Goodman and Whitfield (202) have performed a complete CBED space group analysis for GaS, which also has the space group $P6_3/mmc$. Thus, this analysis was followed for determining the space group of both the α-titanium and extracted precipitates. Figure 82 is a CBED map of α-titanium, which shows the relationship among the zone axes which were used in these analyses. The zone axes of interest are the [0001] principal zone, and the $[1\bar{1}04]$, $[1\bar{1}02]$ and $[3\bar{3}02]$ zone axes, which are all reached by rotating the specimen about a $[11\bar{2}0]$ axis from the [0001] principal zone.

Figure 83 shows several CBED patterns obtained from the [0001] principal zone. For a complete indexing of the discs in the FOLZ refer to the [0001] diffraction pattern in Fig. 58 (b). Notice that both the whole pattern (WP) and bright-field (BF) disc in the ZOLZ patterns shown in Figs. 83 (a) and (b) have 6mm symmetry. That is, they possess 6-fold rotational symmetry about an axis which lies in the center of the BF disc (asterisk in Fig. 83 (a)) and runs perpendicular to the plane of the figures, and also contain two mirror planes which lie along the horizontal and vertical axes in these figures, perpendicular to the plane of the figures. Also notice that the FOLZ shown in Fig. 83 (c) displays the same 6mm symmetry. Thus, reference to columns 2 and 3 in Table 1 (from Buxton et al. (172)) shows that the only two diffraction groups in which both the BF disc and WP show 6mm symmetry are 6mm and $6mm1_R$.

Column 4 in Table 1 shows that it is possible to further distinguish between the diffraction groups 6mm and $6mm1_R$ by examining the symmetry present within a DF disc when it is located at a "special" position in the pattern. In this case, a $\langle 01\bar{1}0\rangle$ disc located at its Bragg

position on one of the mirror lines in the pattern is in a "special" position and thus, will display only m symmetry if the diffraction group is 6mm, but will display 2mm symmetry if the diffraction group is $6mm1_R$. Also notice from column 6 in Table 1, that these two diffraction groups can be similarly distinguished by comparing the intensity distributions between $\pm\mathbf{g}$ pairs of $\langle 01\bar{1}0\rangle$ discs when they are set at their respective Bragg positions. These pairs of discs will be related by a 180° rotation (2) if the diffraction group is 6mm, but will be related by a perfect translation operation where the detail within each disc also contains 2-fold rotational symmetry (21_R) if the diffraction group is $6mm1_R$. Figures 84 (a) and (b) show the intensity distributions within the $[\bar{1}010]$ and $[10\bar{1}0]$ discs when they are set at their respective Bragg positions. Notice that the detail within each of these discs displays 2mm symmetry as indicated in the figures, and that the detail between the discs is also related by a perfect translation operation. Thus, the diffraction group of α-titanium is $6mm1_R$. The point group of of this material can then be determined by referring to Table 2 (from Buxton et al. (172)). By locating the diffraction group at the top of the left column in Table 2, moving across this row to the X and then following this column down to the bottom row shows that the point group of α-titanium is 6/mmm, which is correct for the space group $P6_3/mmc$.

As mentioned in Sect. 5.7., Tanaka et al. (175) have introduced a slightly different method for determining the diffraction group of a crystal. Their method uses the detail within all of the discs in a symmetric many-beam pattern in order to obtain the diffraction group. Figure 84 (c) shows a 6-beam pattern from the Ti sample, where the incident

beam has been tilted such that the [$\bar{1}$010] disc is now centered on the optic axis with the [0000] and [$\bar{2}$020] discs positioned symmetrically on either side. The diffraction group of Ti can be determined directly from this pattern by comparing the detail within the six CBED discs in Fig. 84 (c) with the symmetries in the discs in Fig. 12. Notice that the [$\bar{2}$020] disc in Fig. 84 (c) displays 2mm symmetry as indicated in the figure, and that the [0000] disc and four remaining excited discs surrounding the optic axis all have m symmetry. Also notice that the mirror lines in these discs intersect the center of the [$\bar{2}$020] diffracting disc. According to the notation of Tanaka et al. (175) in Fig. 12, the 0 and G discs correspond to the [0000] and [$\bar{2}$020], or 2**g** disc in Fig. 83 (c). Examination of the symmetries in the G discs in Fig. 12 shows that the only diffraction group which contains 2mm symmetry is $6mm1_R$, in the lower-right corner in Fig. 12. In addition, notice that the 0 disc and four remaining discs in Fig. 12 all possess m symmetry, where the mirror lines intersect the center of the G disc, just as in Fig. 84 (c). Thus, it is possible to conclude that the diffraction group of α-titanium is $6mm1_R$ by comparing the single 6-beam pattern in Fig. 84 (c) with the schematic many-beam patterns in Fig. 12. The point group is then found to be 6/mmm from Table 2, as described in the preceding paragraph. Hence, both the Buxton et al. (172) and Tanaka et al. (175) methods for point group determination give the same results for the α-titanium sample.

Also notice that the mirror planes in Fig. 84 (c) are spaced at 30° intervals in the pattern. Figure 84 (d) shows a different many-beam pattern for the Ti sample, which was obtained by tilting the incident elec-

tron beam about the $[\bar{1}100]$ axis such that the $[2\bar{1}\bar{1}0]$ and $[\bar{1}2\bar{1}0]$ reflections are evenly excited. Notice that the mirror lines which bisect all of the $\langle 11\bar{2}0\rangle$ discs indicated in the figure are also spaced at 30° intervals around the pattern. These features indicate the presence of horizontal 2-fold axes at intervals of 30° around the zone axis, parallel to the $\langle 0\bar{1}10\rangle$ and $\langle 11\bar{2}0\rangle$ directions (202).

The space group of α-titanium can now be determined by identifying the presence of kinematically forbidden reflections in the CBED patterns. There are only four space groups which have 6/mmm symmetry. They are: P6/mmm, P6/mcc, $P6_3/mcm$ and $P6_3/mmc$, which appear as space group numbers 191 through 194, respectively, in Volume I of the "International Tables for X-ray Crystallography" (180). Examination of the conditions limiting possible reflections for these four space groups indicates that they can be readily distinguished by determining the presence or absence of two types of forbidden reflections: 1) $h\bar{h}0l$, $l=2n+1$ and 2) $hh2\bar{h}l$, $l=2n+1$. As summarized in Table 12, space group P6/mmm does not have any forbidden reflections, space groups P6/mcc and $P6_3/mcm$ both contain forbidden reflections of the type $h\bar{h}0l$, $l=2n+1$ while space group $P6_3/mmc$ has forbidden reflections of the type $hh2\bar{h}l$, $l=2n+1$, as illustrated in Fig. 85.

In Fig. 83 (c), each of the discs in the FOLZ which are centered between the pairs of $\langle 11\bar{2}0\rangle$ Kossel lines have dark bands through their centers. One of these bands is indicated by the arrow in Fig. 83 (c) and is shown in greater detail in Fig. 83 (d), where it is set at the Bragg position. These dark bands or lines of negligible intensity are Gjonnes-Moodie (G-M) lines and their presence is due to either glide

planes or screw axes in the crystal. Gjonnes and Moodie (178) have determined the conditions under which kinematically forbidden reflections remain at zero intensity when dynamic interactions are included. In the case where the forbidden reflection is due to a vertical glide plane and HOLZ interactions are included, the lines of dynamical absence are present when the incident beam lies in the plane defined by the reciprocal lattice vector of the forbidden reflection. This condition is satisfied for the $\langle 11\bar{2}1\rangle$ reflections in Figs. 83 (c) and (d), indicating that they are due to a c-glide plane parallel to the electron beam direction. Thus, reflections of the type $\langle 11\bar{2}1\rangle$ or $hh2\bar{h}l$, $h=2n+1$ are forbidden for α-titanium. This rules out P6/mmm and $P6_3/mcm$ as possible space groups for this material (Table 12).

In order to distinguish between the space groups P6/mcc and $P6_3/mmc$, the sample must be tilted to a zone axis where $h\bar{h}0l$, $l=2n+1$ reflections can be tested for dynamic absences. Reflections of this type occur in both the $[3\bar{3}02]$ and $[1\bar{1}04]$ zones and were examined in this study. These zone axes were reached by tilting the sample along a $\langle 11\bar{2}0\rangle$ Kossel line pair, as shown in Fig. 82. Figure 86 (a) shows the exact $[3\bar{3}02]$ zone axis pattern. Notice that when opposite $\langle\bar{1}103\rangle$ reflections are set at their respective Bragg positions in Figs. 86 (b) and (c), they display strong intensity fringes and HOLZ effects, indicating that they are not kinematically forbidden, i.e. reflections of the type $h\bar{h}0l$, $l=2n+1$ are allowed. Thus, reference to Table 12 indicates that the only possible space group for α-titanium is $P6_3/mmc$, as expected. Also notice that the detail between the $[\bar{1}103]$ and $[1\bar{1}0\bar{3}]$ discs is related by a perfect translation operation, further verifying the presence of a center

of symmetry in the crystal. The [11$\bar{2}$0] and [$\bar{1}\bar{1}$20] discs in Figs. 86 (d) and (e) are also related by a similar perfect translation operation and in addition, notice that the mirrors in these discs are perpendicular to their reciprocal lattice vectors. This feature indicates the presence of a horizontal 2-fold rotation axis which is parallel to the <11$\bar{2}$0> axis in the crystal, as was observed for Figs. 84 (c) and (d). Also notice that the [3$\bar{3}$02] zone axis pattern is nearly square. This is different from the highly rectangular [3$\bar{3}$02] CBED pattern shown in Fig. 3 of Goodman and Whitfield (202), indicating that they identified the wrong zone axis pattern as [3$\bar{3}$02] in their paper. However, this does not detract from their results.

Figure 87 shows the [1$\bar{1}$04] CBED zone axis pattern and three 4-beam patterns which were obtained by tilting the incident beam such that it is symmetrically positioned among the four discs, as indicated in the figures. Notice that the intensities within the <2$\bar{2}$01> reflections in these patterns are quite strong, and that they do not display evidence of G-M lines, further verifying that h$\bar{h}$01, l=2n+1 reflections are not forbidden. Also notice that opposite pairs of both <11$\bar{2}$0> and <$\bar{2}$201> reflections show perfect translational symmetry as well as the presence of horizontal 2-fold rotation axes. In addition, the detail within the <$\bar{1}$3$\bar{2}$1> CBED discs has almost perfect inversion symmetry (1_R), indicating the presence of a horizontal mirror (/m) in the crystal, i.e. perpendicular to the electron beam. Thus, all of the symmetry elements for the space group $P6_3/mmc$ have been directly identified from these CBED patterns except for the 6_3 screw axis, which can only be identified by examining the specimen in a <11$\bar{2}$0> orientation, 90° to the <0001> axis.

Also notice how much stronger the HOLZ lines are in the $[1\bar{1}04]$ zone axis pattern in Fig. 87 (b), than in the <0001> zone axis patterns in Figs. 83 (a) and (b), where weak HOLZ lines are barely visible. Kohler et al. (203) have shown that the fine HOLZ lines in the $[1\bar{1}04]$ zone axis vary sensitively with the lattice parameters in hcp crystals and therefore, can be used to make lattice parameter measurements which are accurate up to 0.1%, as illustrated by the example in Fig. 88. Thus, the α-titanium standard is suitable for this purpose. In addition, notice that the intersection of the Ewald sphere with the FOLZ in Fig. 83 (c) leads to a bright ring which can be easily measured to obtain the lattice spacing along the c-axis with an accuracy of about 2%. In fact, this measurement was performed and the lattice parameter along the c-direction was determined to be c = 4.746 Å by using Eqn. (33) and assuming that $d_{01\bar{1}0}$ = 2.555 Å. This is about 0.2% larger than the accepted value of 4.68312 Å.

6.9.2. Effect of Specimen Thickness on Symmetry Determinations by CBED

As mentioned in Sect. 6.9., interest in the validity of center of symmetry determinations by CBED resulted from the application of this technique to the study of the extracted γ' plate-shaped precipitates. Initial space group analyses of these plates yielded confusing results; that is, the combination of symmetry elements and Gjonnes-Moodie lines of dynamical extinction (178) that were observed in the patterns indicated that the precipitates should contain a center of symmetry, although ±g experiments in several orientations failed to verify this symmetry element. Subsequently, this same space group analysis was performed on the α-titanium standard for comparison with the precipitates

as shown in the previous section and in addition, ±**g** experiments were performed over a range of sample thicknesses for the α-titanium in a [1$\bar{1}$02] orientation, because it was suspected that the limited thickness of the γ' precipitates might be responsible for their apparent loss of symmetry. This section reports the results of these ±**g** experiments.

As illustrated in the previous section, one of the most commonly used procedures for determining the point group of a material requires a detailed examination of the intensity distributions and HOLZ lines within the CBED discs, and comparison with Tables 1 and 2 (from Buxton et al. (172)). One of the most important tests for determining the point group of a material by this method is the ±**g** experiment, where the intensity distributions within opposite hkl discs are compared after having been set at their respective Bragg conditions. Such a test indicates whether the material possesses a center of symmetry. Columns 6 and 7 in Table 1 list the symmetries observed between ±**g** pairs of reflections for the 31 diffraction groups. One of the main advantages that CBED has over x-ray diffraction for determining the point group of a material is the ability to readily distinguish between centrosymmetric and noncentrosymmetric crystals simply by comparing the intensity distributions between pairs of hkl discs, due to the breakdown of Friedel's law (140,204) for a noncentrosymmetric crystal in electron diffraction (176,177). For electron diffraction, this law can be expressed as:

$$(I_{hkl})^{uvw} = (I_{\overline{hkl}})^{\overline{uvw}} \qquad (40)$$

where I_{hkl} represent the dynamic intensities corresponding to the incident beam direction (uvw). Formal testing of this law requires that

the intensity distributions be compared between the diffraction patterns of a crystal which has been rotated 180°. However, since HOLZ lines may introduce asymmetry into a CBED pattern, the condition of centrosymmetry for a convergent-beam pattern or group of patterns may be defined by:

$$(I_{hk0})^{uvw} = (I_{\overline{hk0}})^{\overline{uvw}} \tag{41}$$

for all possible reflections for a structure which is at least centered in a [001] projection (177). Consequently, violation of this law indicates a lack of a center of symmetry in the projection and thus, in the crystal as a whole.

Goodman (179) and Goodman and Whitfield (202) have shown that the ± $\underline{g}$ test for centrosymmetry is most effective if performed at a low-symmetry zone axis, where the electron intensity is concentrated in the pair of hkl discs of interest and these discs lack mirror symmetry perpendicular to the horizontal rotation diad, thus enabling the perfect translation operation between hkl and $\overline{hkl}$ discs in a centrosymmetric material to be easily identified. In this investigation the $[1\bar{1}02]$ zone axis was chosen for the center of symmetry versus thickness tests, because the zone-axis pattern and $[\bar{1}101]/[1\bar{1}0\bar{1}]$ discs satisfy these conditions. The $[1\bar{1}02]$ zone axis lies at an angle of about 11° from the high-symmetry [0001] principal zone and can usually be reached by rotating the specimen about a $[11\bar{2}0]$ axis from this zone (Fig 82). However, the Ti thin foil used here contained a grain at the edge of the hole which was already near a $[1\bar{1}02]$ zone axis and hence, a rotation of only a few degrees was required to achieve an exact zone axis orientation.

The letters (a) through (d) in Fig. 89 (a) indicate where the probe was positioned relative to the edge of the foil (lower-right corner) for the thickness versus center of symmetry determinations, and correspond directly to the four series of $\pm\mathbf{g}$ CBED patterns labelled (a) through (d) in Fig. 90. The probe was located at these positions by observing the ghost image with the 2nd condenser lens in an underfocussed condition, as illustrated in Fig. 89 (b), where the probe is located at position (d) in the thinnest region of the foil. The results of the center of symmetry tests are shown in Fig. 90, where the sample thickness decreases from (a) to (d), and $[\bar{1}101]$ and $[1\bar{1}0\bar{1}]$ discs are shown on either side of the $[\bar{1}102]$ zone axis pattern for each thickness.

Examination of the intensity fringes and HOLZ lines within the ZOLZ discs in the zone axis pattern in Fig. 90 (a) shows that both the BF disc and WP have 1m symmetry, as indicated in the figure. In addition, the $[\bar{1}101]$ and $[1\bar{1}0\bar{1}]$ discs both have the same 1m symmetry when located at the Bragg position, and the detail within these discs is related by a perfect translation operation rather than by a 180° rotation. Thus, reference to Table 1 indicates that the diffraction group of this specimen is $2_R mm_R$, where the perfect translation operation (2_R) between the hkl and $\bar{h}\bar{k}l$ reflections consists of a rotation of either hkl disc by 180° about the center of the pattern, followed by an additional rotation of 180° about its own center. Further knowing that the zone axis is $[1\bar{1}02]$, allows determination of the point group from Table 2 as 6/mmm, which is correct for the space group $P6_3/mmc$. Also notice that there is no evidence of G-M lines in the $\langle\bar{1}101\rangle$ discs, further verifying that $h\bar{h}0l$, l=2n+1 reflections are allowed for this space group.

Figure 90 (b) shows a similar series of patterns taken in a thinner area of the specimen, where HOLZ lines are just visible in the BF disc in the zone axis pattern. Analysis of these patterns yields the same results as above, and the point group is again identified as 6/mmm. However, when the same $\pm\mathbf{g}$ experiment is performed in a slightly thinner area, where HOLZ lines are no longer visible in the pattern and only weak 3-dimensional dynamical diffraction is occurring, a different point group is obtained. First, notice that the intensity fringes in the zone axis ZOLZ discs in Fig. 3 (c) have 2mm symmetry. This is not different from the previous patterns, but the the absence of HOLZ lines now allows this pattern to be interpreted as having a higher symmetry than before. In addition, although the $[\bar{1}101]$ and $[1\bar{1}0\bar{1}]$ discs still have 1m symmetry, they are no longer related by a perfect translation operation but rather, by a 180° rotation. Hence, reference to Table 1 now indicates that the diffraction group of this specimen is 2mm, rather than 2_Rmm_R, and similar reference to Table 2 yields a lower-symmetry point group of $\bar{6}m2$, which is incorrect for the space group $P6_3/mmc$. The same experiment was again repeated in the thinnest areas of the foil, where intensity distributions were just visible within the ZOLZ discs. As shown by Fig. 90 (d), the same incorrect diffraction and point groups are obtained.

These results demonstrate conclusively that pattern symmetries which are not representative of the actual projected symmetry of a material may be obtained by CBED from thin specimens. In this investigation, two separate but related effects were observed. First, Friedel's law (Eqn. (40)) is a valid test for centrosymmetry only under dynamical scattering conditions, where the intensities in the CBED patterns are

sensitive to the phases of the structure factors and hence, to all of the symmetry elements of the space group. Thus, under conditions where dynamical scattering is very weak and approaching kinematical scattering, Eqns. (40) and (41) may not apply. The result of approaching kinematical scattering conditions in the CBED patterns in Fig. 90 is evidenced by an increase in the overall symmetry of the zone axis patterns, as large angle scattering is reduced to the extent that HOLZ lines, which lower the symmetry of the zone axis patterns, are no longer present. Second, Goodman and Moodie (205) have shown by n-beam dynamical theory, that the presence of an incomplete unit cell at the surface of a crystal can significantly alter the diffracted amplitudes from that crystal. Goodman (206) has also illustrated the effect of having such an incomplete unit cell on the element of centrosymmetry in CBED. Hence, if relaxations or rearrangements of atoms occur on the surfaces of specimens or through part of the bulk due to a loss of elastic constraint in the thin dimension, the alterations of phases introduced by these changes may be severe enough in thin specimens to mask the element of centrosymmetry actually present in the material. This effect is thought to have resulted in the failure of the specific $\pm\mathbf{g}$ test to identify the element of centrosymmetry in thinner areas of the specimen in Figs. 90 (c) and (d), where only weak dynamical diffraction is occurring. A similar effect might also be observed for thin specimens which are slightly bent. Thus, both of these effects lead to the result that the symmetry which is observed in the CBED pattern may be related to the conditions of the specimen, rather than to the actual space group of the material. Obviously the ideal case of an infinitely thick, parallel-sided specimen is never achieved in practice; however, for correct

interpretation of CBED patterns during point and space group determinations, these conditions should be satisfied as nearly as possible.

It is also significant that the failure of the $\pm\mathbf{g}$ test for centrosymmetry occurs at about the same specimen thickness as the loss of HOLZ lines and concurrent increase in the overall symmetry of the zone axis patterns. Thus, as long as HOLZ lines are visible within the convergent-beam discs, the $\pm\mathbf{g}$ test for centrosymmetry appears to be valid. The presence of these HOLZ lines in CBED patterns can then be used to experimentally verify that symmetry determinations are being performed in an area of the specimen which satisfies the required conditions of strong dynamical scattering.

In summary, the results of specific $\pm\mathbf{g}$ CBED tests for centrosymmetry performed over a range of specimen thicknesses in α-titanium demonstrate experimentally that thin specimens may display a lack of centrosymmetry and/or a higher zone axis pattern symmetry due to the limited specimen thickness, rather than to the space group of the material. It is therefore important that point and/or space group determinations be performed on specimens which are thick enough for strong dynamical diffraction to occur, as evidenced by the presence of HOLZ lines within the CBED discs. Particular care must be taken when performing symmetry determinations on the small particles (< 1000 Å) which are of greatest interest to materials scientists because of their strong influence on the properties of engineering materials.

6.9.3. Space Group and Lattice Parameter Determinations for γ' Precipitates

Sections 6.9.1. and 6.9.2. demonstrated the complete space group analysis for α-titanium, which has the space group $P6_3/mmc$ and also, how the specimen thickness can affect center of symmetry determinations. In addition, the lattice parameter along the c-direction of the crystal was calculated by measuring the radius of the FOLZ. Based on the results from these analyses, the present section explains the results of similar space group and lattice parameter determinations which were performed on the extracted γ' precipitates. As mentioned in Sect. 6.9., these analyses were performed in order to follow any symmetry or lattice parameter changes which might occur during the early stages of precipitate growth. However, it was not possible to find any γ' precipitates which were thick enough to display intensity fringes in the CBED discs for the sample which was aged for only 10 min. at 350°C. In fact, while a number of extracted precipitates could be readily found for analysis in the 120 min. sample, only a few precipitates in the 30 min. sample were thick enough to display any intensity fringes in the CBED patterns. Hence, the effect of precipitate thickening during aging was directly reflected in the CBED analyses, and only precipitates from samples which were aged for times of 30 min. or longer could be examined. In addition, slight distortion of the intensity distributions within the CBED discs from the extracted precipitates sometimes occurred, because the thin precipitates always bent when irradiated by the electron beam. This bending caused the precipitates to be filled with bend contours (see Fig. 54 for example), and the probe was placed within these bend contours for the CBED

analyses. Thus, if the probe was not entirely contained within the zone axis determined by the bend contours, slight distortion of the patterns within the CBED discs resulted.

Figure 91 shows a series of [0001] CBED patterns obtained from a γ' precipitate which was extracted from the sample aged for 30 min. at 350°C. These patterns can be compared directly with the same series of patterns for the Ti sample in Fig. 83. Although the precipitate is so thin that there is no detail within the BF disc in Fig. 91 (b), notice that the WP in Fig. 91 (a) and FOLZ in Fig. 91 (c) both display 6mm symmetry. Thus, reference to Table 1 shows that the diffraction group of the precipitate is either 6mm or $6mm1_R$.

Figure 92 shows another series of $\pm\mathbf{g}$ and tilted-illumination CBED patterns, which may be compared directly with the patterns for the Ti sample in Fig. 84. Notice that the $[\bar{1}010]$ and $[10\bar{1}0]$ discs at their Bragg positions in Figs. 92 (a) and (b) display only m symmetry as indicated in the figures, rather than 2mm symmetry as for the Ti sample in Figs. 84 (a) and (b). In addition, these discs are also related by a 180° rotation, unlike the Ti sample in which the $\pm\mathbf{g}$ pair is related by a perfect translation operation. Thus, reference to Table 1 indicates that the diffraction group for the precipitate which was aged for 30 min. at 350°C is 6mm, and not $6mm1_R$ as for the previous Ti sample. By using Table 2, the point group of the precipitate is then identified as 6mm.

If the Tanaka et al. (175) 6-beam CBED pattern in Fig. 92 (c) is now used to determine the diffraction group of the precipitate instead of the Buxton et al. (172) method above, a different result is obtained. Although the detail within some of the CBED discs in the SMB pattern is

slightly distorted due to bending of the precipitate, the $[20\bar{2}0]$ disc displays nearly perfect 2mm symmetry. In addition, the [0000] disc and four remaining excited discs all have m symmetry as indicated in the figure, where the mirror lines intersect the center of the $[20\bar{2}0]$ disc. Thus, comparison with the SMB patterns in Fig. 12 indicates that the diffraction group of the precipitate is $6mm1_R$, which is the same as the α-titanium sample in Fig. 84 (c). Further reference to Table 2 then identifies the point group of the precipitate as 6/mmm.

Thus, the Buxton et al. (172) and Tanaka et al. (175) methods of point group determination yield two different results for the precipitate. However, because the centrosymmetry versus thickness experiment in Sect. 6.9.2. showed that a loss of perfect translational symmetry between $\pm\mathbf{g}$ discs can occur in thin specimens due only to their limited thickness along the beam direction, it is possible that this effect is responsible for the 180° rotational symmetry observed between the $[\bar{1}010]$ and $[10\bar{1}0]$ discs in Figs. 92 (a) and (b). This is likely since no HOLZ lines are present in the CBED patterns, and the precipitate is just thick enough for weak dynamical diffraction to occur. Thus, it is best to assume that the precipitate has the higher-symmetry diffraction group given by the SMB pattern in Fig. 92 (c) and therefore, that its point group is 6/mmm. Also notice that the mirror planes in both Figs. 92 (c) and (d) are spaced at 30° intervals in the patterns, indicating the presence of horizontal 2-fold rotation axes at 30° intervals around the [0001] zone axis, parallel to the $\langle 0\bar{1}10\rangle$ and $\langle 11\bar{2}0\rangle$ directions.

The space group of the precipitate is further obtained by identifying the presence of forbidden reflections in the CBED patterns. Assuming

that the point group of the precipitates is 6/mmm, the only four possible space groups are those listed in Table 12, which can be distinguished by the presence or absence of forbidden reflections of the type $hh\bar{0}l$, l=2n+1 and $hh2\bar{h}l$, l=2n+1. Notice that G-M lines are present in the $\langle 11\bar{2}1\rangle$ discs in Figs. 91 (c) and (d), indicating the presence of $hh2\bar{h}l$, l=2n+1 forbidden reflections in the precipitate, exactly as for the α-titanium sample. Thus, the space group of the precipitate must be either P6/mcc or $P6_3/mmc$. Again, these two space groups can be distinguished by tilting the precipitate to $[1\bar{1}02]$ and $[1\bar{1}04]$ zone axes, and examining the detail within $\langle hh\bar{0}l\rangle$, l=2n+1 discs.

Figure 93 (a) shows the $[1\bar{1}02]$ zone axis CBED pattern. Notice that the overall pattern displays 2mm symmetry due to a lack of HOLZ lines, as explained in Sect. 6.9.2. These mirror lines are also present in the two sets of ±**g** pairs shown for the $\langle 11\bar{2}0\rangle$ and $\langle\bar{1}101\rangle$ reflections in Figs. 93 (b) through (d). In particular, notice that the $[\bar{1}101]$ and $[1\bar{1}0\bar{1}]$ discs in Figs. 93 (c) and (d) are related by a 180° rotation rather than by a perfect translation operation. This relation was observed between the same pair of discs in thin areas of the α-titanium sample in Set. 6.9.2., further indicating that the limited thickness of the precipitate may be responsible for its apparent loss of the /m symmetry element. The limited thickness of the precipitate is evidenced by the lack of detail within these discs due to the weak dynamical diffraction which is occurring. Also notice that there is no evidence of G-M lines in the $\langle\bar{1}101\rangle$ discs, indicating that $hh\bar{0}l$, l=2n+1 reflections are allowed for the precipitate and therefore, that their space group is $P6_3/mmc$, exactly as for the α-titanium sample.

Figure 94 shows the $[1\bar{1}04]$ CBED zone axis pattern and three 4-beam patterns which can be compared directly with the same series of micrographs for the α-titanium sample in Fig. 87. Notice the resemblance between the detail within the the $\langle\bar{2}201\rangle$ discs in Figs. 87 and 94. The strong intensities of these reflections and lack of evidence that they are forbidden further verifies that $h\bar{h}0l$, l=2n+1 reflections are allowed for the precipitate and that its space group is $P6_3/mmc$. In addition, notice that there is almost perfect translational symmetry between opposite $\langle\bar{2}201\rangle$ and $\langle 11\bar{2}0\rangle$ reflections in the 4-beam patterns and that these reflections also demonstrate the presence of horizontal 2-fold rotation axes in the precipitate. Further, the detail within the $\langle\bar{1}3\bar{2}1\rangle$ discs has almost perfect inversion symmetry (1_R), indicating the presence of a horizontal mirror (/m) in the precipitate. Thus, the symmetries obtained from the CBED patterns in this zone axis appear to be less sensitive to the limited thickness of the precipitate than the patterns obtained in the previous orientations. The evidence for a center of symmetry and horizontal mirror obtained in this orientation also confirms that the space group of the precipitate is $P6_3/mmc$ and therefore, that the correct point group is 6/mmm as determined by the SMB pattern in Fig. 92 (c).

One reason why this zone axis may reveal the true symmetry elements in thinner specimens may be due to the fact that HOLZ interactions are stronger in this orientation than in the [0001] and $[1\bar{1}02]$ orientations, as evidenced by the presence of HOLZ lines within the BF disc in Fig. 94 (b). However, these HOLZ lines are still not strong enough to obtain accurate lattice parameter information for the precipitate by comparing

their positions with those in the Ti standard, as was done in Fig. 88. However, by measuring the diameter of the bright ring in the FOLZ (which is barely visible in Fig. 91 (c)) and assuming that $d_{01\bar{1}0} = 2.477$ Å for the γ' precipitate, the lattice spacing along the c-direction was determined to be c = 4.676 Å using Eqn. (33). This spacing is about 1.5% larger than the value of 4.607 Å which is usually given for these precipitates (Fig. 2), and is equal to the lattice spacing of two {111} matrix planes, i.e. $d_{111} = 2.338$ Å. One reason for this spacing may be that the precipitates are probably less than 300 Å thick and still in the early stages of growth. Thus, they may not have achieved the full contraction along the c-direction which is characteristic of latter stage precipitates, as illustrated in Fig. 2. However, Howe et al. (61) have measured the lattice spacings of the same precipitates by optical diffraction from HREM negatives, and their results showed that there is about a 2.5% contraction among the basal planes in the precipitates when compared to the octahedral matrix planes. Thus, the larger c-spacing obtained from the CBED pattern could also be due to the error made in measuring the diameter of the FOLZ, since the bright ring associated with the FOLZ is barely visible in the pattern. In either case, the minimal contraction associated with the basal planes indicates that the edges of these precipitates should be largely coherent, as was observed in previous lattice images.

Identical space group analyses and lattice parameter determinations were also performed on extracted precipitates from the sample which was aged for 120 min. at 350°C. The results from from one precipitate are shown in Figs. 95 through 97. Since they are basically identical with

those just discussed, only the differences between the analyses for the 30 and 120 min. precipitates are described.

The [0001] CBED patterns for the 120 min. precipitate in Figs. 95 and 96 are similar to those in Figs. 91 and 92, except that detail is present within the BF disc for the precipitate in Fig. 95 (b). However, notice that the hexagon within the BF disc does not have 6-fold rotational symmetry. This is due to the fact that the electron probe was focussed slightly above the specimen when the CBED pattern was taken and thus, the detail is slightly elongated in one direction. Therefore, it may be concluded that the BF disc possesses 6mm symmetry when the probe is correctly focussed, and that the diffraction group of this precipitate is either 6mm or $6mm1_R$.

Examination of Figs. 96 (a) through (c) again shows that the SMB technique for point group determination (Fig. 96 (c)) yields a higher-symmetry point group than the $\pm\mathbf{g}$ technique (Figs. 96 (a) and (b)). The mirror lines in the 6-beam pattern are accurate to a high degree in Fig. 96 (c) and clearly indicate that the point group of the precipitate is $6mm1_R$ when compared to Fig. 12. Thus, the SMB CBED technique developed by Tanaka et al. (175) appears to be preferred over the $\pm\mathbf{g}$ method of Buxton et al. (172) for determining the point group of thin specimens. In addition, notice that G-M lines are present in the $\langle 11\bar{2}1\rangle$ discs in the FOLZ in Figs. 95 (c) and (d), while there is no evidence in Figs. 97 (b), (c) and (e) that reflections of the type $h\bar{h}0l$, $l=2n+1$ are forbidden. The detail within these discs is also similar to that observed for both the α-titanium and 30 min. precipitate and thus, it can be concluded that the space group of this precipitate, which was aged for 120

min. at 350°C, is also $P6_3/mmc$.

The lattice parameter along the c-direction was also calculated for this precipitate from the diameter of the bright ring in the FOLZ in Fig. 95 (c). By assuming that $d_{01\bar{1}0} = 2.477$ Å and using Eqn. (33), the spacing was found to be c = 4.624 Å. This is about 0.4% larger than the value of 4.607 Å which was determined by x-ray diffraction (80), but agrees with these results within the accuracy of the present measurements.

The fact that the space group of the γ' precipitates which were aged for both 30 and 120 min. at 350°C is $P6_3/mmc$, does not agree with the model structure proposed for the 30 min. sample in Fig. 64. That is, the space group $P6_3/mmc$ represents a disordered, hexagonal close-packed crystal, where the two atom unit-cell basis is randomly occupied by either Al or Ag. This does not agree with the γ' structure shown in Fig. 64, where there is long-range order on alternate basal planes in the precipitate and possible short-range order within the Al-rich planes in this structure. As explained below, there are several possible reasons for this discrepancy between the CBED results and the results obtained from conventional diffraction information, HREM images and image simulations.

First, Hren and Thomas (35) observed that γ' precipitates are initially ordered during the early stages of growth at 350°C, but that these precipitates subsequently disordered during the later stages of growth, as evidenced by the disappearance of the <0001> reflections. Unfortunately, these authors did not specify the times involved for these reactions. However, since only the coarsest γ' precipitates from

the 30 min. aging treatment were suitable for CBED, it is possible that these precipitates were undergoing the disorder transformation described by Hren and Thomas (35), thus yielding the space group $P6_3/mmc$ in the CBED analyses. Further evidence for this explanation is given in Appendix 10.3.

Another possible explanation for the conflicting results, is that the order was not detected in the CBED analyses due to the limited thickness of the extracted γ' precipitates analyzed. In his study of β-Si_3N_4, Bando (207) found that CBED patterns from thin crystals were not sensitive to the weak antisymmetric part of the noncentrosymmetric crystal structure due to the low atomic number of the N atoms. This resulted in an apparent /m symmetry element in the space group because the CBED patterns depended mainly on the crystal potential of the Si atom arrangement. Since there is also a large difference between the atomic scattering factors of Ag and Al, it is possible that the CBED patterns from the thin precipitates examined in this study were not sensitive to the preferred distribution of the weaker scattering Al atoms on alternate basal planes. In addition, notice that the extinction distance for the <0001> reflection in Fig. 72 is roughly double that of the other first-order beams in the ordered hcp precipitate. Since the precipitates from the 30 min. sample were just thick enough for some dynamical diffraction to cause intensity fringes within the CBED discs in the OOLZ, they were probably only slightly thicker than one extinction distance for the first-order OOLZ beams. Since the periodicity of the <0001> beam is almost double the periodicities of the other first-order beams, it may not have contributed sufficiently to the dynamic intensi-

ties to alter the CBED pattern symmetries, thus leading to a higher symmetry space group. Note that if the 6_3 screw axis and c-glide plane are removed from the space group $P6_3/mmc$ due to ordering of Ag on alternate basal planes, the 000l, l=2n+1 and $hh2\bar{h}l$, l=2n+1 reflections are allowed, and the resulting space group is P6/mmm. This space group has the symmetry of the model crystal in Fig. 64. Thus, both explanations are quite possible and more work is needed to distinguish which effect is dominant.

7. CONCLUSIONS

The purpose of the present research was to perform highly detailed analyses of both the structural and chemical aspects required for growth of γ' precipitates, so that the mechanisms of growth can be modelled on an atomic level. In order to accomplish this, the techniques of HREM, image simulations, electron diffraction, EDS and CBED were used. The major findings of this study are summarized below.

1. Comparison between experimental HREM images of Shockley partial dislocation ledges and simulated images based on isotropic elastic theory show that both the faces and edges of γ' precipitate plates grow by the passage of Shockley partial dislocations along alternate {111} matrix planes. In addition, the terraces between ledges are atomically flat and ledges are uniformly stepped-down from the centers to the edges of isolated precipitates, leading to the shape predicted by the general theory of precipitate morphology. There is also a strong tendency for diffusional and elastic interactions among ledges, which results in the formation of multiple-unit ledges on the faces of precipitates.

2. All interfaces of the γ' precipitates are largely coherent and are faceted along low-energy {111} and {110} planes within the matrix, thereby minimizing both the chemical and structural interfacial energies associated with the interphase boundary. In addition, the configuration of dislocations at the precipitate edges shows that equal numbers of all three types of Shockley partial dislocations on the same {111} faces of precipitates are nucleated during growth, in order to minimize the elastic strain energy associated with the fcc → hcp structural transformation.

3. Energy-dispersive x-ray spectroscopy reveals that the chemical composition of γ' precipitates is Ag_2Al, and that this composition does not vary during aging times from 10 to 120 min. at 350°C. Electron diffraction patterns from γ' precipitates and simulated HREM images performed on a model γ' structure indicate that the precipitates also possess long-range order on alternate basal planes, where the A-planes in the precipitate contain nearly pure Ag and the B-planes have the composition Al_2Ag. Further short-range order within the B-planes was also observed, where each Ag atom is surrounded by six Al atoms.

4. Agreement between calculated and experimental HREM images of the precipitate/matrix interface shows that the Shockley partial dislocation ledges on the faces and edges of γ' precipitate plates grow by a terrace-ledge-kink mechanism, where the limiting step in the growth process is the substitutional diffusion of Ag across kinks in the Shockley partial dislocations, which terminate in the Ag-rich A-planes of the precipitate. Because thickening of the precipitates requires the nucleation of new ledges on the precipitate faces, it is overall a much slower process than the diffusion-controlled growth of the edges, leading to the large aspect ratios of the γ' precipitates.

5. The space group of γ' precipitates aged for 30 and 120 min. at 350°C was found to be $P6_3/mmc$ by CBED. Since this space group represents a disordered hcp lattice, the CBED results disagree with the conventional diffraction patterns and HREM images and simulations which indicate that the γ' precipitates are ordered. This discrepancy may be due to the limited thickness of the γ' precipitates, which fails to reveal the the true 3-dimensional crystal symmetry elements in the CBED ana-

lyses, or to the fact that they are undergoing an order-disorder transformation at the longer aging times examined. Lattice parameter measurements of the c-spacing in well-developed γ' precipitates by CBED agree with the results of previous x-ray studies within the accuracy of the technique employed.

6. Point group determinations performed by CBED over a range of specimen thicknesses in α-titanium show that thin specimens may appear to lack a center of symmetry due only to their limited thickness along the electron beam direction, rather than to the actual space group of the material. Conversely, zone axis CBED patterns from thin specimens may display a symmetry which is higher than the actual symmetry of the material, due to a loss of higher-order Laue zone lines in the patterns under weak dynamical scattering conditions. Extreme care must therefore be taken to ensure that point and/or space group determinations are performed on specimens which closely satisfy the conditions of an infinitely thick, parallel-sided crystal.

8. FUTURE WORK

Several areas of this study which might benefit from further research were outlined in the Results and Discussion section. In particular, the effect of ordering within the γ' precipitates could be further investigated using a dedicated scanning transmission electron microscope (STEM) with small probe (~ 10 Å) capabilities. This small probe could be confined within the precipitates in <110>//<11$\bar{2}$0> thin foils, allowing CBED to be performed without interference from the surrounding matrix. In addition, further HREM studies could be performed on a microscope such as the JEOL ARM1000, which has better resolution capabilities than the JEOL 200CX used in this study, to further examine the atomic structures of ledges and the edges of γ' precipitates, and to compare these images with more elaborate models of multiple-high ledges than those examined herein.

The results from this thesis also suggest several possibilities for new areas of research. First, comparison studies could be performed on precipitates which grow by diffusional processes in other alloy systems, in order to investigate how the present model for precipitate growth changes with increasing misfit, interfacial energy and diffusion mechanisms such as interstitial diffusion. In addition, since the mechanisms of growth are now understood on an atomic level in the Al-Ag system, it would be interesting to determine whether growth can be controlled based on this understanding. For example, the addition of certain ternary elements to the Al-Ag alloy used in this study may "poison" the transfer of Ag across kinks in the dislocation ledges, thereby changing the aspect ratios of the γ' precipitates. This would be one of the first applica-

tions of alloy design based on knowledge of the actual atomic mechanisms of the precipitation process involved. Further, now that the growth of γ' precipitates is understood at the atomic level, many of the assumptions that are commonly used in kinetic analyses can be refined to better reflect the atomistics of the growth process. These are just a few of the many possible areas for future research.

9. ACKNOWLEDGEMENTS

This thesis would not have been possible without the help and support of a number of people. Therefore, I take great pleasure in acknowledging the following individuals who helped make it all happen.

First, I would like to thank Professor R. Gronsky for his encouragement, financial support and outstanding advice throughout the course of this investigation. In addition, I thank Professor H.I. Aaronson for his contributions toward the early stages of this work, and also for his critical reviews of the resulting manuscripts. I also take great pleasure in acknowledging Dr. U. Dahmen, whose enthusiastic afternoon discussions helped develop many of the ideas presented in this thesis. Thanks are also extended to Dr. M. Sarikaya for showing me how to run the Philips EM400 and perform CBED, and for finding the Ag_2Al specimens, and to T.R. Dinger for showing me how to run the Kevex system. In addition, I thank J.M. Rose for his help in developing the computer program in Sect. 10.1. and for showing me how to run the A.S.U. multislice programs. I also thank Dr. R. Kilaas for access to his CTF programs and Dr. M.A. O'Keefe for running the amplitude and phase plots on his SHRLI series of programs, and both of these people for their help on the computers. Thanks also goes to D. Ackland for his help on the JEOL 200CX and for keeping the microscope in top condition. I would also like to thank Marilyn, Joan, Chuck, Doug and all the people at the LBL Photo Lab who always seemed to provide those last-minute slides and countless micrographs. I also thank Professor A.M. Portis and Professor J.W. Morris, Jr. for their critical reviews of this thesis. Thanks also to M.S. Moore, K.M. Wilkinson, E.A. Kamenetzky and all of the "Gronsky

Group" for their pleasant working companionship and to J.A. Wolslegel for careful processing of this thesis.

I especially want to thank my wife Sally for her love and support during the last four years and my daughter Lindsay, for making me remember what life is all about.

This work was supported by the Director, Office of Energy Research, Office of Basic Energy Science, Materials Science Division of the U.S. Department of Energy under Contract No. DE-AC03-76SF00098.

10. APPENDICES

10.1. COMPUTER PROGRAM FOR CALCULATING THE ATOMIC POSITIONS OF A 90 DEGREE SHOCKLEY PARTIAL DISLOCATION LEDGE USING ISOTROPIC ELASTIC THEORY

```
LEDGE1,7,500.405316,MAX
*7
*USERPR
*HOLDOUT
MNF4.
FETCHPS,IDDS,ULIB,ULIBX.
FETCHPS,GFACBN7,VAR,VABN.
LINK,F=LGO,F=VAR,P=ULIB,X.
LIBRITE,JH,ALOUT1,ALOUT1,177,G=ARM,W=MAX.
FETCHPS,PLOTTER,GRAPHIC,GRAPHIC.
GRAPHIC,FN=FILM,FT=VA.
EXIT.
DUMP,O.
GRUMP.
FIN.
EOR
      PROGRAM LEDGE1(INPUT,OUTPUT,ALOUT1,TAPE1=ALOUT1,TAPE6=OUTPUT,FILM)
C
C
C     THIS PROGRAM IS DESIGNED TO DETERMINE THE ATOMIC POSITIONS OF
C     A 90 DEG. SHOCKLEY PARTIAL DISLOCATION LEDGE ON THE FACE OF A
C     HCP GAMMA PRECIPITATE USING ISOTROPIC ELASTIC THEORY, AND TO
C     ASSIGN THE CORRECT ATOMIC CONCENTRATIONS OF AG AND AL IN ORDER TO
C     DUPLICATE THE CHEMICAL STRUCTURE OF THE PRECIPITATE.
C
C
C     DESIGNATE ARRAYS FOR ATOM POSITIONS AND DISPLACEMENTS
C
      DIMENSION X(132),Y(132),UX(132),UY(132),RN(3),RD(3),S1(3),S2(3),
     *S3(3),IR(3)
      COMMON /IGSZZZ/ ZMODE(200)
      COMMON /VARI/ X,Y,N,BURG,V,X12,X36,Y11
      EXTERNAL FONT2
C
C     ENTER LATTICE PARAMETERS OF UNIT CELL, ATOMIC NUMBERS AND
C     OCCUPANCIES OF ATOM TYPES
C
      DATA A,B,C,ALPHA,BETA,GAMMA,NZ1,NZ2,OCC1,OCC2,OCC3 /29.724,25.685,
     *2.864,90.0,90.0,90.0,13,47,1.0,0.666,0.334/
C
C     ENTER LIMIT FLAGS AND SYMMETRY OPERATORS
C
      DATA NATOM,NSYM,NCENTR,NAPPLY,NTOL,NPRIN,IPRIN /162,1,1,1,-4,-2,0/
      DATA (RN(J),RD(J),S1(J),S2(J),S3(J),J=1,3) /0.,0.,1.,0.,
     *0.,0.,0.,0.,1.,0.,0.,0.,0.,0.,1./
      DATA (IR(J),J=1,3),DSMAX /0,0,1,2.15/
```

```
C
C     ENTER TEMPERATURE FACTORS AND ATOM TYPES
C
      DATA Z,TISO1,TISO2,NANI,NIND,EPS /0.,0.3,0.25,0,0,1.357/
      DATA TATOM1,TATOM2 /4HAL  ,4HAG  /
C
      WRITE(1,110) A,B,C,ALPHA,BETA,GAMMA
      WRITE(1,120) KATOM,KSYM,NCENTR,NAPPLY,NTOL,NPRIN,IPRIN
      WRITE(1,130) (RN(J),RD(J),S1(J),S2(J),S3(J),J=1,3)
C
C
C     THE FIRST PART OF THIS PROGRAM CALCULATES THE UNSTRAINED POSITIONS
C     OF ATOMS FOR THE FCC/HCP INTERFACE WITH A 90 DEG. SHOCKLEY PARTIAL
C     DISLOCATION LEDGE.
C
C     CALCULATE ATOM SEPARATIONS AS FRACTIONS OF THE UNIT CELL
C
      X12 = 1.0/12.0
      X36 = 1.0/36.0
      Y11 = 1.0/11.0
C
C     ENTER POISSON'S RATIO AND BURGERS VECTOR
C
      V = 0.347
      BURG = 2*(X36)
C
C     DETERMINE POSITIONS OF HCP LATTICE WITH ORIGIN AT LOWER-LEFT CORNER
C     OF UNIT CELL
C
      M = 0
      N = 0
C
   10 M = M+1
C
      DO 30 J = 1,2
      DO 30 I = 1,12
C
      N = N+1
C
      X(N) = (J-1)*(X36)+(I-1)*(X12)
      Y(N) = 2*(Y11)*(M-1)+(J-1)*(Y11)
C
C     TRANSFER CONTROL TO CALCULATE ATOM DISPLACEMENTS DUE TO THE
C     DISLOCATION LEDGE
C
      CALL DISPL(VARI)
C
C
C     THIS PART OF THE PROGRAM ASSIGNS THE CORRECT ATOMIC SPECIES AND
C     CONCENTRATIONS TO THE STRAINED ATOM POSITIONS ON EITHER SIDE OF
C     THE DISLOCATION LEDGE.
C
C     TRANSFER CONTROL FOR DIFFERENT ATOM TYPES ON EACH SIDE OF THE LEDGE
C
      IF (N.GT.66) GO TO 20
      IF (N.GT.60) GO TO 25
C
C     TRANSFER CONTROL FOR DIFFERENT ATOM TYPES IN A AND B LAYERS OF
```

```
C     THE HCP PRECIPITATE
C
      IF (J.EQ.2) GO TO 20
C
C     WRITE STATEMENTS FOR DIFFERENT ATOMIC CONCENTRATIONS OF AL AND AG
C
      WRITE(1,140) TATOM2,NZ2,OCC1,X(N),Y(N),Z,TISO2,NANI,NIND
      GO TO 30
C
   20 WRITE(1,140) TATOM1,NZ1,OCC2,X(N),Y(N),Z,TISO1,NANI,NIND
      WRITE(1,140) TATOM2,NZ2,OCC3,X(N),Y(N),Z,TISO2,NANI,NIND
      GO TO 30
C
   25 WRITE(1,140) TATOM1,NZ1,OCC1,X(N),Y(N),Z,TISO1,NANI,NIND
C
   30 CONTINUE
C
C
C     THESE STATEMENTS REPEAT THE DO LOOP TO CONSTRUCT THE HCP
C     PRECIPITATE TWO LAYERS AT A TIME
C
      IF (N.EQ.24) GO TO 10
      IF (N.EQ.48) GO TO 10
C
C
C     NOW CREATE UPPER ATOM PLANE OF LEDGE AND FCC MATRIX WITH PROPER
C     ATOMIC POSITIONS. NOTE THAT ATOM POSITIONS IN THE UPPER ATOM PLANE
C     OF THE LEDGE HAVE BEEN SHIFTED FROM C MATRIX POSITIONS OUTSIDE THE
C     LEDGE, AND A PRECIPITATE POSITIONS INSIDE THE LEDGE BY +/-(BURG/2)
C     TO B POSITIONS, AS DICTATED BY THE DISPLACEMENT EQUATIONS FOR UX
C     AND UY GIVEN IN HIRTH AND LOTHE, (191a) PG.202.
C
      DO 50 J = 1,2
      DO 50 I = 1,12
C
      N = N+1
C
      X(N) = J*(X36)+(I-1)*(X12)
      Y(N) = 2*(Y11)*(M)+(J-1)*(Y11)
C
C     AGAIN TRANSFER CONTROL TO COMPUTE ATOM DISPLACEMENTS
C
      CALL DISPL(VARI)
C
C     TRANSFER CONTROL FOR DIFFERENT ATOM TYPES ON EACH SIDE OF THE LEDGE
C     AND OUTSIDE THE HCP PRECIPITATE
C
      IF (N.GT.84) GO TO 35
      IF (N.GT.78) GO TO 40
C
C     WRITE STATEMENTS FOR DIFFERENT ATOMIC CONCENTRATIONS OF AL AND AG
C
   35 WRITE(1,140) TATOM1,NZ1,OCC1,X(N),Y(N),Z,TISO1,NANI,NIND
      GO TO 50
C
   40 WRITE(1,140) TATOM2,NZ2,OCC1,X(N),Y(N),Z,TISO2,NANI,NIND
C
   50 CONTINUE
```

```
C
C
C     NOW CREATE ATOM POSITIONS FOR FCC MATRIX ABOVE THE INTERFACE
C
      M = M+1
C
      DO 70 J = 1,3
      DO 70 I = 1,12
C
      N = N+1
C
      X(N) = (J-1)*(X36)+(I-1)*(X12)
      Y(N) = 2*(Y11)*(M)+(J-1)*(Y11)
C
C     AGAIN TRANSFER CONTROL TO COMPUTE ATOM DISPLACEMENTS
C
      CALL DISPL(VARI)
C
C     WRITE STATEMENT FOR AL MATRIX
C
      WRITE(1,140) TATOM1,NZ1,OCC1,X(N),Y(N),Z,TISO1,NANI,NIND
C
   70 CONTINUE
C
C     END OF PROGRAM FOR CALCULATING ATOM POSITIONS AND WRITING ATOM TYPES
C
      WRITE(1,150) (IR(J),J=1,3),DSMAX
C
C
C     CALL GRAPHIC PACKAGE AND PLOT ATOM POSITIONS (FIG. 98)
C
      CALL MODESG (ZMODE,6,0)
      CALL SUBJEG (ZMODE,0.,0.,1.,1.)
      CALL OBJCTG (ZMODE,10.0,10.0,80.0,70.5)
      CALL VECIG (ZMODE,FONT2,0)
      CALL SETSMG (ZMODE,51,1.)
      ENCODE (3,160,ICHAR)
      CALL SETSMG (ZMODE,84,ICHAR)
      CALL GRID (ZMODE,0)
      CALL POINTG (ZMODE,N,X,Y)
      CALL EXITG (ZMODE)
      CALL EXIT
C
  110 FORMAT(1H,2X,*90 DEG. SHOCKLEY PARTIAL DISLN. LEDGE*,/,6F10.6)
  120 FORMAT(7I5)
  130 FORMAT(15F3.0)
  140 FORMAT(A4,2X,I2,2X,5F10.7,10X,2I5)
  150 FORMAT(3I5,F10.5)
  160 FORMAT(*$0*)
C
      END
C
C
      SUBROUTINE DISPL
C
C
C     THIS PART OF THE PROGRAM COMPUTES THE DISPLACEMENTS OF THE
C     UNSTRAINED ATOMS DUE TO THE PRESENCE OF THE LEDGE AND THEN ADDS
```

```
C     THESE DISPLACEMENTS TO THE UNSTRAINED POSITIONS TO ACHIEVE THE
C     FINAL STRAINED ATOM POSITIONS.
C
      COMMON /VARI/ X(132),Y(132),N,BURG,V,X12,X36,Y11
C
C     TRANSLATE ORIGIN FROM LOWER-LEFT CORNER TO THE DISLOCATION CORE
C
      X(N) = X(N)-((X12)*5.5+(X36))
      Y(N) = Y(N)-(Y11)*5.5
C
C     SET DISPLACEMENTS INITIALLY TO ZERO
C
      UX = 0
      UY = 0
C
C     CALCULATE DISPLACEMENTS AT UNSTRAINED ATOM POSITIONS
C
      UX = (BURG/(2*3.1416))*(-ATAN(X(N)/Y(N))+(X(N)*Y(N))/(2*(1-V)*
     *(X(N)**2+Y(N)**2)))
      UY = -(BURG/(2*3.1416))*((1-2*V)/(4*(1-V))*ALOG(X(N)**2+Y(N)**2)+
     *(X(N)**2-Y(N)**2)/(4*(1-V)*(X(N)**2+Y(N)**2)))
C
C     NOW ADD DISPLACEMENTS TO UNSTRAINED ATOM POSITIONS TO GET
C     STRAINED ATOM POSITIONS
C
      X(N) = X(N)+UX
      Y(N) = Y(N)+UY
C
C     TRANSLATE ORIGIN BACK TO LOWER-LEFT CORNER OF UNIT CELL
C
      X(N) = X(N)+((X12)*5.5+(X36))
      Y(N) = Y(N)+(Y11)*5.5
C
C     ACCOUNT FOR DISPLACEMENTS WHICH MAKE ATOM POSITIONS NEGATIVE
C
      IF (X(N).LT.0) X(N) = 1+X(N)
C
      RETURN
      END
```

10.2. Simulated Images for HCP Crystals Containing 33 to 66 a/o Ag

In the early stages of this study, a different extraction procedure than the one outlined in Sect. 5.3. was used to separate the γ' precipitates from the Al matrix for EDS analysis. While this procedure works well for most Al alloys (208), it was not reproducible when applied to the Al-Ag alloy in this study and was later discontinued in favor of the extraction procedure in Sect. 5.3. However, initial EDS analyses were performed on precipitates which had been extracted using the earlier method. Although the precipitate compositions obtained by this procedure varied considerably, they yielded an average composition of 33 a/o Ag or Al_2Ag. Hence, several image simulations were performed for an hcp crystal based on compositions which ranged from 33 a/o Ag (Al_2Ag) to 66 a/o Ag (Ag_2Al). One result from this investigation is shown in Fig. 99.

Figure 99 shows a series of computed images at -1460 Å defocus for a hcp crystal which is 54.3 Å thick and contains different concentrations of Ag on the B-planes. The initial hcp crystal in Fig. 99 (a) contains an average of 33 a/o Ag, where the B-planes are pure Al and all of the Ag is contained in the A-planes. The concentration of Ag on the B-planes is then increased by 10 a/o in each of the subsequent figures until they contain 66 a/o Ag and an average crystal composition of 66 a/o Ag is reached in Fig. 99 (h). Two features are of particular interest in this series of micrographs. First, notice that the contrast of atoms in the B-planes does not increase regularly with the Ag concentration. Instead, the atoms remain invisible above the background until a concentration of about 50 a/o Ag is achieved. Thus, it is not possible to determine the Ag concentrations of the B-planes by their contrast at

this crystal thickness and objective lens defocus when they contain less than 50 a/o Ag. However, notice that the brightness of the A-planes steadily decreases as more Ag is added to the B-planes, although this subtle effect would be very difficult to observe experimentally. In addition, notice that at this thickness and defocus value both the A and B-planes in the images with more than 50 a/o Ag on the B-planes (Figs. 99 (f) through (h)) all display similar contrast.

The second feature of interest is that the computed image for the hcp crystal which contains 33 a/o Ag in Fig. 99 (a) is indistinguishable from the computed image for a crystal which contains 66 a/o Ag, as shown in Fig. 69 (d) at 37.2 Å thickness. This is particularly apparent when these two images and their corresponding projected potentials are compared side-by-side, as in Fig. 100. Since the Al_2Ag crystal in Fig. 100 (a) contains only half as much Ag as the Ag_2Al crystal in Fig. 100 (b), both the projected potentials and contrast in these images appears to relate more to the difference in Ag concentration between the A and B-planes than to the average composition of the crystal. Also notice that in this case, the A-planes in both crystals contain 66 a/o more Ag than the B-planes.

10.3. Anomalous Order in γ' Precipitates

Additional reflections were sometimes observed in $\langle 111\rangle//\langle 11\bar{2}0\rangle$ diffraction patterns from γ' precipitates. An example of these reflections is shown in Fig. 101 (a). The reflections indicated by arrows in between the <0000> and <0002> beams in Fig. 101 (a) and those also indicated between higher-order beams by the black spots, occur at the $1/6\langle 0002\rangle$ and $1/3\langle 0002\rangle$ positions for the hcp precipitate, as seen by

comparison with Fig. 62 (b). These precipitate periodicities are also observed in corresponding HREM images, as shown in Fig. 101 (b). Notice that bright planes (arrows) occur every sixth {0001} plane in some parts of the precipitate, and that in the area of the precipitate enclosed by the box, a six-plane repeating pattern with two bright {0001} planes followed by four dark {0001} planes occurs. Such image contrast leads to 1/6<0002> and 1/3<0002> periodicities in the optical diffraction pattern from the precipitate also shown in the top-right corner of Fig. 101 (b). However, notice that the image contrast among the basal planes changes irregularly throughout the precipitate.

Also notice that in Fig. 101 (a), the spots at the <0001> precipitate positions are much weaker than those at the 1/6<0002> and 1/3<0002> positions. In fact, two types of spot patterns along the <0001> direction were generally observed for the γ' precipitates: 1) those which displayed strong <0001> spots but negligible 1/6<0002> and 1/3<0002> spots (for example Figs. 21 and 62), and 2) those which displayed weak <0001> spots but strong 1/6<0002> and 1/3<0002> reflections (Fig. 101). If both types of spots are due to long-range order among the basal planes, then these two patterns suggest that the precipitates are ordered in two slightly different ways. That is, there is either regular long-range order on alternate basal planes in the precipitate as shown in the precipitate model in Fig. 64, or there is long-range order among groups of two, four and six basal planes, which varies with location in the precipitate. This latter order is considerably less regular and may represent a transitional state, where the precipitates are either approaching the highly ordered arrangement shown in Fig. 64, or they are

becoming disordered after having already obtained the highly ordered arrangement. The latter situation seems more likely since Hren and Thomas (35) have reported that γ' precipitates have nearly perfect order among the basal planes during the early stages of growth at 350°C, but become disordered for longer aging times at this temperature. This may also partly explain why CBED analyses of extracted γ' precipitates failed to reveal the long-range order among the basal planes, as discussed in Sect. 6.9.3.

An alternative explanation for the spots at the 1/6<0002> and 1/3<0002> positions is that they are not due to long-range order but rather, to double diffraction between the precipitate and matrix. The distance between these spots corresponds to the spacing between precipitate and matrix reflections such as $[0\bar{1}11]$ and [020], as seen by inspection of Fig. 62, indicating that the possibility for double diffraction between the precipitate and matrix exists. In particular, notice that these spots are strong in the $[110]//[11\bar{2}0]$ diffraction pattern shown in Fig. 63 (b), but that they readily disappear as the crystal is tilted slightly off the zone axis orientation in Fig. 63 (c) indicating that they are not permanent in the hcp crystal. Also notice the similarity between the image contrast of the precipitates in Fig. 101 (b) with the contrast at the edge of the precipitate in Fig. 21, which is due to the effects of overlapping precipitate and matrix through the thickness of the foil. Thus, this anamolous order may also be due to the fact that these precipitates do not extend through the thickness of the foil and thus, the wave functions at the exit face of the specimen contain diffraction effects from both the precipitate and matrix.

A final possibility for these spots can be that the precipitates are faulted. That is, if there are irregularities in the stacking sequence of the basal planes, extra spots will appear along the <0001> directions in reciprocal space depending on the periodicities of these stacking faults (209). Although the atoms in some basal planes in images such as Fig. 101 (b) do appear to be in incorrect positions for a perfect hcp lattice, it is difficult to determine whether this is due to actual faults in the precipitates, or to the effects of overlapping matrix as discussed above. Further diffraction experiments and image simulations need to be performed in order to positively determine the origin of these extra reflections.

10.4. Influence of Surface and Elastic Strain Energies on the Aspect Ratios of γ' Precipitate Plates

As mentioned at the start of Sect. 3., there is currently considerable debate as to whether interfacial energy effects, strain energy effects or the atomic mechanisms of the growth process are responsible for the large aspect ratios of plate-shaped precipitates, such as the γ' precipitate shown in Fig. 7. This section examines the influence of both the elastic and surface energy contributions to the total work required to form γ' precipitates which possess different aspect ratios over a range of precipitate thicknesses. First, values for the total work necessary to form γ' precipitates with aspect ratios of 1:1, 5:1 and 20:1 due to the surface energies alone (W_S) are calculated by using the following equation:

$$W_S(\text{ergs}) = \underset{(\text{faces})}{2\pi r^2 \gamma_c} + \underset{(\text{edges})}{2\pi r h \gamma_i} \qquad (42)$$

where γ_c and γ_i = the surface energies of the coherent faces and edges of the γ' precipitates, respectively, r = precipitate radius and h = precipitate thickness. Although Aaronson et al. (83,92) have estimated the surface energies of the coherent faces and incoherent edges of γ plate-shaped precipitates as about 40 and 350 ergs/cm^2, respectively, using the "broken-bond" model discussed in Sects. 3.3.1. and 3.3.3., more recent estimates by Lee and Aaronson (210) indicate that these values may be too high, particularly since this study has shown that the edges of γ' plates are not incoherent as was originally thought. Thus, a value of 10 ergs/cm^2 was chosen as a lower-limit for γ_c, and γ_i was scaled according to the particular aspect ratio under consideration, i.e. if the aspect ratio was 5:1 then γ = 50 ergs/cm^2. The value of 10 ergs/cm^2 is thought to be a reasonable minimum estimate for γ_c, since LeGouges et al. (211) have obtained this value for the interfacial energy of coherent {111} faces of G.P. zones in Al-Ag alloys at about 0.6 of the critical temperature of the coherent miscibility gap. Thus, while this value is still based on calculations which employ a "broken-bond" model and the true surface energy is not actually known, it should represent the lowest reasonable value and hence, emphasize the significance of any differences which might occur between the magnitudes of the interfacial and strain energies.

In this investigation, an alloy was chosen where there is a small difference in size between the matrix and solute atom (Al and Ag atoms differ by only 0.7%) and the structural transformation is such that the influence of coherency strains on the reaction is minimized. While it is possible to obtain a reasonable value for the strain energy per unit

volume of γ' precipitate by using Eqn. (10), Mayo and Tsakalakos (212) have derived an exact expression for the elastic energy function $Y(\mathbf{n})$ for a hexagonal precipitate with a <0001> habit-plane, using the reciprocal-space formulation of Khachaturyan (213). In this case, the elastic strain energy function Y[0001] is given as:

$$Y[0001]\ (\text{dynes/cm}^3) = \varepsilon_{11}^2[C_{11} + C_{12} - 2(C_{13}^2/C_{33})] \qquad (43)$$

where ε_{11} = principal stress-free transformation strain in the basal-plane of the precipitate and C_{11}, C_{12}, C_{13} and C_{33} = elastic constants of the precipitate, which are given for Ag_2Al by Lee et al. (214). Thus, values for the total work necessary to form γ' precipitates with aspect ratios of 1:1, 5:1 and 20:1 due to the elastic strain energy alone (W_e) were calculated by assigning a maximum reasonable value of $\varepsilon_{11} = 0.005$, i.e. the largest value determined from x-ray measurements on equilibrium γ precipitates shown in Fig. 2, and multiplying this value by the precipitate volume as given below:

$$W_e(\text{ergs}) = Y[0001]\ \pi r^2 h. \qquad (44)$$

Thus, the total work needed to form a given volume of precipitate due to the elastic strain energy was estimated using maximum reasonable values, again in order to emphasize the significance of any differences which might occur between the magnitudes of the elastic and surface energies. Note that any additional energy associated with the presence of the transformation dislocations at the edges of the precipitate plates has been equally neglected from both the surface and strain energy calculations in Eqns. (42) and (44).

The results from these calculations are summarized in Fig. 102. In this figure, the total work needed to form a given thickness of

precipitate due to the surface energy is indicated by dashed lines for aspect ratios of 1:1, 5:1 and 20:1, while the total work for the corresponding elastic strain energy is indicated by solid lines. By comparing these curves, it is evident that the surface energies associated with the formation of early-stage γ' precipitates are on average about one order-of-magnitude greater than the elastic strain energies for the same precipitates, up to precipitate thicknesses of around 150 Å. Also notice that this relation is essentially independent of the value of γ_i used for each aspect ratio, indicating that the major contribution to the interfacial energy of the precipitates is due to the faces. In addition, if an even lower value for the surface energy of the coherent faces (γ_c) such as 5 ergs/cm^2 is used for a precipitate with an aspect ratio of 1:1, the total work needed to form the precipitate due to the surface energy is still an order-of-magnitude greater than for the elastic strain energy until the precipitate is about 70 Å thick, as shown in Fig. 102. Thus, these calculations indicate that the contribution of the surface energy should dominate over the elastic strain energy in determining the aspect ratios of γ' precipitates during the early stages of growth, while the elastic strain energy should determine the morphology after a critical thickness is exceeded during the later stages of growth.

Although these approximate calculations indicate that the surface energy has a stronger effect in determining the aspect ratios of γ' precipitates than the elastic strain energy during the early stages of growth, the ratio of the surface energy at the precipitate edges (γ_i) to that at the faces (γ_c) appears to be insufficient to account for the

large aspect ratios of these precipitates. The reason for this is that HREM images of precipitate edges obtained in this investigation have shown that the edges of γ' plates are largely coherent and therefore, that they should possess a surface energy which is only slightly greater than that at the faces. As demonstrated by Fig. 7, γ' precipitates can have aspect ratios as large as 20:1 during the initial stages of growth, and such large aspect ratios cannot be predicted from the classic surface energy calculations just discussed. Further, since the surface energy dominates over the strain energy, strain energy arguements cannot be used to explain the large aspect ratios of early-stage precipitates. Although both interfacial and strain energy effects influence the growth process as demonstrated by the HREM images in Sects. 6.2.2. and 6.2.4., they do not appear to limit it per se. Thus, these results indicate that the atomic mechanisms of the growth process may be responsible for the large aspect ratios of the precipitates. One way to confirm this possibility might be to measure the thicknesses and aspect ratios of many γ' precipitates throughout the early stages of growth by HREM, and compare these values with those predicted by surface energy, strain energy and kinetic calculations similar to those above.

11. REFERENCES

1. J.W. Gibbs, "On the Equilibrium of Heterogeneous Substances, Collected Works," Longman, Green and Company, New York (1928).

2. C. Elbaum and B. Chalmers, Can. J. Phys., 33, 196 (1955).

3. A. Rosenberg and W.A. Tiller, Acta Met., 5, 565 (1957).

4. J.W. Cahn, Acta Met., 8, 556 (1960).

5. J.W. Cahn, W.B. Hillig and G.W. Sears, Acta Met., 12, 1421 (1964).

6. M.C. Flemings, "Solidification Processing," McGraw-Hill, New York (1974).

7. R. Becker and W. Doring, Ann. Phys., 24, 719 (1935).

8. W.K. Burton and N. Cabrera, Disc. Faraday Soc., 5, 33 (1949).

9. W.K. Burton, N. Cabrera and F.C. Frank, Phil. Trans. Roy. Soc., A243, 299 (1950-51).

10. F.C. Frank, in "Growth and Perfection of Crystals," John Wiley, New York, 411 (1958).

11. J.P. Hirth and G.M. Pound, Prog. Metal Phys., 11, 1 (1963).

12. J.W. Christian, "The Theory of Transformations in Metals and Alloys," Pergamon Press, Oxford (1965).

13. H.I. Aaronson, in "Decomposition of Austenite by Diffusional Processes," Interscience Pub., 387 (1962).

14. H.I. Aaronson, C. Laird and K.R. Kinsman, in "Phase Transformations," ASM, Metals Park, Ohio, 313 (1970).

15. H.I. Aaronson, J. Microscopy, 102(3), 275 (1974).

16. K.M. Knowles, Phil. Mag., 45(3), 357 (1982).

17. D.L Kohlstedt and J.B. Vander Sande, in "Electron Microscopy in Mineralogy," Springer-Verlag, Berlin, 234 (1976).

18. J.H. Mazur, in "Proc. 41st EMSA Conf.," San Francisco Press, San Francisco, 106 (1983).

19. D.R. Clarke and G. Thomas, J Amer. Cer. Soc., 60, 491 (1977).

20. G.C. Weatherly, Acta Met., 19, 181 (1971).

21. C. Laird and H.I. Aaronson, Trans. Met. Soc. AIME, 242, 1393 (1968).

22. Ibid., 1437.

23. P. Merle and E. Fouquet, Acta Met., 29, 1919 (1981).

24. Ibid., 1929.

25. P. Merle and R.D. Doherty, Scripta Met., 16, 357 (1982).

26. R. Sankaran and C. Laird, Acta Met., 22, 957 (1974).

27. G. Thomas and M.J. Whelan, Phil. Mag., 6(2), 1103 (1961).

28. E.P. Simonen, H.I. Aaronson and R. Trivedi, Met. Trans., 4, 1239 (1973).

29. K.R. Kinsman, E. Eichen and H.I. Aaronson, Met, Trans., 6A, 303 (1975).

30. J.R. Bradley, J.M. Rigsbee and H.I. Aaronson, Met. Trans., 8A, 783 (1977).

31. K.R. Kinsman and H.I. Aaronson, in "Transformations and Hardenability in Steels," Climax Molybdenum Co., Ann Arbor, MI, 39 (1967).

32. E.P. Simonen and R. Trivedi, Acta Met., 25, 945 (1977).

33. H.I. Aaronson, Trans. Met. Soc. AIME, 218, 299 (1960).

34. M.G. Hall, K.R. Kinsman and H.I. Aaronson, Met. Trans., 3, 1320 (1970).

35. J.A. Hren and G. Thomas, Trans. Met. Soc. AIME, 227, 308 (1963).

36. C. Laird and H.I. Aaronson, Acta Met., 17, 505 (1969).

37. K. Abbott and C.W. Hawarth, Acta Met., 21, 951 (1973).

38. K.K. Sagoe-Crentsil and L.C. Brown, Met. Trans., 15A, 1969 (1984).

39. M. Ferrante and R.D. Doherty, Scripta Met., 10, 1059 (1976).

40. R. Trivedi, Met. Trans., 1, 921 (1970).

41. G.J. Jones and R. Trivedi, J. Appl. Phys., 42, 4299 (1971).

42. R. Trivedi, Acta Met., 18, 287 (1970).

43. G.J. Jones and R. Trivedi, J. Cryst. Growth, 29, 155 (1975).

44. G.J. Shiflet, H.I. Aaronson and T.H. Courtney, Acta Met., 27, 377 (1979).

45. M. Hillert, Met. Trans., 6A, 5 (1975).

46. C. Atkinson, Proc. Roy. Soc. London, A378, 351 (1981).

47. A. Papapetrou, Zeit. Krist., 92, 108 (1935).

48. G.P. Ivanstov, Dolk. Akad. Nauk. SSR, 58, 567 (1947).

49. M. Hillert, Jernkontorets Annaler, 141, 757 (1957).

50. C. Zener, J. Appl. Phys., 20, 950 (1949).

51. R.F. Mehl and C.A. Dube, in "Phase Transformations in Solids," John Wiley, New York, 545 (1951).

52. C. Zener, Trans. Met. Soc. AIME, 167, 550 (1957).

53. L. Kaufmann, S.V. Radcliffe and M. Cohen, in "Decomposition of Austenite by Diffusional Processes," Interscience Pub., 313 (1962).

54. G. Horvay and J.W. Cahn, Acta Met., 9, 695 (1961).

55. W.P. Bosze and R. Trivedi, Met. Trans., 5, 511 (1974).

56. R. Trivedi and G.M. Pound, J. Appl. Phys., 38, 3569 (1967).

57. C. Atkinson, Acta Met., 16, 1019 (1968).

58. C. Atkinson, H.B. Aaron, K.R. Kinsman and H.I. Aaronson, Met. Trans., 4, 783 (1973).

59. H.I. Aaronson, Trans. Indian Inst. Metals, 32(1), 1 (1979).

60. J.M. Howe, H.I. Aaronson and R. Gronsky, Acta Met., in press.

61. Ibid.

62. J.M. Howe, in "Proc. 41st EMSA Conf.," San Francisco Press, San Francisco, 238 (1983).

63. C. Laird and H.I. Aaronson, Acta Met., 15, 73 (1967).

64. R.J. Bucci, Eng. Fract. Mech., 12, 407 (1974).

65. R. Baur and V. Gerold, Z. Metallkde, 52, 671 (1961).

66. G. Borelius and L.E. Larsson, Ariv. Fur Fysik, 11, 137 (1956).

67. Bulletin of Alloy Phase Diagrams, 1(1), 36 (198).

68. H.I. Aaronson and K.C. Russell, "Precipitation Processes in Solids," TMS-AIME, New York, 100 (1979).

69. L.F. Mondolfo, "Aluminum Alloys: Structure and Properties," Butterworths, London, 213 (1979).

70. A. Guinier and C.B. Walker, Acta Met., 1, 568 (1963).

71. E.J. Freise, A. Kelly and R.B. Nicholson, Acta Met., 9, 250 (1961).

72. R. Baur and V. Gerold, Acta Met., 10, 637 (1962).

73. J.M. Howe and R. Gronsky, to be published in Scripta Met.

74. R.B. Nicholson and J. Nutting, Acta Met., 9, 332 (1961).

75. J.E. Gragg and J.B. Cohen, Acta Met., 19, 507 (1971).

76. R. Gronsky, in "Proc. 40th EMSA Conf.," Claitors Pub., Baton Rouge, 722 (1982).

77. K.B. Alexander, F.K. LeGoues, H.I. Aaronson and D.E. Laughlin, Acta Met., in press.

78. K. Hono and K. Hirano, Scripta Met., 18, 945 (1984).

79. C.S. Barrett and A.H. Geisler, J. Appl. Phys., 11, 733 (1940).

80. C.S. Barrett, A.H. Geisler and R.F. Mehl, Trans. Met. Soc. AIME, 143, 134 (1941).

81. A. Guinier, Z. Metallkde, 43, 217 (1952).

82. G.R. Frank, D.L. Robinson and G. Thomas, J. Appl. Phys., 32(1), 1763 (1961).

83. H.I. Aaronson, K.C. Russell and G.W. Lorimer, Met. Trans., 8A, 1644 (1977).

84. A.H. Geisler, C.S. Barrett and R.F. Mehl, Trans. Met. Soc. AIME, 152, 182 (1943).

85. J.B. Clark, in "High-Temperature, High-Resolution Metallography," Gordon and Breach, 347 (1967).

86. W.B. Pearson, "A Handbook of Lattice Spacings and Structures of Metals and Alloys," Pergamon Press, Oxford, 261 (1958).

87. C.S. Barrett and T.B. Massalski, "Structure of Metals," Pergamon Press, Oxford, 96,496 (1980).

88. J.P Neumann, Acta Met., 14, 505 (1966).

89. J.W. Morris, Jr., A.G. Khachaturyan and S.H. Wen, in "Proceedings of an International Conference on Solid - Solid Phase Transformations," The Met. Soc. AIME, Warrendale, PA, 101 (1982).

90. J.W. Christian, "Transformations in Metals and Alloys - Part I. Equilibrium and General Kinetic Theory," Pergamon Press, Oxford, 21, 476 (1975).

91. G.B. Olsen and M. Cohen, Acta Met., 27, 1907 (1979).

92. H.I. Aaronson, J.B. Clark and C. Laird, Met. Sci. J., 2, 155 (1968).

93. I. Servi and D. Turnbull, Acta Met., 14, 161 (1966).

94. F.C. Frank and J.H. van der Merwe, Proc. Roy. Soc. London, 198A, 205 (1949).

95. Ibid., 216.

96. J.H. van der Merwe, Proc. Phys. Soc., 63A, 616 (1950).

97. D. Turnbull, "Impurities and Imperfections," ASM, 121 (1955).

98. J.W. Taylor, J. Inst. Metals, 86, 456 (1957-58).

99. D.A. Porter and K.E. Easterling, "Phase Transformations in Metals and Alloys," Van Nostrand Reinhold Co., New York, 146 (1981).

100. V. Vitek, A.P. Sutton D.A. Smith and R.C. Pond, in "Grain Boundary Structure and Kinetics," ASM, 115 (1979).

101. S.L. Sass and P.D. Bristowe, ibid., 71.

102. W.T. Read, "Dislocations in Crystals," McGraw-Hill, New York, 196 (1953).

103. A. Brockman and R.W. Ballufi, Acta Met., 29, 1703 (1981).

104. W. Bollman, "Crystal Defects and Crystalline Interfaces," Springer-Verlag, New York, (1970).

105. W. Bollman, Sur.Sci., 31, 1 (1972).

106. J.H. van der Merwe, J. Microscopy, 102(3), 261 (1974).

107. P.G. Shewmon, "Transformations in Metals," McGraw-Hill, New York, 274, (1969).

108. J.W. Martin and R.D. Doherty, "Stability of Microstructure in Metallic Systems," Cambridge University Press, 14, (1976).

109. B.E. Sundquist, Acta Met., 12, 67 (1964).

110. F.K. LeGoues, H.I. Aaronson, Y.W. Lee and G.J. Fix, in "Proceedings of an International Conference on Solid - Solid Phase Transformations," The Met. Soc. AIME, warrendale, PA, 427 (1982).

111. C. Herring, Phys. Rev., 82, 87 (1951).

112. G. Wulff, Z. Kristallogr., 34, 449 (1901).

113. A.G. Khachaturyan, "Theory of Structural Transformations in Solids," John Wiley and Sons, New York (1983).

114. Toshio Mura, "Micromechanics of Defects in Solids," Martinus Nijhoff Pub., The Hague, 63 (1982).

115. J.D. Eshelby, Proc. Roy. Soc., A241, 376 (1957).

116. J.D. Eshelby, Proc. Roy. Soc., A252, 561 (1959).

117. L.M. Brown and D.R. Clarke, Acta Met., 23, 821 (1975).

118. U. Dahmen and K.H. Westmacott, in "Proceedings of an International Conference on Solid - Solid Phase Transformations," The Met. Soc. AIME, Warrendale, PA, 433 (1982).

119. C. Zener, "Elasticity and Anelasticity of Metals," University of Chicago Press, (1948).

120. J.S. Bowles and J.K. Mackenzie, Acta Met., 2, 129 (1954).

121. Ibid., 138.

122. Ibid., 224.

123. D.M. Barnett, J.K. Lee, H.I. Aaronson and K.C. Russell, Scripta Met., 8, 1447 (1974).

124. T. Mori, P.C. Cheng, M. Kato and T. Mura, Acta Met., 26, 1435 (1978).

125. J.K. Lee and W.C. Johnson, Scripta Met., 11, 477 (1977).

126. M. Hayakawa and M. Oka, Acta Met., 32(9), 1415 (1984).

127. J.W. Christian, Acta Met., 6, 377 (1958).

128. F.R.N. Nabarro, Proc. Roy. Soc., A175, 519 (1940).

129. J.M. Howe, M.S. Thesis, University of California, Berkeley, LBL-15933, (1983).

130. J.M. Cowley and S. Iijima, Z. Naturf. A., 27, 445 (1972).

131. D.J. Smith, W.O. Saxton, M.A. O'Keefe, G.J. Wood and W.M. Stobbs, Ultramicroscopy, 11, 263 (1983).

132. J.C.H. Spence, "Experimental High-Resolution Electron Microscopy," Claredon Press, Oxford (1981).

133. R. Gronsky, in "Treatise on Materials Science and Technology: Experimental Techniques, 19B," Academic Press, New York, 325 (1983).

134. J.M. Cowley and A.F. Moodie, Acta Cryst., 10, 609 (1957).

135. J.M. Cowley and A.F. Moodie, Acta Cryst., 12, 353 (1959).

136. Ibid., 360.

137. J.M. Cowley, Acta Cryst., 12, 367 (1959).

138. J.M. Cowley, Acta Cryst., A29, 529 (1973).

139. Ibid., 537.

140. J.M. Cowley, "Diffraction Physics," North-Holland Pub. Co., Amsterdam (1975).

141. J.M. Cowley, in "Introduction to Analytical Electron Microscopy," Plenum Press, New York, 1 (1979).

142. O. Scherzer, J. Appl. Phys., 20, 20 (1949).

143. J. Frank, Optik, 38, 519 (1973).

144. P. Goodman and A.F. Moodie, Acta Cryst., A30, 280 (1974).

145. D. van Dyck, in "Diffraction and Imaging Techniques in Materials Science," North-Holland, Amsterdam, 355 (1978).

146. P.G. Self, M.A. O'Keefe, P.R. Buseck and A.E.C. Spargo, Ultramicroscopy, 11, 35 (1983).

147. J.G. Allpress and J.V. Sanders, Acta Cryst., 6, 165 (1973).

148. J.G. Allpress, E.A. Hewat, A.F. Moodie and J.V. Sanders, Acta Cryst., A28, 528 (1972).

149. D.F. Lynch and M.A. O'Keefe, Acta Cryst., A28, 536 (1972).

150. G.R. Anstis, D.F. Lynch, A.F. Moodie and M.A. O'Keefe, Acta Cryst., A29, 138 (1973).

151. M.A. O'Keefe, Acta Cryst., A29, 389 (1973).

152. D.F. Lynch, A.F. Moodie and M.A. O'Keefe, Acta Cryst., A31, 300 (1975).

153. M.A. O'Keefe and J.V. Sanders, Acta Cryst., A31, 307 (1975).

154. R. Gronsky, Ph.D. Thesis, University of California, Berkeley, LBL-5784 (1976).

155. R. Sinclair, in "Introduction to Analytical Electron Microscopy," Plenum Press, New York, 507 (1979).

156. T. Tanji and H. Hashimoto, Acta Cryst., A34, 453 (1978).

157. O.L. Krivanek, Optik., 45, 97 (1976).

158. J.I. Goldstein, D.A. Newberry, P. Echlin, D.C. Joy, C. Fiori and E. Lifshin, "Scanning Electron microscopy and X-Ray Microanalysis," Plenum Press, New York (1981).

159. J.I. Goldstein, N.J. Zaluzec, T.A. Hall and B.L. Gupta, in "Introduction to Analytical Electron Microscopy," Plenum Press, New York, 83, 121, 169 (1979).

160. D.B. Williams, "Practical Analytical Electron Microscopy in Materials Science," Philips Electron Optics Publishing Group, New Jersey (1984).

161. H.G.J. Moseley, Phil. Mag., 26, 1024 (1913).

162. H.G.J. Moseley, Phil. Mag., 27, 703 (1914).

163. J. Philibert and R. Tixier, British J. Appl. Phy., 1, 685 (1968).

164. P. Ducumb, J. de Microscopie, 7, 581 (1968).

165. G. Cliff and G.W. Lorimer, J. Microscopy, 110, 107 (1975).

166. G. Cliff and G.W. Lorimer, Proc. 5th European Congress on Elecron Microscopy, Institute of Physics, Bristol, 140 (1972).

167. J.W. Steeds, in "Introduction to Analytical Electron Microscopy," Plenum Press, New York, 387 (1979).

168. P.M. Kelly, A. Jostons, R.G. Blake and J.G. Napier, Phys. Stat. Sol. A, 31, 771 (1975).

169. S.M. Allen and E.L. Hall, Phil. Mag. A, 46(2), 243 (1982).

170. S.M. Allen, Phil. Mag. A, 43, 325 (1981).

171. J. Glazer, R. Ramesh, M. Hilton and M. Sarikaya, to be published in Phil. Mag.

172. B.F. Buxton, J.A. Eades, J.W. Steeds and G.M. Rackham, Phil. Trans. Roy. Soc. London, Ser. A, 281, 171 (1976).

173. J.W. steeds and R. Vincent, J. Appl. Cryst., 16, 317 (1983).

174. J.W. Steeds and R. Vincent, J. Micros. Spectros. Electron., 8, 419 (1983).

175. M. Tanaka, R. Saito and H. Sekii, Acta Cryst., A39, 357 (1983).

176. P. Goodman and G. Lehmpfuhl, Acta Cryst., A24, 339 (1968).

177. A.P. Pogany and P.S. Turner, Acta Cryst., A24, 103 (1968).

178. J. Gjonnes and A.F. Moodie, Acta Cryst., 19, 65 (1965).

179. P. Goodman, Acta Cryst., A31, 804 (1975).

180. "International Tables for X-ray Crystallography - Vol. I," The Kynoch Press, Birmingham (1976).

181. M. Tanaka, H. Sekii and T. Nagasawa, Acta Cryst., A39, 825 (1983).

182. P.M. Jones, G.M. Rackham and J.W. Steeds, Proc. Roy. Soc. London A, 354, 197 (1977).

183. R.C. Ecob, M.P. Shaw, A.J. Porter and B. Ralph, Phil. Mag. A, 44(5), 1117 (1981).

184. Ibid., 1135.

185. V.L. Kohler, C.G. Shelton and B. Ralph, in "Proc. 41st EMSA Conf.," San Francisco Press, Inc., San Francisco, 258 (1983).

186. P.R. Okamoto and G. Thomas, Acta Met., 15, 1325 (1967).

187. J.D. Mote, K. Tanaka and J.E. Dorn, Trans. Met. Soc. AIME, 221, 856 (1961).

188. M.A. O'Keefe, P.R. Buseck and S. Iijima, Nature, 274(5669), 322 (1978).

189. J.C.H. Spence, "Notes Accompanying the A.S.U. Multislice Programs," (1980).

190. I. Miller and J.E. Freund, "Probability and Statistics for Engineers," Prentice-Hall, Inc., New Jersey, 151 (1977).

191. A. Olsen and J.C.H. Spence, Phil. Mag. A, 43(4), 945 (1981).

191a. J.P. Hirth and J. Lothe, "Theory of Dislocations," McGraw-Hill, New York, 144 (1960).

192. R. Trivedi, in "Proceedings of an International Conference on Solid - Solid Phase Transformations," The Met. Soc. AIME, Warrendale, PA, 477 (1982).

193. U. Dahmen, A.R. Pelton, M.J. Witcomb and K.H. Westmacott, in "Proceedings of an International Conference on Solid - Solid Phase Transformations," The Met. Soc. AIME, Warrendale, PA, 637 (1982).

194. U. Dahmen and K.H. Westmacott, Phys. Stat. Sol. (A), 80, 249 (1983).

195. G.C. Weatherly, Can. Met. Quart., 8(2), 105 (1969).

196. U. Dahmen, submitted to Scripta Met.

197. C. Laird and H.I. Aaronson, J. Inst. Metals, 96, 222 (1968).

198. J.M. Howe, unpublished research.

199. J.W. Edington, "Practical Electron Microscopy in Materials Science Vol. 2 - Electron Diffraction in the Electron Microscope," Philips Technical Library, 60 (1975).

200. R. Kilaas, unpublished research.

201. "Metals Handbook - Desk Edition," ASM, Metals Park, Ohio, 1.48 (1985).

202. P. Goodman and H.J. Whitfield, Acta Cryst., A36, 219 (1980).

203. V.L. Kohler, C.G. Shelton and Brian Ralph, in "Proc. 41st EMSA Conf.," San Fransisco Press, San Francisco, 258 (1983).

204. M.G. Friedel, C.R. Acad. Sci. Paris, 157, 1533 (1913).

205. P. Goodman and A.F. Moodie, Acta Cryst., A30, 280 (1974).

206. P. Goodman, Nature, 251, 698 (1974).

207. Y. Bando, Acta Cryst., B39, 185 (1983).

208. J.M. Howe, Metallography, 16, 275 (1983).

209. D. Van Dyck, G. Van Tendeloo and S. Amelinckx, Ultramicroscopy, 15, 357 (1984).

210. Y.W. Lee and H.I. Aaronson, Acta Met., 28, 539 (1980).

211. F.K. LeGouges, R.N. Wright, Y.W. Lee and H.I. Aaronson, Acta Met., 32(10), 1865 (1984).

212. W.E. Mayo and T. Tsakalakos, Met. Trans., 11A, 1637 (1980).

213. A.G. Khachaturyan, Sov. Phys. Solid State, 8, 2163 (1967).

214. J.K. Lee, D.M. Barnett and H.I. Aaronson, Met. Trans., 8A, 963 (1977).

215. G. Thomas, R. Gronsky, O.L. Krivanek and R.K. Mishra, presented at the 7th LBL/MMRD International Materials Symposium, LBL-11413 (1980).

216. "Energy-Dispersive X-ray Microanalysis—An Introduction," Kevex Corp., Foster City, CA, 9 (1983).

217. N. Thompson, Proc. Phys. Soc. B, 66, 481 (1953).

12. TABLES

Table 1. CBED pattern symmetries for the 31 diffraction groups. Where a dash appears in column 7, the special symmetries can be deduced from columns 5 and 6 (after 172).

Diffraction Group	Bright Field	Whole Pattern	Dark Field		±G		Projection Diffraction Group
			General	Special	General	Special	
1	1	1	1	none	1	none	1_R
1_R	2	1	2	none	1	none	
2	2	2	1	none	2	none	21_R
2_R	1	1	1	none	2_R	none	
21_R	2	2	2	none	21_R	none	
m_R	m	1	1	m	1	m_R	$m1_R$
m	m	m	1	m	1	m	
$m1_R$	2mm	m	2	2mm	1	$m1_R$	
$2m_Rm_R$	2mm	2	1	m	2	—	$2mm1_R$
2mm	2mm	2mm	1	m	2	—	
2_Rmm_R	m	m	1	m	2_R	—	
$2mm1_R$	2mm	2mm	2	2mm	21_R	—	
4	4	4	1	none	2	none	41_R
4_R	4	2	1	none	2	none	
41_R	4	4	2	none	21_R	none	
$4m_Rm_R$	4mm	4	1	m	2	—	$4mm1_R$
4mm	4mm	4mm	1	m	2	—	
4_Rmm_R	4mm	2mm	1	m	2	—	
$4mm1_R$	4mm	4mm	2	2mm	21_R	—	
3	3	3	1	none	1	none	31_R
31_R	6	3	2	none	1	none	
$3m_R$	3m	3	1	m	1	m_R	$3m1_R$
3m	3m	3m	1	m	1	m	
$3m1_R$	6mm	3m	2	2mm	1	$m1_R$	
6	6	6	1	none	2	none	61_R
6_R	3	3	1	none	2_R	none	
61_R	6	6	2	none	21_R	none	
$6m_Rm_R$	6mm	6	1	m	2	—	$6mm1_R$
6mm	6mm	6mm	1	m	2	—	
6_Rmm_R	3m	3m	1	m	2_R	—	
$6mm1_R$	6mm	6mm	2	2mm	21_R	—	

XBL 852-1372

Table 2. Relation between the 31 diffraction groups and the 32 crystal point groups (after 172).

Diffraction Groups	Relation between the diffraction groups and the crystal point groups																												
$6mm1_R$																									X				
$3m1_R$																								X					
6mm																							X						
$6m_Rm_R$																						X							
61_R																					X								
31_R																				X									
6																			X										
6_Rmm_R																		X											X
3m																	X											X	
$3m_R$																X											X		
6_R															X											X			
3														X											X				
$4rnm1_R$													X																X
4_Rmm_R												X																X	
4mm											X																		
$4m_Rm_R$										X																	X		
41_R									X																				
4_R								X																					
4							X																						
$2mm1_R$								X					X												X		X		X
2_Rmm_R					X			X		X			X				X			X				X		X		X	
2mm							X																	X					
$2m_Rm_R$						X					X		X									X				X		X	
$m1_R$							X					X	X										X	X				X	
m				X			X					X	X				X			X			X	X				X	
m_R			X			X	X		X	X		X	X	X				X			X			X	X	X		X	X	
21_R					X														X										
2_R		X			X			X			X				X		X			X			X			X		X	
2			X															X											
1_R				X															X										
1	X		X	X		X	X		X	X		X	X	X		X		X	X		X	X		X	X	X		X	X	
Point Groups	1	$\bar{1}$	2	m	2/m	222	mm2	mmm	4	$\bar{4}$	4/m	422	4mm	$\bar{4}2m$	4/mmm	3	$\bar{3}$	32	3m	$\bar{3}m$	6	$\bar{6}$	6/m	622	6mm	$\bar{6}m2$	6/mmm	23	m3	432	$\bar{4}3m$	m3m

XBL 852-1370

Table 3. Integrated x-ray intensities (number of counts) of Al and Ag Kα peaks and surrounding background from Ag_2Al standard.

Spectrum I.D.	Background Left	Al Kα	Background Right	Background Left	Ag Kα	Background Right
Ag_2Al-1	4487	20730	4485	1483	17055	1345
Ag_2AL-2	6021	28258	6099	2045	22177	1670
Ag_2Al-3	3509	20050	3390	1186	14758	1029

Table 4. Concentrations of Ag to Al (C_{Ag}/C_{Al}) obtained from the peak intensities in Table 3 (x_i, $\bar{x}$, s and C.V. are defined in Sect. 5.6.).

Spectrum I.D.	C_{Ag}/C_{Al}	$x_i - \bar{x}$
Ag_2Al-1		2.081
Ag_2Al-2		2.187
Ag_2Al-3		2.432
$s = \pm 0.180$	C.V. = 8.1% $\bar{x} = 2.233$	$\Sigma(x_i - \bar{x})^2 = 0.065$

Table 5. Integrated x-ray intensities (number of counts) of Al and Ag Kα peaks and surrounding background for extracted precipitates from samples aged for 10, 30 and 120 min. at 350°C.

Spectrum I.D.	Background Left	Al Kα	Background Right	Background Left	Ag Kα	Background Right
Ppt10-1	2830	12835	2609	880	10551	807
Ppt10-2	2484	12432	2860	872	10399	732
Ppt10-3	2352	11534	2095	708	7673	710
Ppt10-4	2537	11280	2631	906	8641	800
Ppt10-5	3559	16988	3900	1167	12936	1023
Ppt10-6	2031	11009	2040	864	8672	724
Ppt10-7	2464	12221	2097	722	9158	679
Ppt10-8	2500	11611	2502	752	8619	714
Ppt30-1	2476	10384	2130	717	7390	639
Ppt30-2	2482	11352	2500	993	8847	857
Ppt30-3	2566	11223	2497	890	9479	807
Ppt30-4	2506	12300	2439	824	9436	752
Ppt30-5	2450	11069	2503	875	8615	773
Ppt30-6	2577	13118	2683	955	10055	955
Ppt30-7	2516	12775	2310	886	9574	813
Ppt30-8	2573	12533	2660	1009	10092	830
Ppt30-9	2402	12412	2471	847	9819	729
Ppt30-10	2498	11668	2550	875	9597	771
Ppt120-1	2390	11639	2310	972	8694	858
Ppt120-2	2263	11066	2413	825	8218	724
Ppt120-3	3021	11164	2538	827	7504	763
Ppt120-4	2954	11243	3237	1042	7404	937
Ppt120-5	3185	10318	3303	1273	7570	1082
Ppt120-6	2462	11263	2459	837	7467	737
Ppt120-7	2768	10441	2628	973	7375	906
Ppt120-8	3545	10268	3516	1794	6529	1720
Ppt120-9	2305	10992	2413	970	8507	851
Ppt120-10	3275	11005	3126	1417	9136	1350

Table 6. Concentrations of Ag to Al (C_{Ag}/C_{Al}) obtained from the peak intensities in Table 5 (x_i, $\bar{x}$, s and C.V. are defined in Sect. 5.6.).

Spectrum I.D.	C_{Ag}/C_{Al}	$x_i - \bar{x}$	Spectrum I.D.	C_{Ag}/C_{Al}	$x_i - \bar{x}$	Spectrum I.D.	C_{Ag}/C_{Al}	$x_i - \bar{x}$
Ppt10-1	2.143	0.168	Ppt30-1	1.855	-0.160	Ppt120-1	1.870	0.002
Ppt10-2	2.196	0.221	Ppt30-2	2.003	-0.012	Ppt120-2	1.904	0.036
Ppt10-3	1.670	-0.305	Ppt30-3	2.239	0.224	Ppt120-3	1.787	-0.081
Ppt10-4	2.000	0.025	Ppt30-4	1.964	-0.051	Ppt120-4	1.780	-0.088
Ppt10-5	1.995	0.020	Ppt30-5	2.025	0.010	Ppt120-5	2.018	0.150
Ppt10-6	1.963	-0.012	Ppt30-6	1.955	-0.060	Ppt120-6	1.695	-0.173
Ppt10-7	1.900	-0.075	Ppt30-7	1.880	-0.135	Ppt120-7	1.856	-0.012
Ppt10-8	1.933	-0.042	Ppt30-8	2.065	0.050	Ppt120-8	1.582	-0.286
			Ppt30-9	2.022	0.007	Ppt120-9	1.965	0.097
			Ppt30-10	2.143	0.128	Ppt120-10	2.218	0.350
s =	C.V. =	$\bar{x}$ =	$\Sigma(x_i - \bar{x})^2$	s =	C.V. =	$\bar{x}$ =	$\Sigma(x_i - \bar{x})^2$	s =	C.V. =	$\bar{x}$ =	$\Sigma(x_i - \bar{x})^2$
±0.160	8.1%	1.975	±0.179	±0.115	5.7%	2.015	= 0.119	±0.177	9.5%	1.868	= 0.282

Table 7. Summary of thin film analyses of extracted precipitates.

Aging Time at 350°C (min.)	C_{Ag}/C_{Al}	Standard Deviation	Coefficient of Variance (%)	Composition (a/o)
10	1.975	±0.160	8.1	66.4 Ag 33.6 Al
30	2.015	±0.115	5.7	66.8 Ag 33.2 Al
120	1.868	±0.177	9.5	65.1 Ag 34.9 Al

Table 8. Integrated x-ray intensities (number of counts) of Al and Ag Kα peaks and background from solid-solution Al - 14.92 and 3.76 w/o Ag (4.2 and 1.0 a/o Ag) alloys.

Spectrum I.D.	Background Left	Al Kα	Background Right	Background Left	Ag Kα	Background Right
14.92-1	5530	280768	5534	1476	10901	1314
14.92-2	5461	259019	5161	1410	10210	1299
3.76-1	12798	894155	13070	3243	10050	2975
3.76-2	12390	864664	13069	3086	10105	3009
3.76-3	12297	957275	12971	2529	10069	2189

Table 9. Concentration of Ag to Al (C_{Ag}/C_{Al}) obtained from the peak intensities in Table 8 (x_i, $\bar{x}$, s and C.V. are defined in Sect. 5.6.).

Spectrum I.D.	C_{Ag}/C_{Al}	$x_i - \bar{x}$
14.92-1		1.274
14.92-2		1.261
3.76-1		1.270
3.76-2		1.207
3.76-3		1.225
$s =$ ±0.030	C.V. = 2.4%	$\bar{x} =$ 1.251	$\Sigma(x_i - \bar{x})^2 = 0.004$

Table 10. Integrated x-ray intensities (number of counts) of Al and Ag Kα peaks and background of matrix after aging for 30 min. at 350°C.

Spectrum I.D.	Background Left	Al Kα	Background Right	Background Left	Ag Kα	Background Right
matrix-1	17830	485924	17274	4728	11718	4450

Table 11. Solid solubility of Ag in Al for temperatures from 27 to 566°C (after Mondolfo (69)).

°C	°F	w/o	a/o	°C	°F	w/o	a/o
566	1050	55.6	23.7	327	620	5.8	1.5
547	1016	52.0	21.5	550	530	3.8	1.0
527	980	49.5	19.8	227	440	1.8	0.47
477	890	24.0	7.5	177	350	1.0	0.22
427	800	12.5	3.7	127	260	0.65	0.16
377	710	7.5	2.0	77	170	0.40	0.10
				27	80	0.15	0.04

Table 12. Summary of forbidden reflections for space groups 191-194.

Space Group (Number)	Kinematically Forbidden Reflections
P6/mmm (191)	None
P6/mcc (192)	$h\bar{h}0l$, $l=2n+1$ and $hh2\bar{h}l$, $l=2n+1$
$P6_3/mcm$ (193)	$h\bar{h}0l$, $l=2n+1$
$P6_3/mmc$ (194)	$hh2\bar{h}l$, $l=2n+1$

13. FIGURE CAPTIONS

Fig. 1. (a) Al-Ag equilibrium phase diagram showing the range of the γ phase field, and (b) partial Al-Ag equilibrium phase diagram including the metastable G.P. zone solvus. The asterisk in the lower-right corner of (b) indicates the location of the Al-14.92 w/o Ag (4.2 a/o Ag) alloy at 350°C (after 65,67).

Fig. 2. Crystal structures and lattice parameters of the Al supersaturated solid solution, metastable γ' and equilibrium γ phases at room temperature (after 69).

Fig. 3. (a) An edge Shockley partial dislocation with a Burgers vector $b = a/6[11\bar{2}]$ on (111) in a crystal, and (b) the same dislocation locally changes the stacking sequence from fcc to hcp (after 99).

Fig. 4. Illustration of two different ways of transforming cubic close-packed planes into hexagonal close-packed planes: (a) using the same Shockley partial dislocation, and (b) using equal numbers of all three types of Shockley partial dislocations. Each block represents two (111) matrix planes (after 107).

Fig. 5. A section through a γ-plot showing the equilibrium disc-shape predicted for a precipitate containing one coherent or semicoherent interface and one incoherent interface (after 99).

Fig. 6. Illustration of a thin plate-shaped precipitate which has a large misfit (ε_{33}) perpendicular to the habit plane, and a small misfit (ε_{11}) along the faces. The minimum strain energy

is achieved if the disc lies perpendicular to elastically soft directions in the matrix (after 99).

Fig. 7. HREM image of an early-stage γ' precipitate with an aspect ratio of about 20:1. The foil normal is <110> and the hcp γ' precipitate lies on a {111} matrix plane. The stacking change across the precipitate is also indicated.

Fig. 8. Precipitate shape predicted by the general theory of precipitate morphology based on the migration of (semi)coherent interfaces (segments A-B, B'-C and C'-D) by a ledge mechanism (13). The growth directions of the disordered ledges (segments B-B' and C-C') and precipitate edges are indicated by arrows and the stacking change across the precipitate/matrix interface is also shown (after 129).

Fig. 9. Schematic illustration of the process of high-resolution image formation in the TEM. The ray diagram on the left can be compared directly with the example wave functions on the right (after 215).

Fig. 10. (a) Illustration of the process of x-ray generation where an electron from a high-energy shell (E_2) fills a vacancy in a lower-energy shell (E_1) created by an incoming energetic electron, and (b) illustration of some typical line types observed in x-ray spectra. Since each shell actually contains several energy levels, the transitions and nomenclature are slightly more complicated than shown (after 216).

Fig. 11. (a) Ewald sphere construction for an electron beam which is incident over a range of angles ($2\alpha_i$), (b) illustration of the resulting CBED pattern showing the appearance of HOLZs, and (c) experimental CBED pattern from α-titanium which may be compared directly with the schematic pattern in (b). The spacing of the reciprocal lattice spots parallel to the electron beam (H) and the radius of the FOLZ (G) are also indicated in these figures. Although it is not shown in (a), the reciprocal lattice spots are actually elongated along the electron beam direction due to the finite thickness of TEM specimens.

Fig. 12. Symmetries of hexagonal six-beam CBED patterns for the diffraction groups which possess 6-fold symmetry (after 175).

Fig. 13. Organization of the experimental results and discussion in Sect. 6.

Fig. 14. BF TEM micrograph illustrating the lengths and thicknesses of γ' precipitates produced by aging the Al-14.92 w/o Ag alloy for 30 min. at 350°C. The foil normal is <110>.

Fig. 15. (a) Low magnification lattice image of γ' precipitates with heights of ledges on the faces indicated, and (b) corresponding imaging condition used for the lattice image. The foil normal is <110> and the precipitates are viewed edge-on, parallel to the faces (after 61).

Fig. 16. (a) through (d) Enlargements from Fig. 15 (a) showing the heights and structures of the interfacial ledges (after 61).

Fig. 17. The (111) face of Thompson's reference tetrahedron showing the possible 1/2<110> and 1/6<112> Burgers vectors (after 217).

Fig. 18. Calculated HREM images for a single 90° Shockley partial dislocation ledge on the face of a γ' precipitate in a <110> orientation, for a foil thickness of 37.2 Å and various values of objective lens defocus. The corresponding projected potential is shown in the top corner, where the dislocation core at the edge of the ledge is circled, and the atomic stacking on either side of the ledge is also indicated. The arrow distinguishes the extra atom plane associated with the dislocation.

Fig. 19. (a) Projected potential for a single 90° Shockley partial dislocation ledge, and (b) simulated HREM image for a foil thickness of 71.6 Å and an objective lens defocus of -1440 Å. The dislocation core is circled and the stacking sequence on either side of the ledge is shown in (a).

Fig. 20. Experimental HREM image of a multiple-unit ledge on the face of a γ' precipitate. The corresponding <110> imaging condition is shown in lower-left corner, and a Burgers circuit drawn around the approximately ten-plane ledge shows a closure failure of four planes, as indicated in the figure.

Fig. 21. Lattice image of the edge of a γ' precipitate in a <110> orientation and corresponding electron and optical diffraction patterns. The atomic positions in the fcc matrix and hcp precipitate, and the staggered appearance of the edge are also indicated in the figure.

Fig. 22. Enlargement of the precipitate edge in Fig. 21 showing that the nearly planar edge parallels a {112} plane in the matrix, but that this interface is further faceted along {111} matrix planes, and that the facets have a six-plane repeating pattern.

Fig. 23. Low magnification lattice image and corresponding diffraction condition from a γ' precipitate whose edge is near the hole in a <110> foil. Spots from two variants of precipitates are present in the SAD pattern due to an intersecting precipitate which is just out of the field of view.

Fig. 24. (a) through (d) A through-focus series of HREM images of the precipitate edge and the optical diffraction patterns from each of the images with the objective lens defocus values indicated. Notice that slight drift is evident in the optical diffraction pattern in (c). Drift was often a problem when working in the thinnest areas of specimens.

Fig. 25. (a) and (b) Burgers circuit which can be used to distinguish a Shockley partial dislocation ledge which is mainly screw in character, and (c) and (d) Burgers circuit which distinguishes a Shockley partial dislocation ledge that is in a pure edge orientation with respect to the electron beam. Note that all of the projected atom positions for both the precipitate and matrix in the <110> orientation are included in the models, where the Al atoms are represented by open circles, the Ag atoms are represented by filled circles and the last atomic layer of the precipitate is connected by a solid line. S_S and

S_e indicate the start of the screw and edge-type Burgers circuits, respectively, while F indicates the finish of the circuits (after 129).

Fig. 26. Enlargement of the precipitate edge at -1460 Å defocus in Fig. 24 (c) showing the closure failures associated with screw and edge-type Burgers circuits constructed around the edge. The precipitate is 48 {111} matrix planes thick and a total of 24 Shockley partial dislocations are distinguished at the edge by the two types of Burgers circuits.

Fig. 27. Enlargement of the precipitate edge at -1690 Å defocus in Fig. 24 (d) showing the closure failures associated with screw and edge-type Burgers circuits constructed around the edge. Again, a 2:1 ratio of screw to edge dislocations is revealed by the circuits.

Fig. 28. A further enlargement of the top-half of the precipitate edge in Fig. 27 showing the atomic positions of four possible 90Å Shockley partial dislocations. Black dots indicate the locations of the atoms which surround the dislocation cores, and the arrows indicate the extra atomic planes associated with the dislocations, similar to the arrows in Fig. 18.

Fig. 29. (a) through (c) WBDF TEM images showing the contrast from dislocation ledges which nucleated on the face of a γ' precipitate due to an impinging precipitate, and (d) BF image of the same. The letters in these figures correspond to particular dislocations whose Burgers vectors were analyzed elsewhere (after 60).

Fig. 30. Low magnification lattice image of a precipitate intersection with the corresponding electron and optical diffraction patterns.

Fig. 31. Enlargement of the intersected region in Fig. 30 showing the ledges which were nucleated by the impinging precipitate. The inset DF image in the top-right corner of the figure was taken using a $\langle 1\bar{1}01\rangle$ precipitate reflection, verifying that the new ledges have a hcp structure. Also notice the inset simulated HREM image of the precipitate in the lower-right corner, and the variation in the image intensity between alternate basal planes.

Fig. 32. Enlargement of the precipitate edge in Fig. 30 showing that it is approximately flat and has a six-plane, staggered repeating pattern, which is outlined in the figure.

Fig. 33. Atomic model of a γ' precipitate formed by the passage of Shockley partial dislocations on every other (111) plane. The figure normal is $[\bar{1}01]$ as shown in the lower-right corner, and the atomic stacking in both the precipitate and matrix is illustrated (after 61).

Fig. 34. Atomic model of a single-atom kink in a Shockley partial dislocation lying along a $\langle 110\rangle$ direction. The figure normal is $\langle 111\rangle$ and atoms which occupy A,B and C positions are distinguished at the top of the figure. Note the open space associated with the kink (after 129).

Fig. 35. Crystallographic features of a γ' precipitate plate oriented perpendicular to the electron beam. The six edges which parallel <110> directions within the (111) matrix plane are numbered, and ledges on the edges which parallel <112> directions are indicate by arrows (after 60).

Fig. 36. (a) BF, and (b) WBDF micrographs showing that ledges along the <112> edges also parallel <110> directions (after 60).

Fig. 37. (a) <111>//<0001> selected-area diffraction pattern containing both matrix and precipitate reflections as indicated, (b) axial diffraction conditions used to obtain HREM images of the precipitate, and (c) tilted-illumination conditions used to resolve the 1.4 Å spacing of the {220} matrix and {11$\bar{2}$0} precipitate planes. Precipitate spots at 1/3 and 2/3<11$\bar{2}$0> positions are indicate by arrows in (a).

Fig. 38. (a) BF image of ledges at the edge of a precipitate, and (b) corresponding DF image. The edge of the foil is visible on the right side in these micrographs, and the ledges enclosed in (a) are shown in subsequent figures. The foil normal is <111>.

Fig. 39. Low magnification axial lattice image of ledges enclosed in Fig. 38 (a). Comparison with the matrix directions shown on the left of this figure reveals that the precipitate/matrix interface parallels a [$\bar{1}\bar{1}$2] direction overall, but that the ledges at the edge closely follow <110> on a nearly atomic level. The foil normal is <111>.

Fig. 40. (a) Enlargement of the corner at the base of the first ledge on the left in Fig. 39 showing that the interphase boundary follows the <110> directions on an atomic-level, and (b) tilted-beam image of the same area showing the continuity of the {220} planes as they cross the precipitate/matrix interface. Optical diffraction patterns from the axial- and tilted-illumination images are also shown.

Fig. 41. (a) Enlargement of the ledge on the left in Fig. 39 showing single-atom facets at the precipitate edge, and (b) corresponding tilted-illumination image.

Fig. 42. (a) Enlargement of second ledge from the left in Fig. 39, and (b) corresponding tilted-beam image which shows that both sets of {220} matrix planes are continuous as they cross the precipitate/matrix interface.

Fig. 43. (a) Enlargement of ledge on the right in Fig. 39 showing the presence of a small ledge (arrow) at its base, and (b) tilted-illumination image of the same area.

Fig. 44. (a) Axial HREM image of the corner of a γ' precipitate and the corresponding optical diffraction pattern, and (b) tilted-beam image and corresponding optical diffraction pattern from the same area. Notice the 20-50 Å ledges on either side of the corner, and the single-atom ledges on the lower-left edge in (b).

Fig. 45. (a) Selected-area diffraction pattern from the matrix and precipitate in Fig. 44, (b) axial imaging conditions cor-

responding to the HREM image in Fig. 44 (a), and (c) tilted-illumination imaging conditions corresponding to the HREM image in Figs. 44 (b).

Fig. 46. Enlargement from an area of the precipitate in Fig. 44 (a) revealing bright atoms (arrows) spaced at $2n\langle 11\bar{2}0\rangle$, n = integral directions in the precipitate, which are indicated in the top-left corner of the figure.

Fig. 47. (a) Enlargement from the axial HREM image in Fig. 44 (a) showing the corner and top edge of the precipitate, and (b) tilted-illumination image of the same area. Notice the 1.4 Å matrix planes and the 2.8 Å precipitate planes indicated in (b).

Fig. 48. Further enlargement of the corner in Fig. 47 (a) demonstrating the continuity of the 1.4 Å {220} matrix planes at the precipitate corner as they cross the interphase boundary to become the $\{11\bar{2}0\}$ precipitate planes.

Fig. 49. (a) Enlargement from the axial HREM in Fig. 44 (a) showing an approximately 50 Å ledge at the edge with single-atom ledges (arrows) on either side, and (b) tilted-illumination HREM image of the same.

Fig. 50. (a) Enlargement of the left edge of the precipitate in the axial HREM image in Fig. 44 (a) which shows a series of single-atom ledges migrating along the precipitate edge toward the corner, and (b) tilted-illumination image of the same.

Fig. 51. Further enlargement from Fig. 50 (b) revealing the atomic structure and continuity of the single-atom ledges (arrows). Notice the slight bending of the 1.4 Å matrix planes as they cross into the precipitate.

Fig. 52. Atomically smooth solid/solid interfaces with atoms represented by cubes, showing by analogy with a solid/liquid interface that: (a) addition of a single atoms onto a flat surface by a continuous normal growth mechanism increases the number of "broken bonds" by four per atom, and (b) addition to a ledge only increases the number of broken bonds by two per atom, whereas at a kink in a ledge, there is no increase (after 129).

Fig. 53. SEM secondary electron image of a 30 min. sample which was etched for about 1 hr. in a 5% NaOH solution showing: (a) precipitates protruding above the matrix along several grain boundaries and the general Widmanstatten pattern of precipitates within the grains, and (b) a high atomic number residue (white) on the surfaces of many precipitates.

Fig. 54. (a) BF TEM image of micron-sized extracted precipitates from 30 min. sample on lacy-carbon film, (b) EDS spectrum from the precipitate in (a) with the Al and Ag $K\alpha$ peaks indicated, and (c) and (d) enlargements of the Al and Ag $K\alpha$ peaks.

Fig. 55. (a), (c) and (e) EDS spectra from Fig. 54, and (b), (d) and (f) comparative spectra obtained from the Ag_2Al standard. Although nearly twice as many counts were obtained for the Ag_2Al standard, the ratio of the heights of the Al $K\alpha$ to the

Ag Kα peaks is about the same as for the extracted precipitate.

Fig. 56. (a) EDS spectrum from the Al-14.92 w/o Ag solid-solution alloy, (b) enlargement of Ag Kα peak in (a), (c) EDS spectrum from the same alloy after aging for 30 min. at 350°C, and (d) enlargement of the Ag Kα peak in (c).

Fig. 57. BF TEM image showing contamination spots from the electron beam in between the γ' precipitates in a <110> thin foil.

Fig. 58. (a) Experimental precipitate/matrix selected-area diffraction pattern in a [111]//[0001] orientation, and (b) corresponding indexed diffraction pattern showing the positions of the matrix and precipitate spots. Notice the additional precipitate reflections at 1/3 and 2/3<$\bar{1}\bar{1}$20> positions indicated by arrows in (a) and x's in (b). The forward-scattered beam is indicated by an asterisk in (a).

Fig. 59. Diffuse x-ray diffraction peaks at 1/3 and 2/3<11$\bar{2}$0> positions ([110]* in hkl reciprocal space notation) from a <0001> Ag_2Al single crystal aged for 10 days at 180°C (after 88).

Fig. 60. Atomic model for short-range order within basal planes containing 66 a/o Ag, to account for the peaks in Fig. 59 (after 88).

Fig. 61. Sharp x-ray diffraction peaks at <0001>, l=2n+1 positions ([001]* in hkl reciprocal space notation) from a <11$\bar{2}$0> Ag_2Al single crystal aged for 10 days at 180°C (after 88).

Fig. 62. (a) Experimental [101]//[$2\bar{1}\bar{1}0$] selected-area diffraction pattern from γ' precipitates and matrix with strong <0001> precipitate spots (arrows) on either side of the forward-scattered beam (asterisk), and (b) corresponding indexed diffraction pattern showing the locations of the <0001>, l=2n+1 reflections.

Fig. 63. (a) Single variant of γ' precipitates within the selected-area aperture used for the tilting experiment, and (b) through (f) SAD patterns obtained from the precipitates in (a) after tilting about the <0001> horizontal axis to the the extent indicated in each of the patterns.

Fig. 64. Atomic model proposed for γ' precipitates. Notice that the A-planes in the hcp structure are pure Ag while the B-planes contain only 33 a/o Ag with a balance of Al. Also note that each Ag atom in the B-planes is surrounded by six Al atoms, although the Ag atoms are not necessarily located in each of the three possible positions within the B-planes in a repeating pattern, as shown in the figure.

Fig. 65. (a) through (l) CTF for the JEOL 200CX microscope over a range of objective lens defocus values, where C_s = 1.2 mm, Δ = 50 mrad, α_i = 0.4 mrad, Acc. Volt. = 200 keV, and Δz_{Sch} = -660 Å.

Fig. 66. (a) CTF at -660 Å showing the initial undamped form and the damping functions due to both the energy spread (Δ) and convergence (α_i) of the electron beam, and (b) the same for -1460 Å defocus.

Fig. 67. (a) through (f) CTF in -20 Å increments from -1400 to -1500 Å for the JEOL 200CX, using the same conditions described in Fig. 65. The spatial frequencies of interest are indicated on the horizontal axes, where the CTF = 0.

Fig. 68. (a) Simulated HREM images of a γ' precipitate containing 66 a/o Ag on both the A and B-planes for a range of objective lens defocus values and a constant thickness of 54.4 Å, and (b) through (d) similar series of images for precipitates in which the Ag concentration in the A-planes is increased by 10 a/o and that in the B-planes is decreased by the same amount until 99 a/o Ag in the A-planes and 33 a/o Ag in the B-planes is reached in (d).

Fig. 69. (a) through (d) A series of simulated HREM images which demonstrates the changes in image contrast which occur between A and B-planes as a function of Ag concentration and crystal thickness, for a constant objective lens defocus of -1460 Å.

Fig. 70. Amplitude of the <0001> precipitate reflection for a γ' precipitate containing 66 a/o Ag, as a function of the difference in Ag concentration between alternate basal planes and increasing crystal thickness.

Fig. 71. Amplitudes of the forward-scattered beam and all of the first-order precipitate reflections as a function of crystal thickness, for a γ' precipitate which contains 99 a/o Ag on the A-planes and 33 a/o Ag on the B-planes. The amplitudes were normalized by dividing by the sum of the amplitudes.

Fig. 72. Phases of the forward-scattered beam and all of the first-order Bragg-scattered beams in Fig. 71 as a function of crystal thickness, for a γ' precipitate which contains 99 a/o Ag on the A-planes and 33 a/o Ag on the B-planes. The phases of the Bragg-scattered beams were normalized by substracting the phase of the forward-scattered <0000> beam.

Fig. 73. Simulated HREM images for a γ' precipitate/matrix interface as a function of objective lens defocus and specimen thickness. The γ' precipitate contains 99 a/o Ag on the A-planes and 33 a/o Ag on the B-planes, just as in Figs. 68 and 69 (d), as evident from the projected potential in the top-left corner of the figure. Also notice from the projected potential that the interface between the precipitate and matrix occurs between the last Ag-rich A-plane in the precipitate, and the first B-plane in the Al matrix.

Fig. 74. Series of computed HREM images for a γ' precipitate/matrix interface over a range of crystal thicknesses for objective lens defocus increments of -20 Å, from -1400 to -1500 Å. The γ' precipitate contains 99 a/o Ag on the A-planes and 33 a/o Ag on the B-planes.

Fig. 75. Experimental HREM image of a γ' precipitate/matrix interface in a <110>//<11$\bar{2}$0> orientation, with the corresponding electron and optical diffraction patterns. Notice the matching between the experimental image and the superimposed simulated image of the interface at -1440 Å defocus and 37.2 Å thickness from Fig. 74.

Fig. 76. (a) HREM image of a second precipitate/matrix interface taken at -1460 Å defocus, (b) diffraction condition used for the image in (a) with the position of the objective aperture indicated, and (c) optical diffraction pattern taken from the area around the box in (a) showing all of the precipitate and matrix periodicities. The arrows in (a) indicate B-atoms which are visible, and the area enclosed by the box is shown enlarged in Fig. 77 (c).

Fig. 77. (a) Projected potential for the precipitate/matrix interface where the γ' precipitate contains 99 a/o Ag on the A-planes and 33 a/o Ag on the B-planes, (b) corresponding simulated image for a crystal thickness of 40.1 Å and an objective lens defocus of -1460 Å, and (c) experimental image from the precipitate/matrix interface shown in Fig. 76 (a).

Fig. 78. HREM image of the $\langle 11\bar{2}0 \rangle$ Ag_2Al single crystal which was solution-annealed and aged for 30 min. at 350°C. The corresponding imaging conditions are also shown and the area contained within the box is enlarged in Fig. 79 (a).

Fig. 79. (a) Enlargement from the Ag_2Al crystal in Fig. 78 with an inset simulated image from Fig. 69 (d) at 37.2 Å thickness (top-left) and an experimental image from the γ' precipitate in Fig. 24 (c) (top-right), and (b) optical diffraction pattern from the HREM image in (a) showing all of the precipitate periodicities.

Fig. 80. (a) $\langle 11\bar{2}0 \rangle$ electron diffraction pattern from the Ag_2Al single crystal, and (b) diffraction pattern after tilting the crystal

about 12° around the <0001> axis. The same <0001>, l=2n+1 spot is indicated in both figures.

Fig. 81. Illustration of two possible ways for a γ' precipitate to thicken by the passage of a Shockley partial dislocation along the C-plane of matrix atoms: (a) when the B-planes in the precipitate are Ag-rich the major chemical change needed for growth occurs in the B-plane below the Shockley partial dislocation, and (b) when the A-planes are Ag-rich both the structural and major chemical changes needed for growth occur in the slip plane (C-plane) of the partial dislocation.

Fig. 82. Partial CBED map for α-titanium around the [0001] principal zone.

Fig. 83. CBED patterns for α-titanium in a [0001] orientation showing: (a) 6mm symmetry of the intensity fringes within the OOLZ discs, (b) detail within the BF disc, (c) 6-fold symmetry of the FOLZ, and (d) G-M line in the $\langle 11\bar{2}1 \rangle$ FOLZ reflection at the Bragg position. The location of the optic axis is indicated by an asterisk in these and all subsequent CBED patterns.

Fig. 84. CBED patterns for α-titanium in a [0001] orientation showing: (a) and (b) 2mm symmetry within the $[\bar{1}010]$ and $[10\bar{1}0]$ discs located at their Bragg positions, respectively, (b) mirror lines in the 6-beam pattern with the $[\bar{1}010]$ reflection centered on the optic axis (asterisk), and (d) symmetric excitation of the $[\bar{1}2\bar{1}0]$ and $[2\bar{1}\bar{1}0]$ reflections with mirror lines in all the $\langle 11\bar{2}0 \rangle$ (and $\langle \bar{1}010 \rangle$) discs spaced at 30° intervals.

Fig. 85. Symmetry elements and reflection conditions for the space group $P6_3/mmc$ (after 180).

Fig. 86. (a) $[3\bar{3}02]$ CBED pattern for α-titanium, (b) and (c) intensity fringes and HOLZ lines within the $[\bar{1}103]$ and $[1\bar{1}0\bar{3}]$ discs at their respective Bragg positions, and (d) and (e) intensity distributions within the $[11\bar{2}0]$ and $[\bar{1}\bar{1}20]$ discs at their respective Bragg positions. The mirror lines are indicated in all of the Bragg reflections, which also display perfect translational symmetry.

Fig. 87. (a), (c) and (d) Three conjugate 4-beam CBED patterns around the $[1\bar{1}04]$ zone axis shown in (b). Notice the translational symmetries between opposite CBED reflections and the nearly perfect inversion symmetry within the $\langle\bar{1}3\bar{2}1\rangle$ discs in these patterns. Also notice the strong HOLZ lines in the zone axis pattern in (b).

Fig. 88. (top) Experimental $[1\bar{1}04]$ CBED patterns from two Zn alloys showing shifts in the HOLZ lines (circled), and (bottom) geometric computer simulations used to quantify the shifts with changes in the lattice parameters (after 203).

Fig. 89. (a) BF TEM image showing where the electron beam was located relative to the edge of the foil (a through d), for the four series of $\pm\mathbf{g}$ CBED experiments in Figs. 90 (a) through (d), and (b) ghost image of foil with the probe positioned at location (d), near the edge of the hole. The probe diameter is about 400 Å.

Fig. 90. (a) through (d) Four series of $\pm g$ experiments performed over a range of specimen thicknesses for α-titanium in a $[1\bar{1}02]$ orientation. For each thickness, the zone axis pattern is shown in the center, with the $[\bar{1}101]$ and $[1\bar{1}0\bar{1}]$ discs at their Bragg positions located to the left and right, respectively. Notice that the decrease in specimen thickness from (b) to (c) produces an increase in the overall symmetry of the zone axis pattern and a loss of translational symmetry between the intensity fringes in the $[\bar{1}101]$ and $[1\bar{1}0\bar{1}]$ CBED discs.

Fig. 91. CBED patterns from extracted γ' precipitate in a [0001] orientation showing: (a) 6mm symmetry of the intensity distributions in the OOLZ discs, (b) absence of detail within the BF disc due to the thinness of the precipitate, (c) 6-fold symmetry of the FOLZ, and (d) G-M line in the $\langle 11\bar{2}1\rangle$ FOLZ reflection at the Bragg position. As for the Ti sample, the position of the optic axis is indicated by an asterisk in all of the CBED patterns.

Fig. 92. CBED patterns for extracted γ' precipitate in a [0001] orientation showing: (a) and (b) a single mirror line and 180° rotational symmetry between the $[\bar{1}010]$ and $[10\bar{1}0]$ discs located at their Bragg positions, respectively, (c) mirror lines in the 6-beam pattern with the $[10\bar{1}0]$ disc centered on the optic axis (asterisk), and (d) symmetric excitation of the $[\bar{1}2\bar{1}0]$ and $[2\bar{1}\bar{1}0]$ reflections with mirrors in all the $\langle 11\bar{2}0\rangle$ (and $\langle\bar{1}010\rangle$) discs spaced at 30° intervals.

Fig. 93. (a) $[1\bar{1}02]$ CBED pattern for γ' precipitate with 2mm symmetry, (b) and (c) intensity distributions in the $[11\bar{2}0]$ and $[\bar{1}\bar{1}20]$ discs at their respective Bragg positions, and (d) and (e) intensity fringes within the $[\bar{1}101]$ and $[1\bar{1}0\bar{1}]$ discs at their respective Bragg positions. Notice that opposite $\langle\bar{1}101\rangle$ discs in (d) and (e) are related by a 180° rotation.

Fig. 94. (a), (c) and (d) Three conjugate 4-beam CBED patterns around the $[1\bar{1}04]$ zone axis shown in (b). As for the Ti sample, notice the translational symmetries between opposite CBED reflections and the nearly perfect inversion symmetry within the $\langle\bar{1}3\bar{2}1\rangle$ discs in these patterns. Also notice the weak HOLZ lines in the zone axis pattern in (b).

Fig. 95. CBED patterns from 120 min. γ' precipitate in a [0001] orientation showing: (a) 6mm symmetry in the OOLZ, (b) 6-fold symmetry within the BF disc, which is elongated because the probe is focussed slightly above the precipitate surface, (c) 6mm symmetry in the FOLZ, and (d) G-M line in the $\langle11\bar{2}1\rangle$ FOLZ reflection at the Bragg position. The position of the optic axis is indicated by an asterisk in all of the CBED patterns. The bright ring in the FOLZ is barely visible in (c).

Fig. 96. CBED patterns for 120 min. γ' precipitate in a [0001] orientation showing: (a) and (b) a single mirror line and 180° rotational symmetry between the $[\bar{1}010]$ and $[10\bar{1}0]$ discs located at their Bragg positions, (c) mirror lines in the 6-beam pattern with the $[10\bar{1}0]$ disc centered on the optic axis (asterisk), and (d) symmetric excitation of the $[\bar{1}2\bar{1}0]$ and $[2\bar{1}\bar{1}0]$

reflections with mirror lines in all the <11$\bar{2}$0> (and <$\bar{1}$010>) discs spaced at 30° intervals.

Fig. 97. (a) [1$\bar{1}$04] zone axis pattern for 120 min. γ' precipitate, (b) 4-beam pattern showing mirrors in the [$\bar{1}\bar{1}$20] and [220$\bar{1}$] discs and the inversion symmetry in the [1$\bar{3}$2$\bar{1}$] disc, (d) [1$\bar{1}$02] zone axis CBED pattern which has 2mm symmetry but is slightly distorted due to a slight off-focus condition, and (c) and (e) opposite <$\bar{1}$101> reflections at their respective Bragg positions. Notice that the intensity fringes in the opposite <$\bar{1}$101> discs have 180° rotational symmetry, but that the faint HOLZ lines which are nearly horizontal in these discs are slightly concave down in both discs, indicating some translational symmetry.

Fig. 98. Plot from the computer program in Appendix 10.1. showing the atomic positions around a Shockley partial dislocation ledge on the face of a γ' precipitate. The last atomic planes in the precipitate on either side of the ledge are indicated by dashed lines, and the position of the dislocation core which terminates at the edge of the ledge is indicated by a cross. The extra plane associated with the dislocation is also indicated by an arrow in the plot.

Fig. 99. (a) through (h) Series of computed images at -1460 Å defocus for a hcp crystal which is 54.3 Å thick and contains 66 a/o Ag on the A-planes, and Ag concentrations on the B-planes which increase from 0 a/o in (a) to 66 a/o Ag in (h).

Fig. 100. (a) Computed image for an Al_2Ag crystal which is 54.3 Å thick and has 66 a/o Ag on the A-planes and no Ag on the B-planes, and (b) computed image for an Ag_2Al crystal which is 37.2 Å thick and has 99 a/o Ag on the A-planes and 33 a/o Ag on the B-planes. Both images are at -1460 Å defocus and are indistinguishable.

Fig. 101. (a) Selected-area diffraction pattern from γ' precipitates which displays strong reflections at 1/6<0002> and 1/3<0002> positions, as indicated by the arrows and dots in the figure, and (b) corresponding HREM image of the γ' precipitates and inset optical diffraction pattern from the same area. Notice the six-plane repeating patterns among the basal planes enclosed by the box and indicated by arrows in (b), and the presence of strong 1/6<0002> and 1/3<0002> periodicities in the optical diffraction pattern.

Fig. 102. Total work necessary to form γ' precipitates with different aspect ratios due to interfacial and strain energy contributions, as a function of the precipitate thickness. The dashed lines represent the total work (W_s) required to form a γ' precipitate due to the surface energy and the solid lines indicate the total work (W_e) required to form the same precipitate due to the elastic strain energy of the transformation.

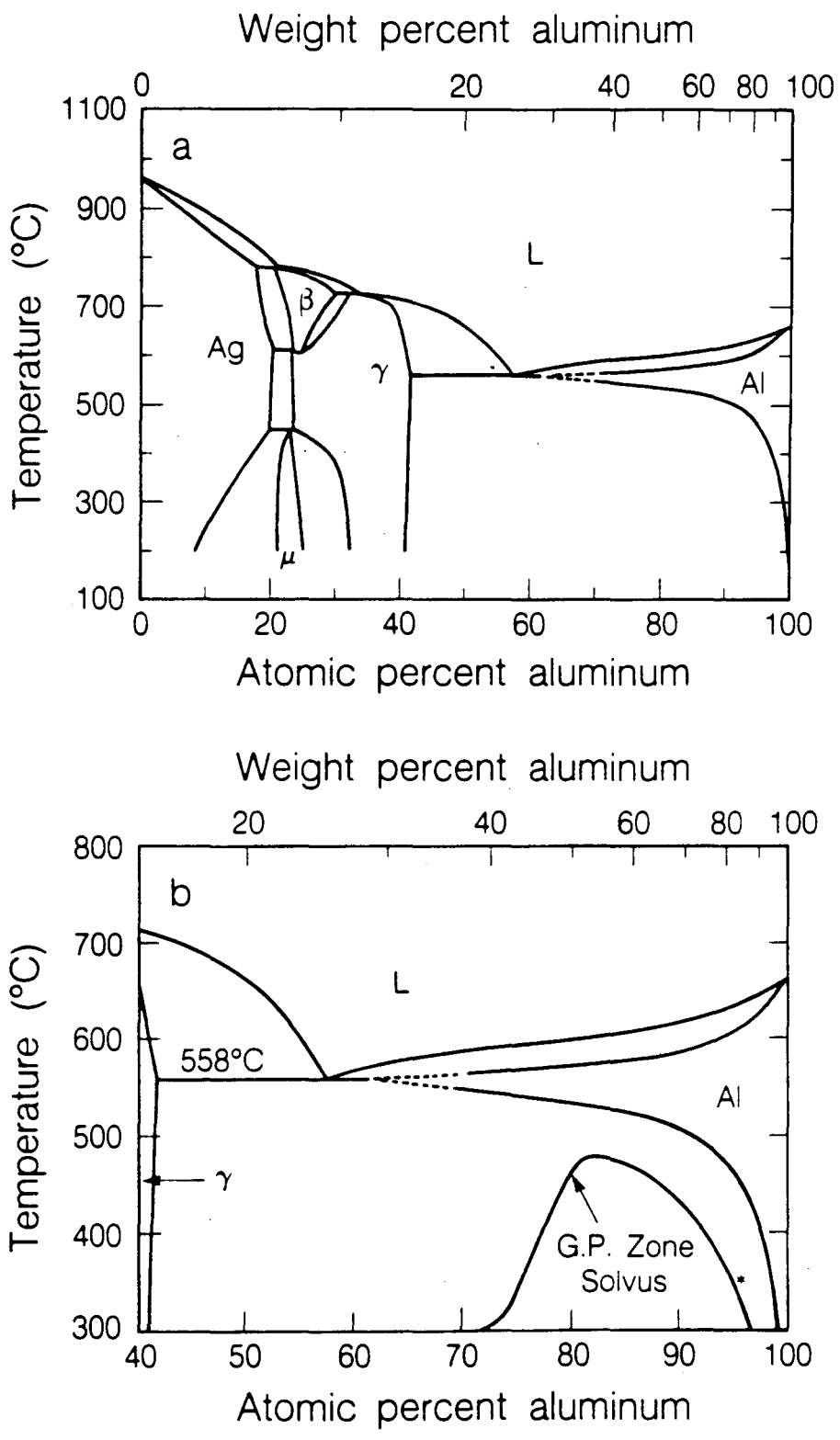

XBL 852-9753

Fig. 1

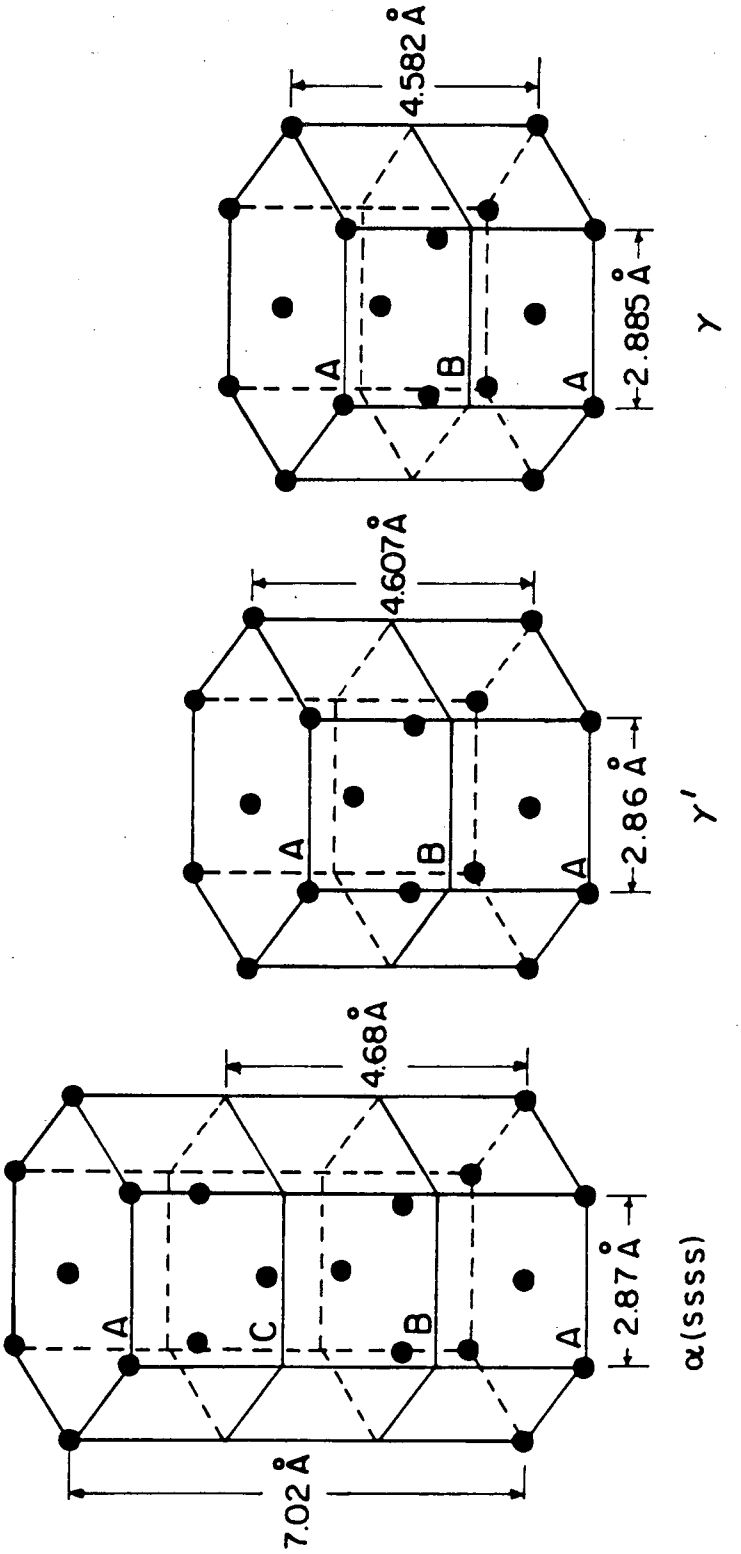

XBL 835-5700

Fig. 2

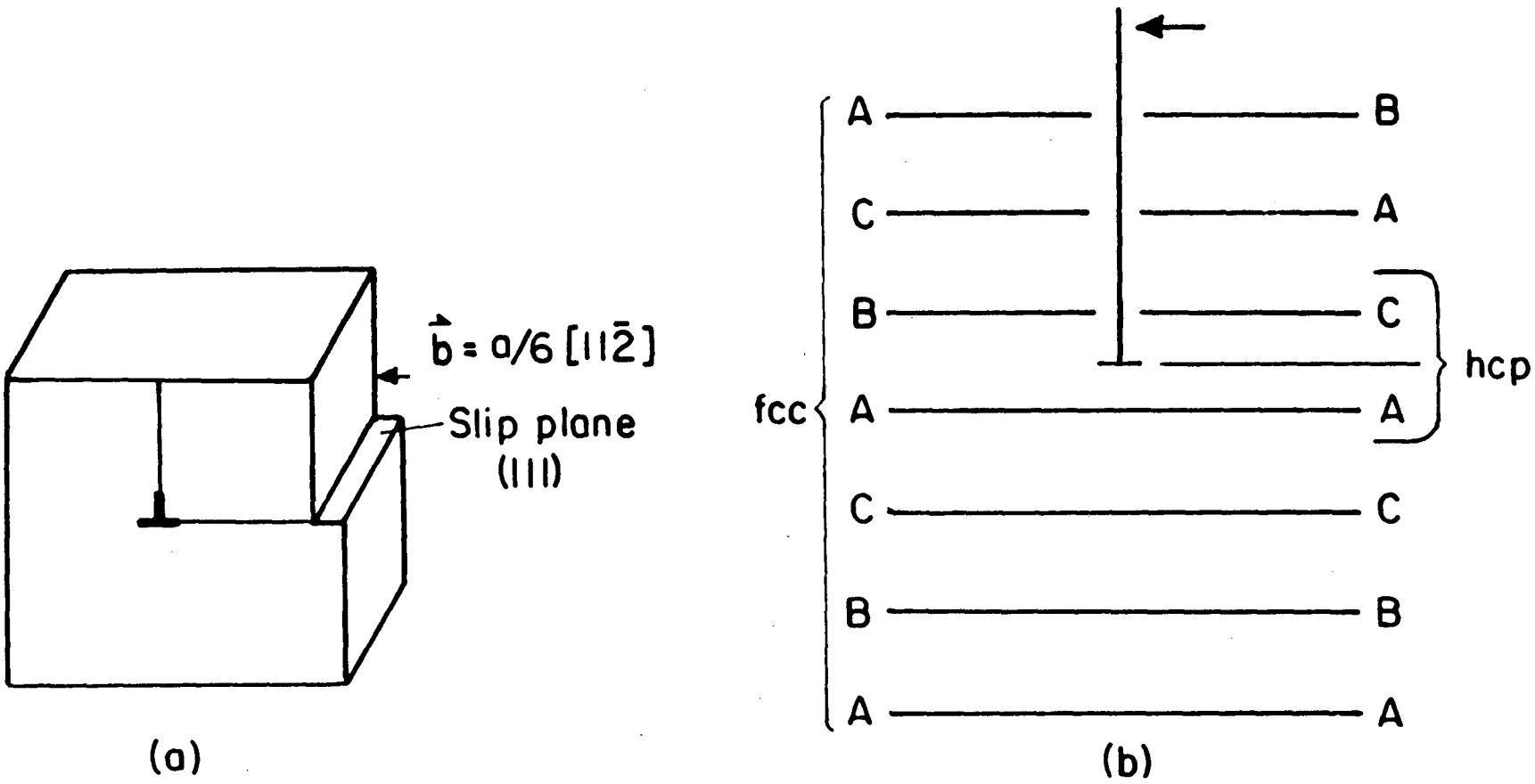

XBL 835-5702

Fig. 3

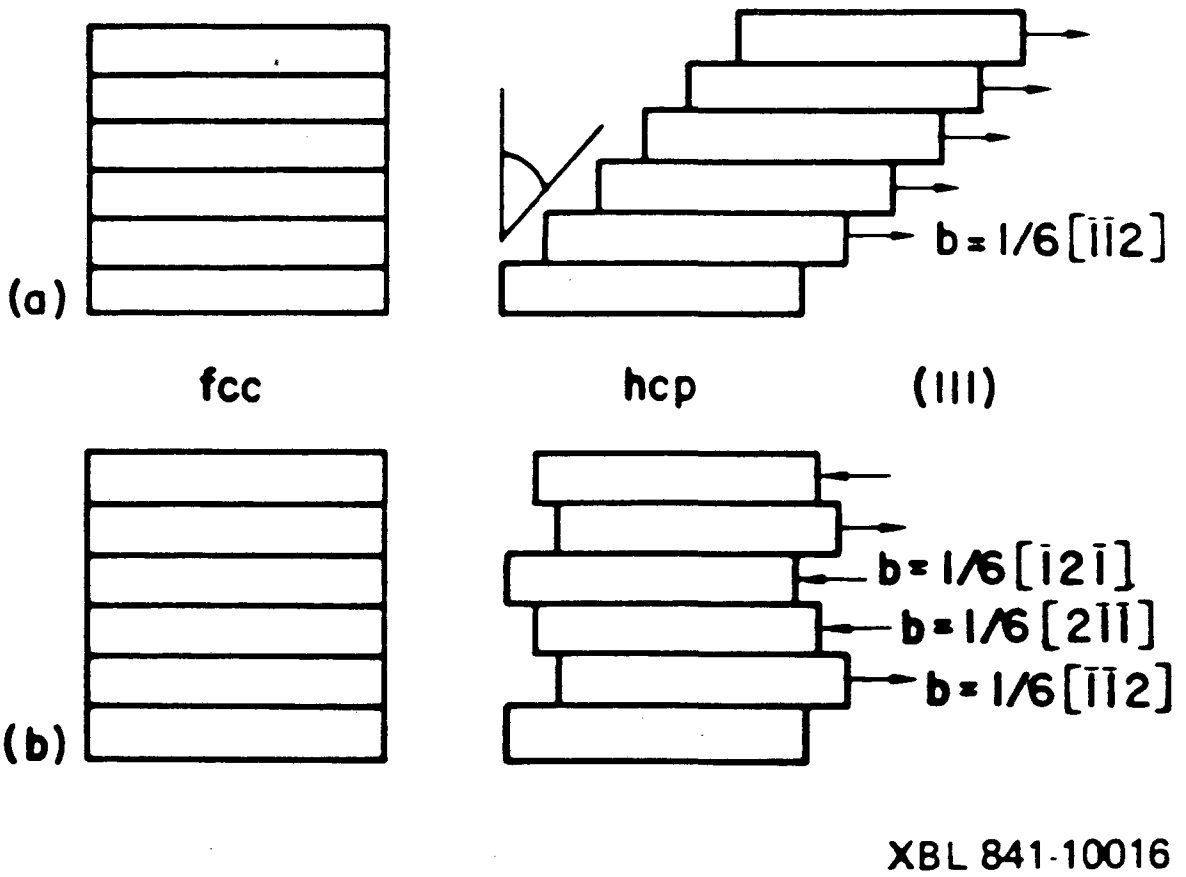

Fig. 4

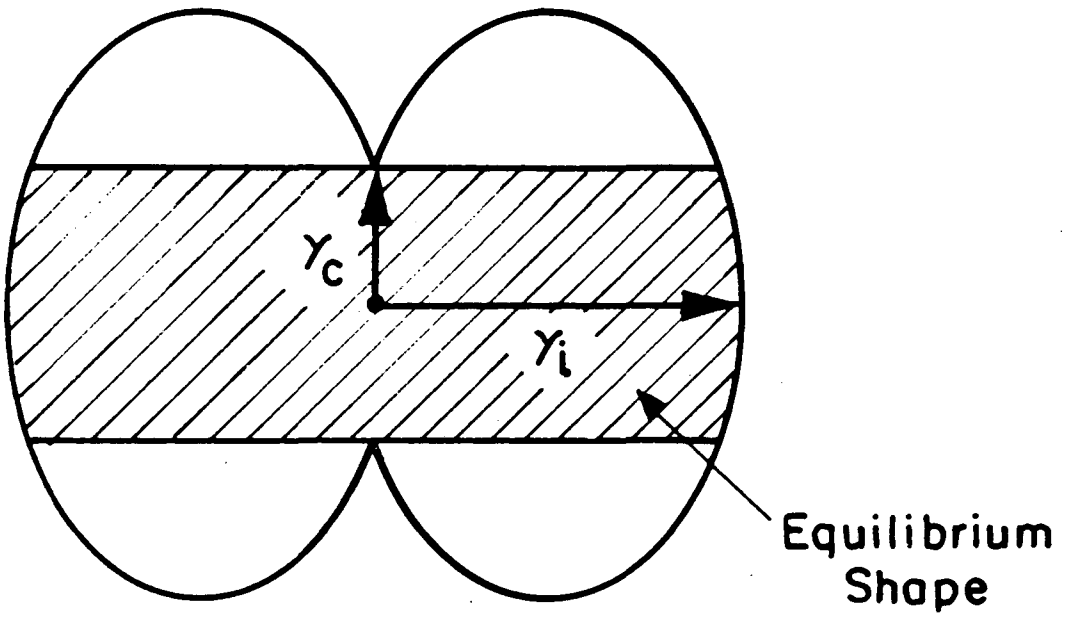

XBL835-5701

Fig. 5

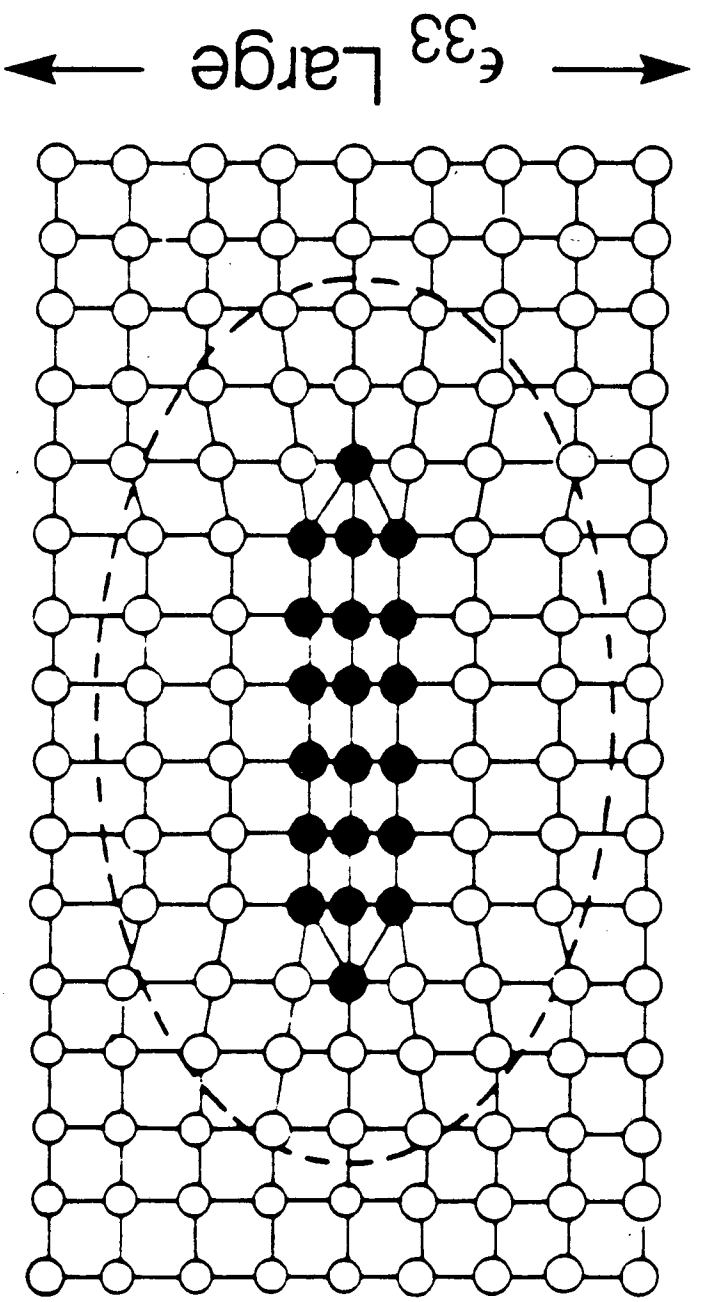

XBL 852-9752

Fig. 6

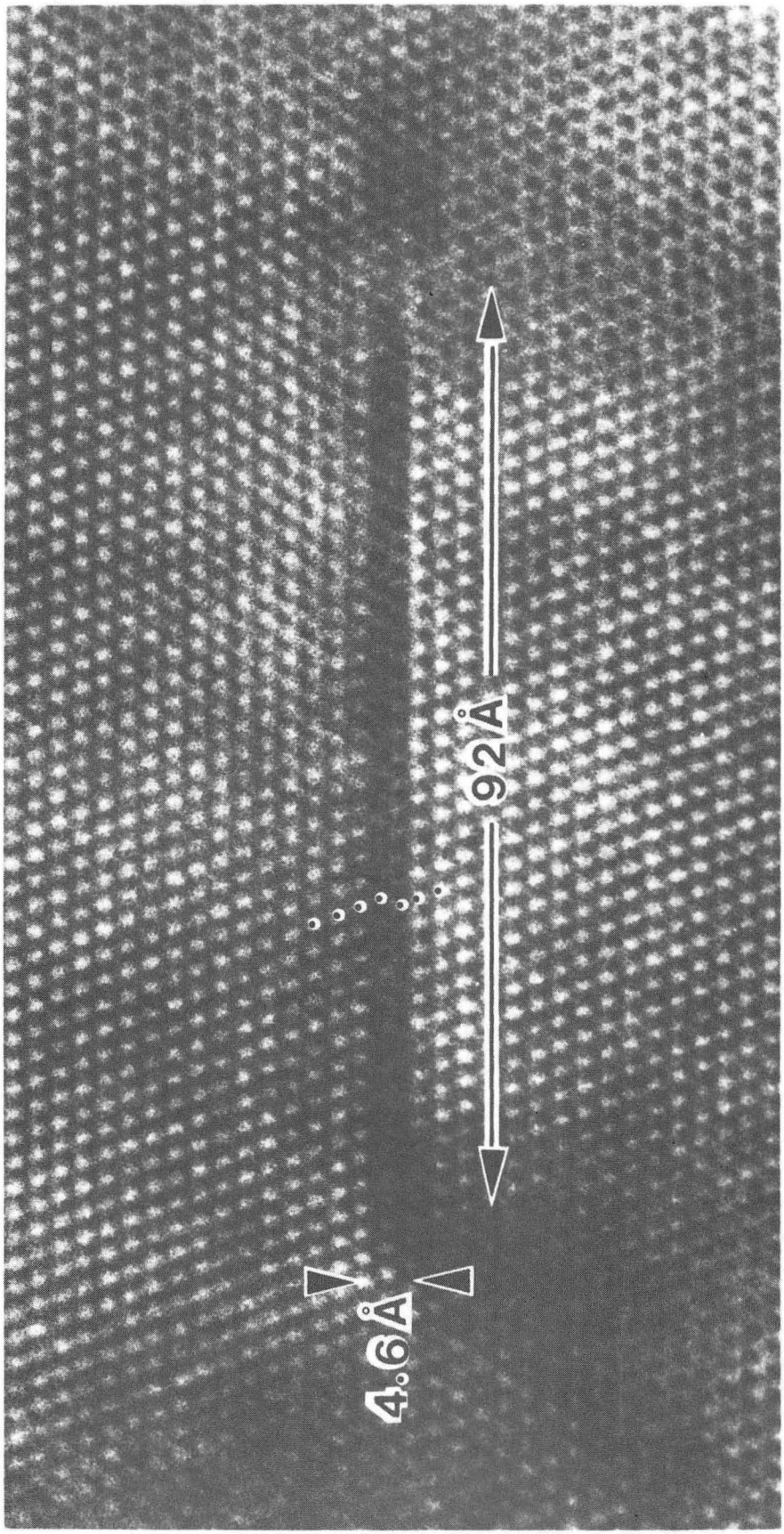

XBB 839-7848A

Fig. 7

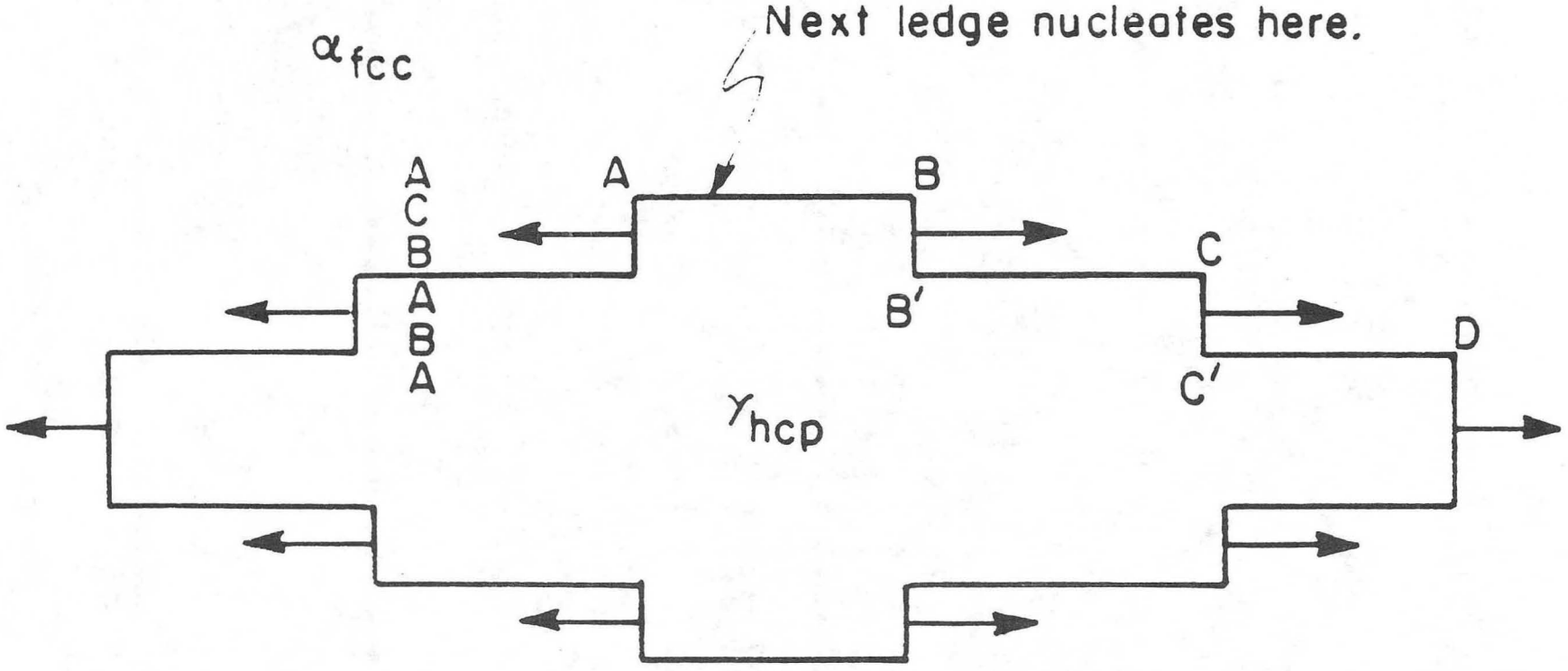

Fig. 8

XBL 835-5706

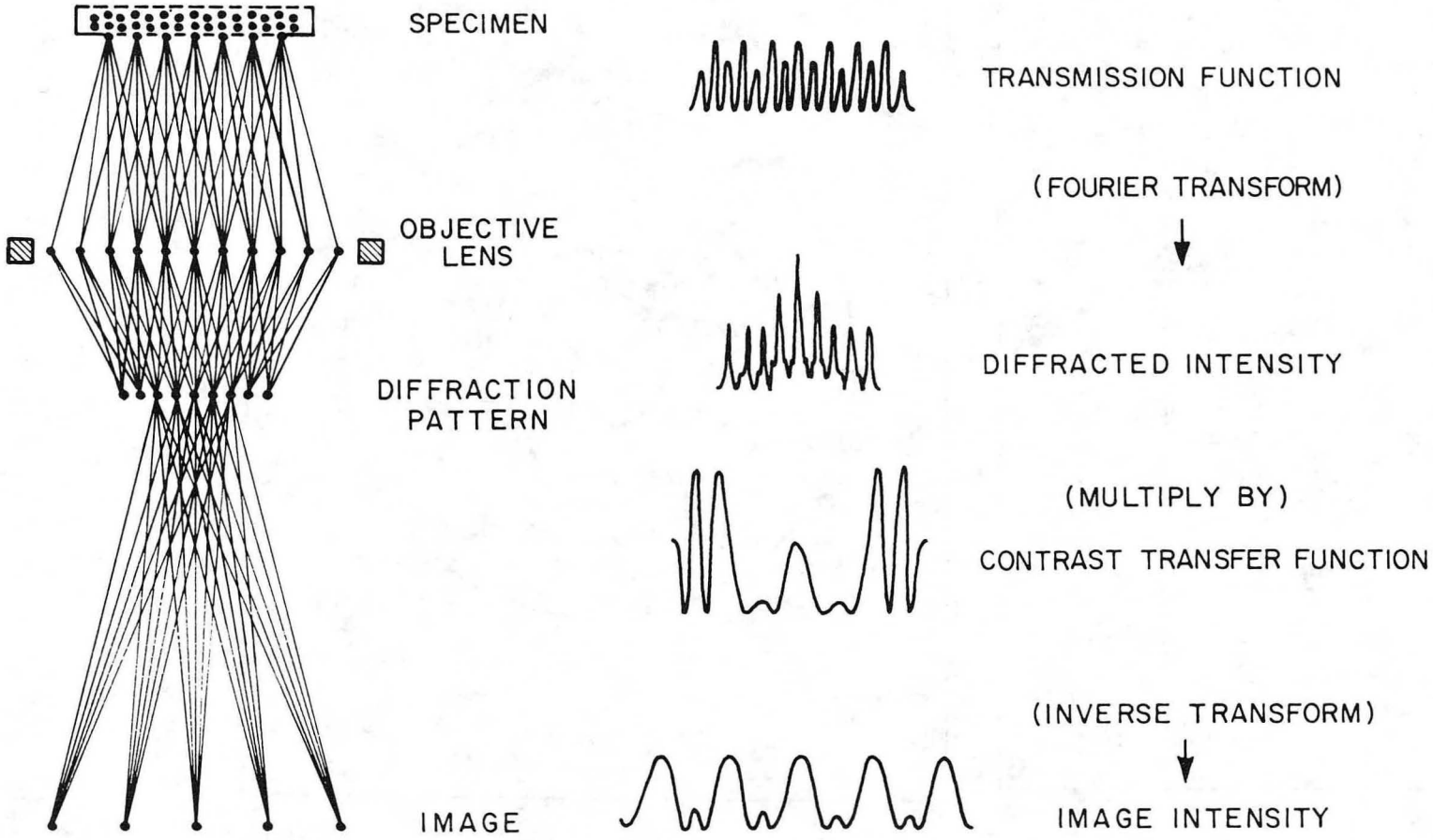
SPECIMEN
OBJECTIVE LENS
DIFFRACTION PATTERN
IMAGE
TRANSMISSION FUNCTION
(FOURIER TRANSFORM)
DIFFRACTED INTENSITY
(MULTIPLY BY)
CONTRAST TRANSFER FUNCTION
(INVERSE TRANSFORM)
IMAGE INTENSITY
XBL7810-5899

Fig. 9

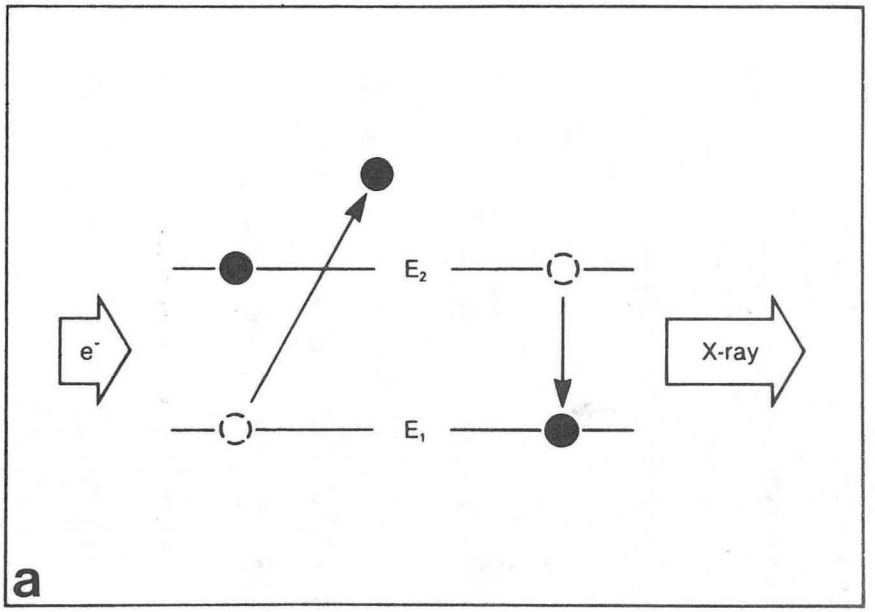

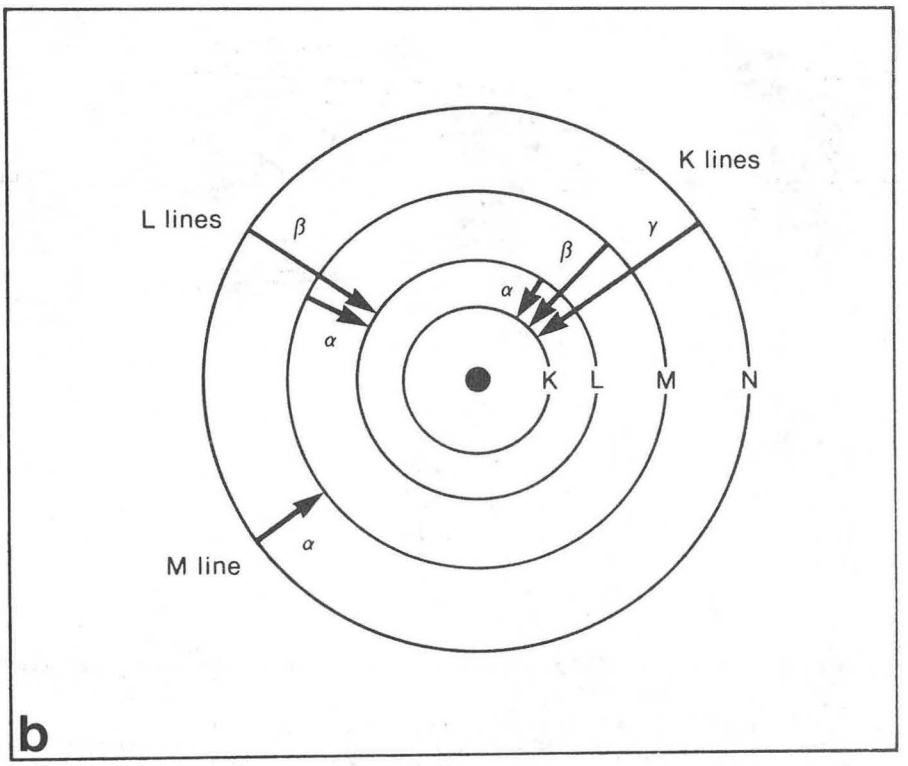

Fig. 10

XBL 852-1371

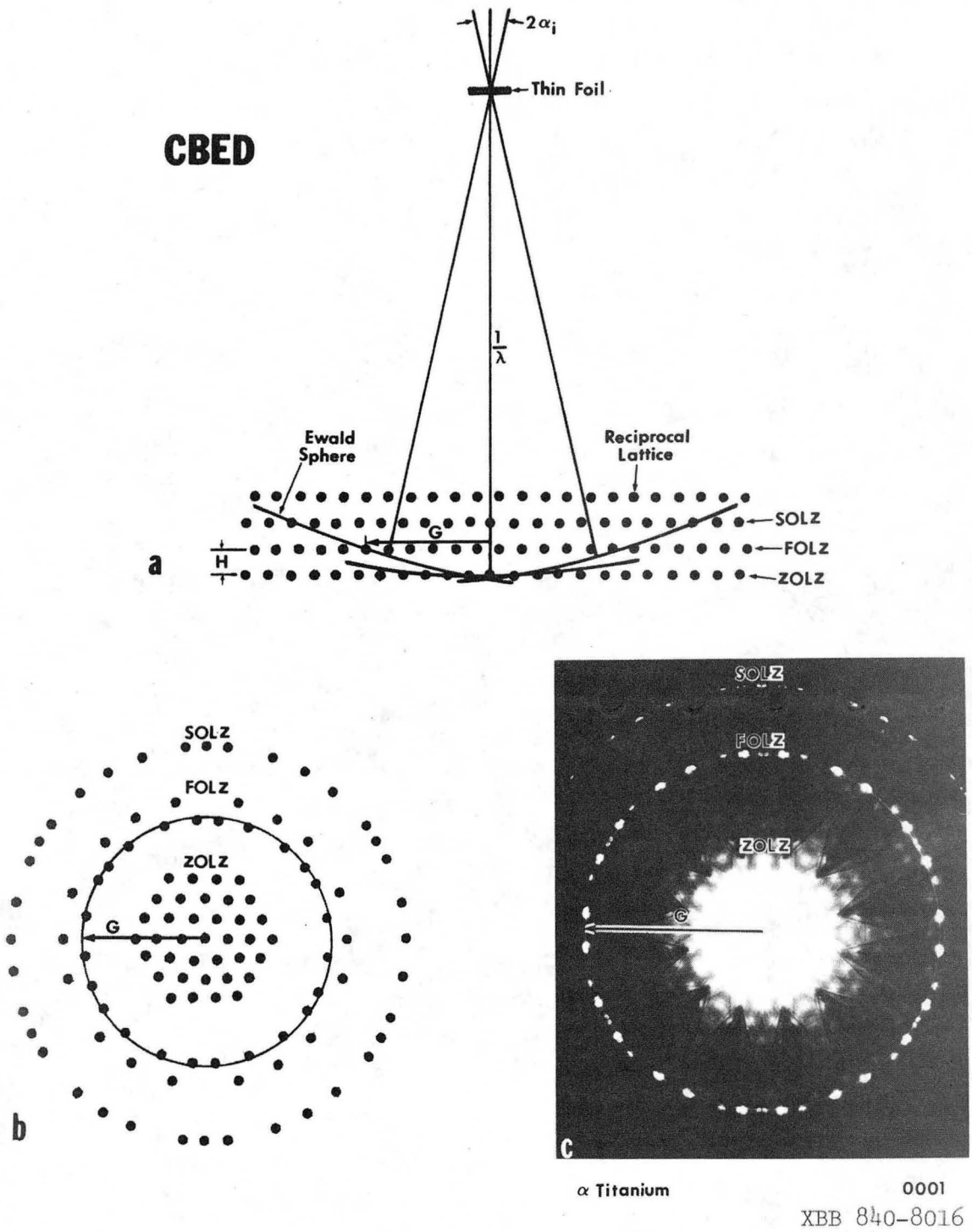
CBED
$2\alpha_i$
Thin Foil
$\frac{1}{\lambda}$
Ewald Sphere
Reciprocal Lattice
G
H
SOLZ
FOLZ
ZOLZ
a
b
c
α Titanium
0001
XBB 840-8016

Fig. 11

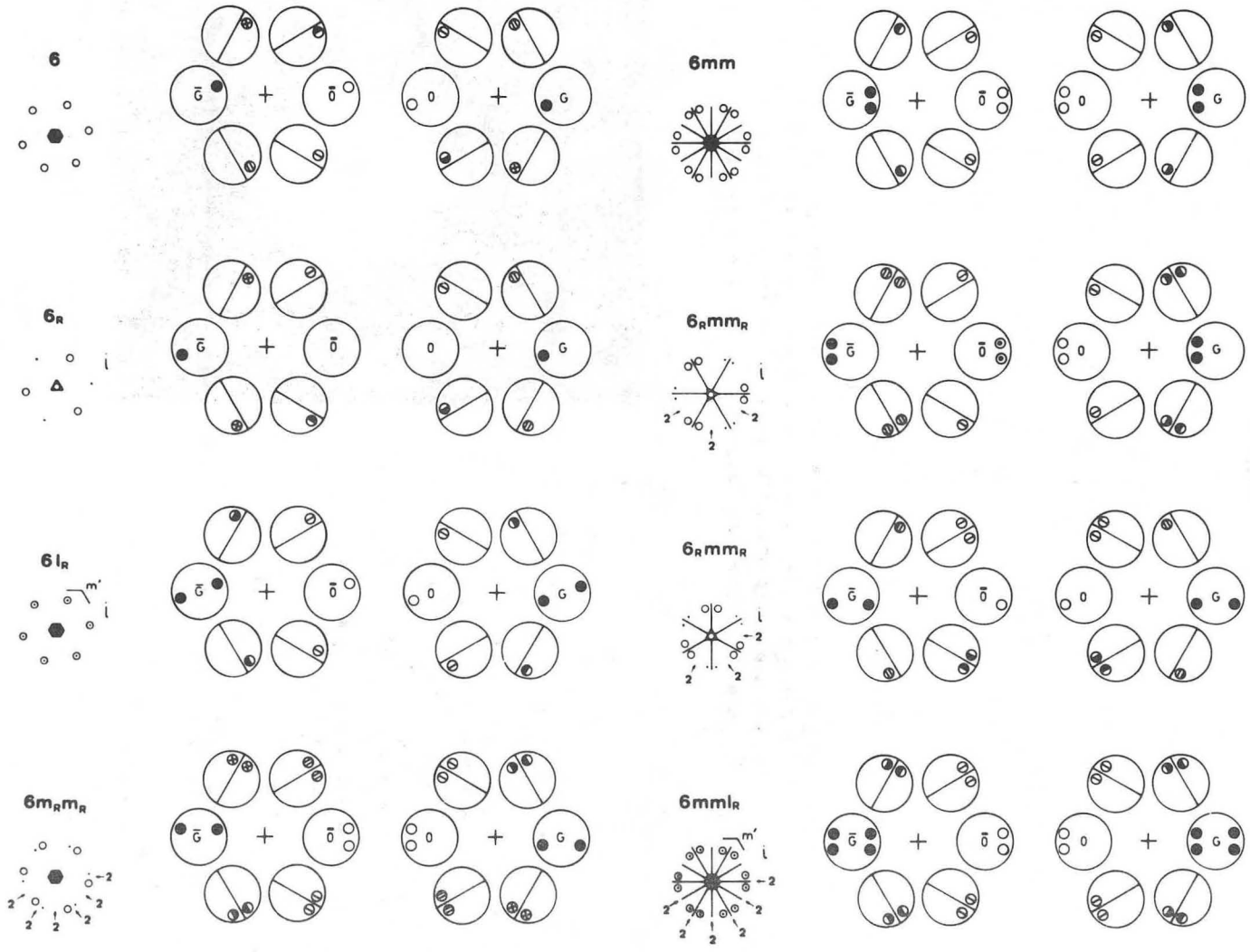

Fig. 12

XBL 852-1380

Plan of Attack

High-Resolution Electron Microscopy
(Interfacial Structure of Precipitate)

+

Energy-Dispersive X-Ray Analyses
(Precipitate and Matrix Chemistry)

+

Electron Diffraction Information
(γ' Precipitate Structure)

↓

Comparison Between Experimental and
Calculated High-Resolution Images
(Atomic Mechanisms of Growth)

******

Convergent-Beam Electron Diffraction
(Space Group and Lattice Parameter)

XBL 853-1518

Fig. 13

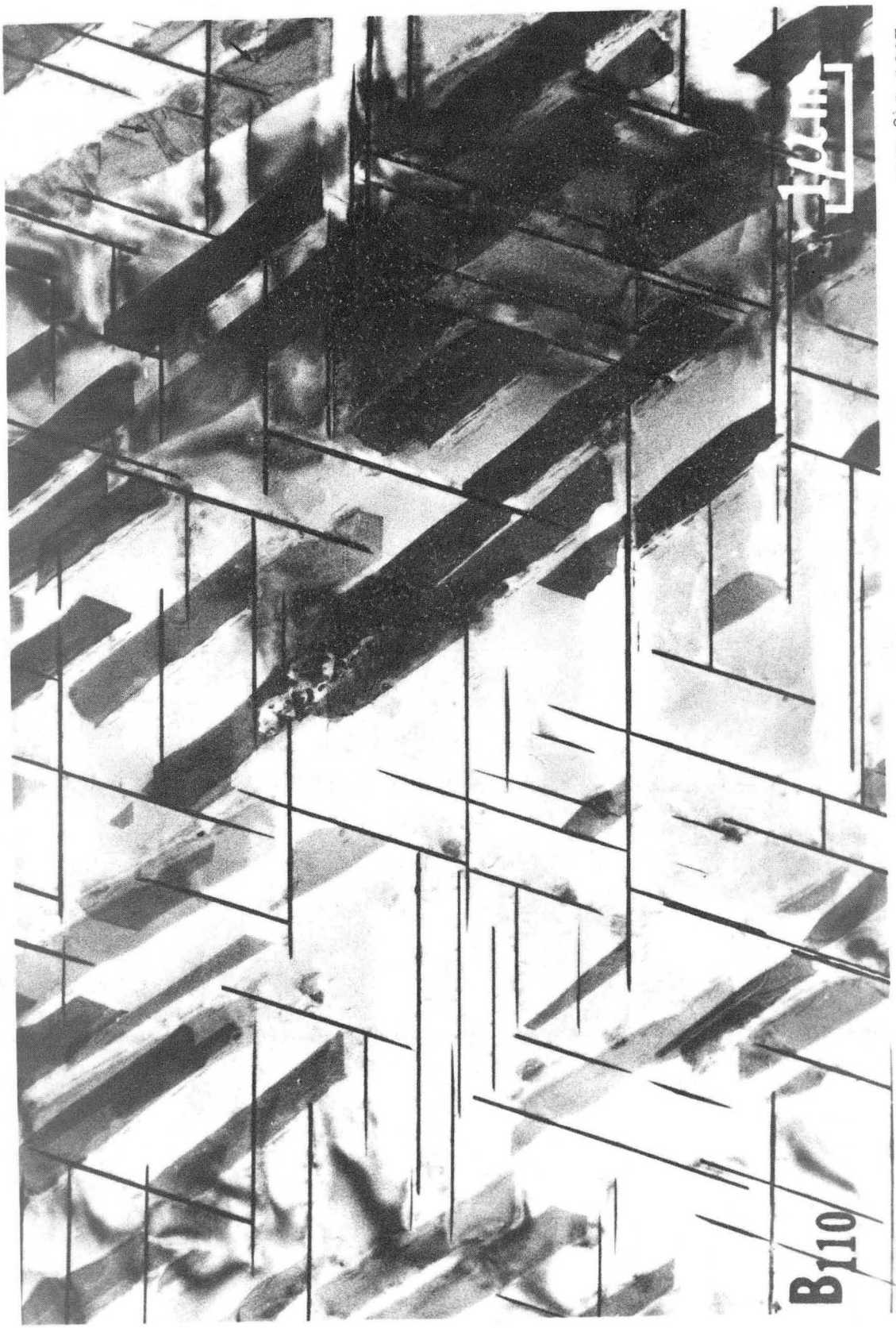

XBB 842-1207

Fig. 14

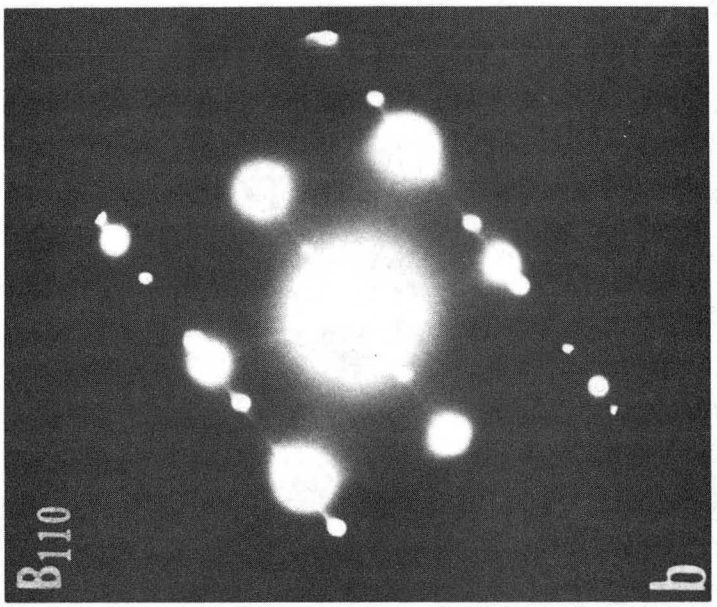

XBB 838-6710

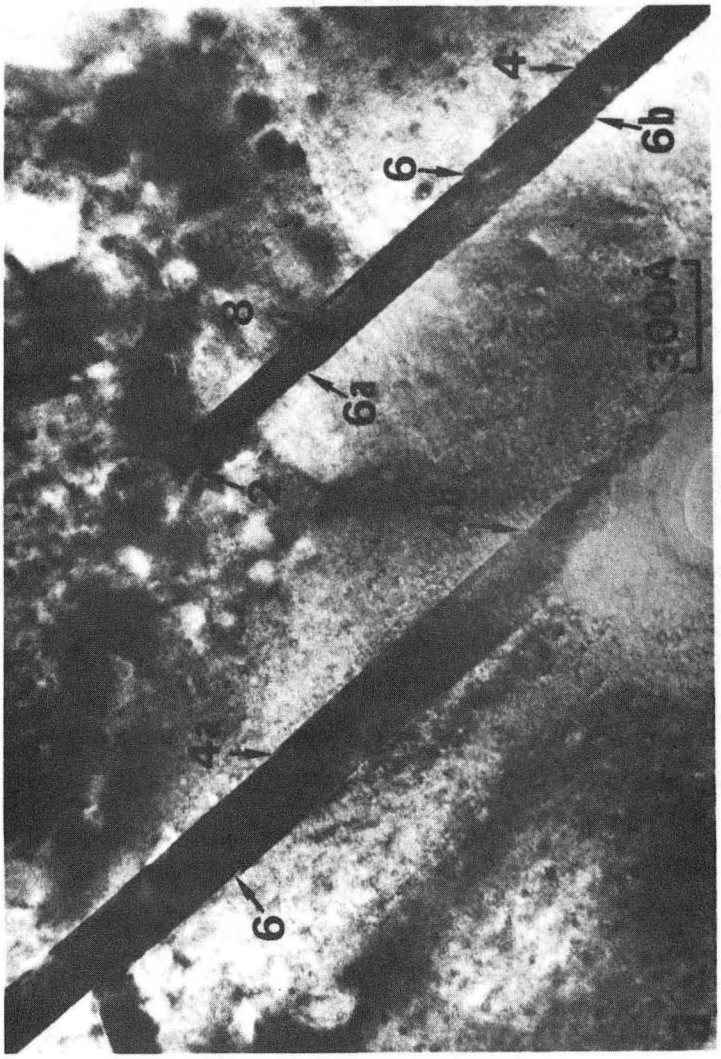

Fig. 15

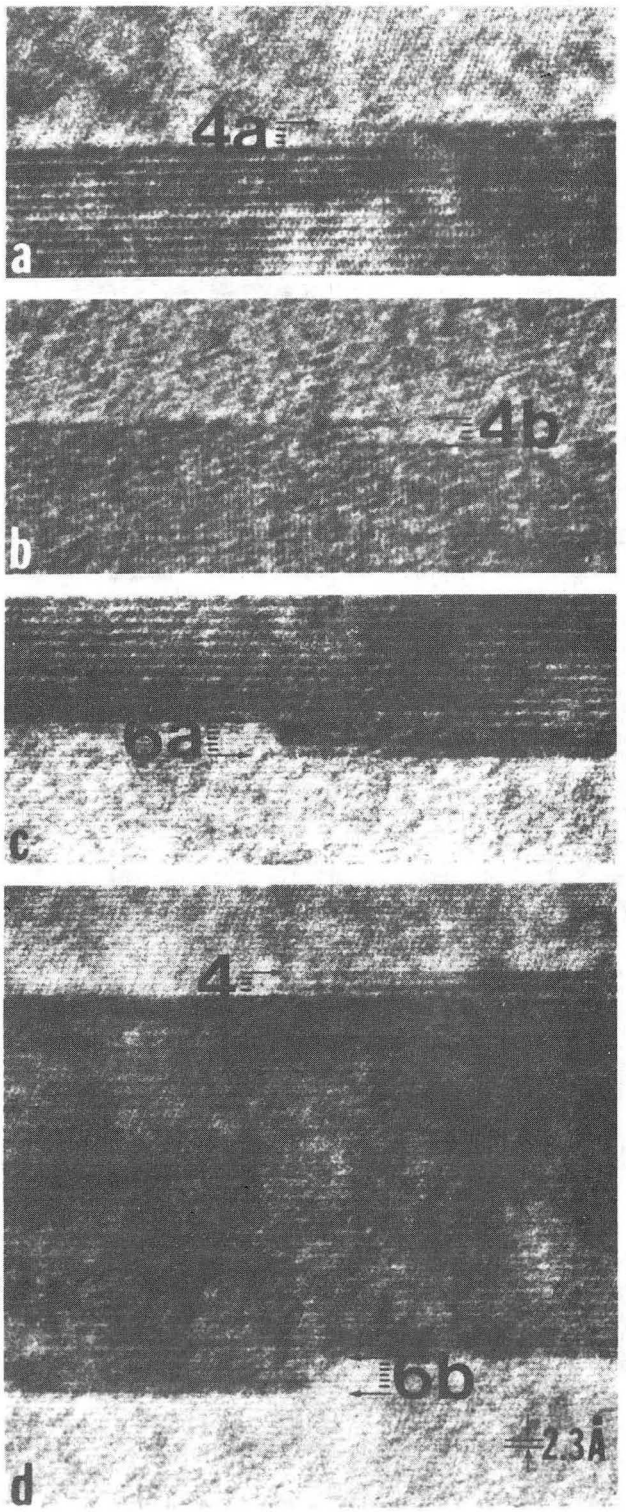

XBB 838-6702

Fig. 16

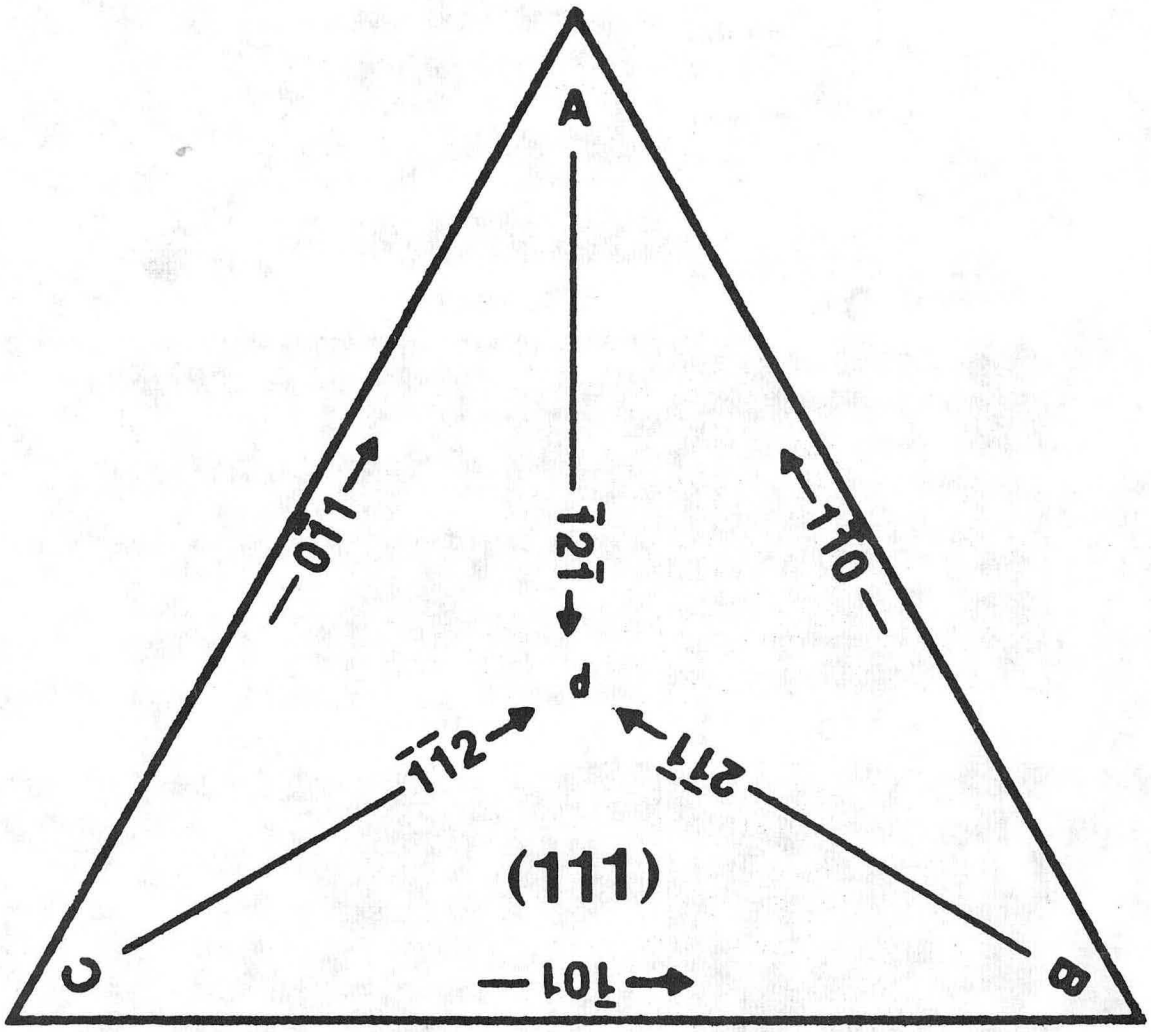

XBL 8412-5239

Fig. 17

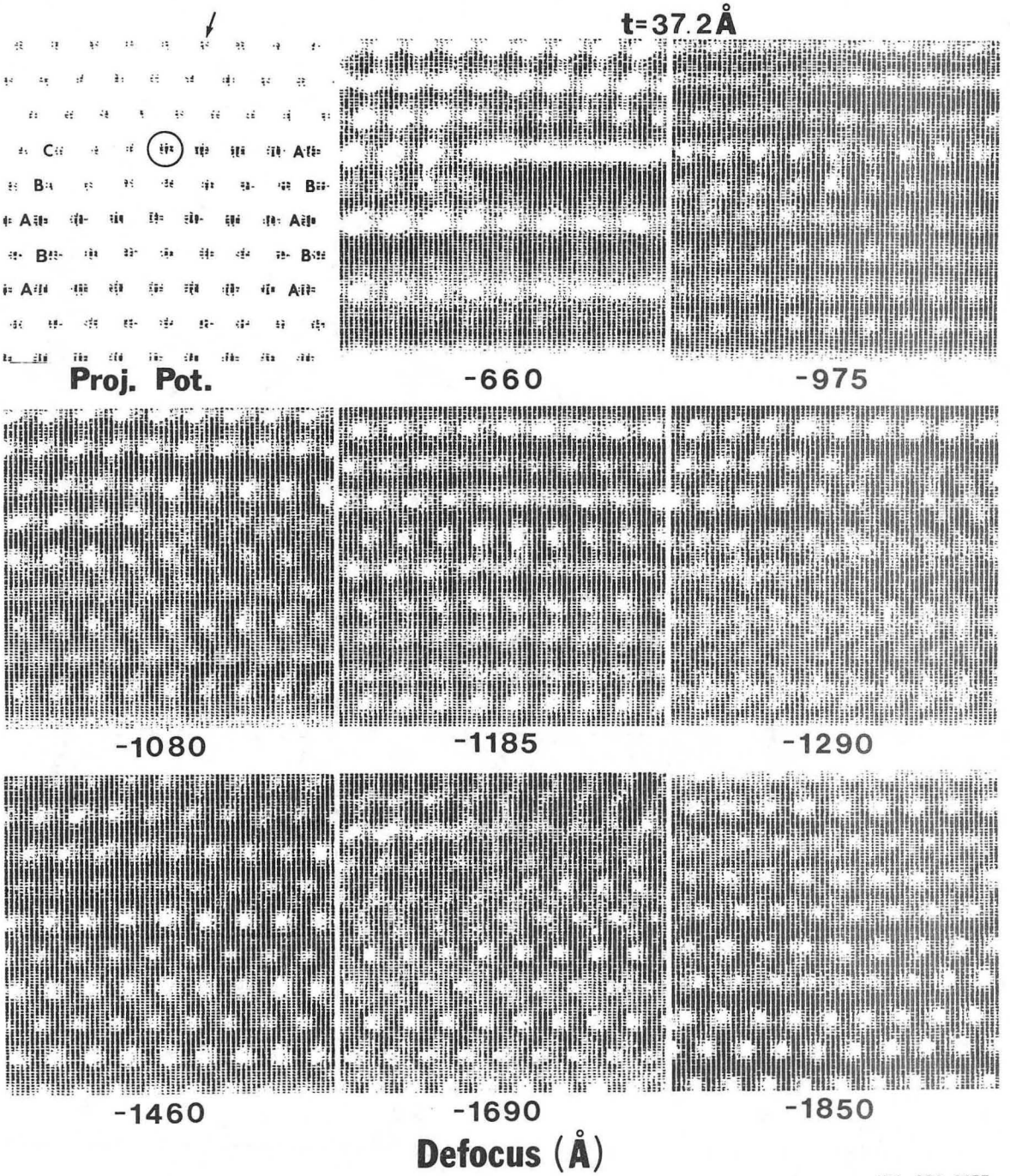

XBL 852-1377

Fig. 18

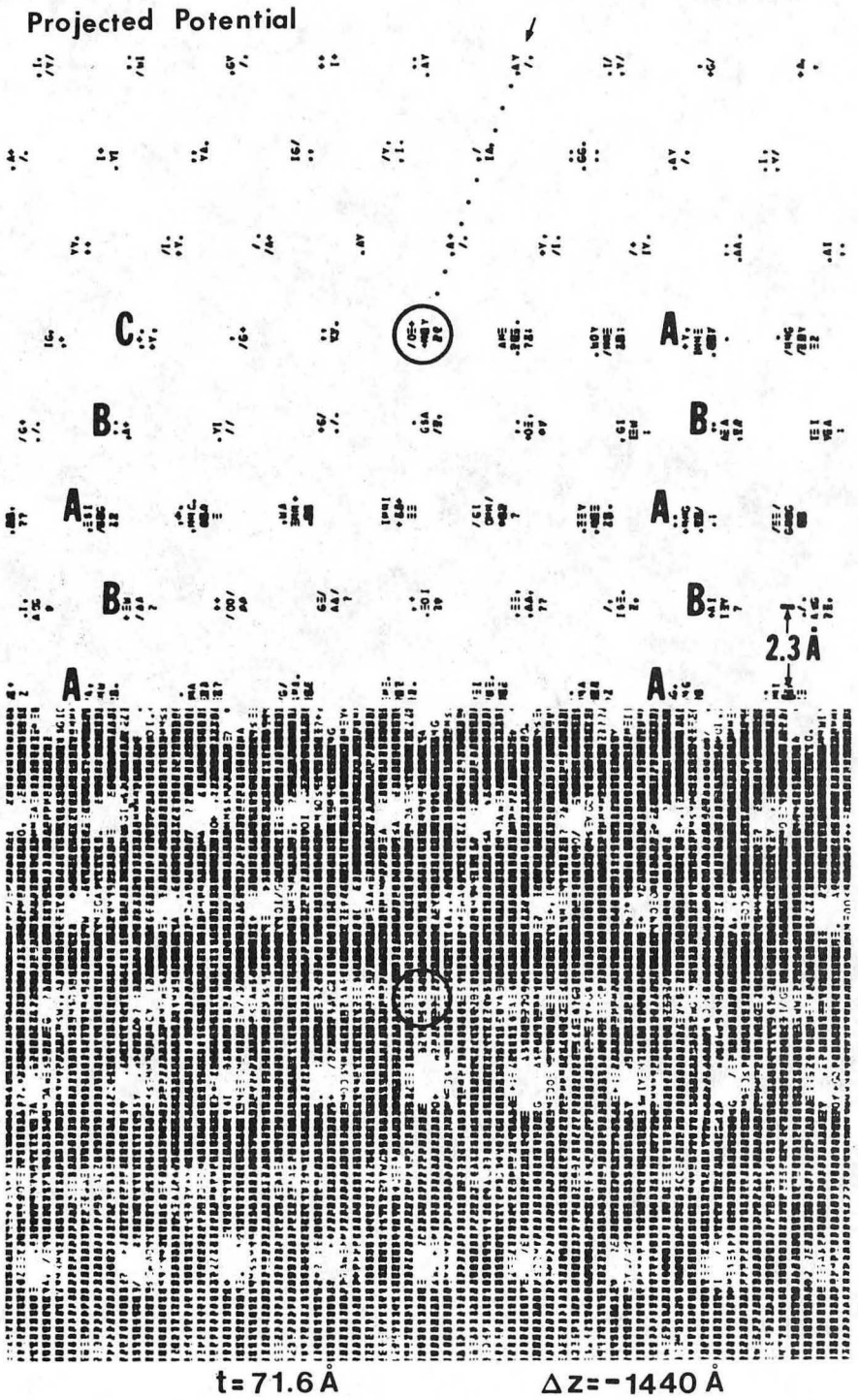

XBL 8412-5491

Fig. 19

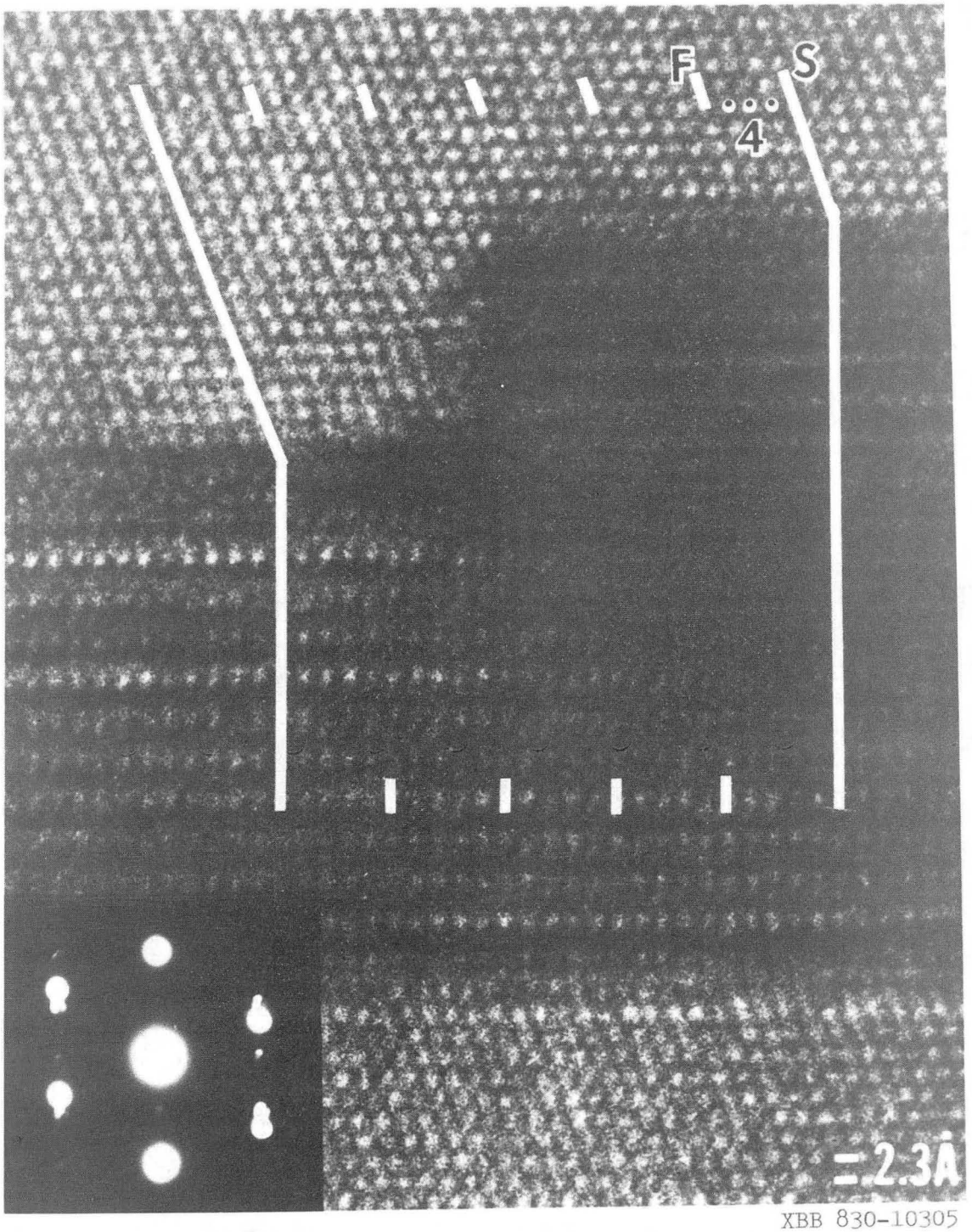

XBB 830-10305

Fig. 20

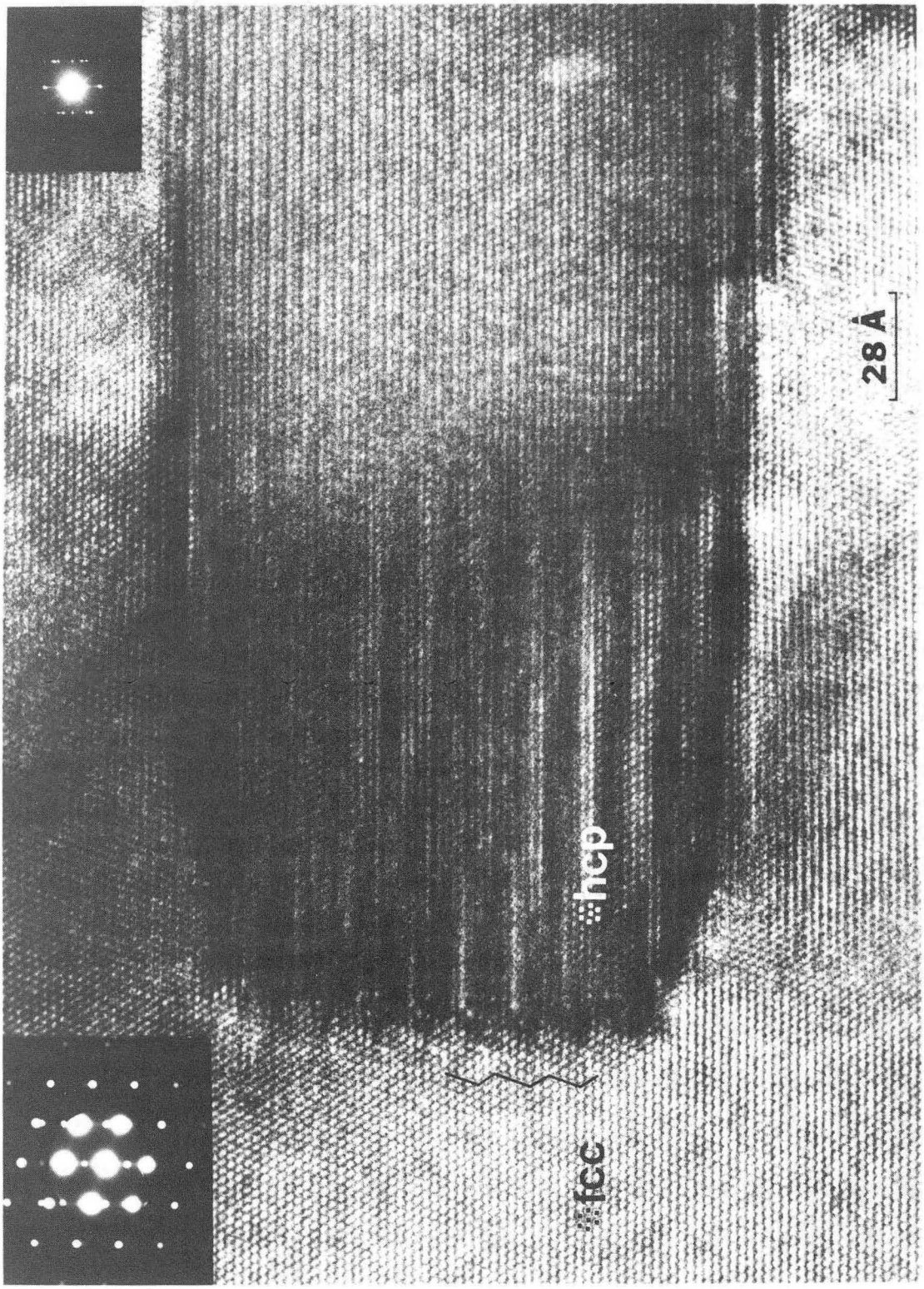

XBB 842-1212A

Fig. 21

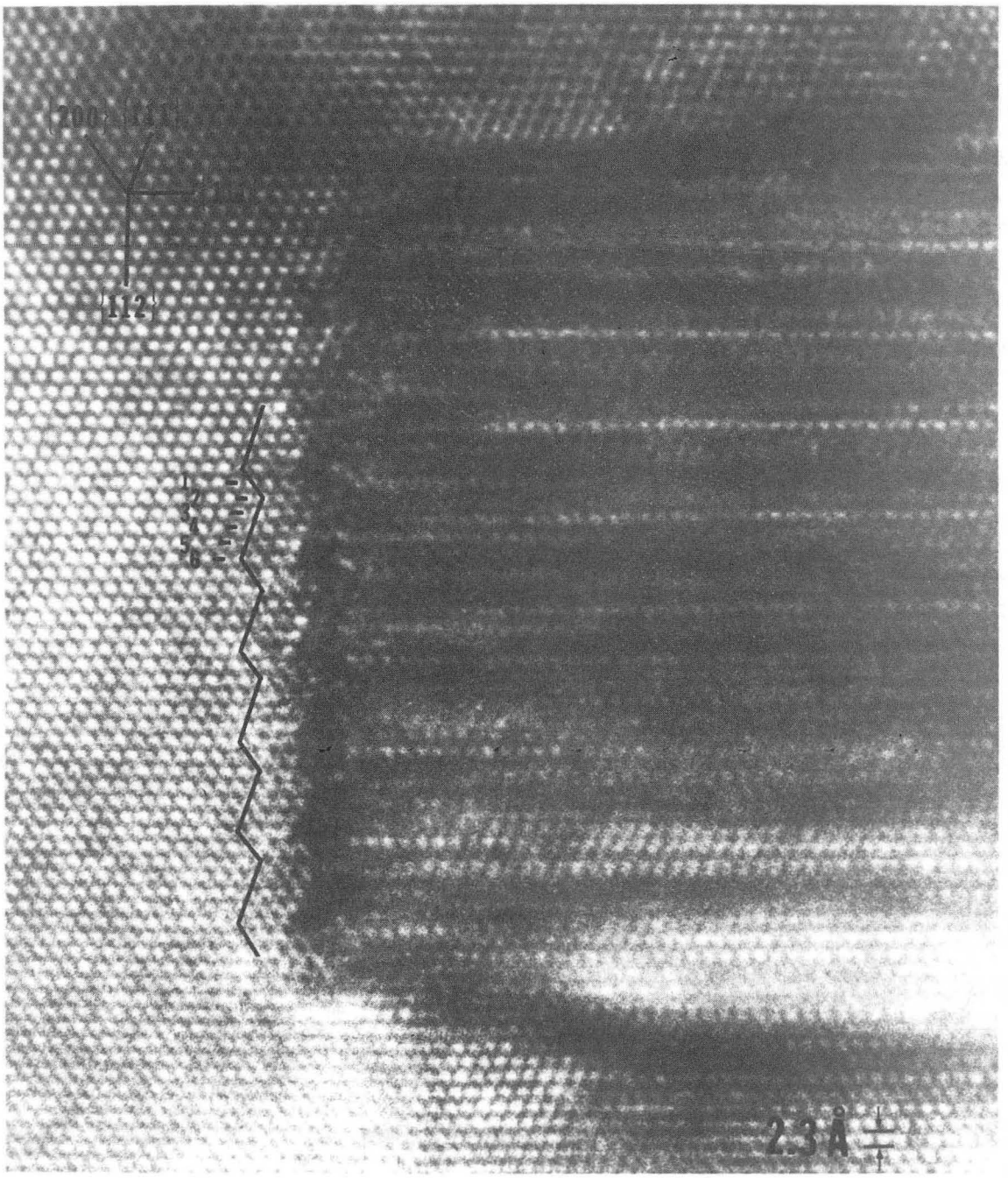

XBB 842-1210

Fig. 22

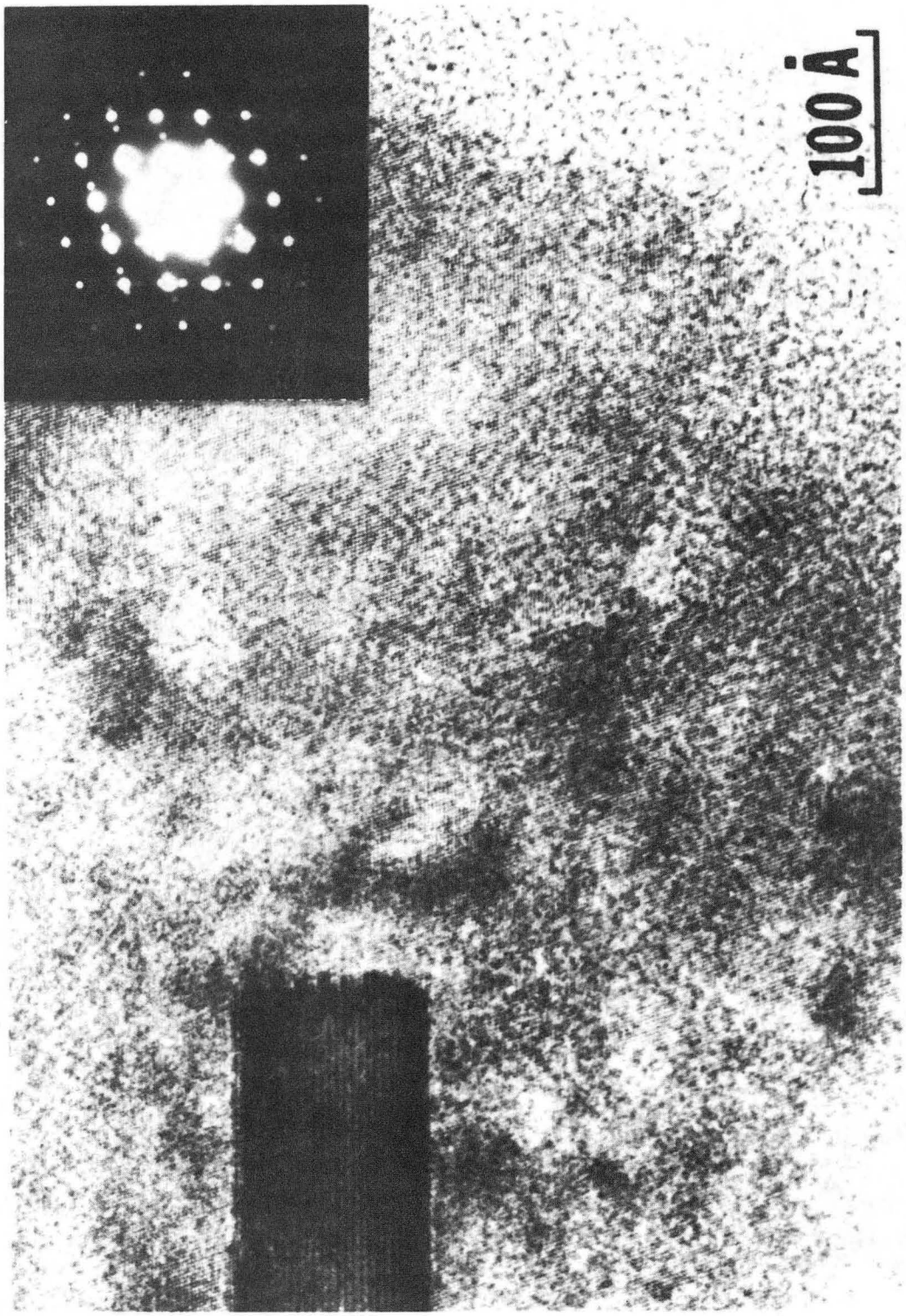

XBB 852-1544

Fig. 23

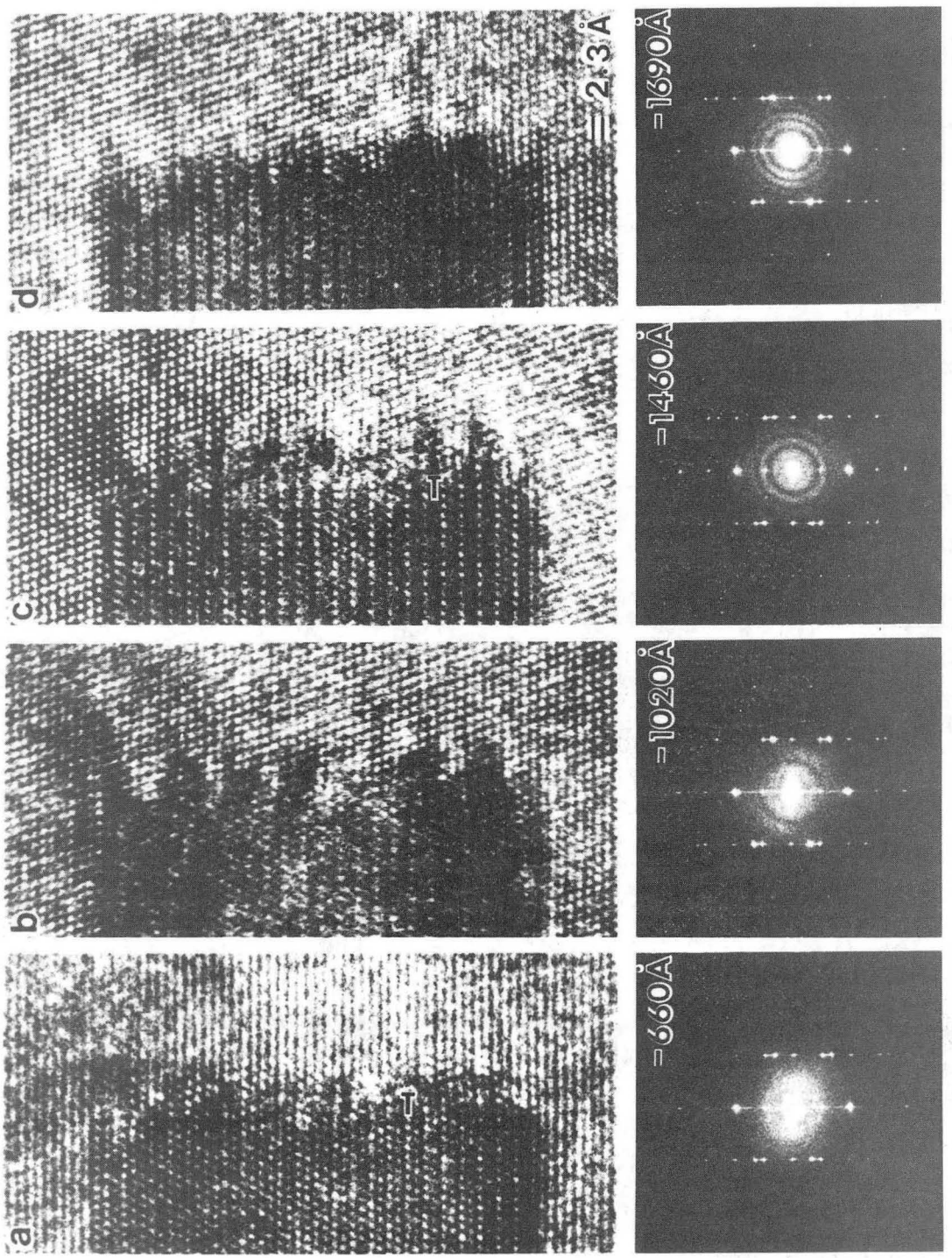

XBB 840-8880

Fig. 24

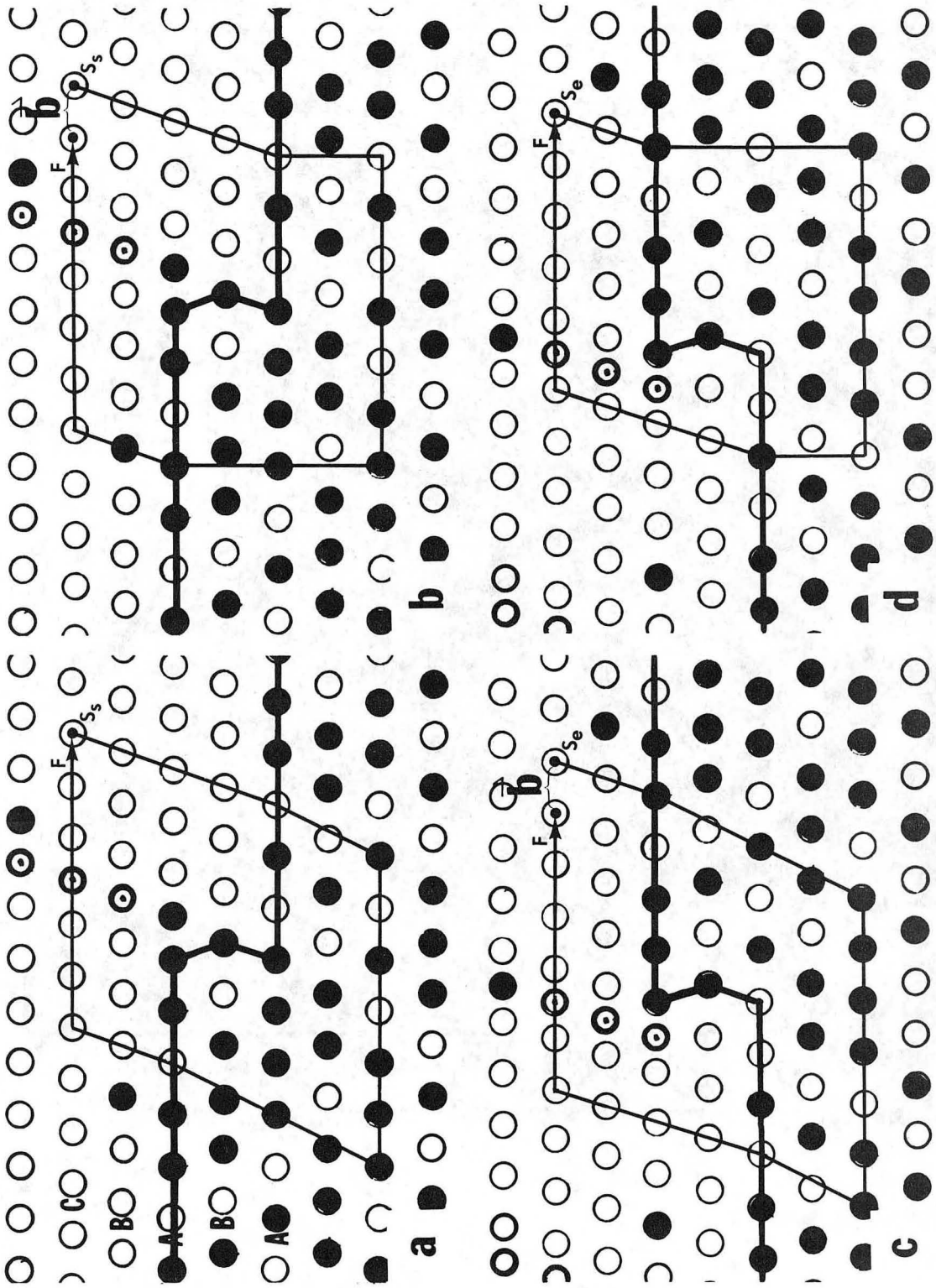

Fig. 25

XBL 832-8290

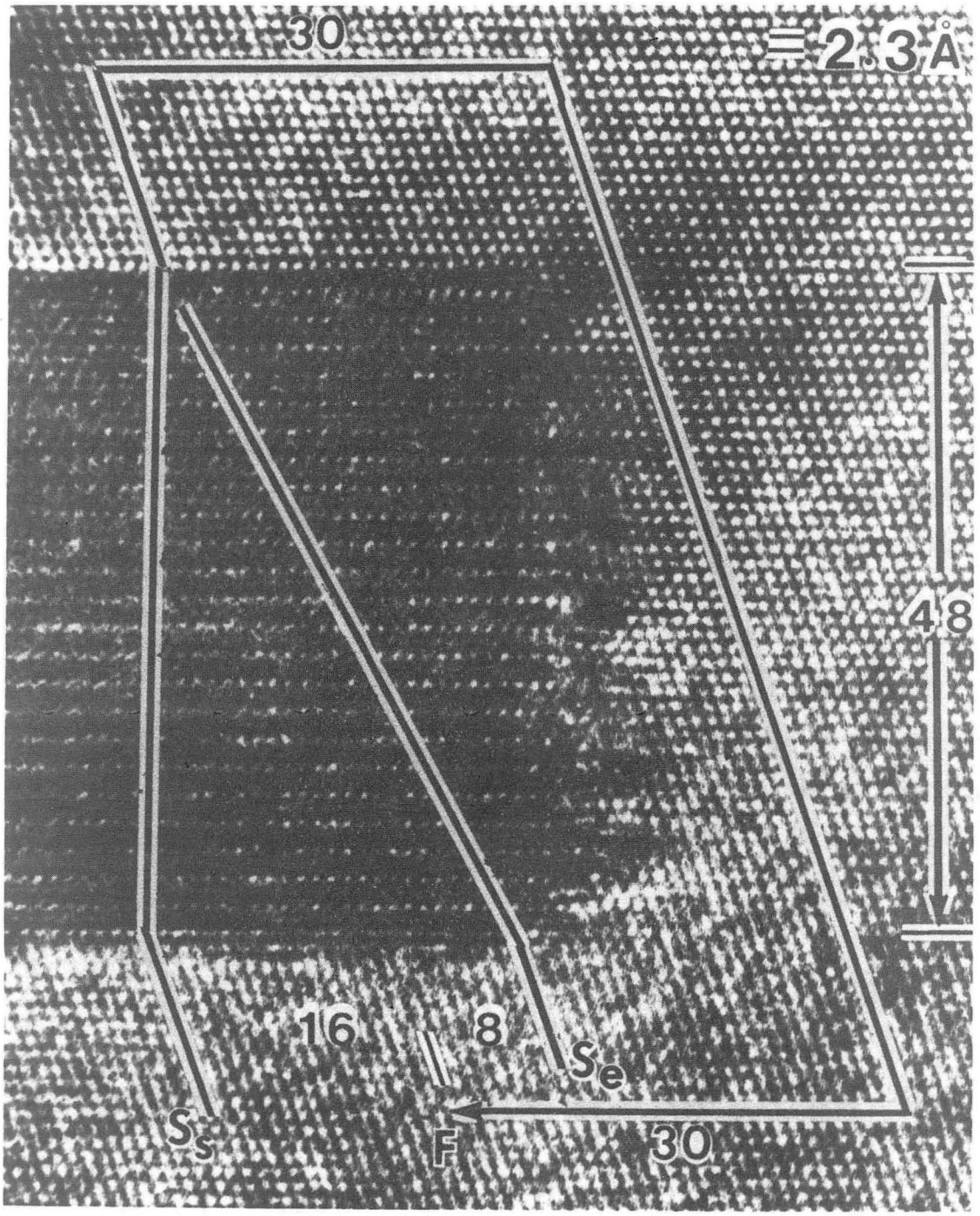

XBB 840-9361

Fig. 26

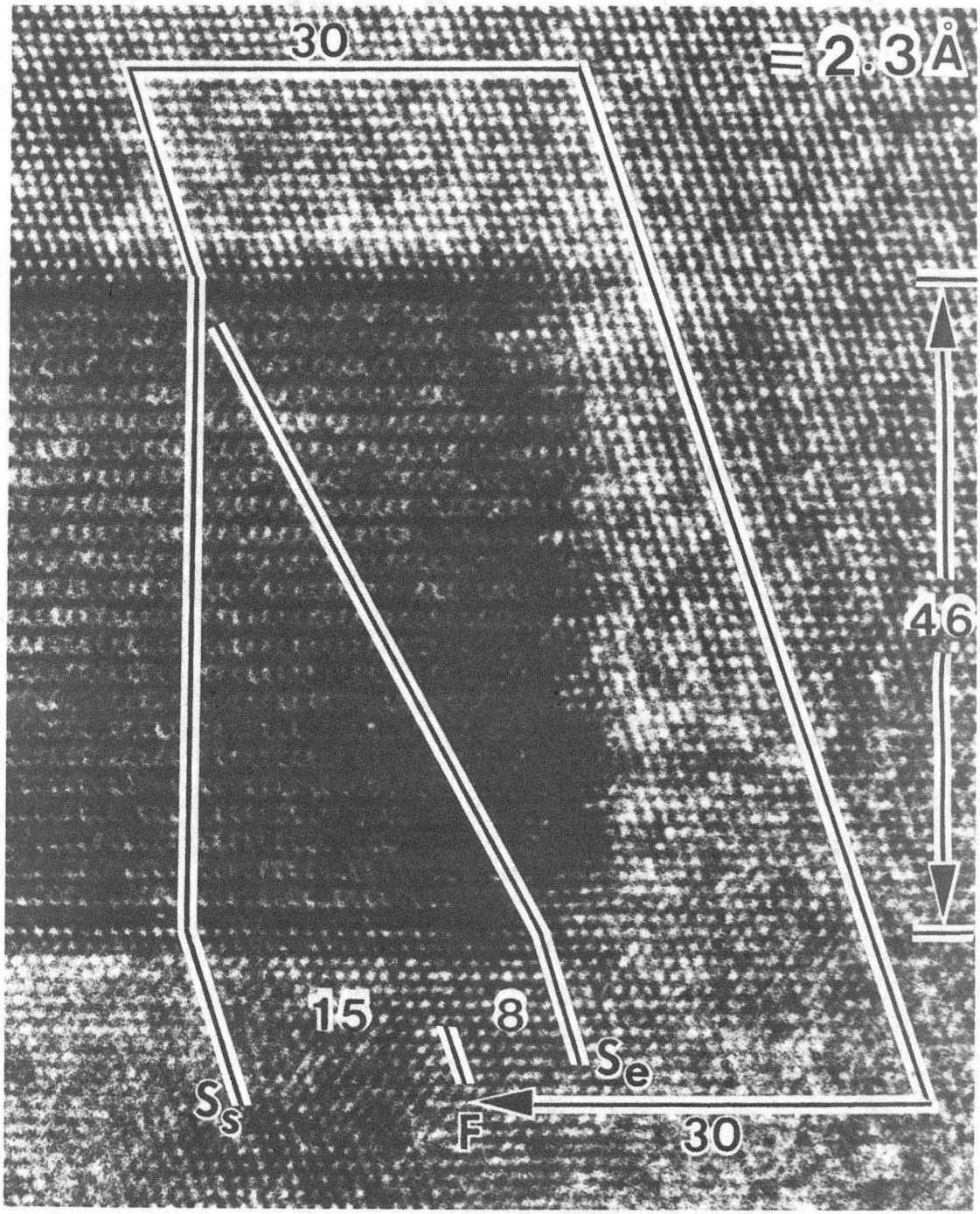

XBB 840-9360

Fig. 27

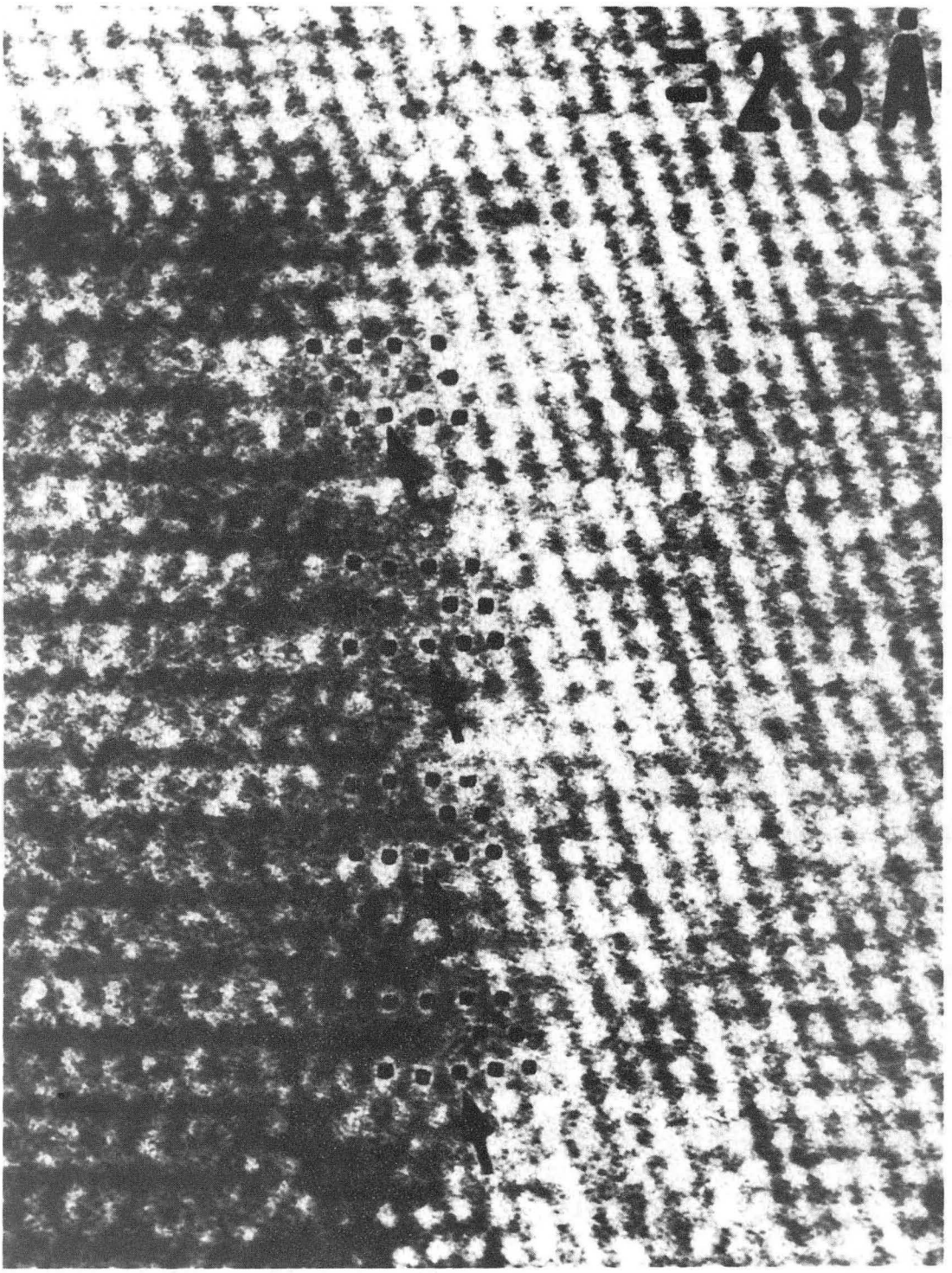

XBB 852-1537

Fig. 28

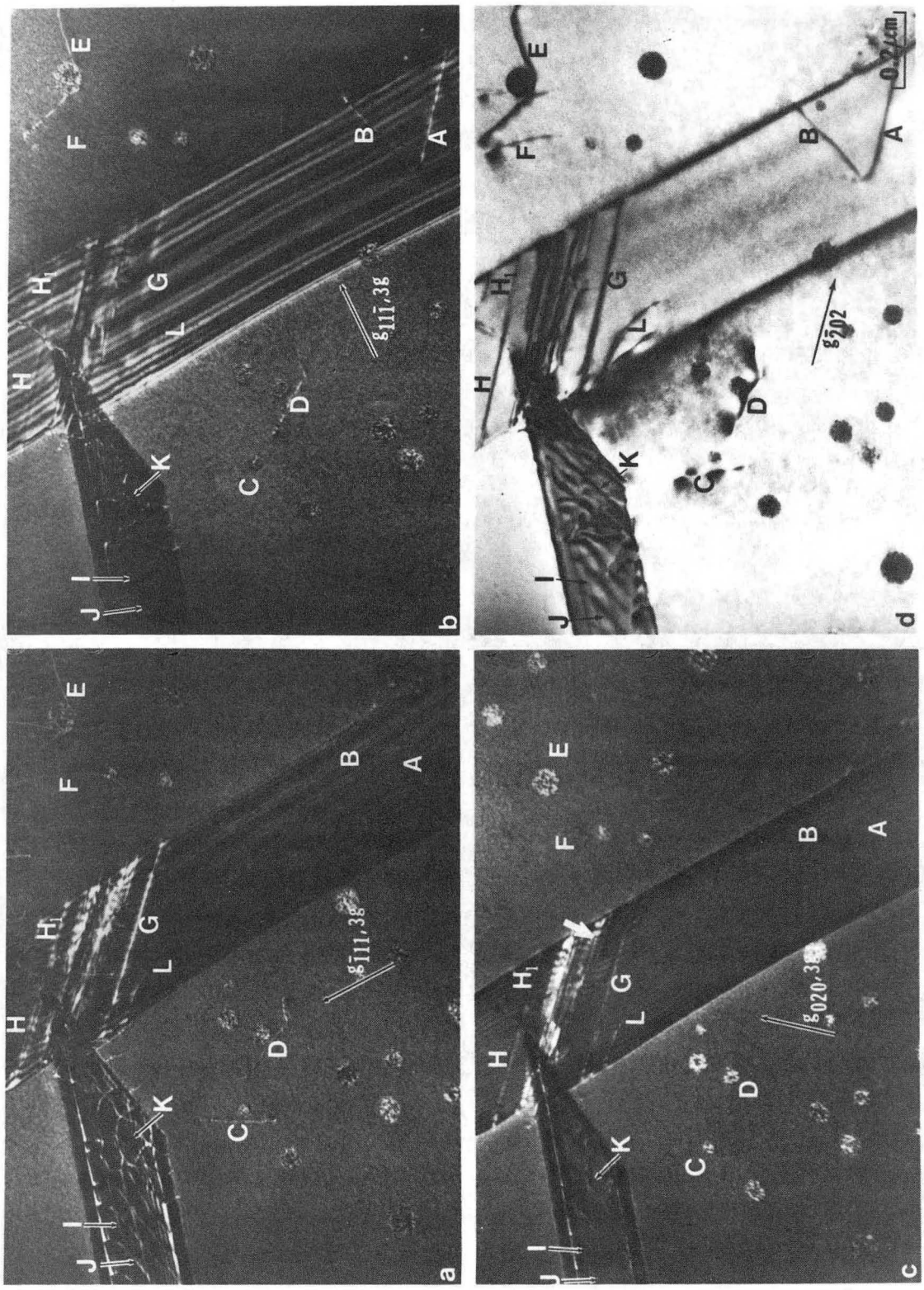

Fig. 29

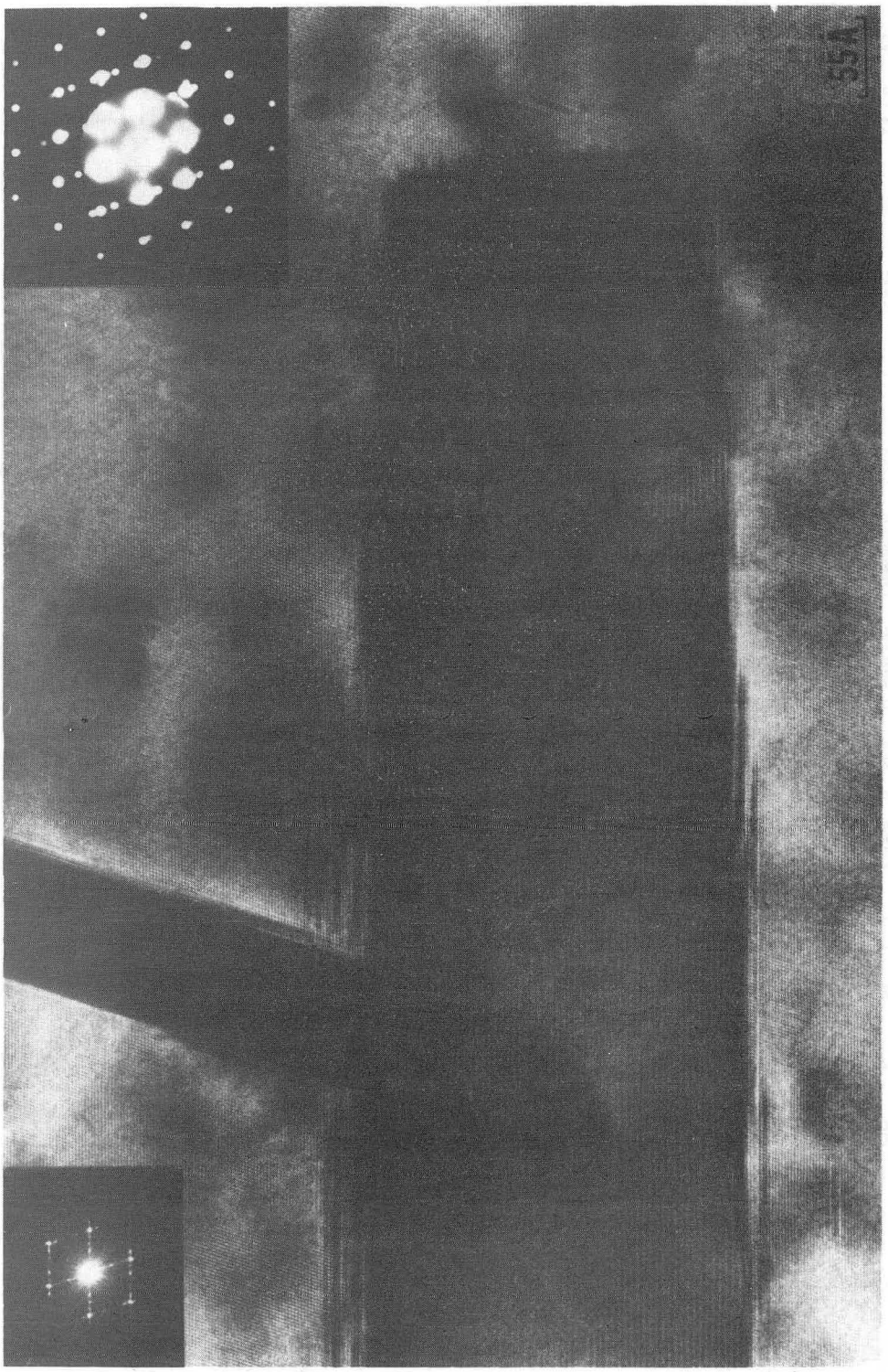

XBB 842-1216

Fig. 30

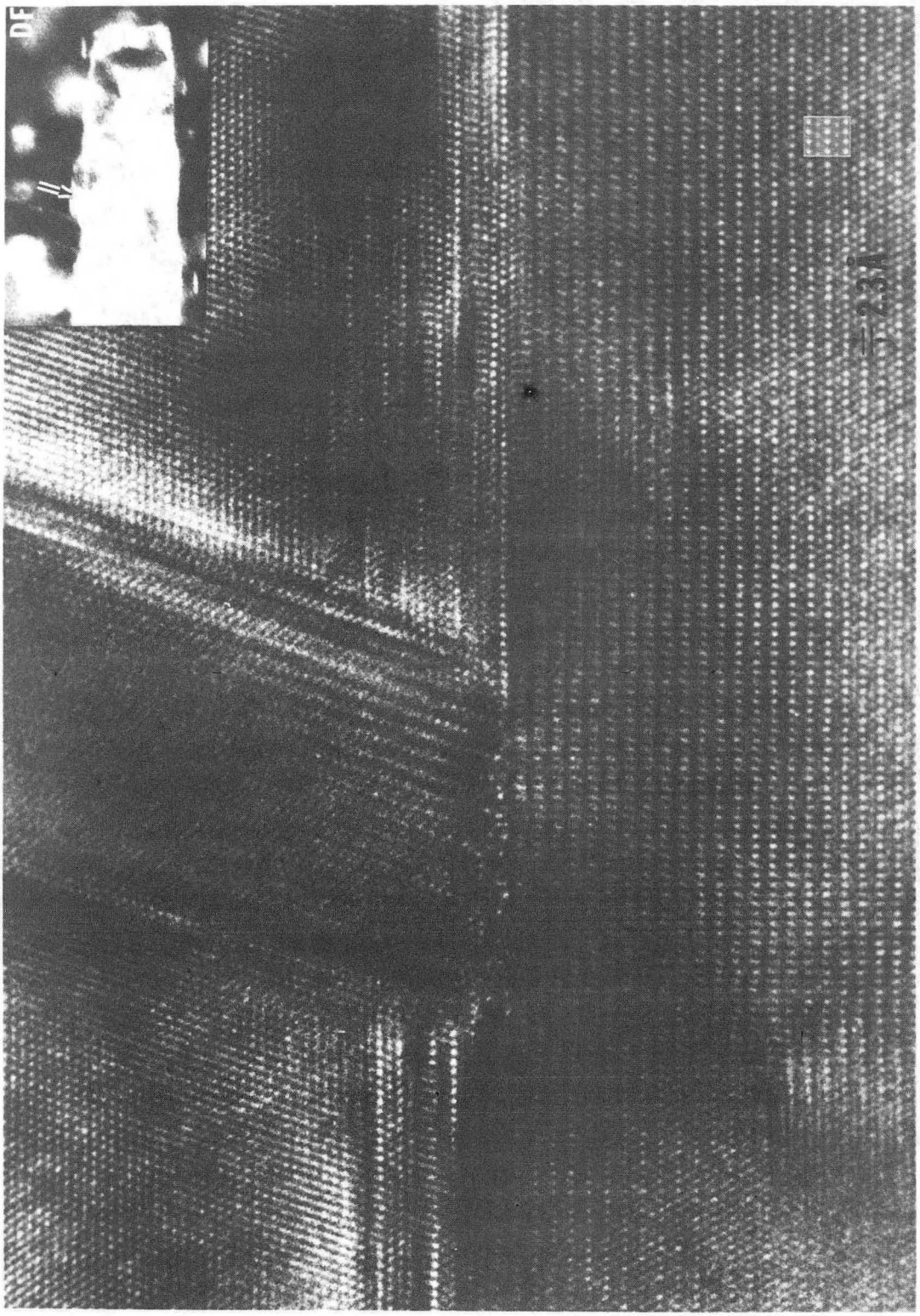

XBB 842-1213

Fig. 31

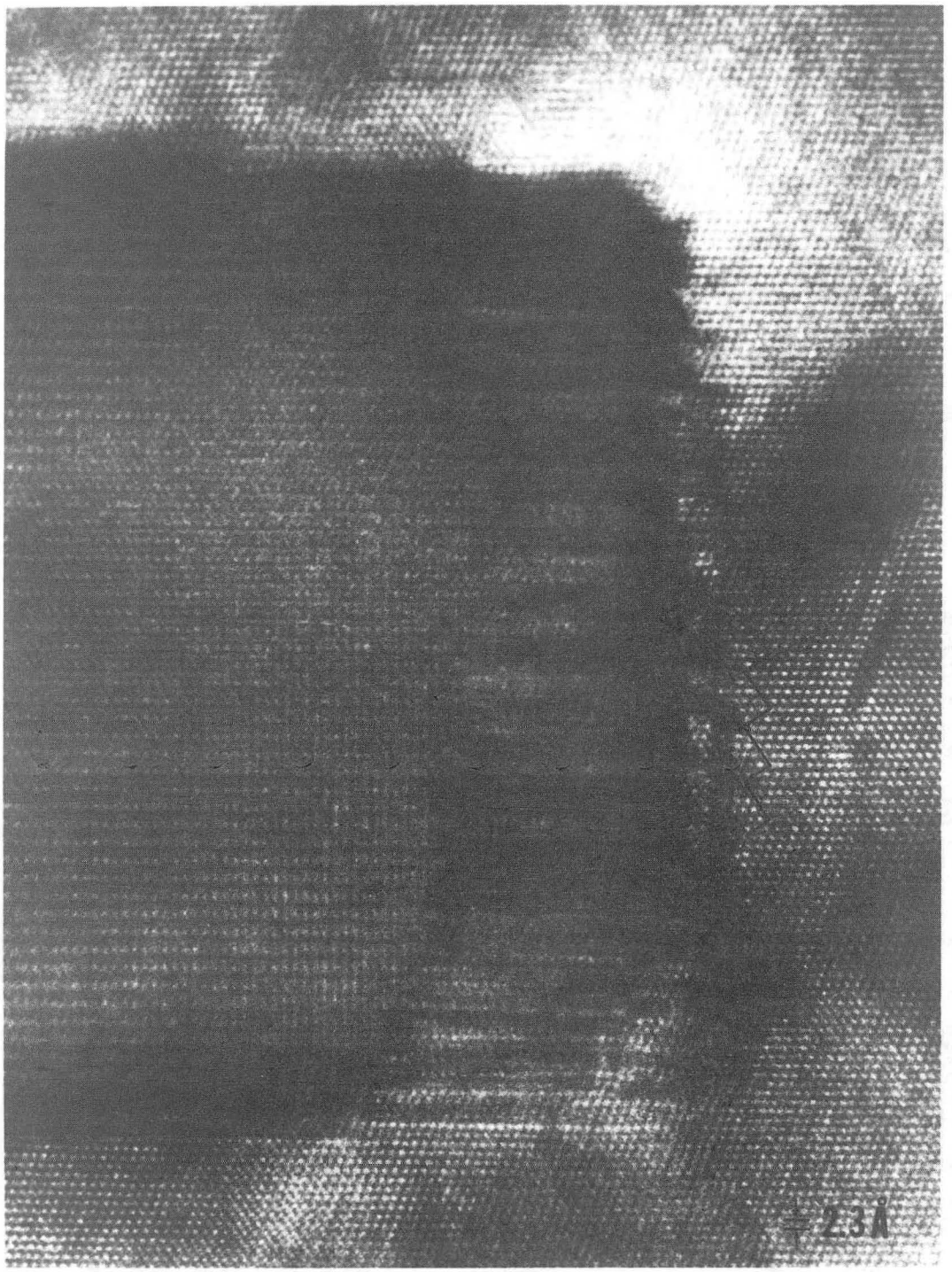

XBB 842-1214

Fig. 32

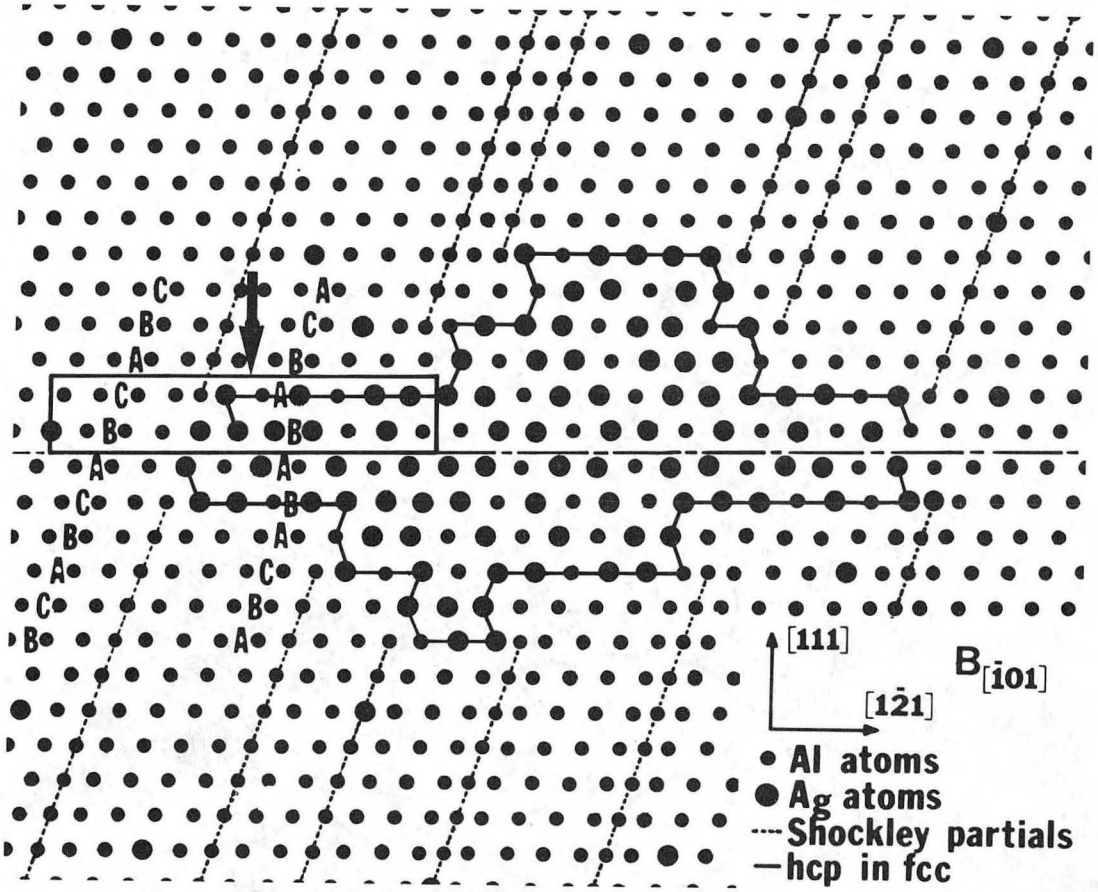

XBL 844-1324

Fig. 33

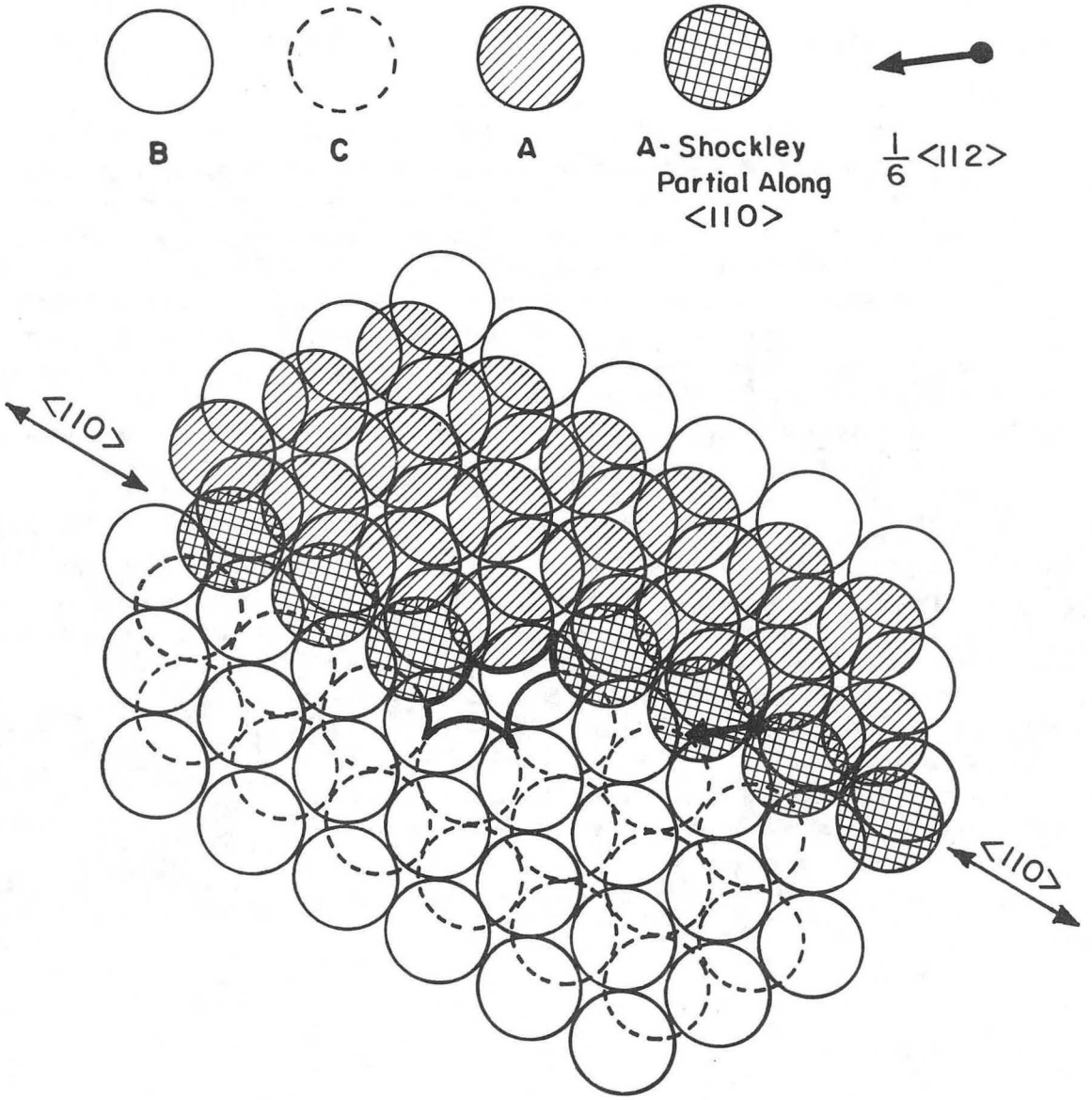

Fig. 34

XBL 835-5723

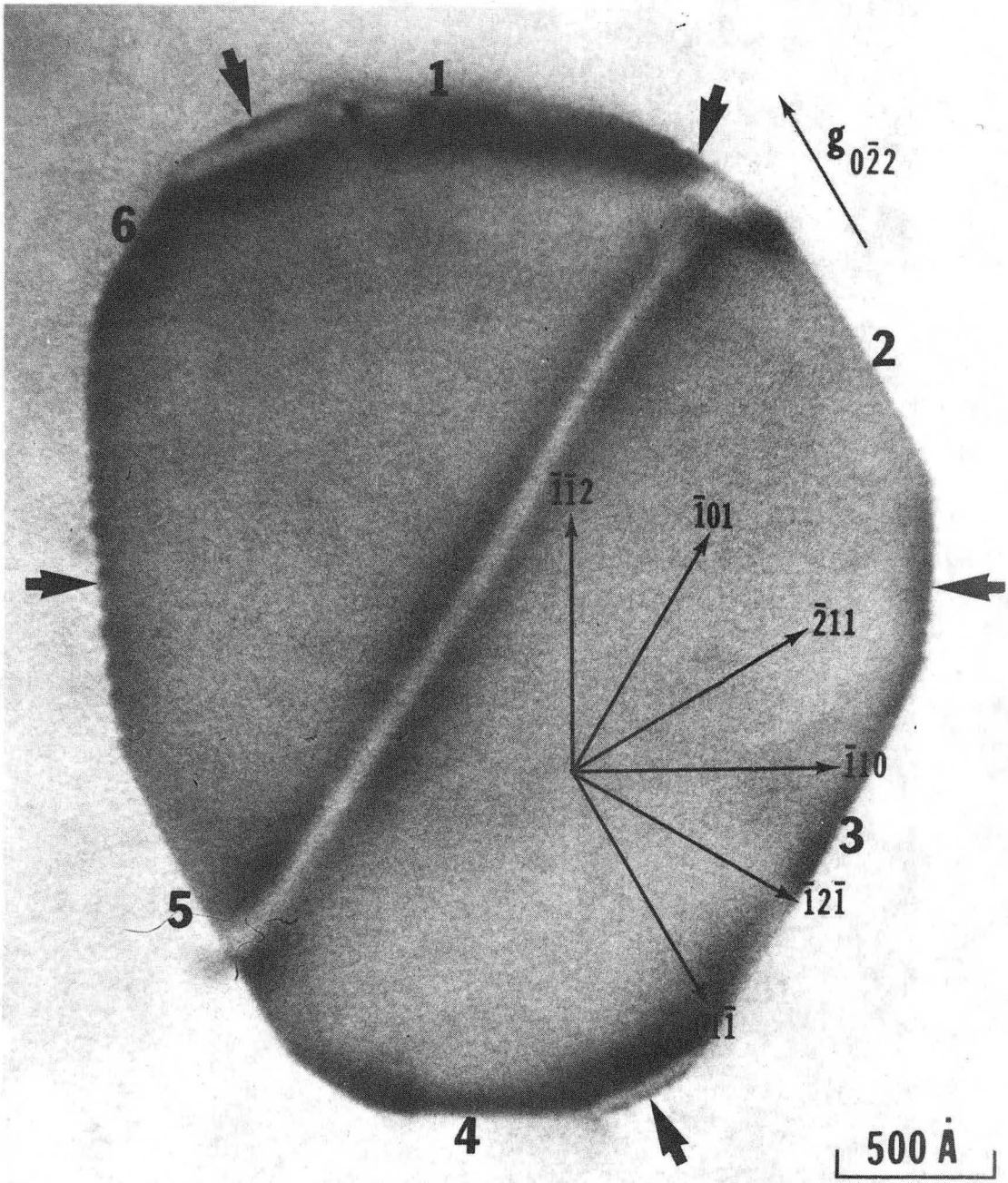

XBB 838-6704

Fig. 35

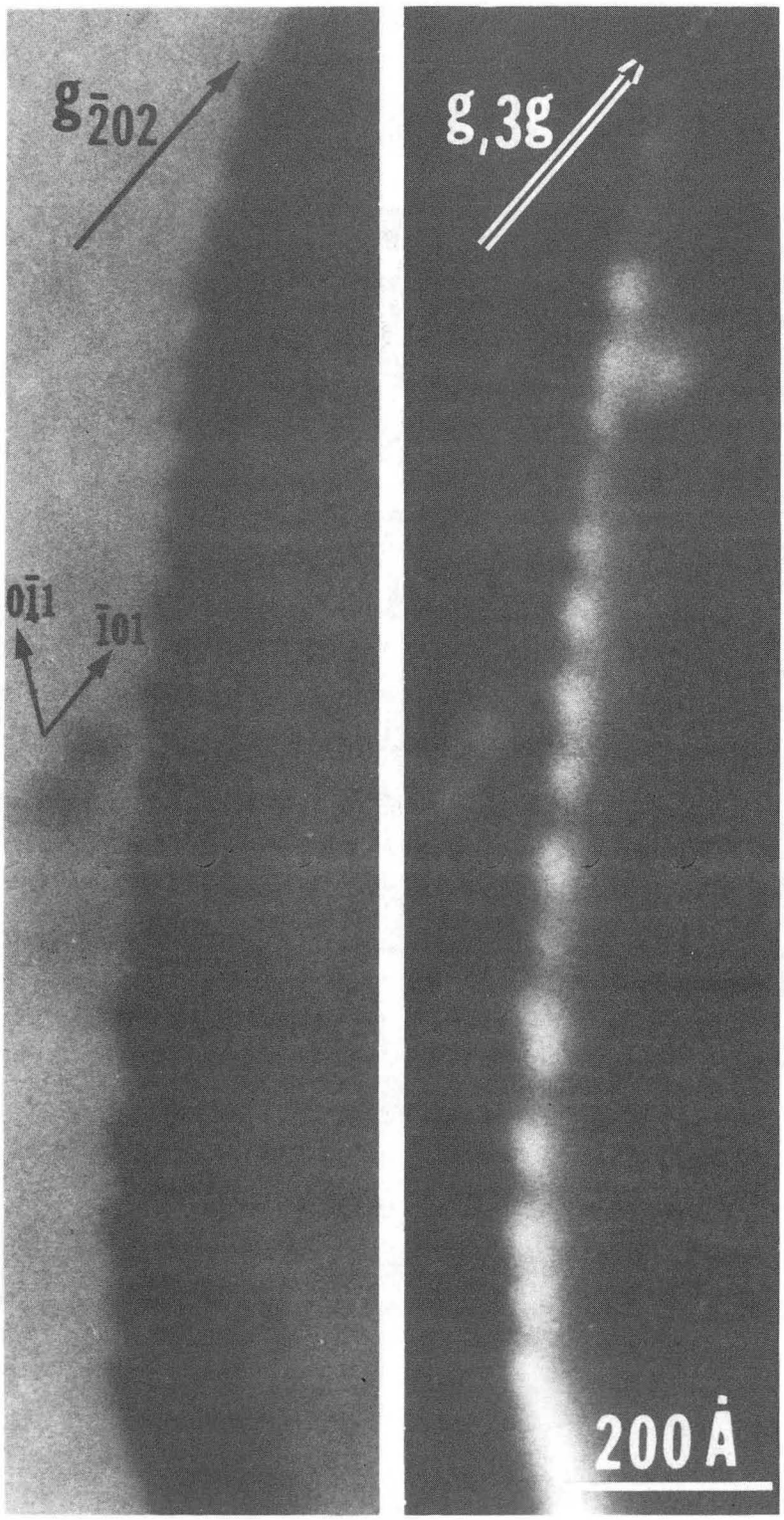

XBB 838-6701

Fig. 36

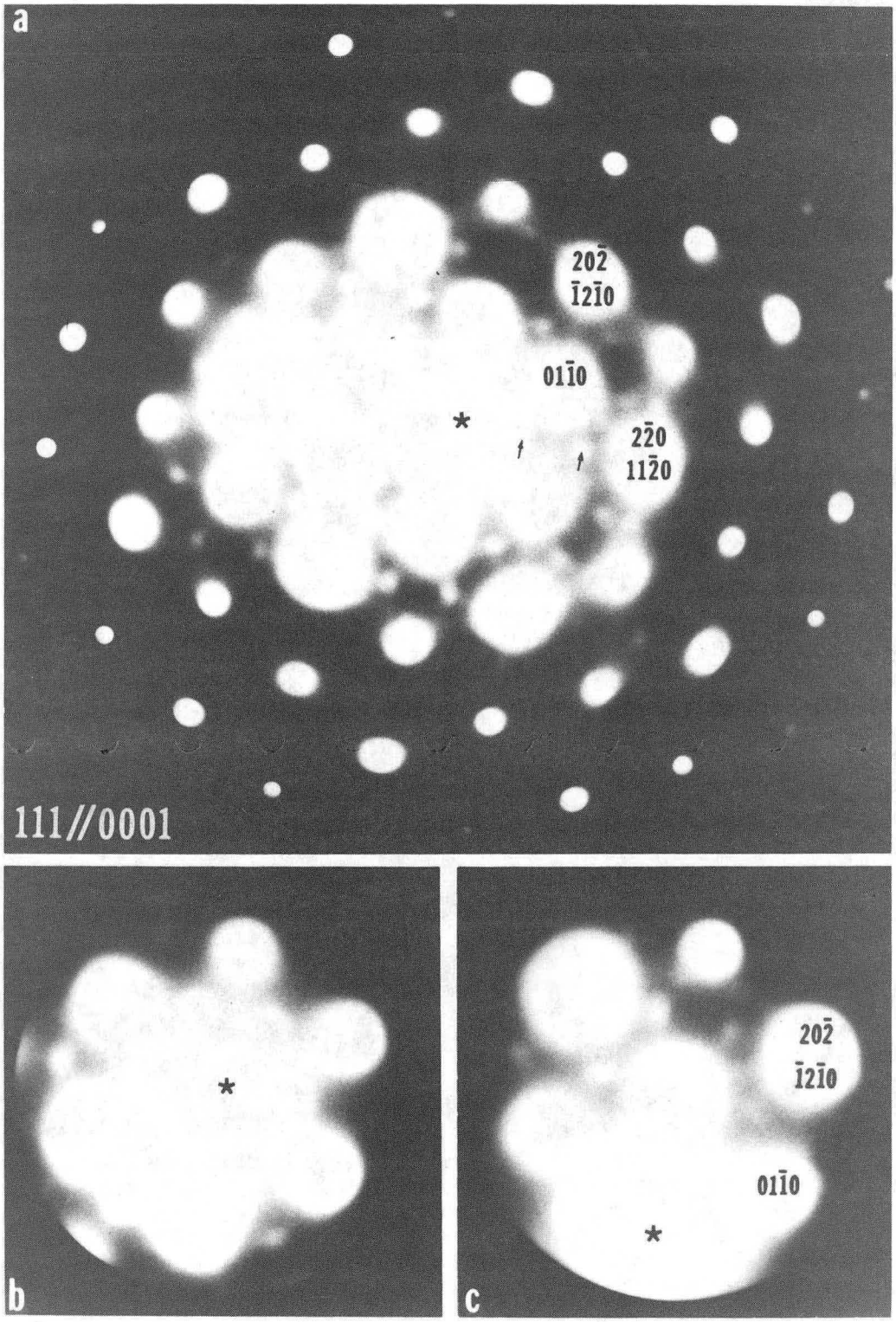

XBB 842-1227

Fig. 37

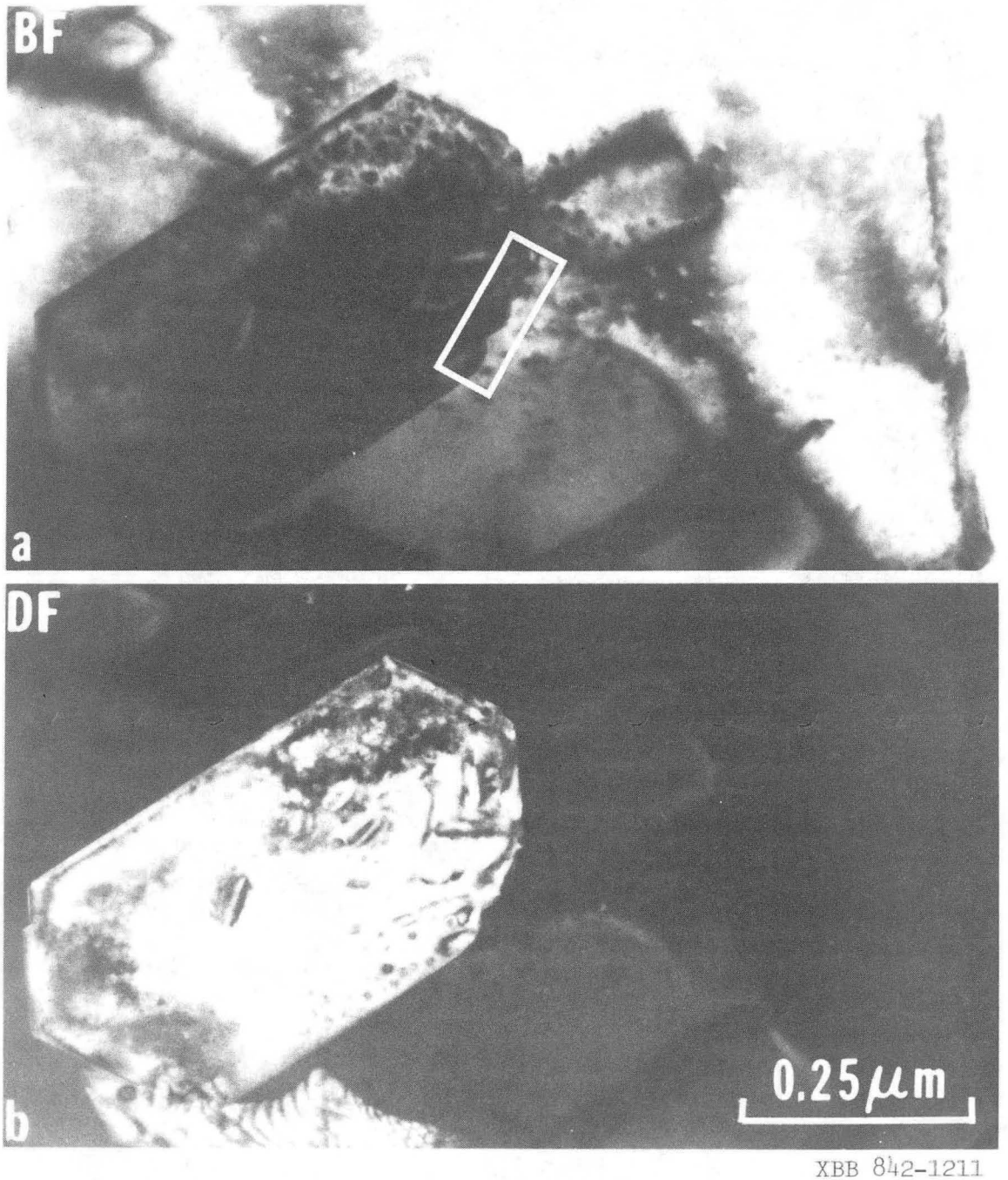

XBB 842-1211

Fig. 38

XBB 842-1225

Fig. 39

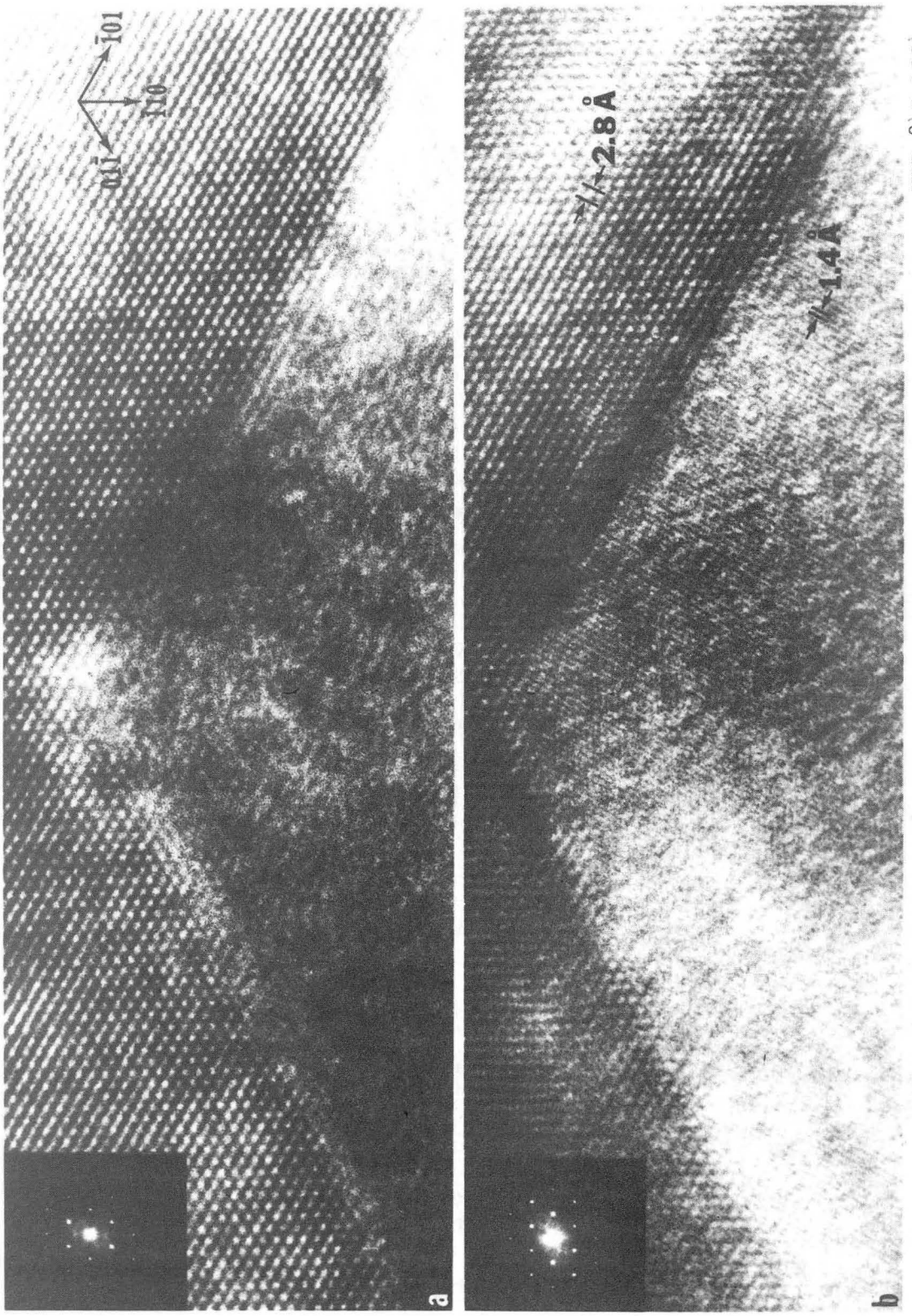

XBB 842-1224

Fig. 40

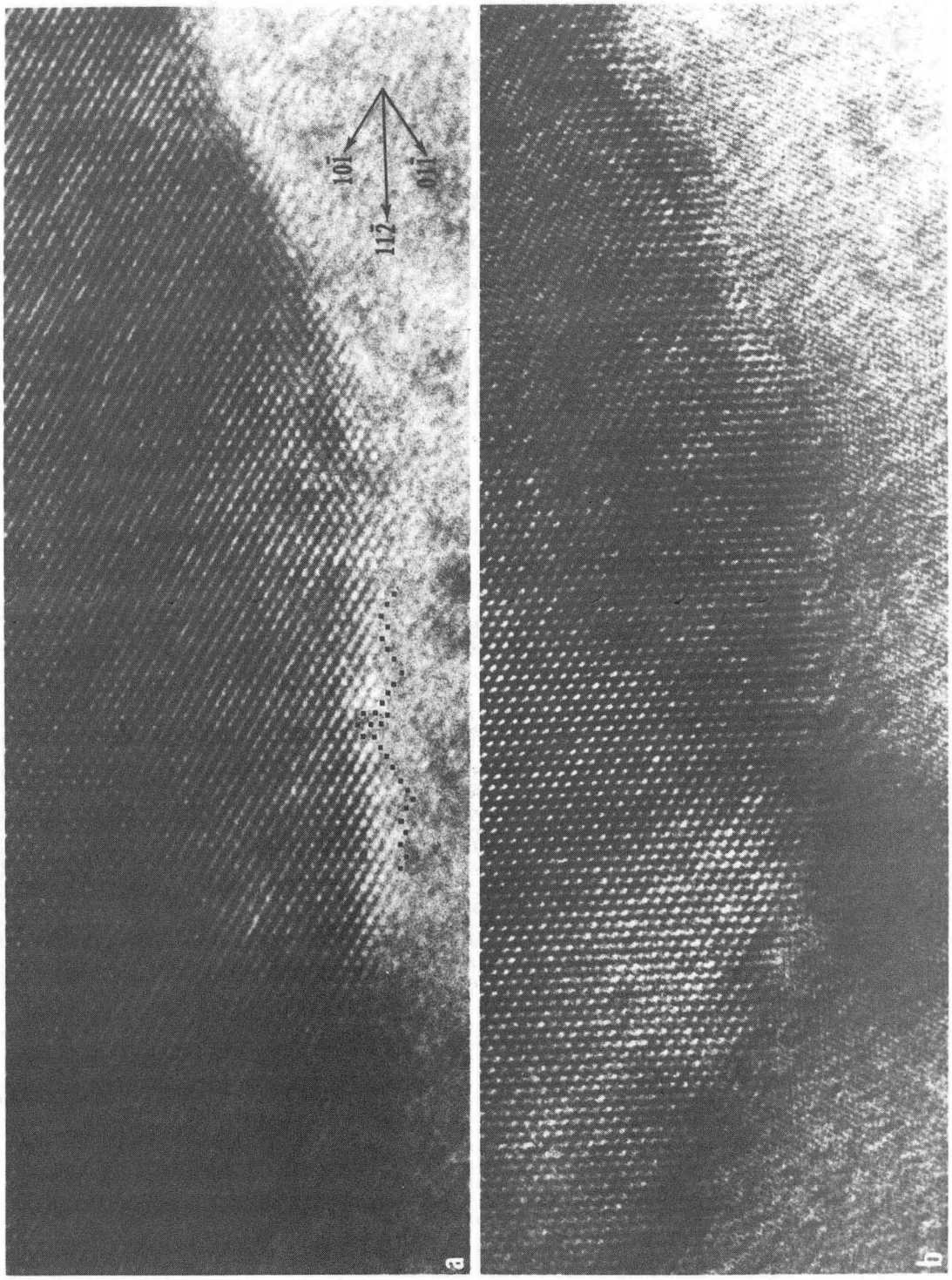

XBB 842-1223

Fig. 41

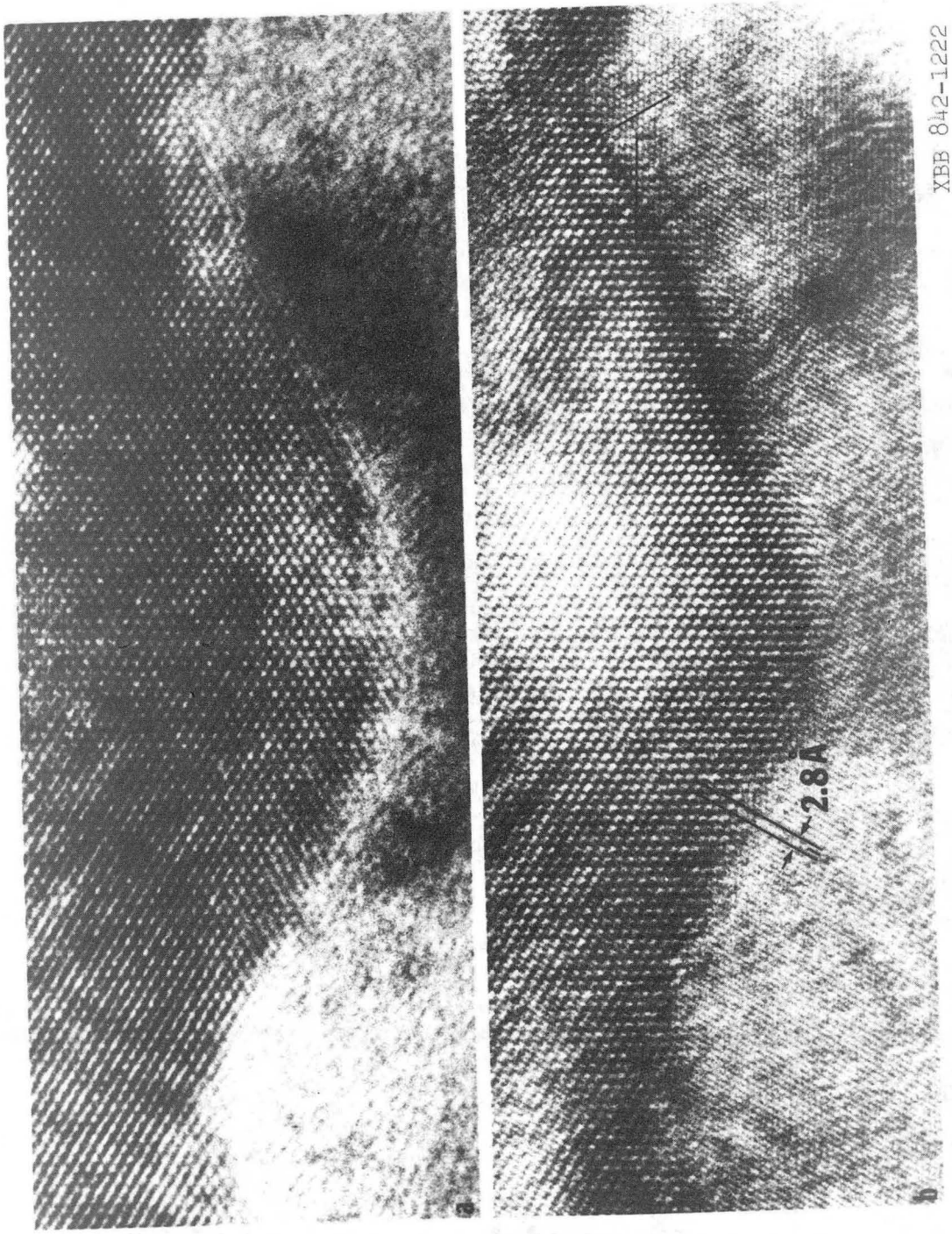

XBB 842-1222

Fig. 42

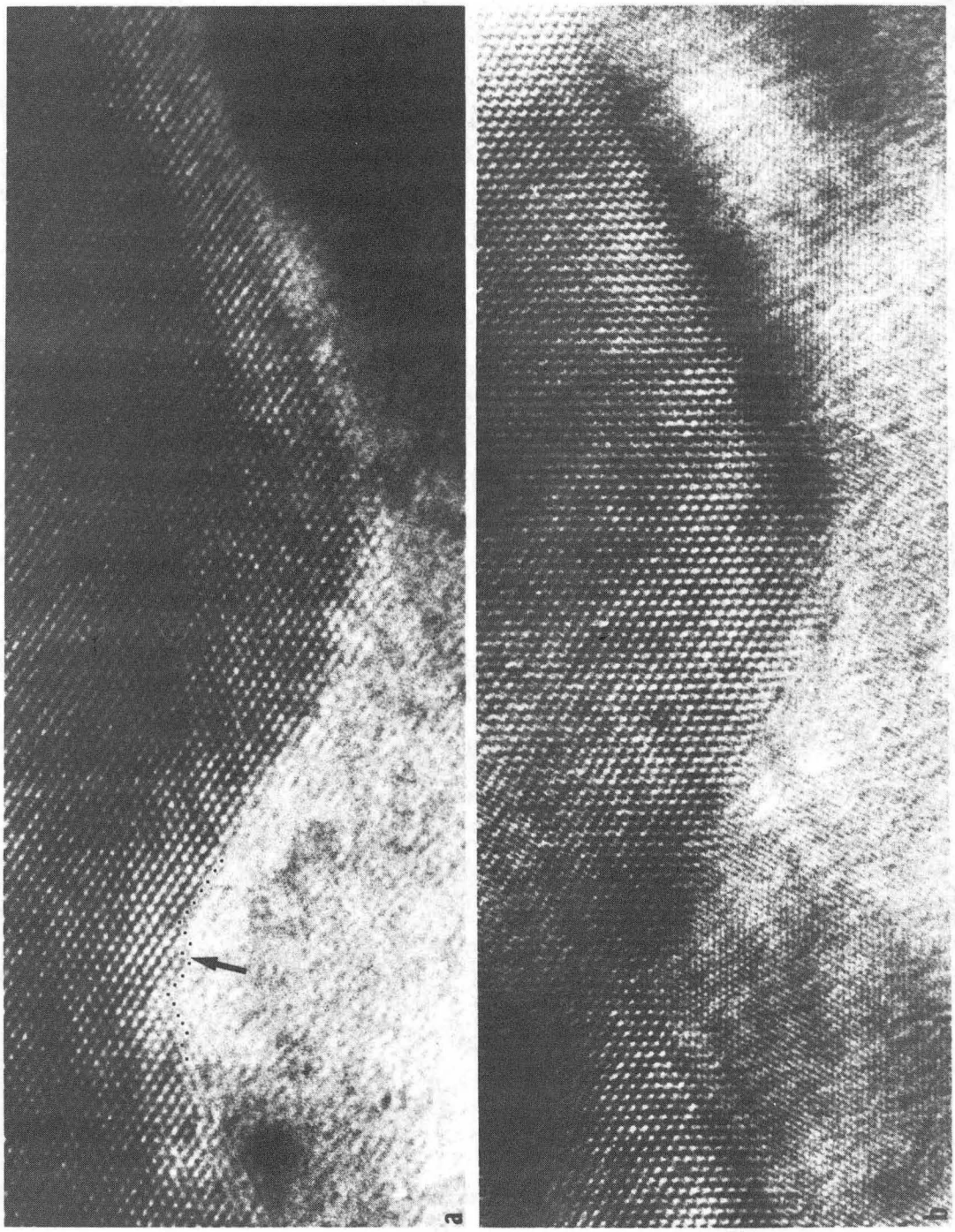

XBB 842-1221

Fig. 43

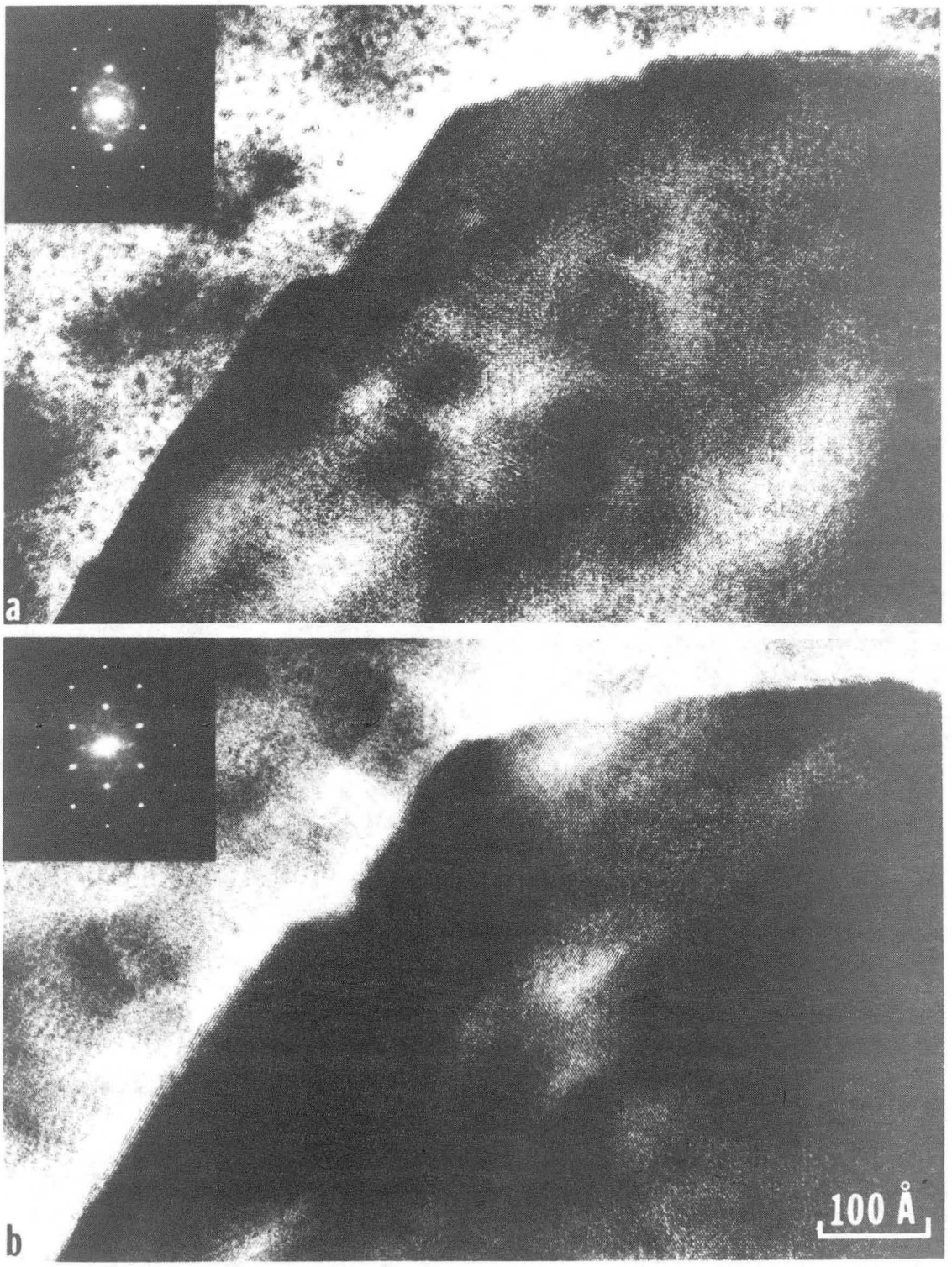

XBB 842-1220

Fig. 44

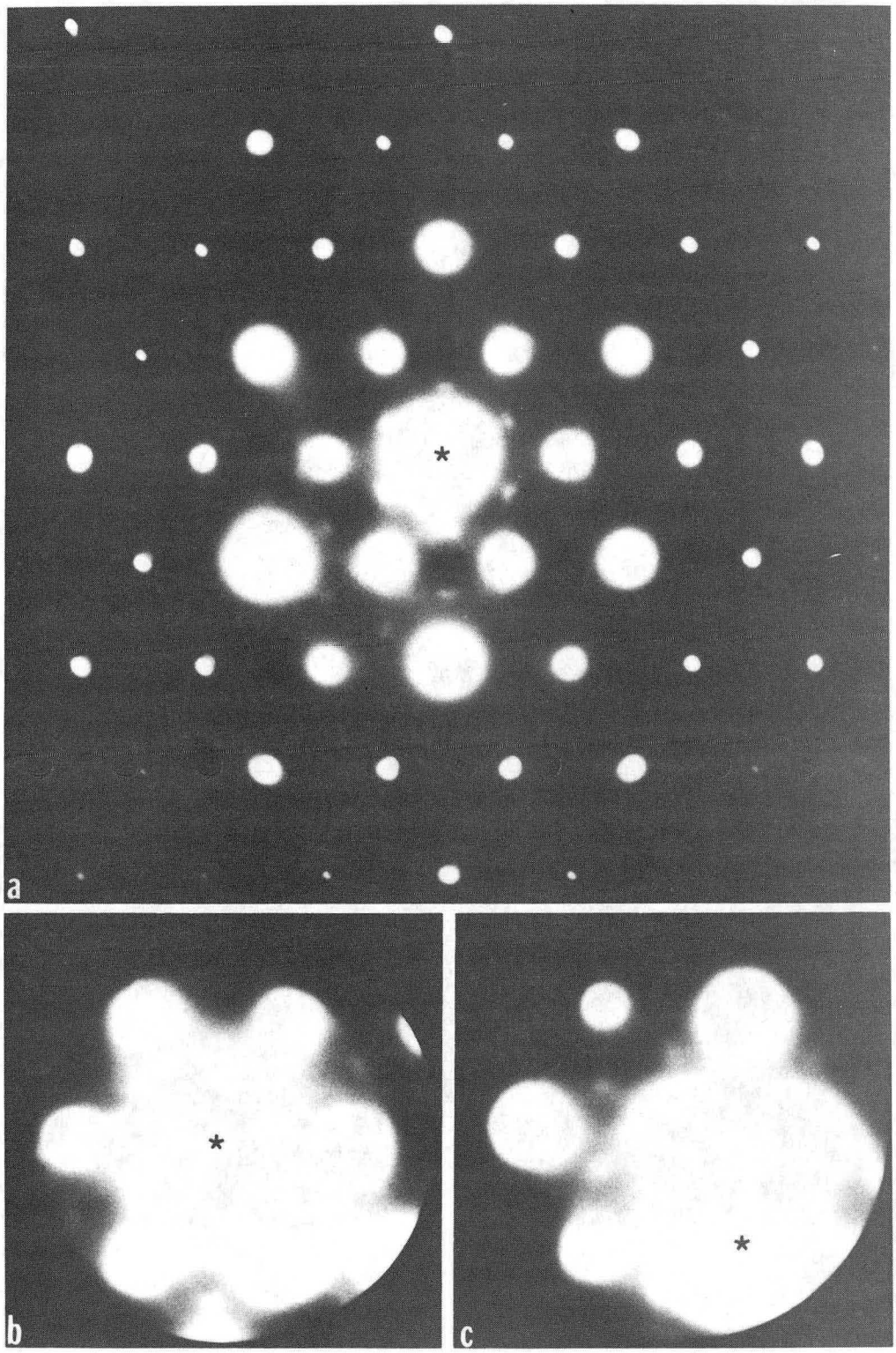

XBB 843-2517

Fig. 45

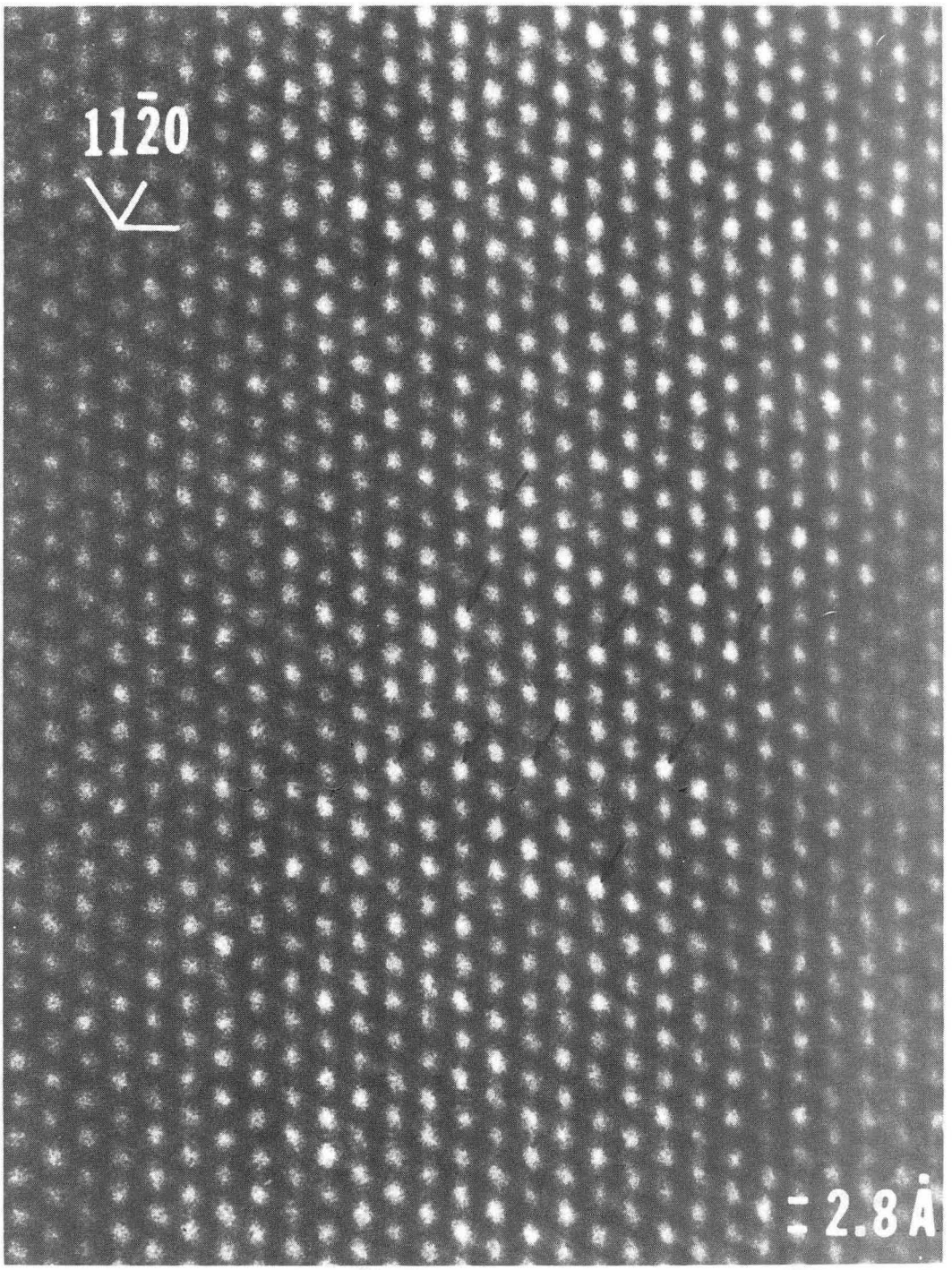

XBB 852-1538

Fig. 46

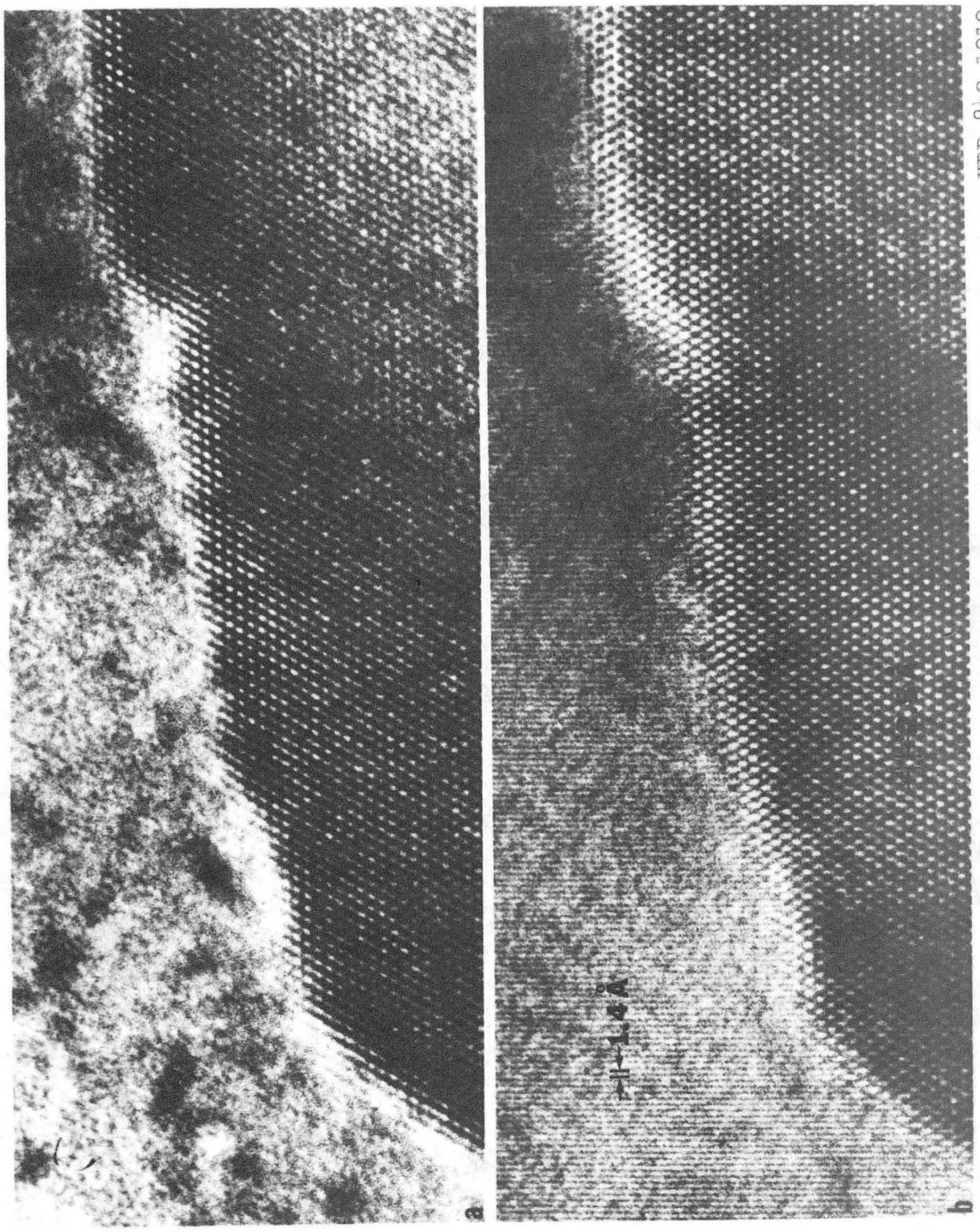

XBB 842-1219

Fig. 47

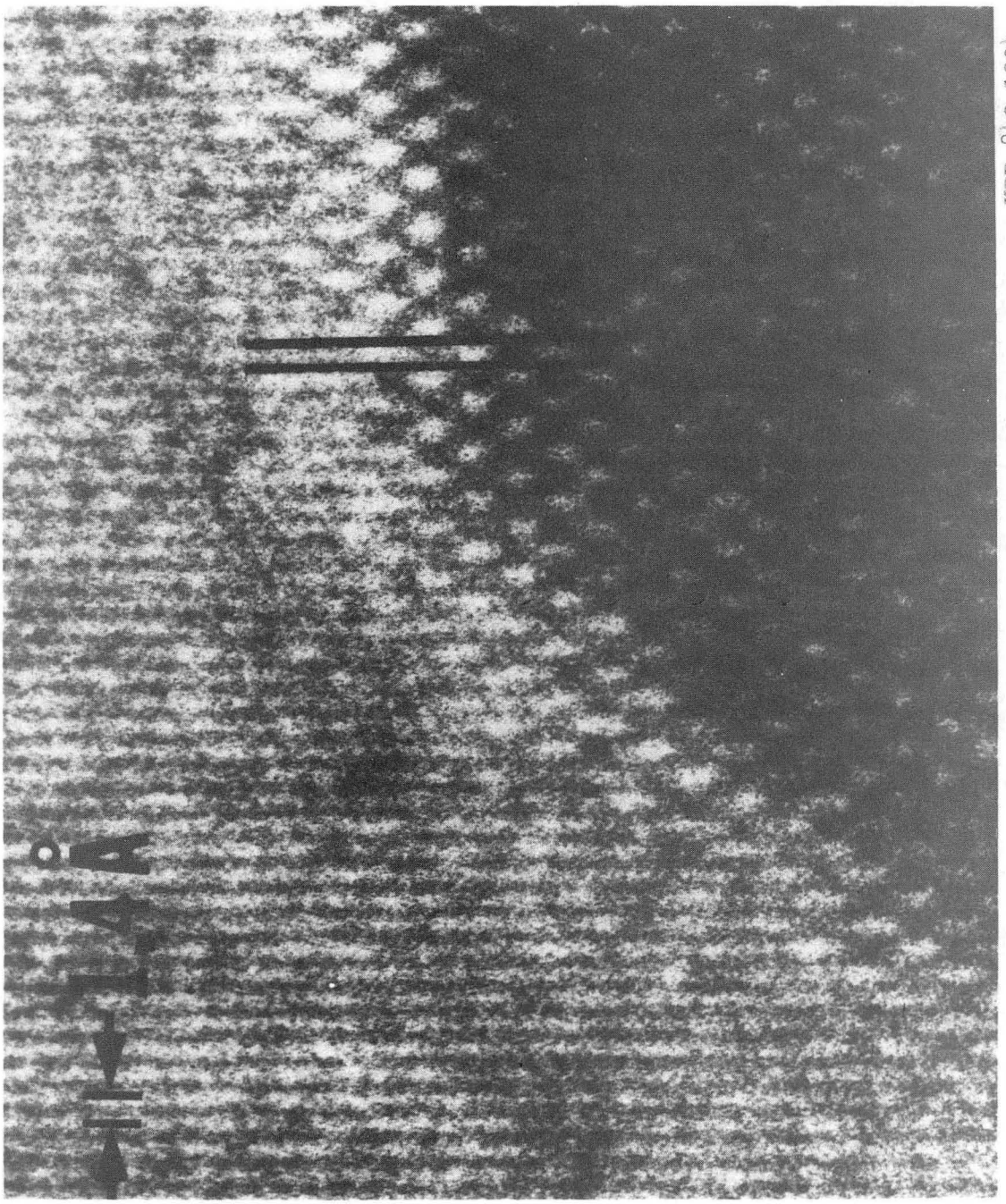

XBB 842-1204

Fig. 48

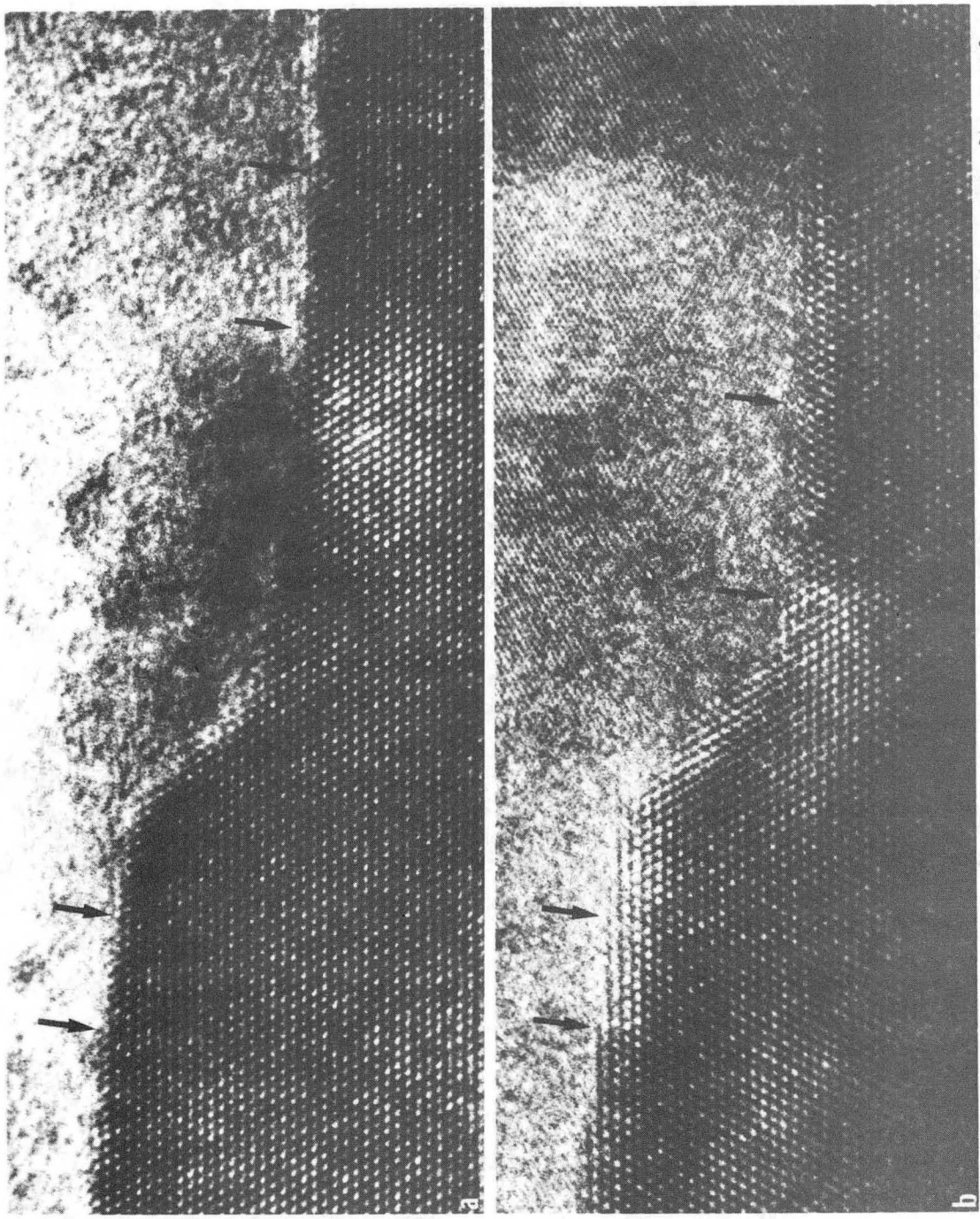

XBB 842-1218

Fig. 49

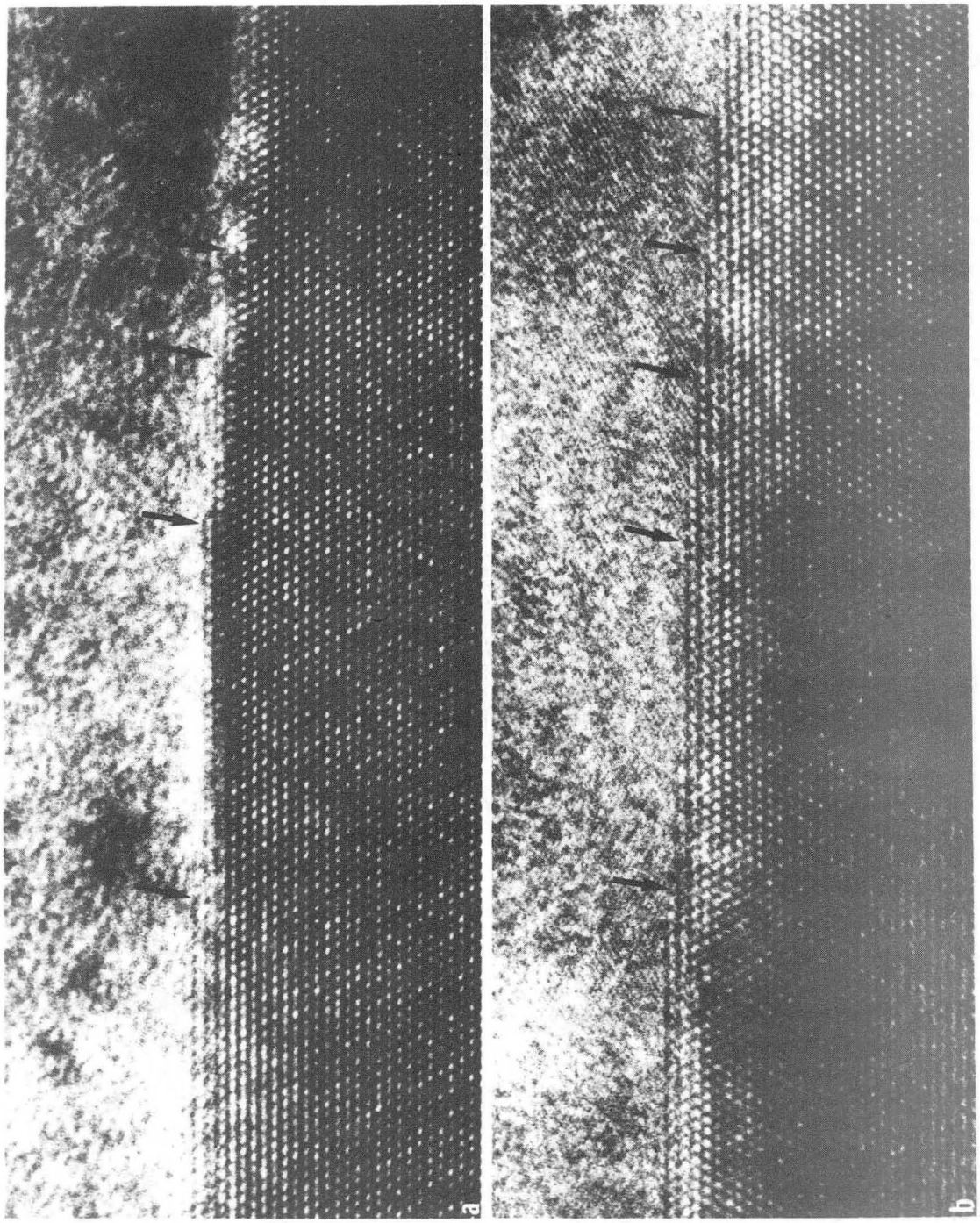

XBB 842-1217

Fig. 50

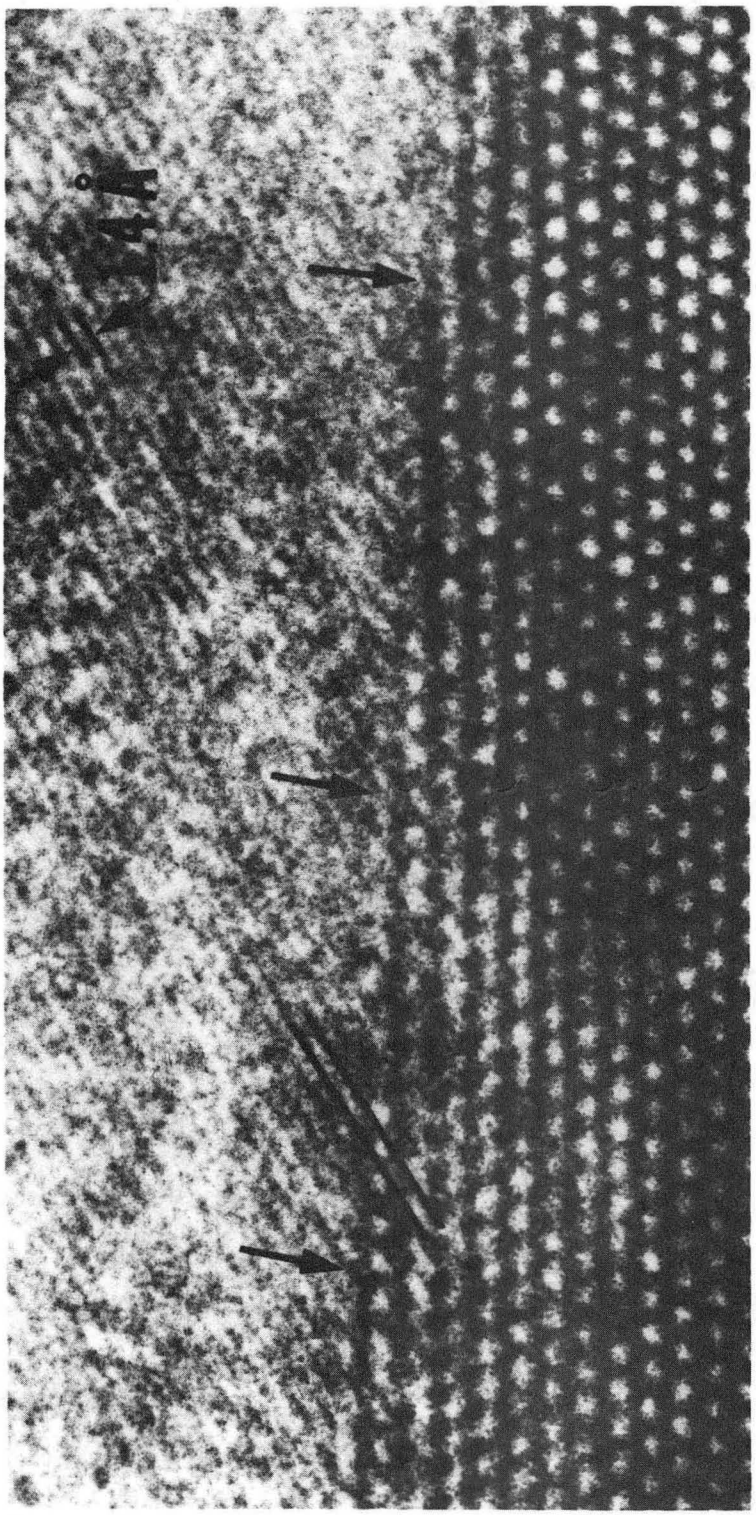

XBB 842-1205

Fig. 51

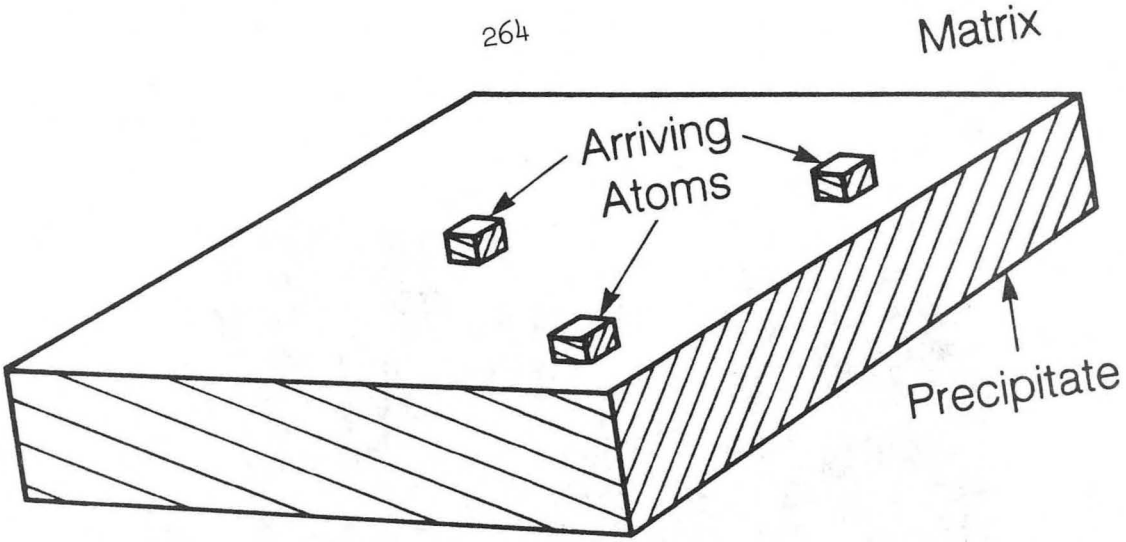

(a)

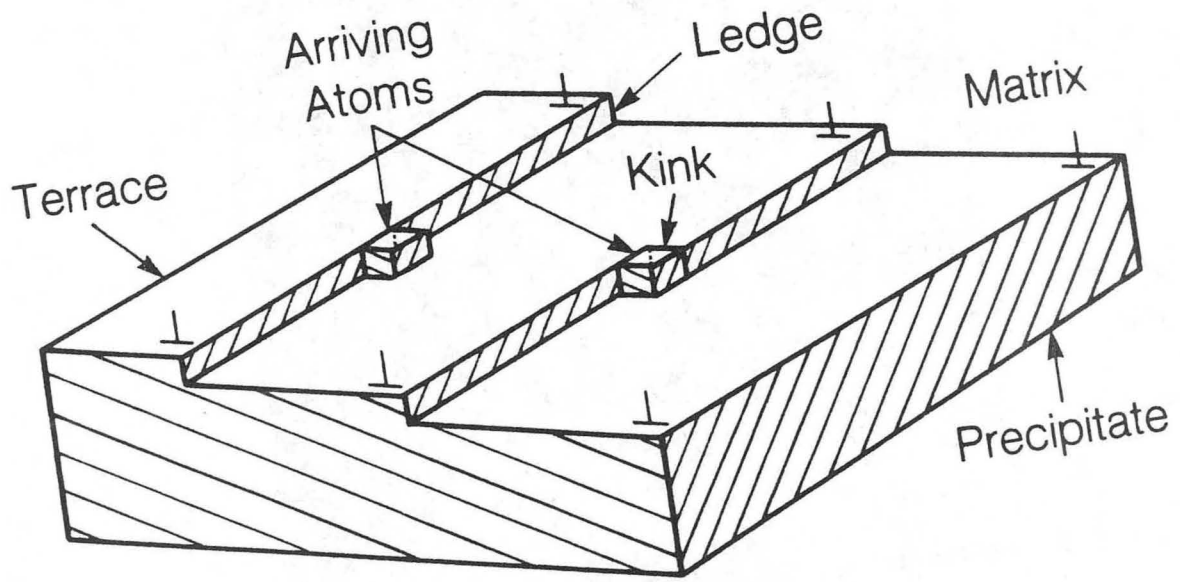

(b)

Fig. 52

XBL 835-5724A

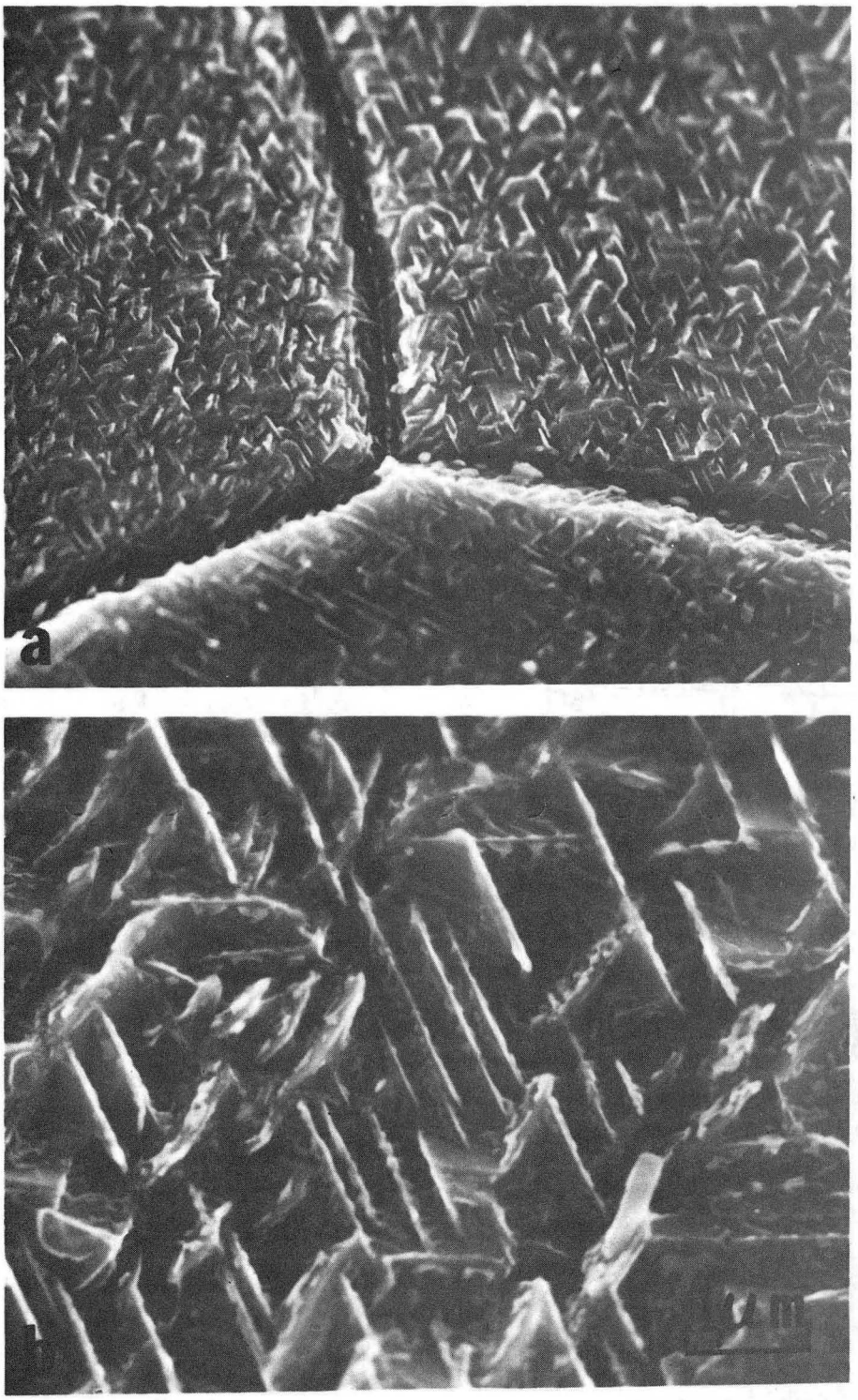

XBB 849-7085

Fig. 52

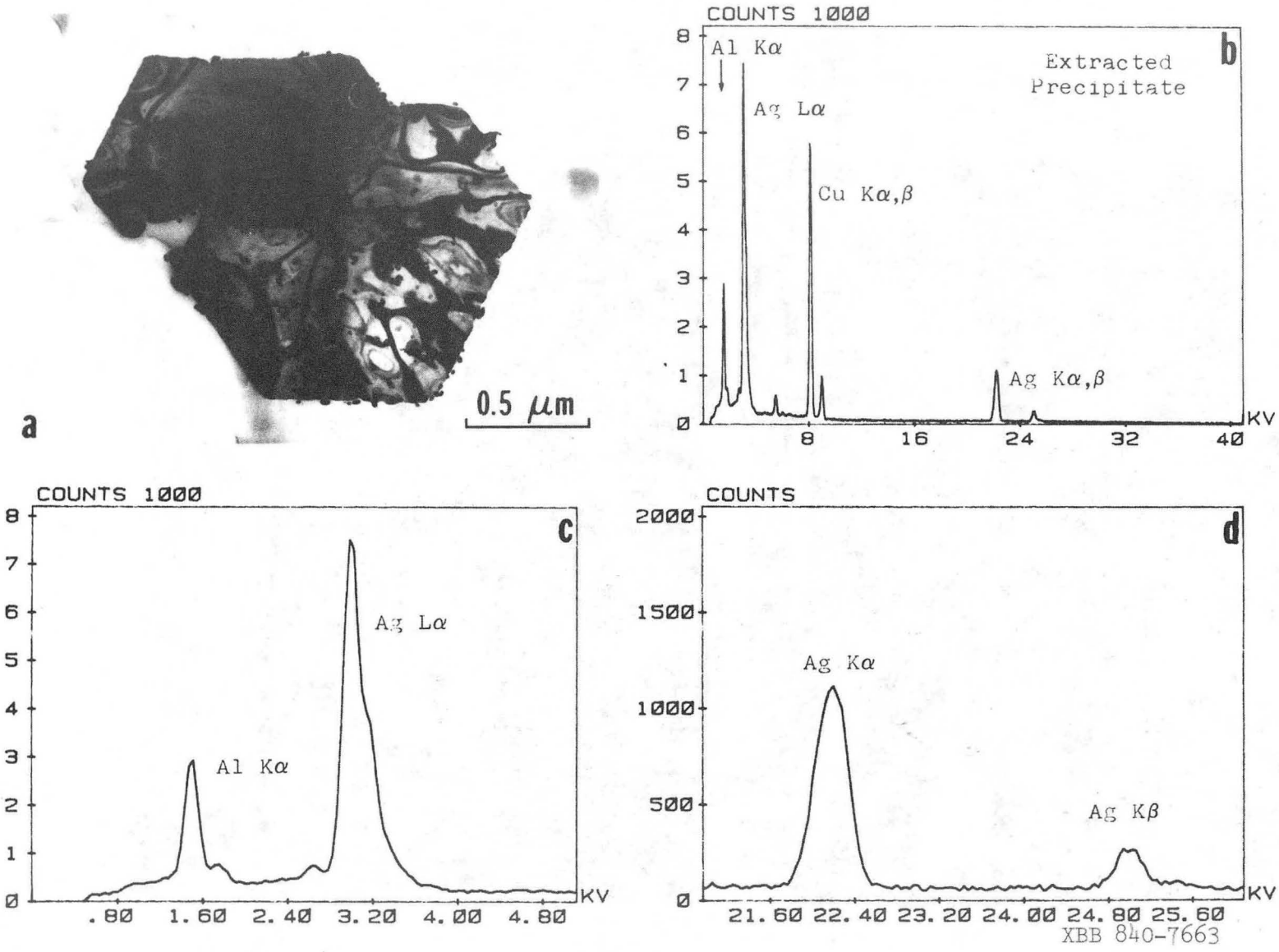
a
0.5 μm
COUNTS 1000
b
Extracted
Precipitate
Al Kα
Ag Lα
Cu Kα,β
Ag Kα,β
KV
COUNTS 1000
c
Ag Lα
Al Kα
KV
COUNTS
d
Ag Kα
Ag Kβ
KV
XBB 840-7663

Fig. 54

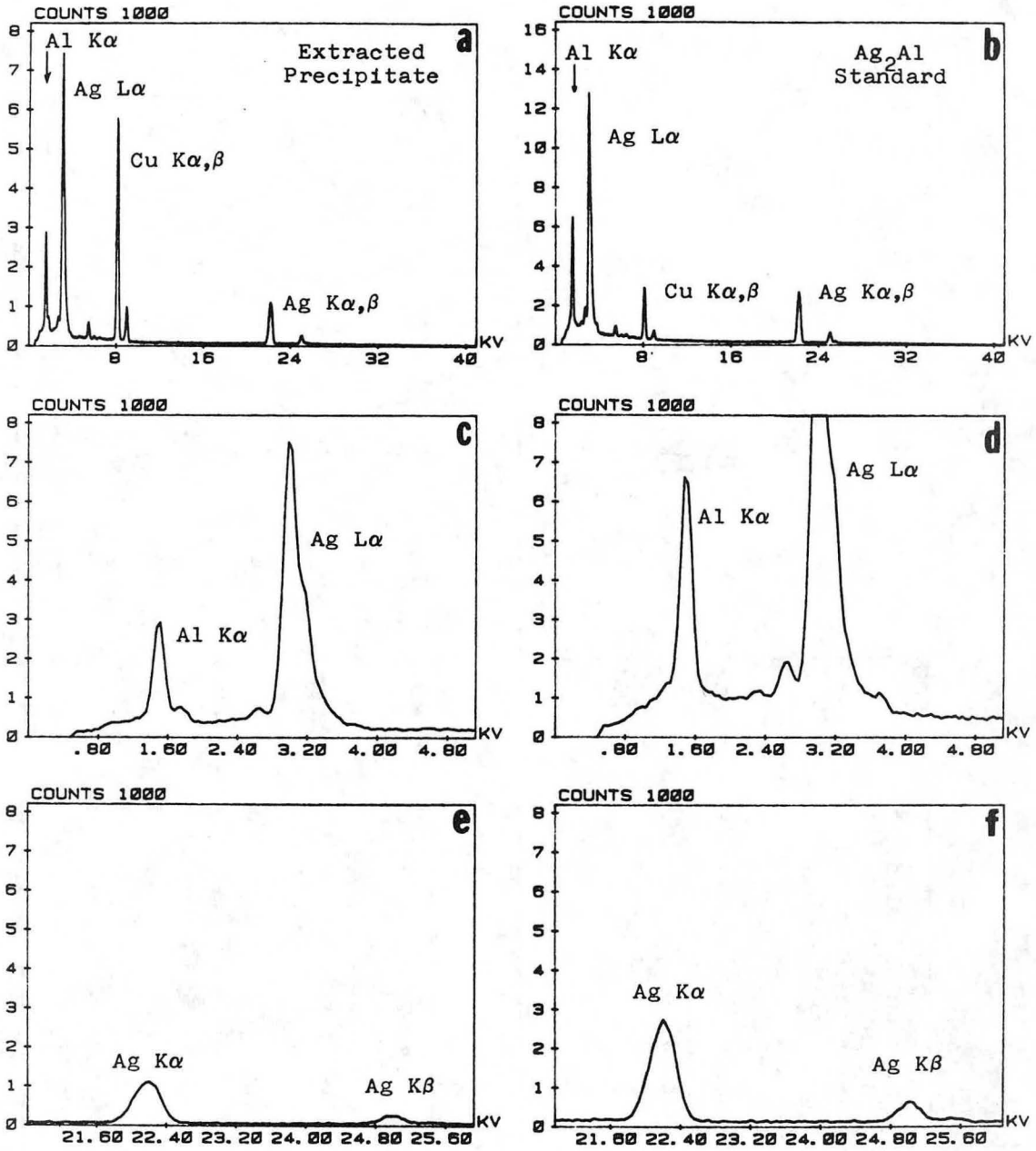

XBL 8410-4157

Fig. 55

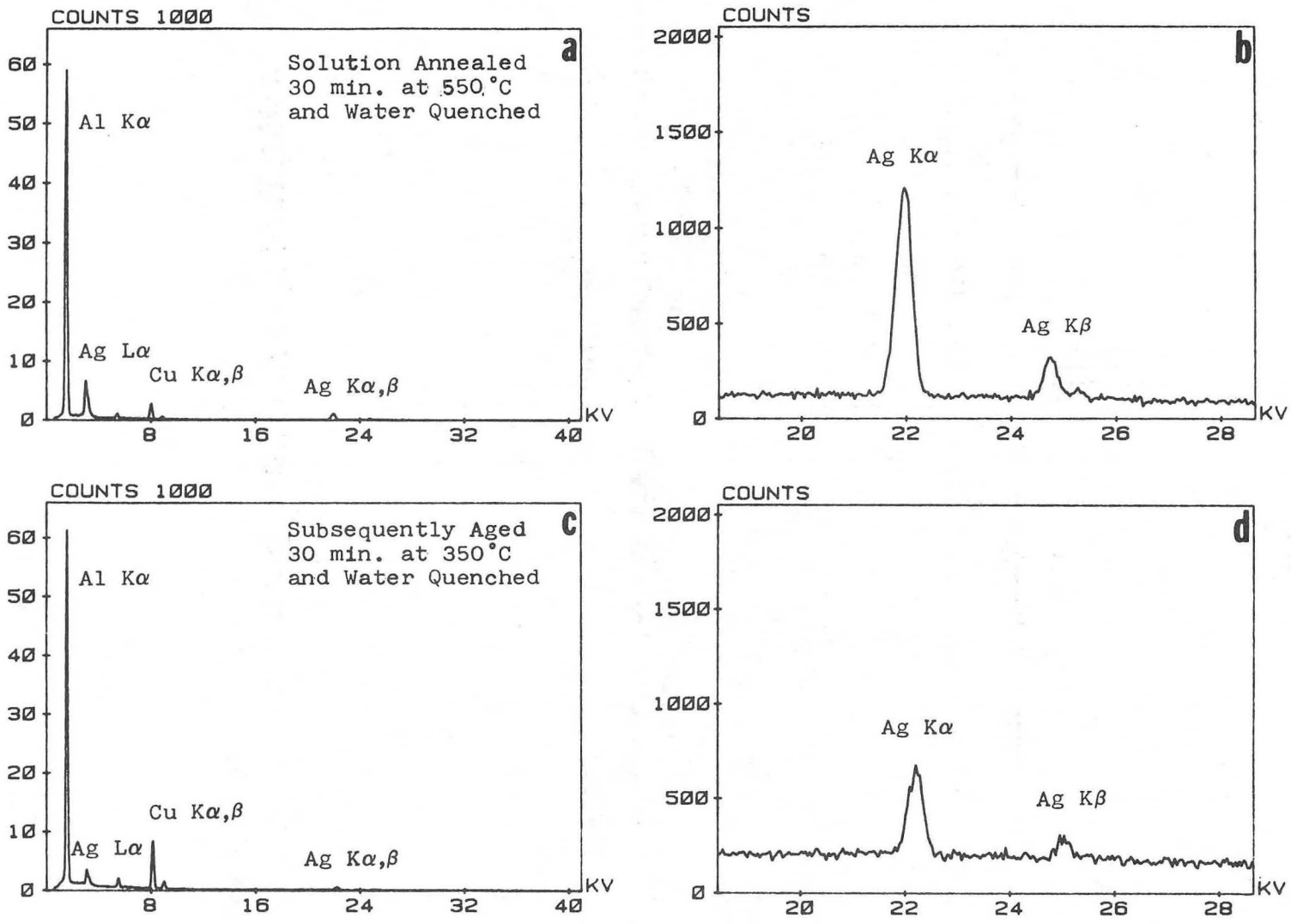

Fig. 56

XBL 8410-4156

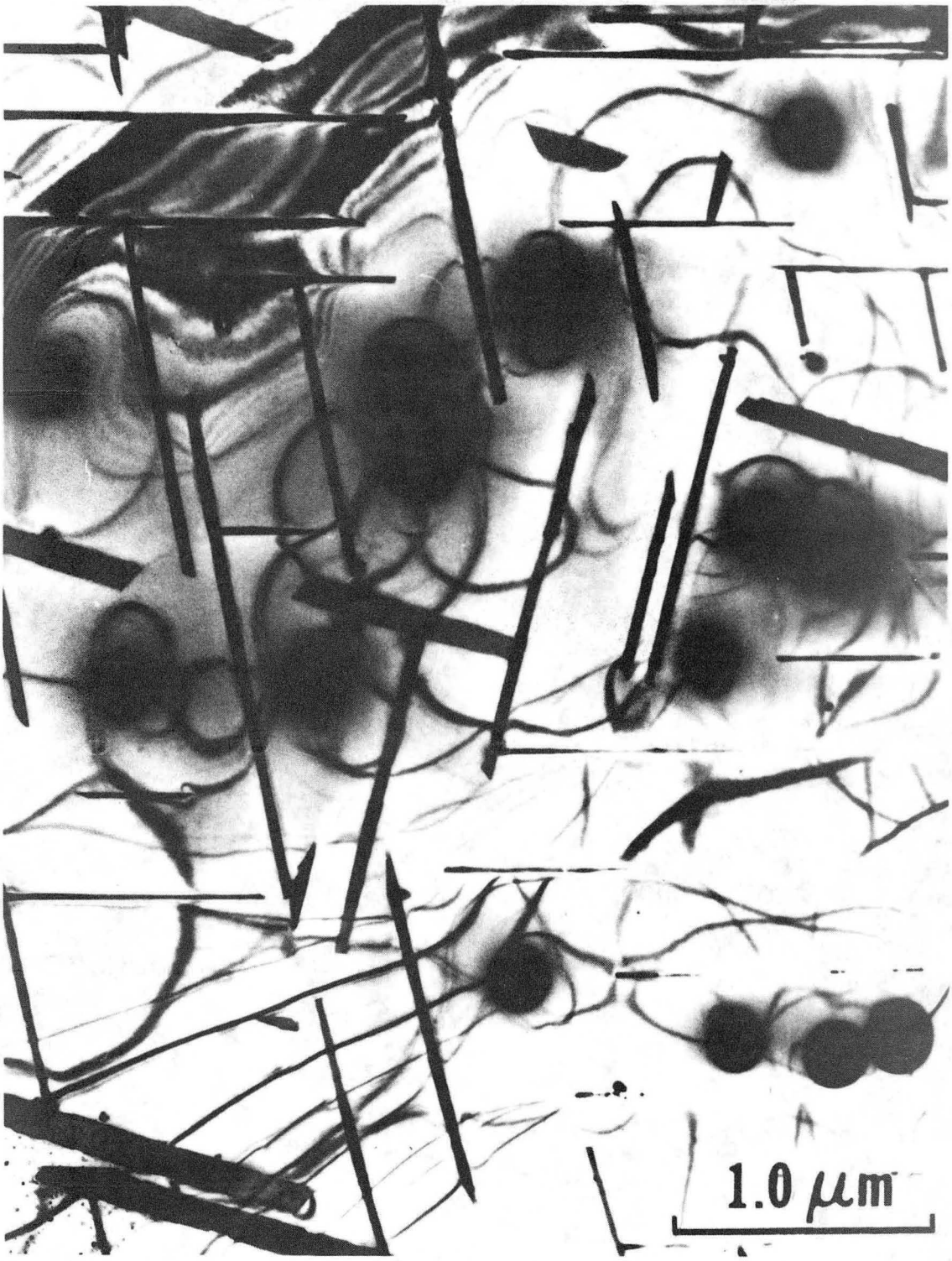

XBB 840-7653

Fig. 57

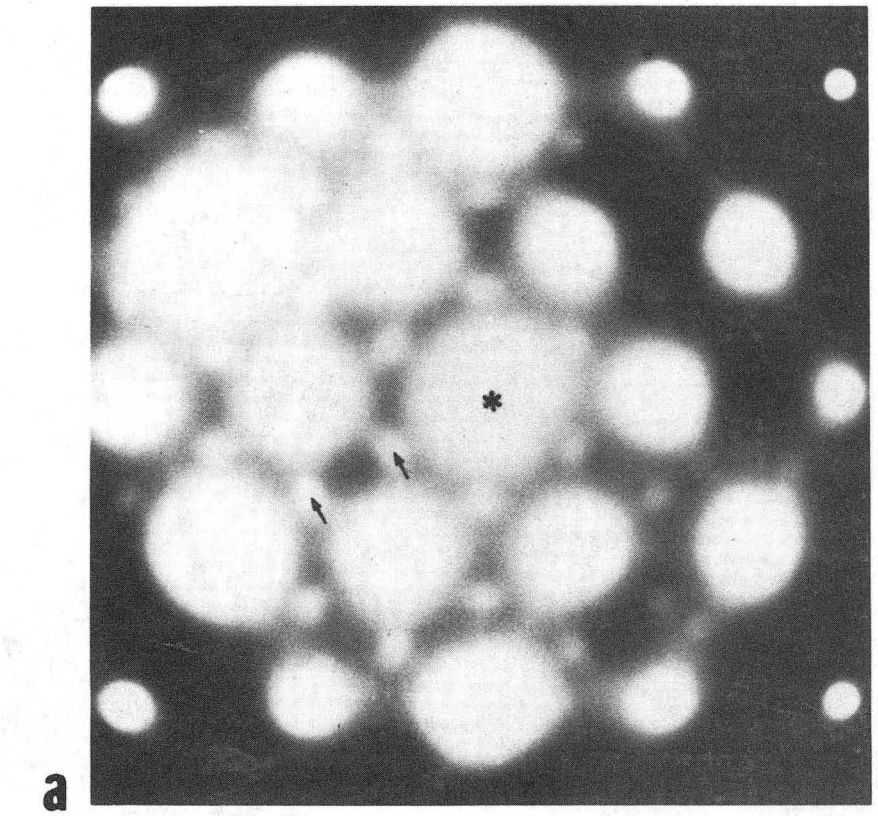

a

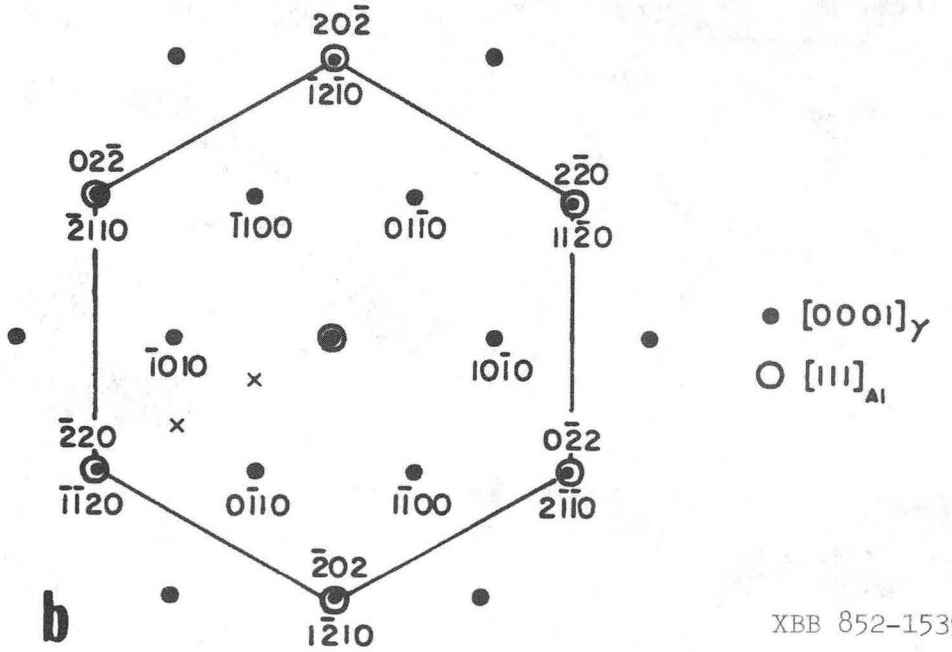

XBB 852-1539

Fig. 58

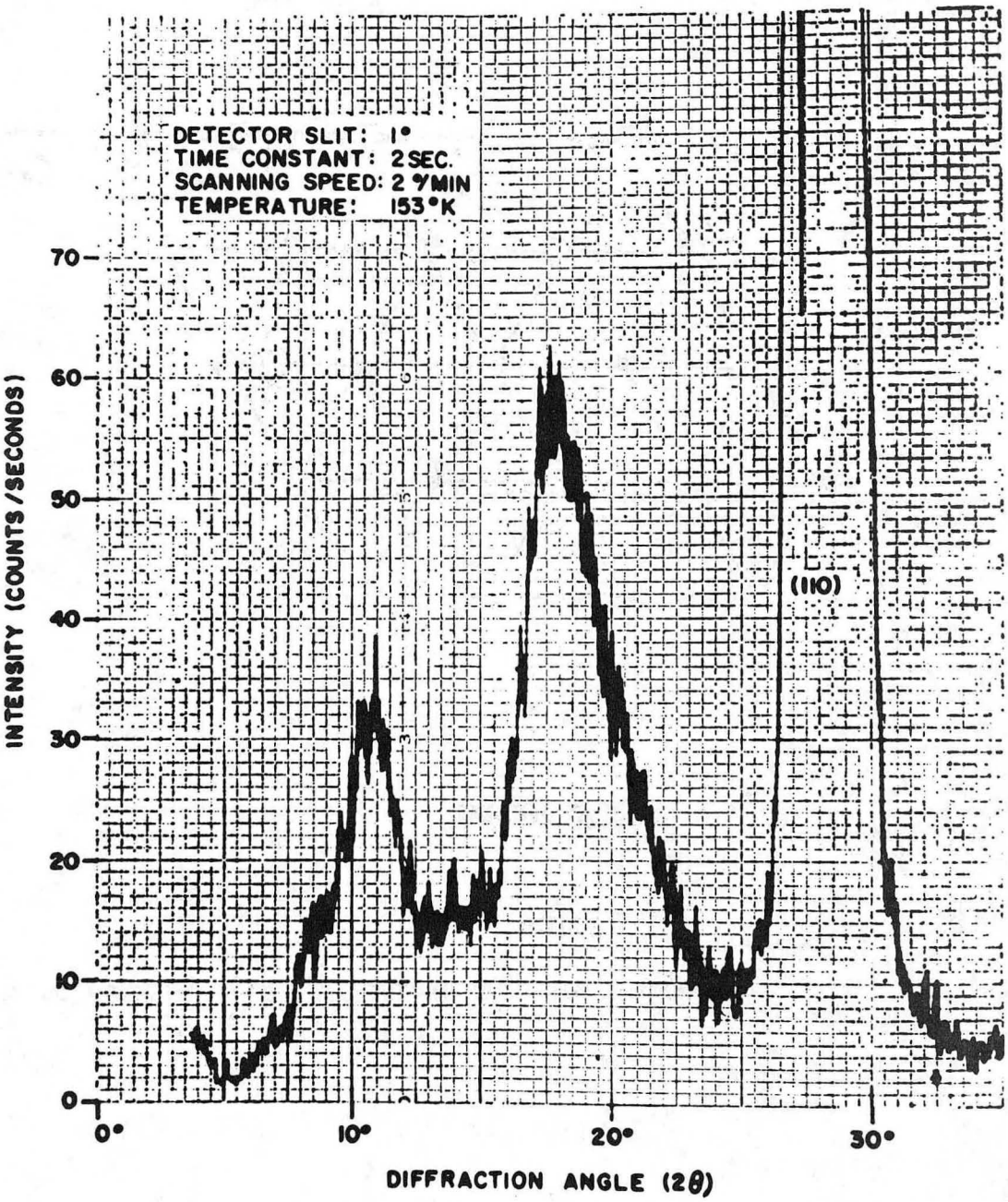

Short-range order peaks along [110]*

XBL 852-1375

Fig. 59

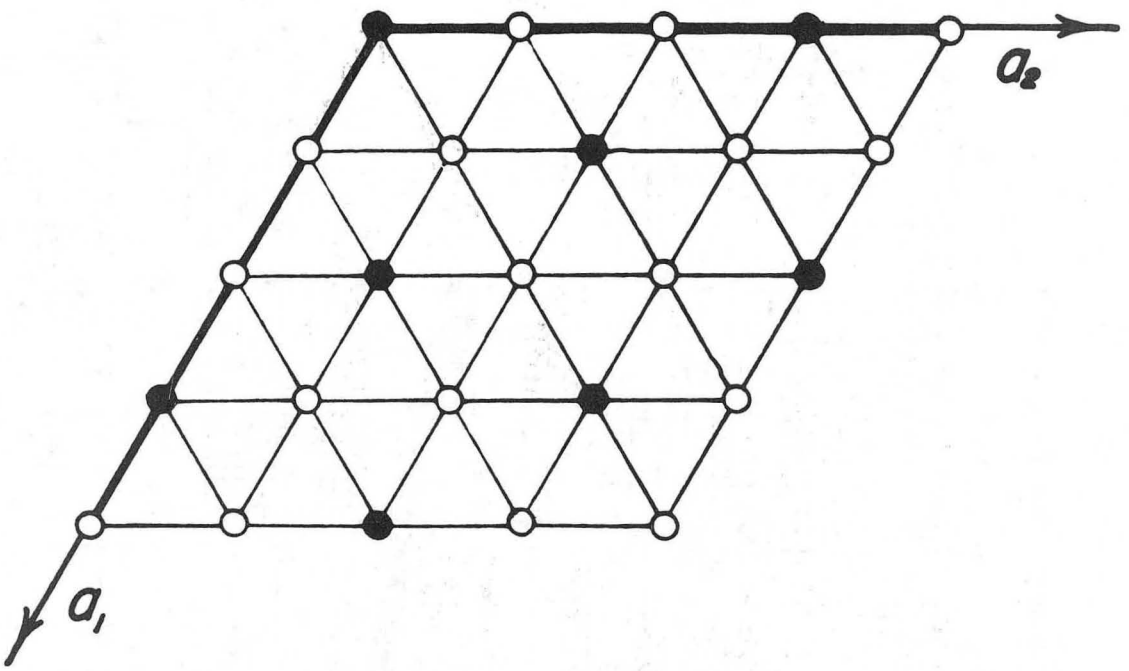

Model of superlattice in basal planes

XBL 852-1374

Fig. 60

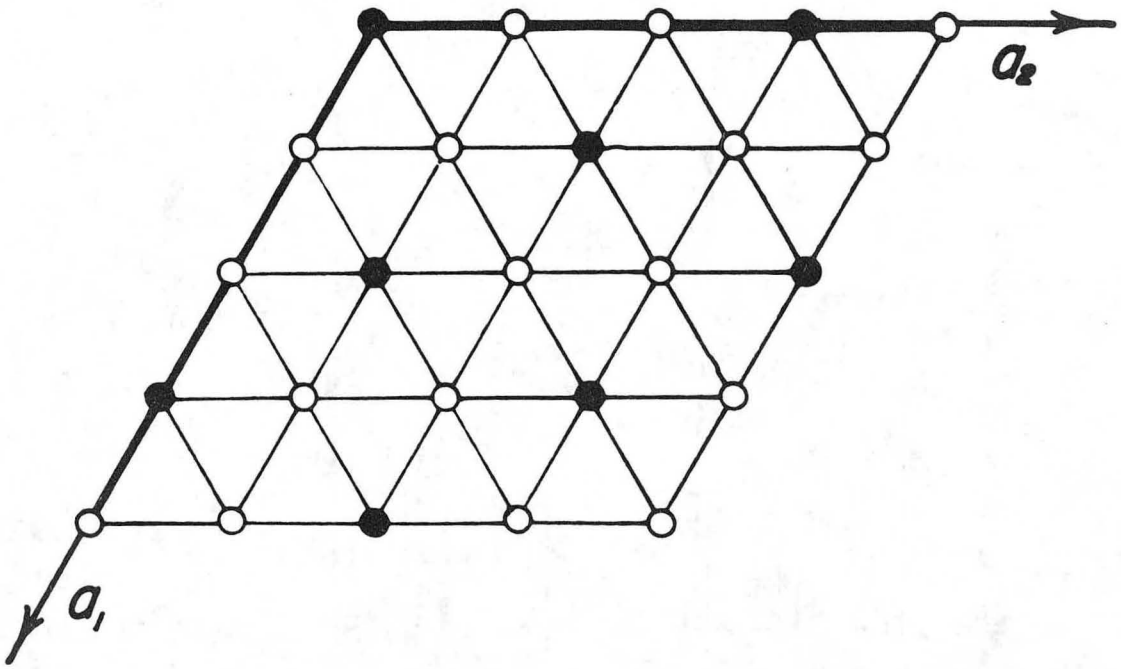

● ALUMINUM

○ SILVER

Model of superlattice in basal planes

XBL 852-1374

Fig. 60

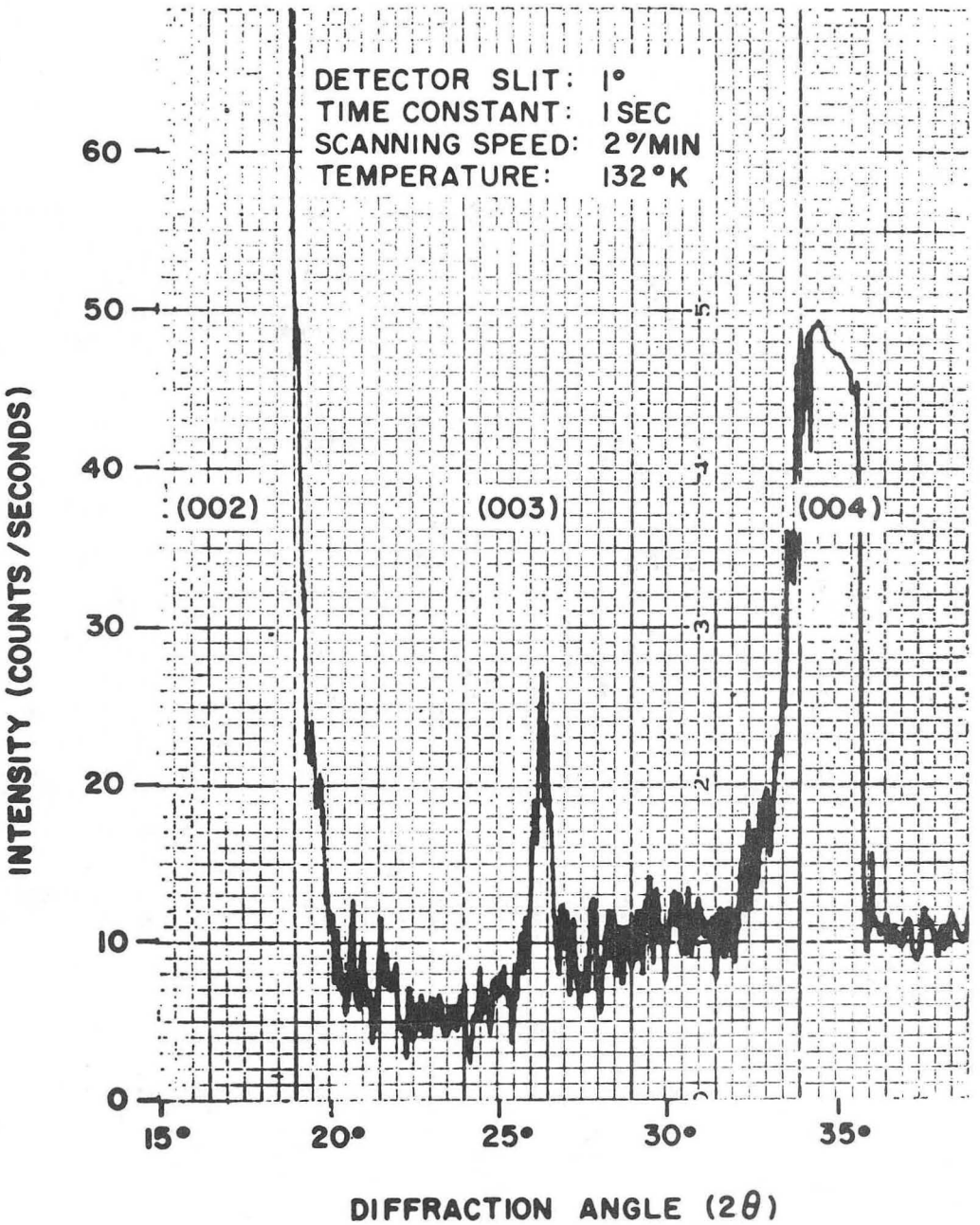

Superlattice line along [001]*

Fig. 61

XBL 852-1373

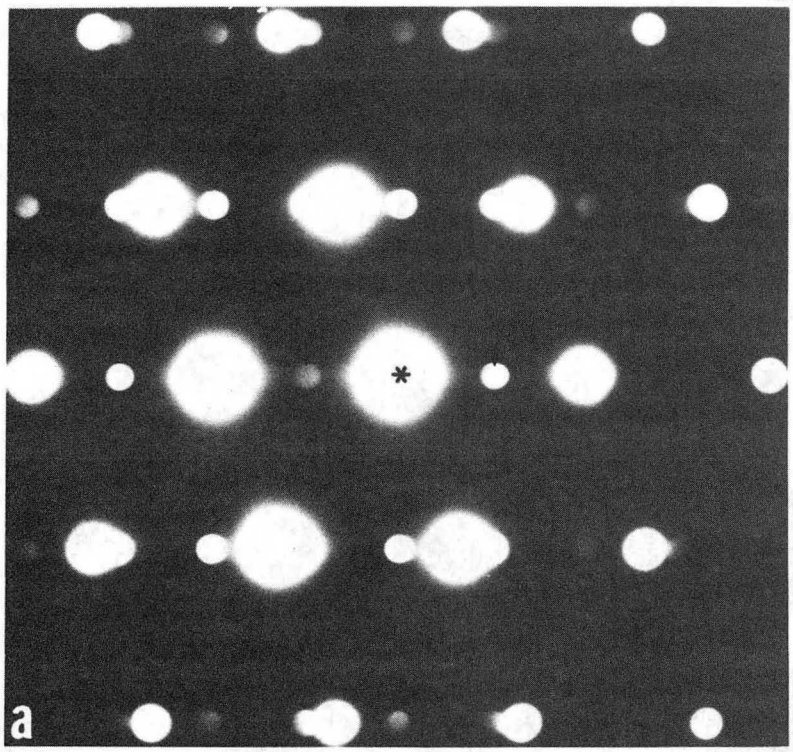

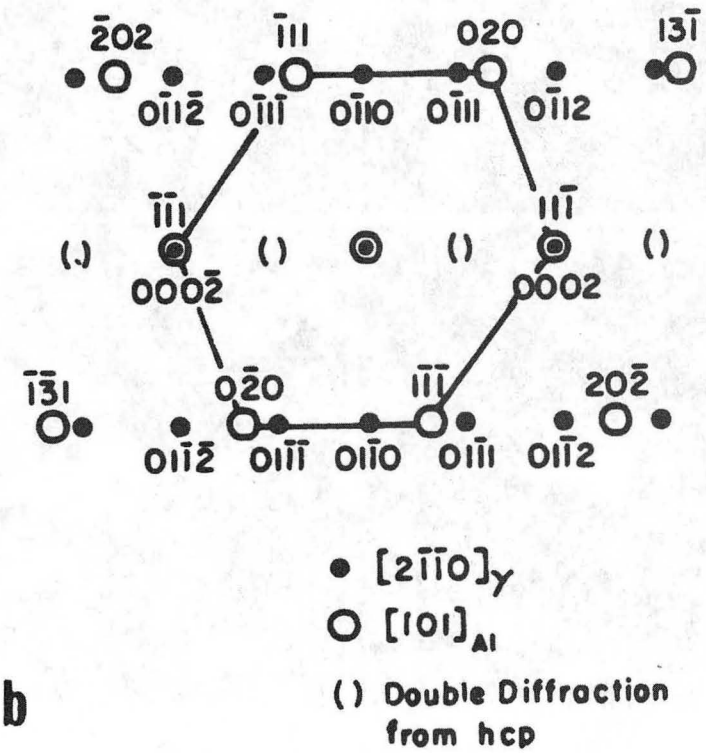

XBB 842-1201

Fig. 62

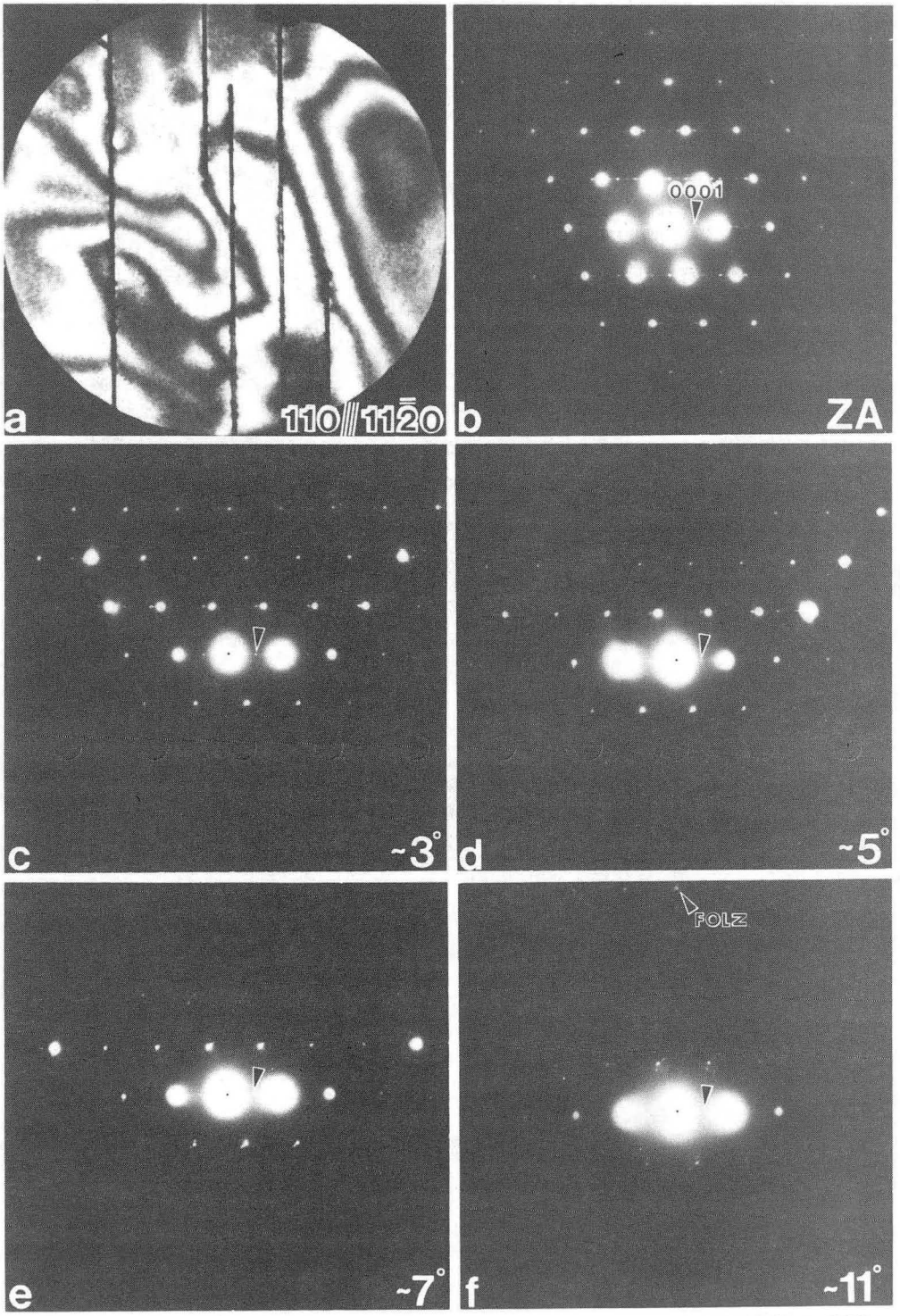

XBB 840-8883

Fig. 63

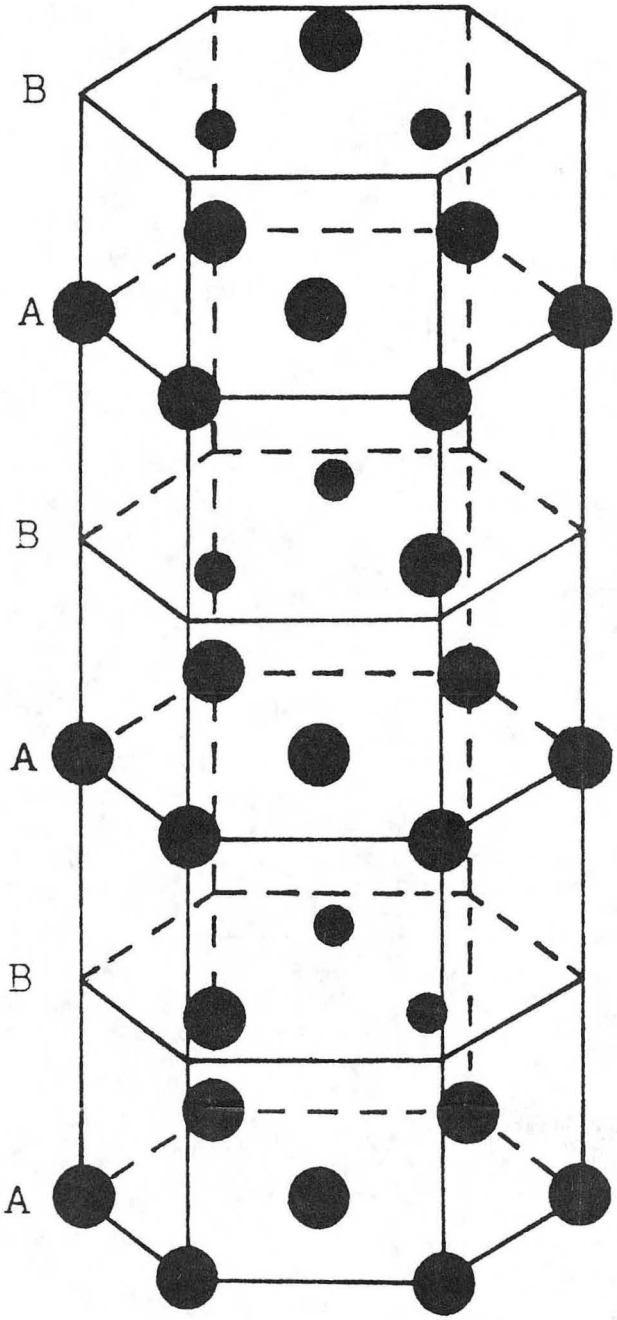

γ'

Ag_2Al

Silver

Aluminum

Fig. 64

XBL 849-3696

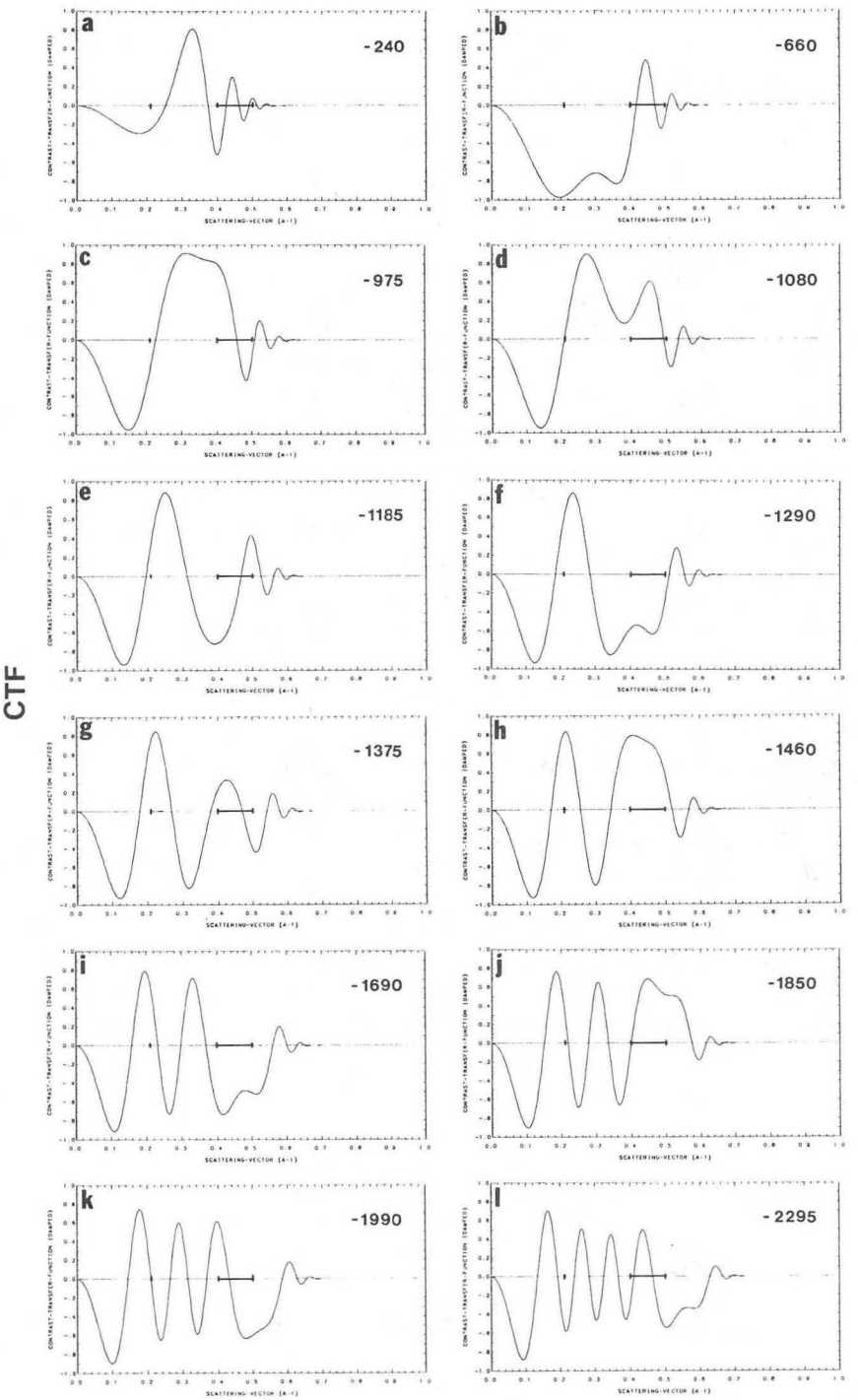

XBL 852-1376

Fig. 65

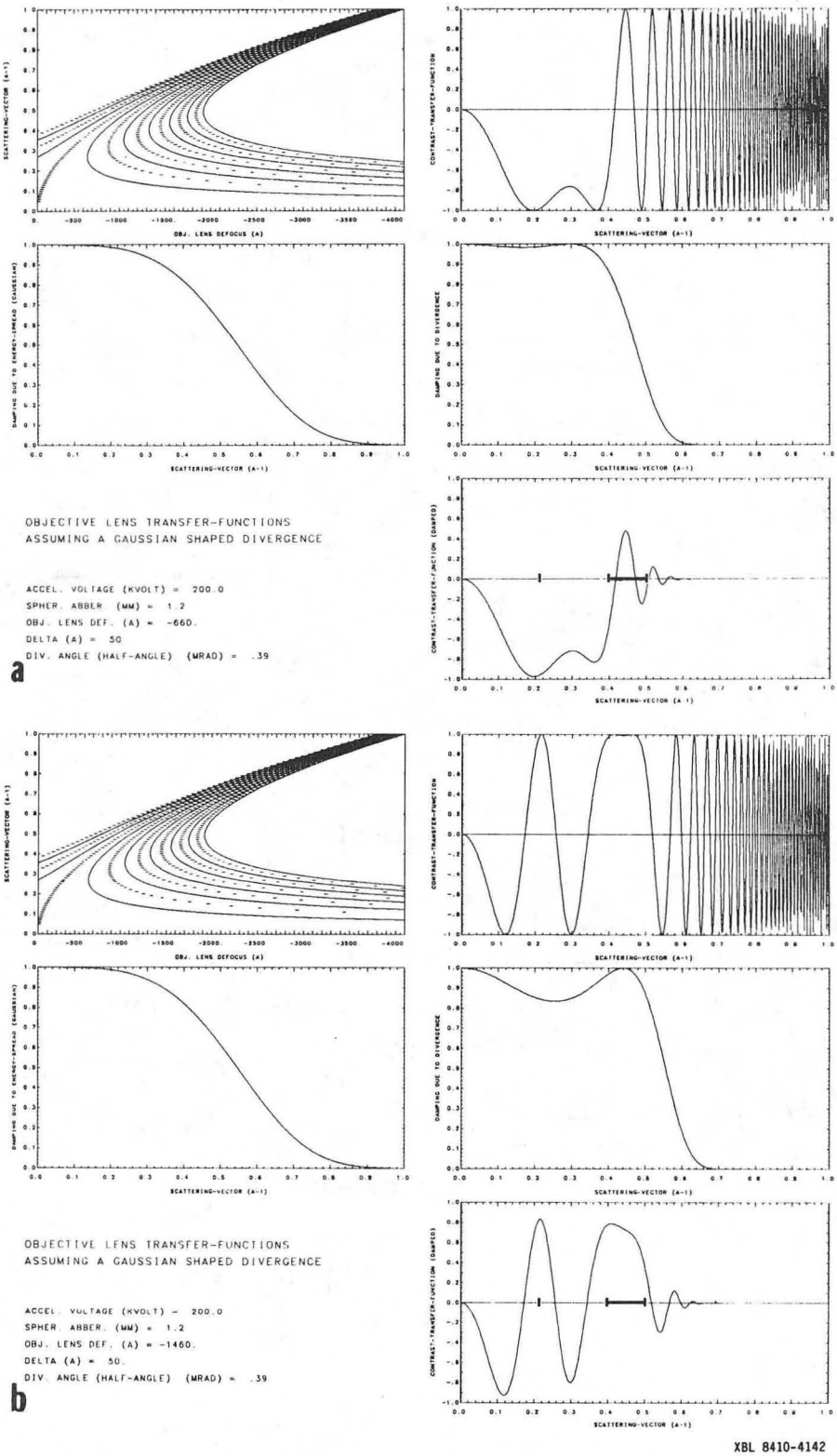
SCATTERING-VECTOR (A-1)
OBJ. LENS DEFOCUS (A)
CONTRAST-TRANSFER-FUNCTION
SCATTERING-VECTOR (A-1)
DAMPING DUE TO ENERGY-SPREAD (GAUSSIAN)
SCATTERING-VECTOR (A-1)
DAMPING DUE TO DIVERGENCE
SCATTERING-VECTOR (A-1)
CONTRAST-TRANSFER-FUNCTION (DAMPED)
SCATTERING-VECTOR (A-1)
OBJECTIVE LENS TRANSFER-FUNCTIONS
ASSUMING A GAUSSIAN SHAPED DIVERGENCE
ACCEL. VOLTAGE (KVOLT) = 200.0
SPHER. ABBER. (MM) = 1.2
OBJ. LENS DEF. (A) = -660.
DELTA (A) = 50
DIV. ANGLE (HALF-ANGLE) (MRAD) = .39
a
SCATTERING-VECTOR (A-1)
OBJ. LENS DEFOCUS (A)
CONTRAST-TRANSFER-FUNCTION
SCATTERING-VECTOR (A-1)
DAMPING DUE TO ENERGY-SPREAD (GAUSSIAN)
SCATTERING-VECTOR (A-1)
DAMPING DUE TO DIVERGENCE
SCATTERING-VECTOR (A-1)
CONTRAST-TRANSFER-FUNCTION (DAMPED)
SCATTERING-VECTOR (A-1)
OBJECTIVE LENS TRANSFER-FUNCTIONS
ASSUMING A GAUSSIAN SHAPED DIVERGENCE
ACCEL. VOLTAGE (KVOLT) = 200.0
SPHER. ABBER. (MM) = 1.2
OBJ. LENS DEF. (A) = -1460.
DELTA (A) = 50.
DIV. ANGLE (HALF-ANGLE) (MRAD) = .39
b
XBL 8410-4142

Fig. 66

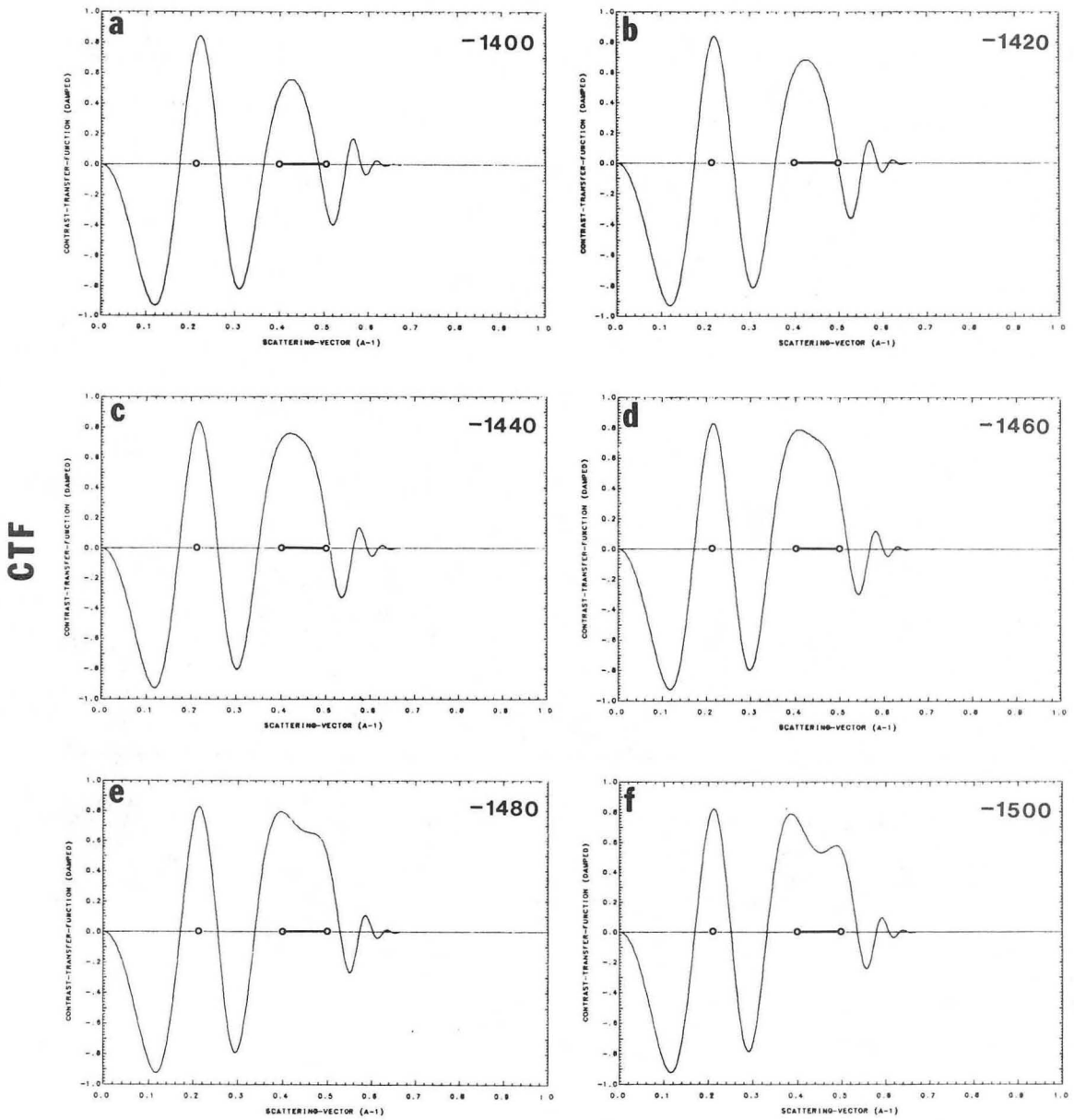
a
-1400
b
-1420
c
-1440
d
-1460
e
-1480
f
-1500
CONTRAST-TRANSFER-FUNCTION (DAMPED)
SCATTERING-VECTOR (A-1)
CTF
Defocus (Å)
XBL 8410-4293

Fig. 67

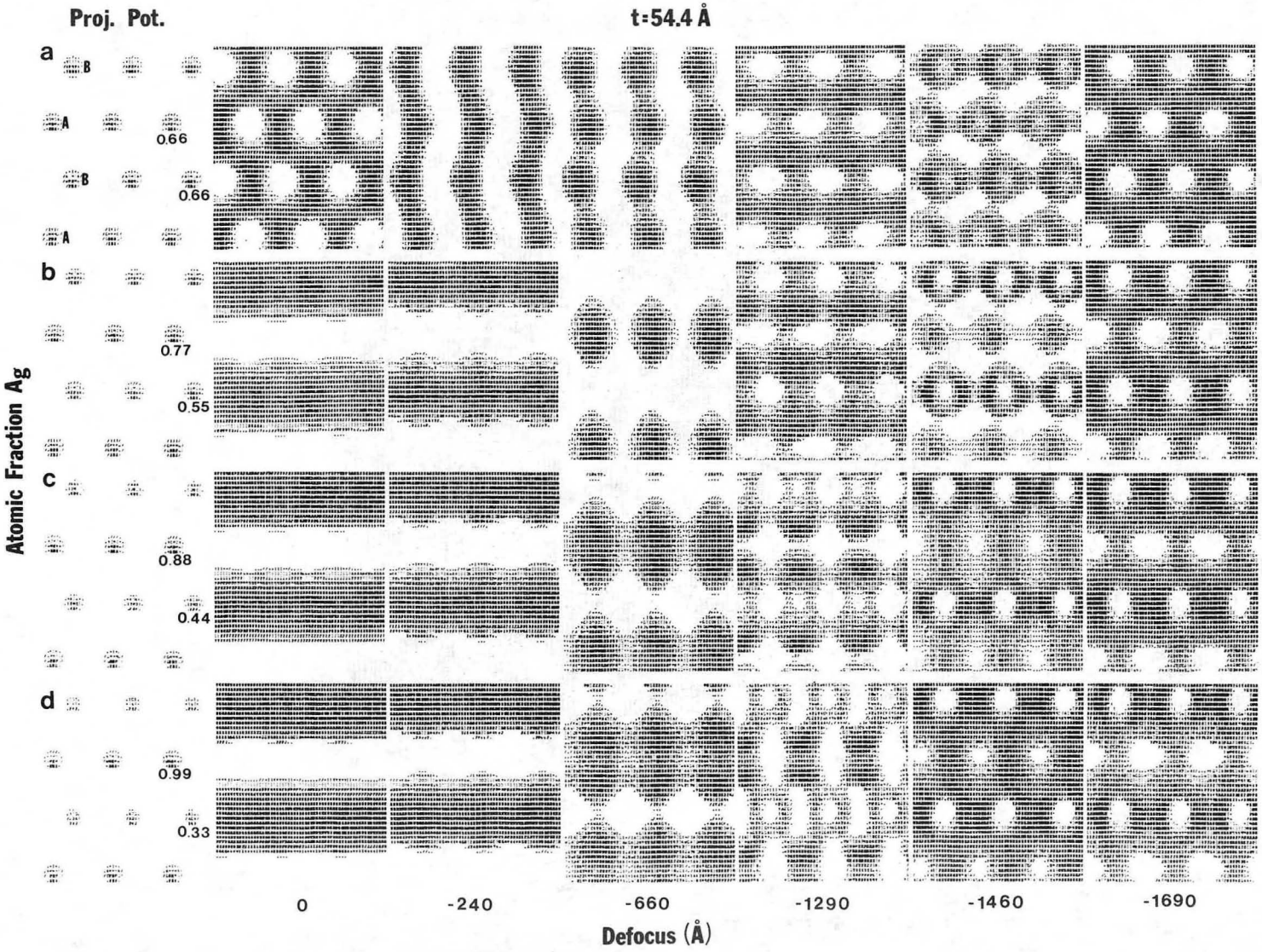

Fig. 68

XBL 852-1382

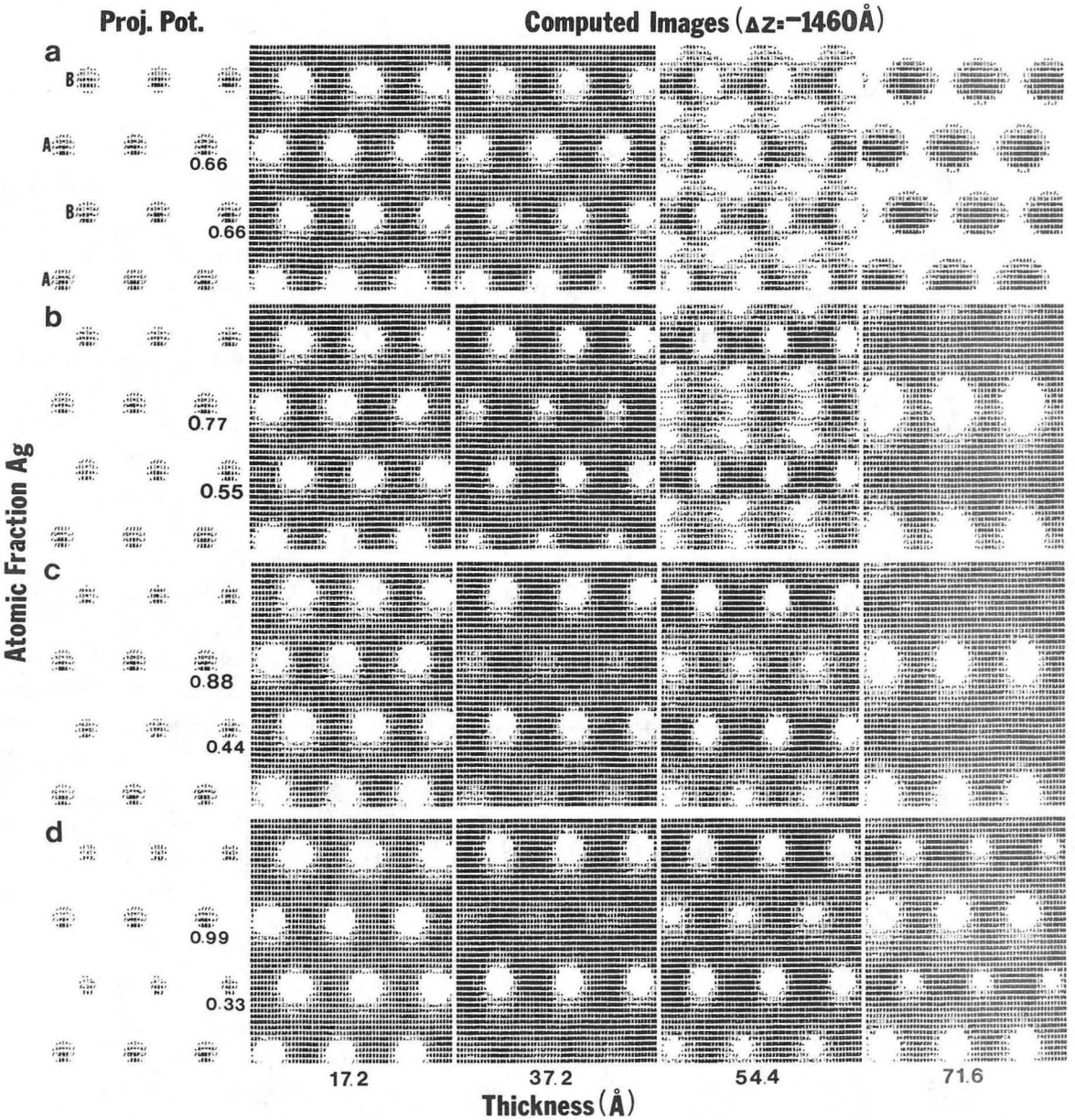
Proj. Pot.
Computed Images (ΔZ=−1460Å)
a
B
A
0.66
B
0.66
A
b
0.77
0.55
c
0.88
0.44
d
0.99
0.33
Atomic Fraction Ag
17.2
37.2
54.4
71.6
Thickness (Å)
XBL 8410-4158

Fig. 69

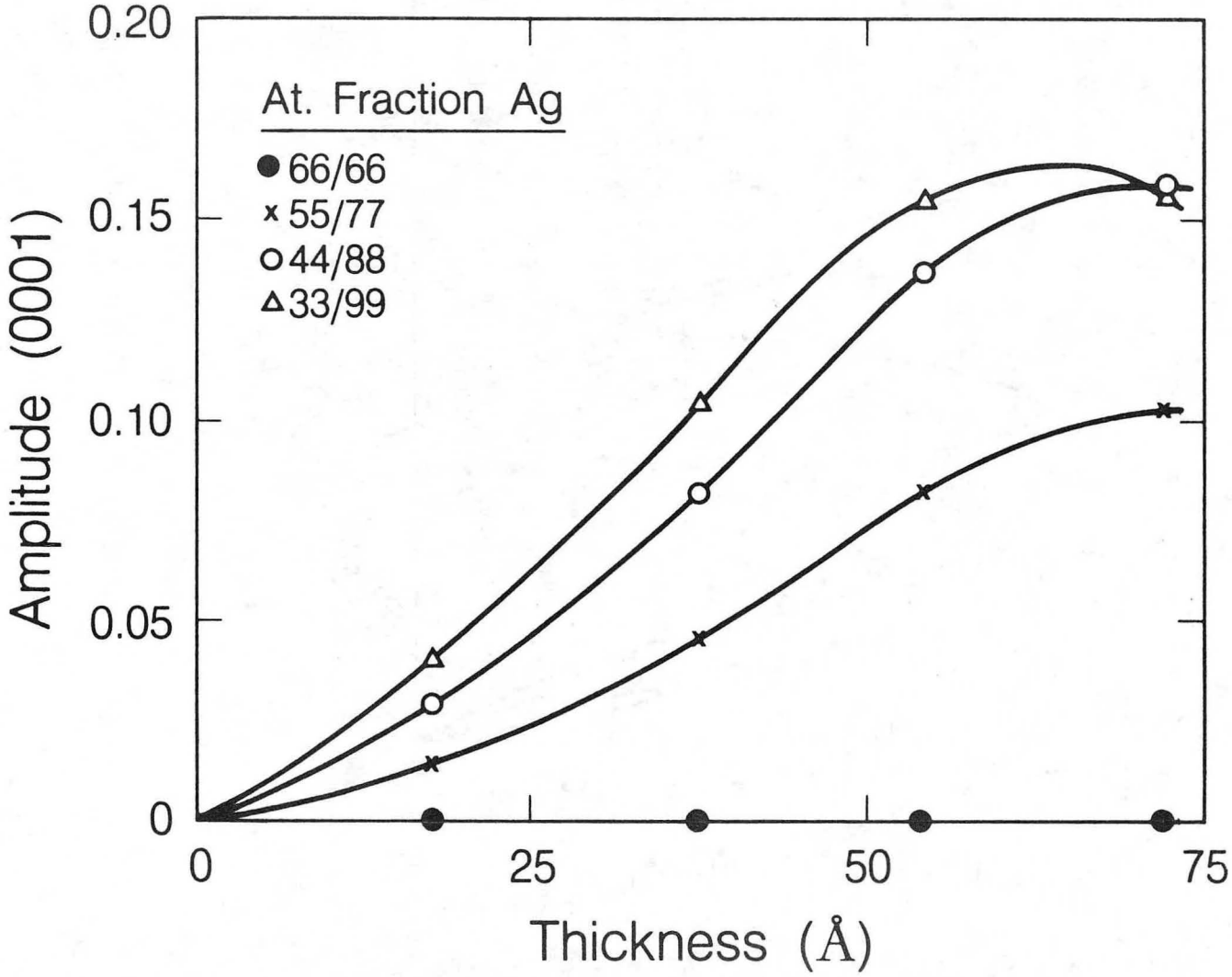

Fig. 70

XBL 852-9754

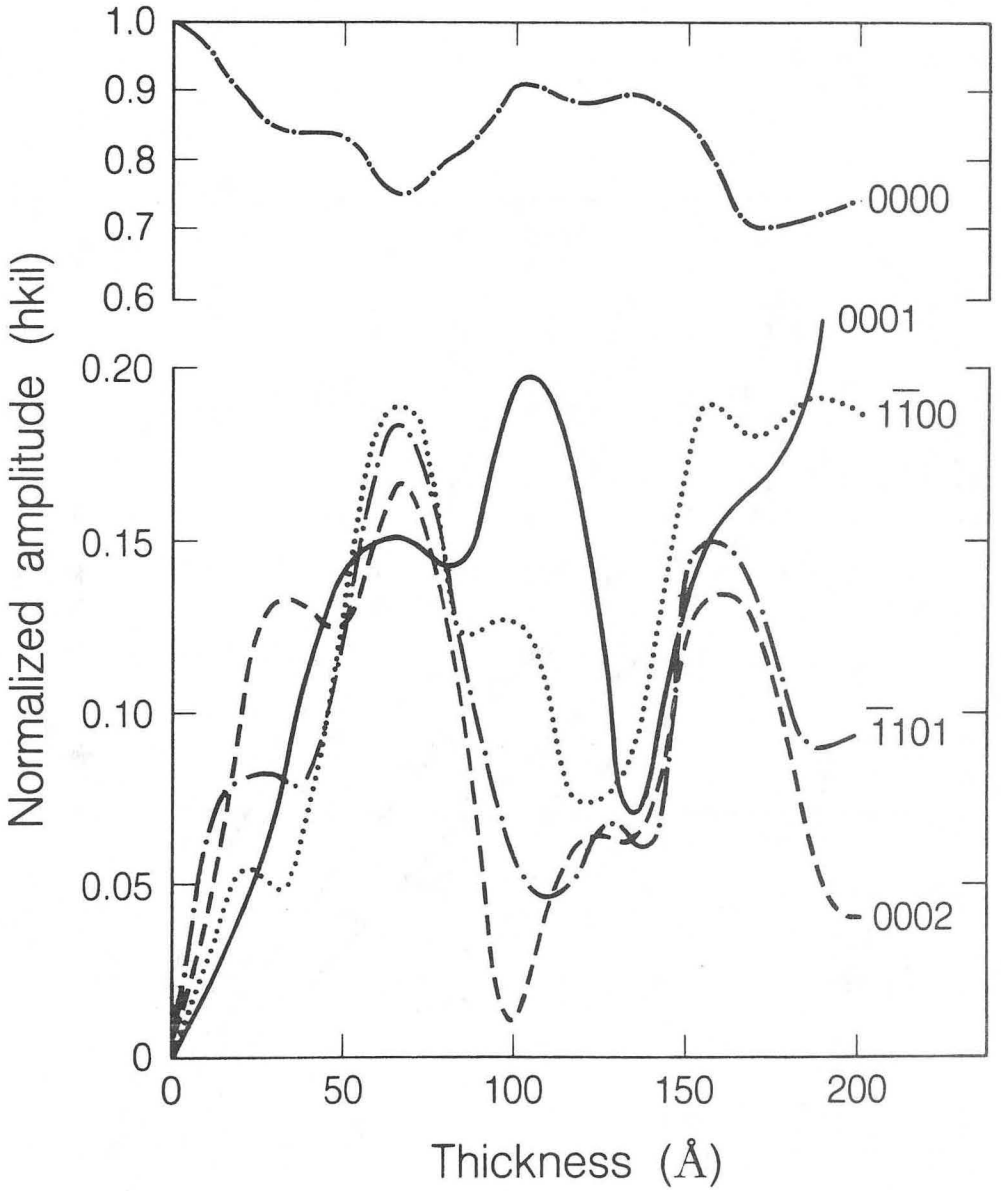

Fig. 71

XBL 852-9755

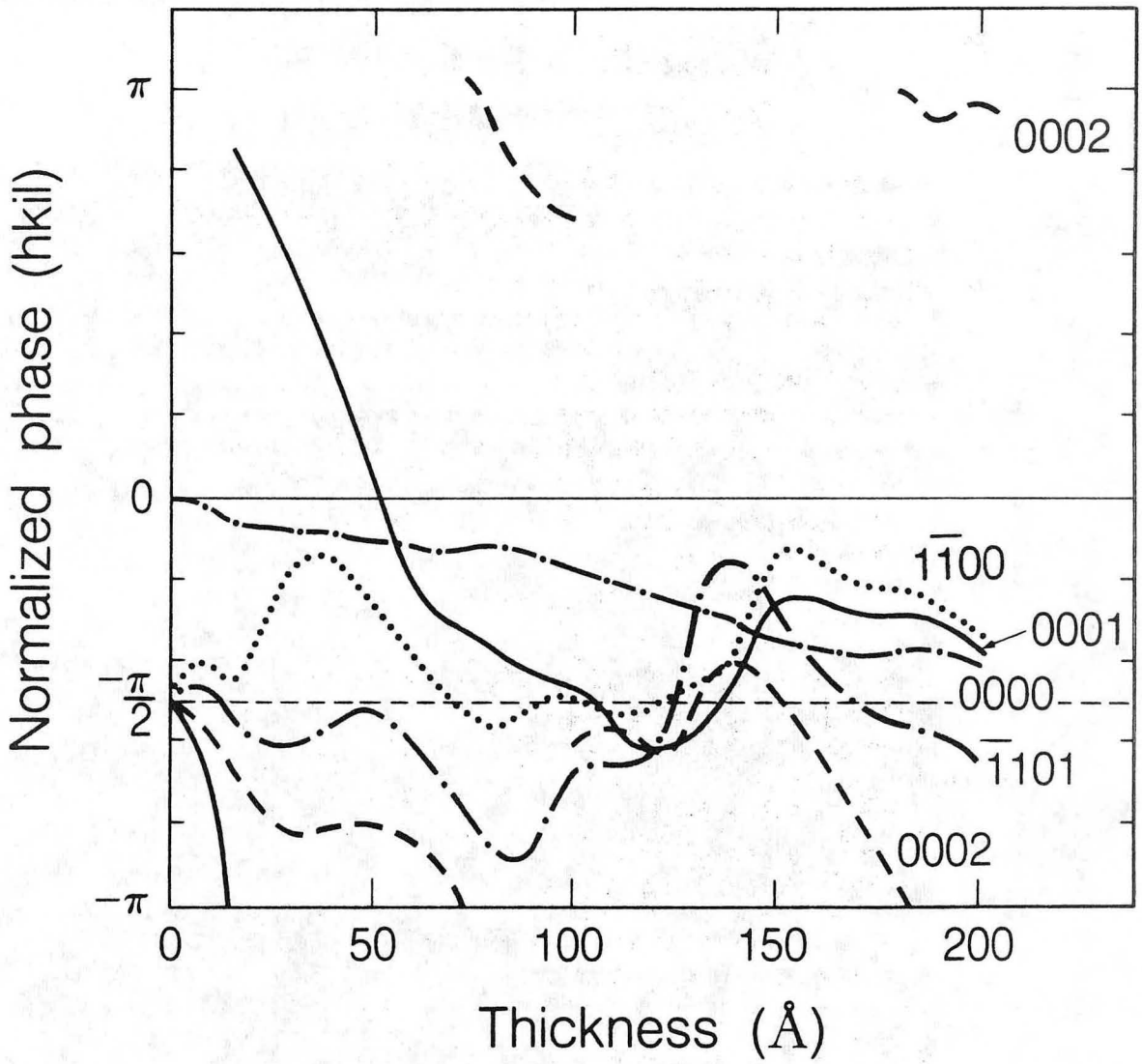

Fig. 72

XBL 852-9756

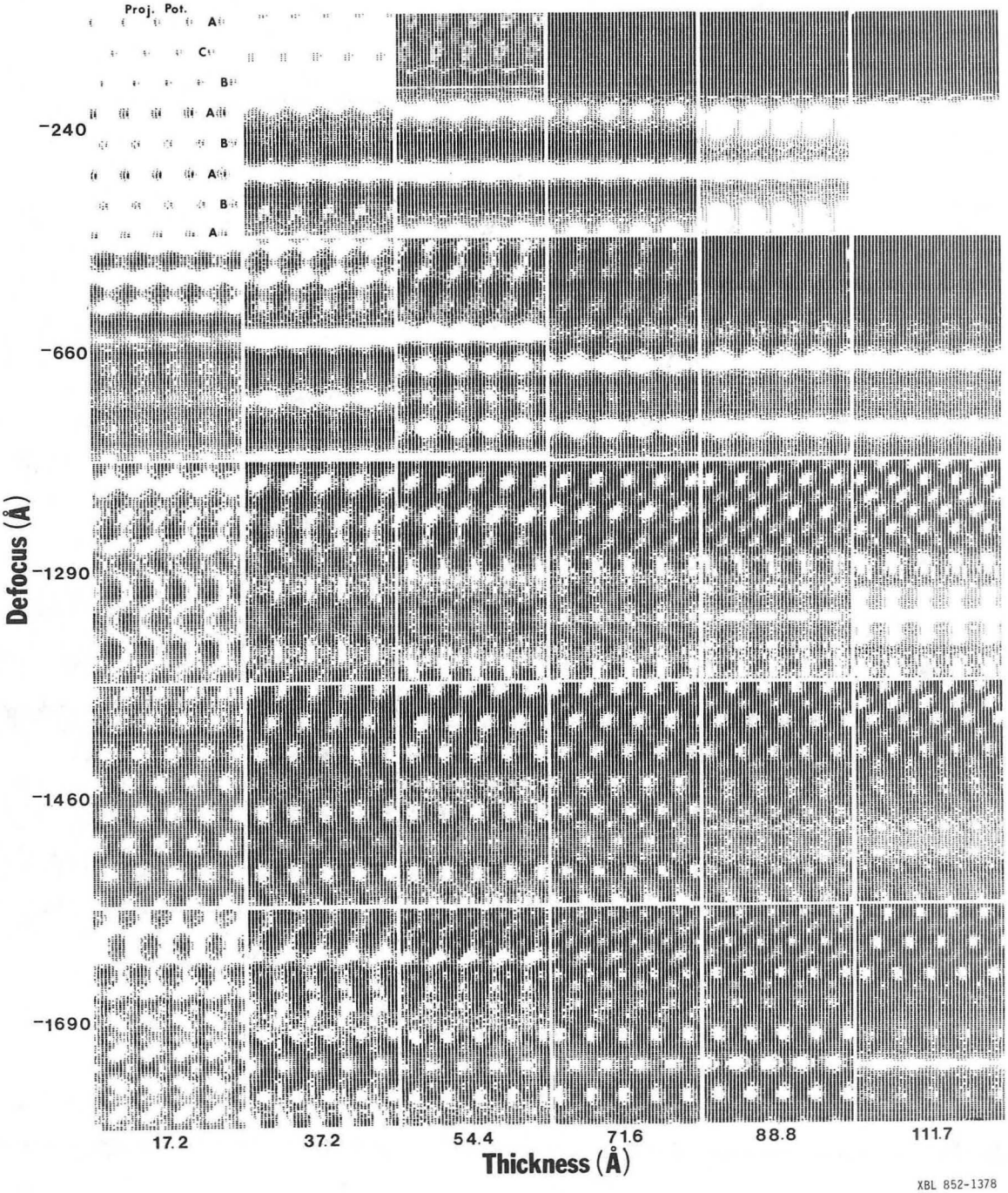
Proj. Pot.
A
C
B
A
B
A
B
A
-240
-660
-1290
-1460
-1690
Defocus (Å)
17.2
37.2
54.4
71.6
88.8
111.7
Thickness (Å)
XBL 852-1378

Fig. 73

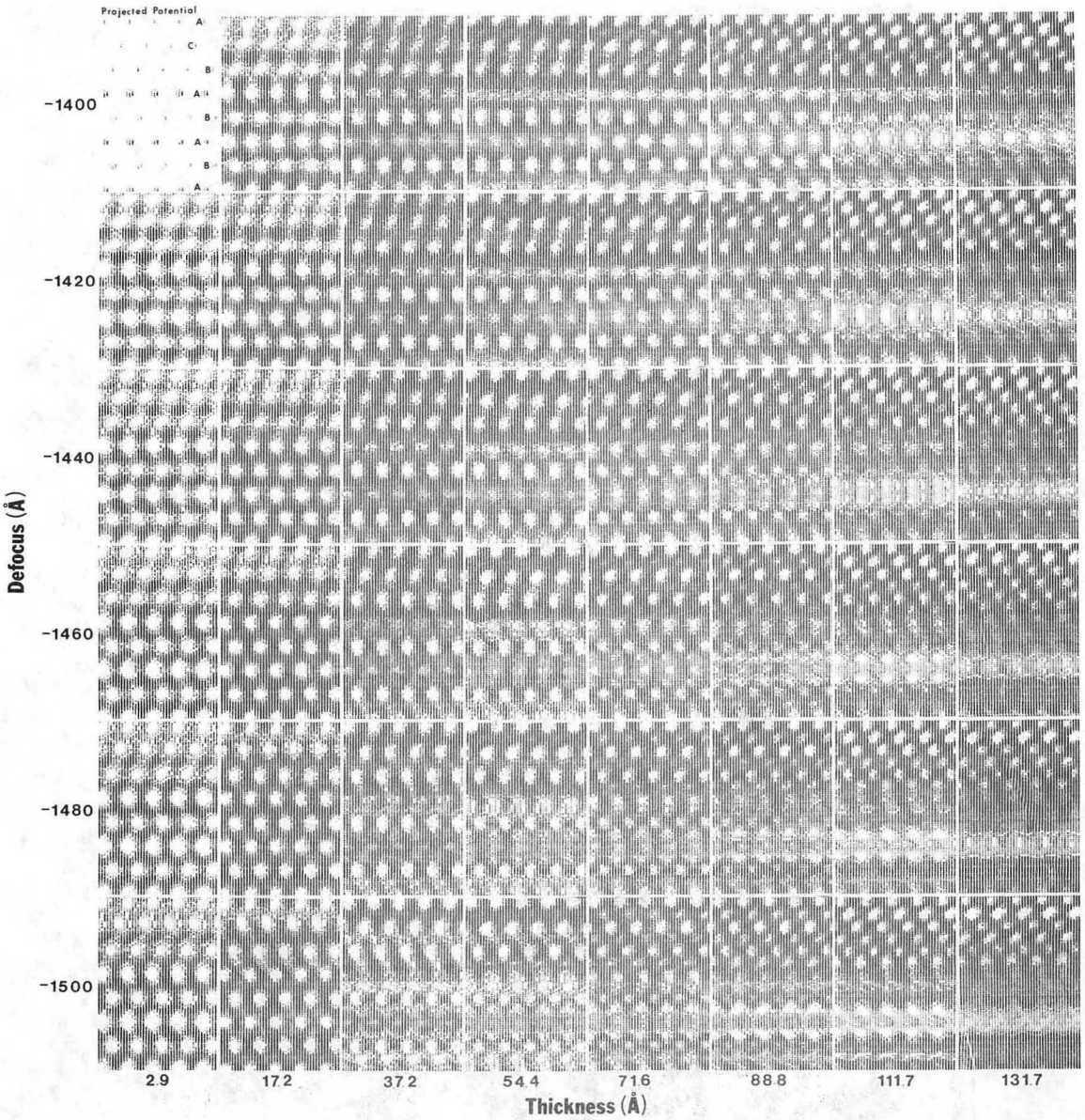

XBL 8410-4159

Fig. 74

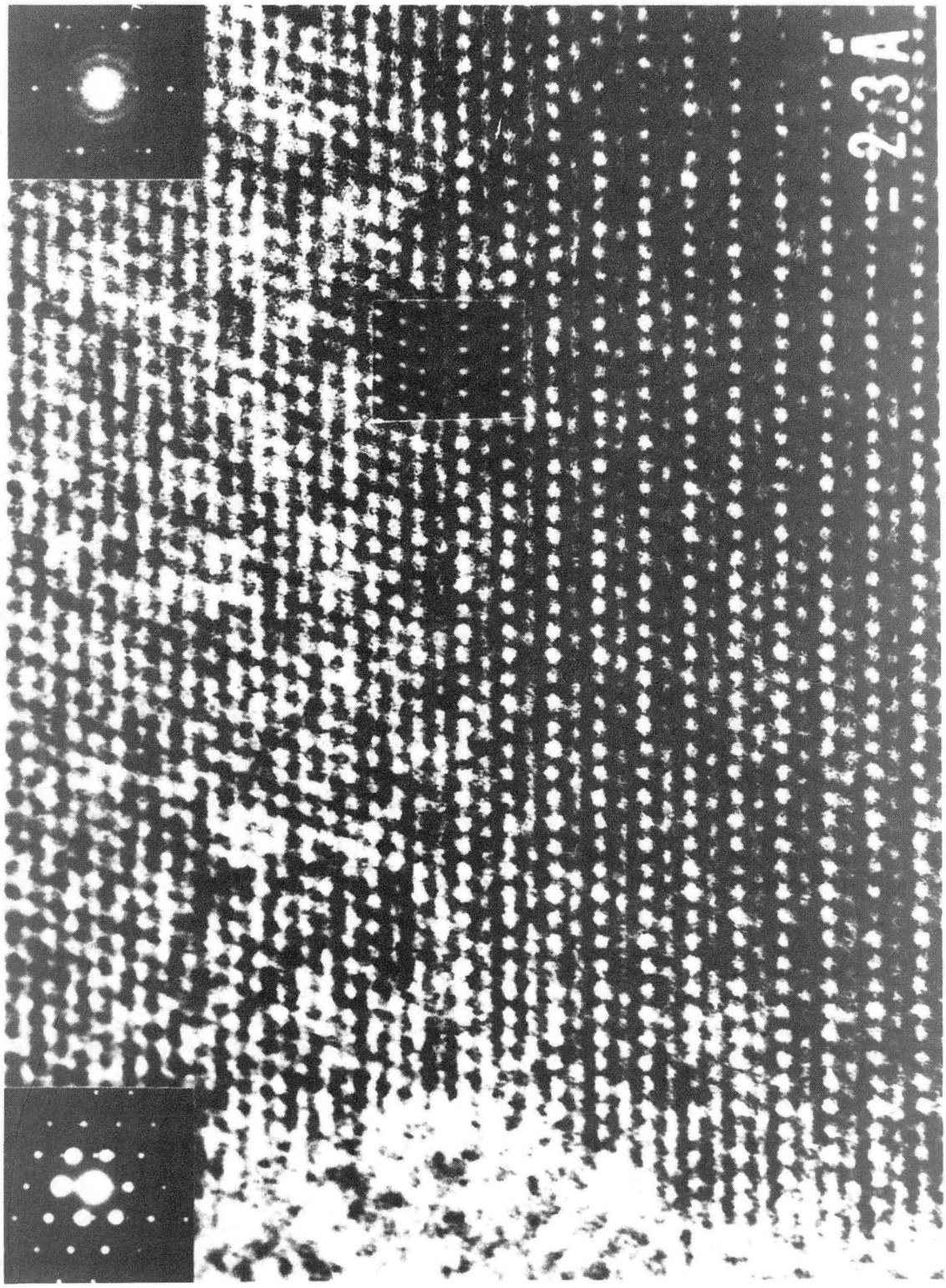

XBB 846-4293

Fig. 75

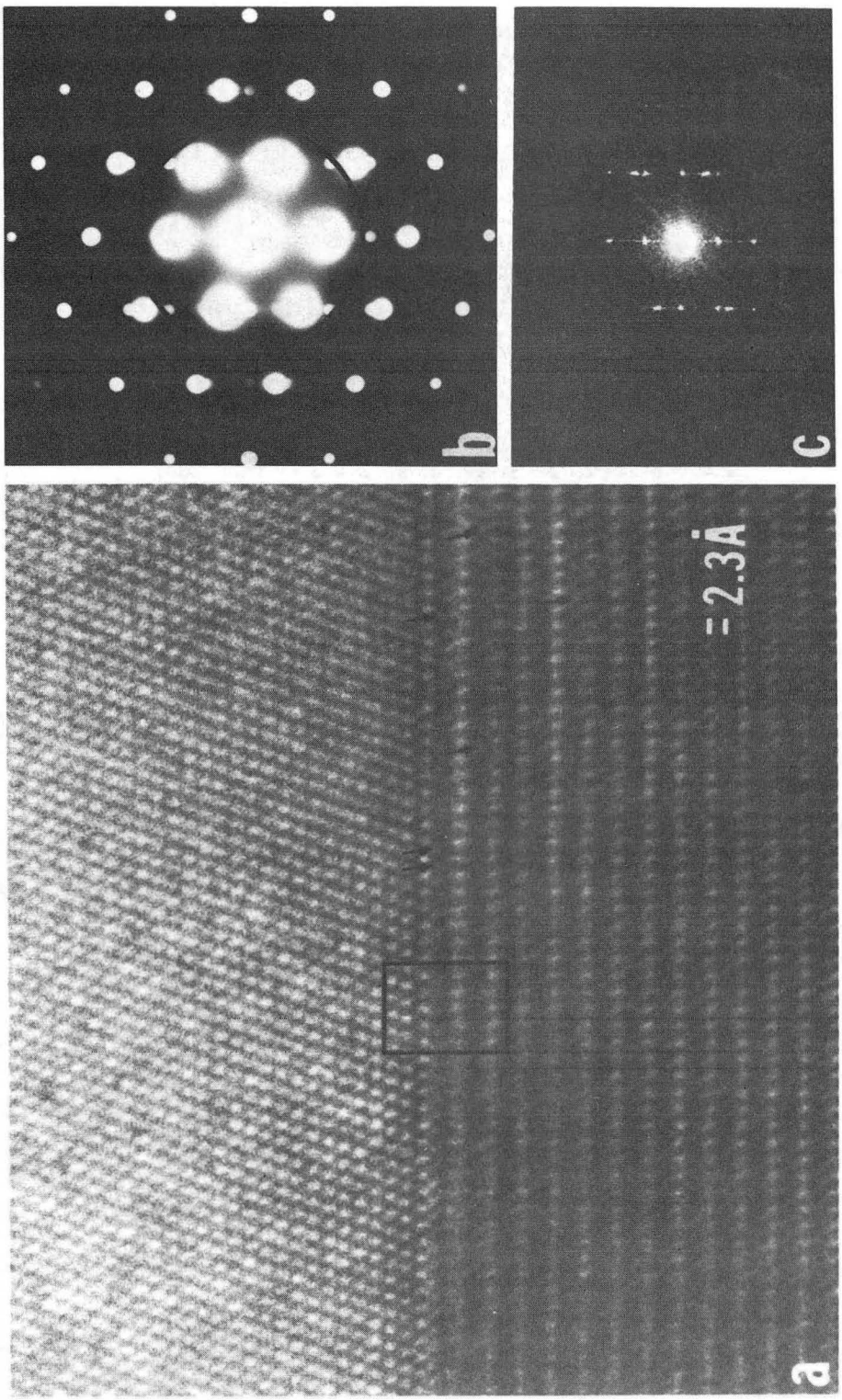

XBB 852-1545

Fig. 76

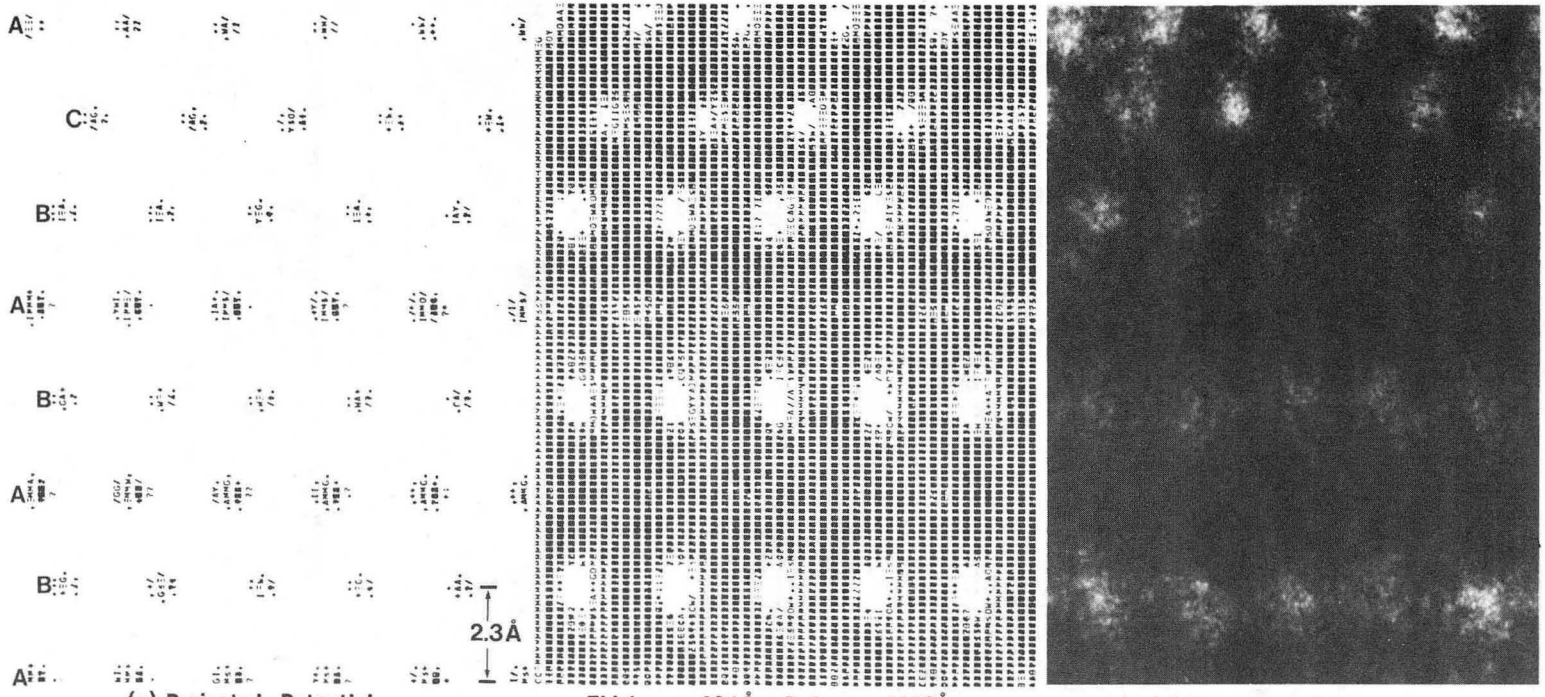

(a) Projected Potential

Thickness = 40.1Å, Defocus = -1460Å

(b) Computed Image

(c) Experimental Image

XBB 842-1226

Fig. 77

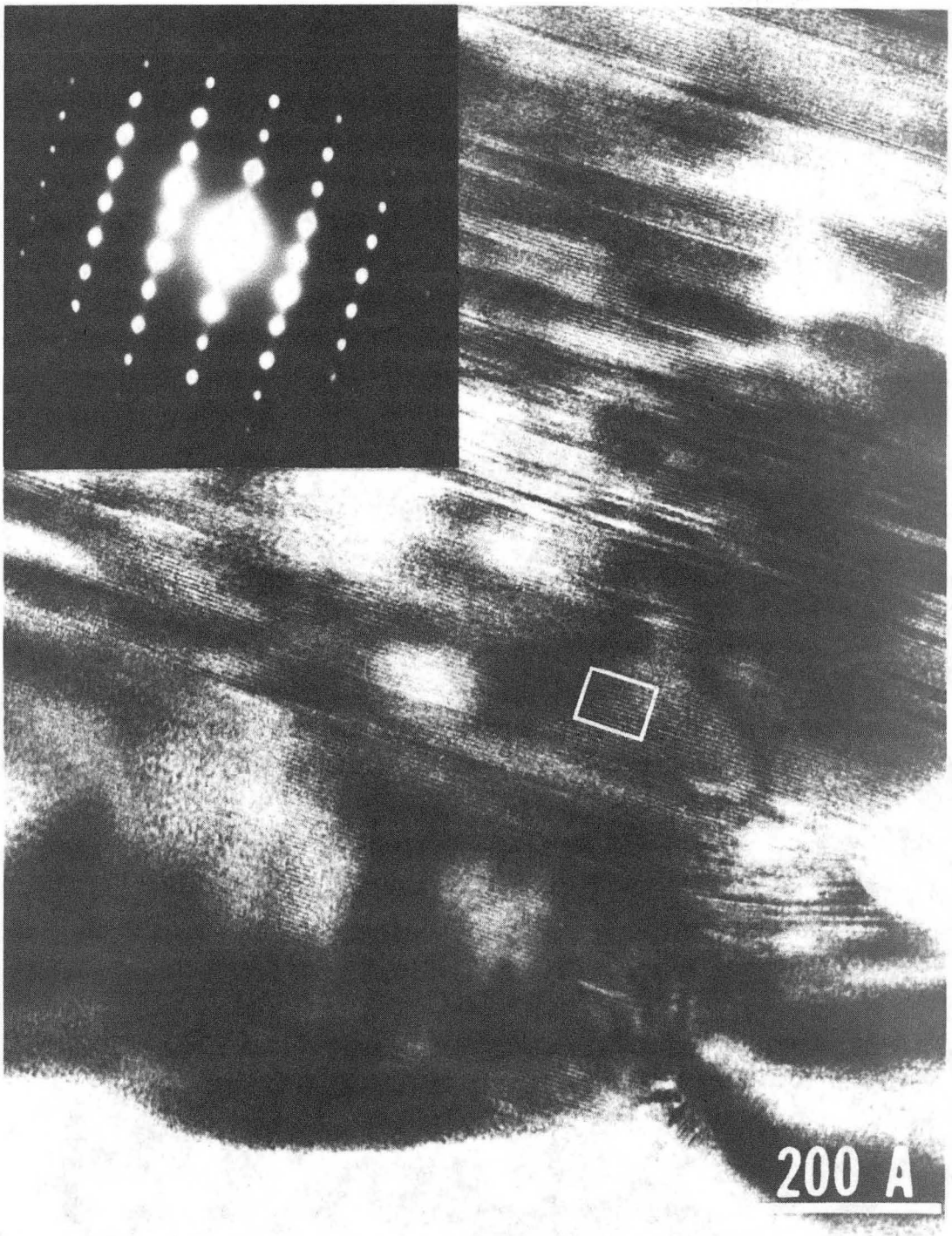

XBB 840-8877

Fig. 78

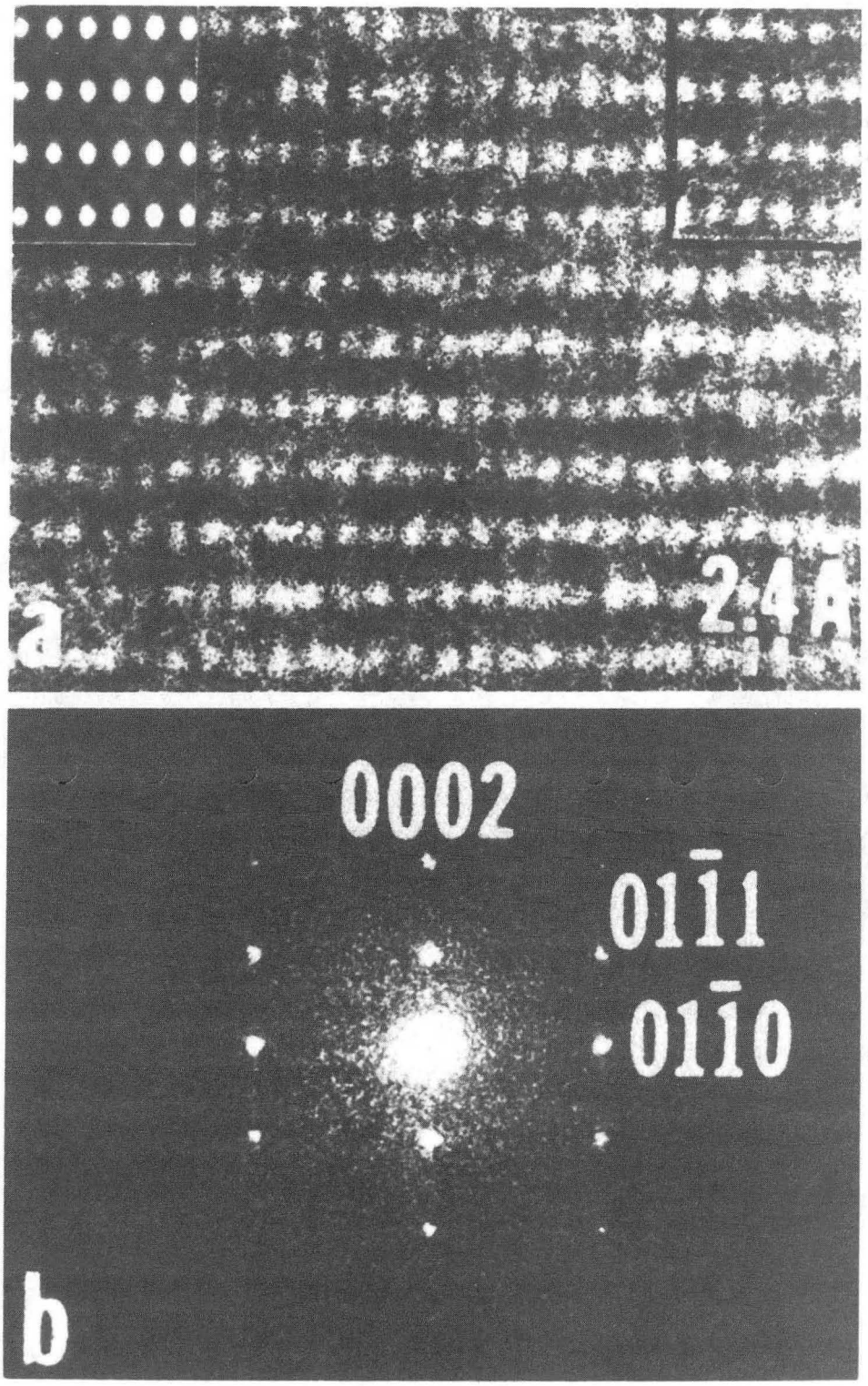

XBB 840-8884

Fig. 79

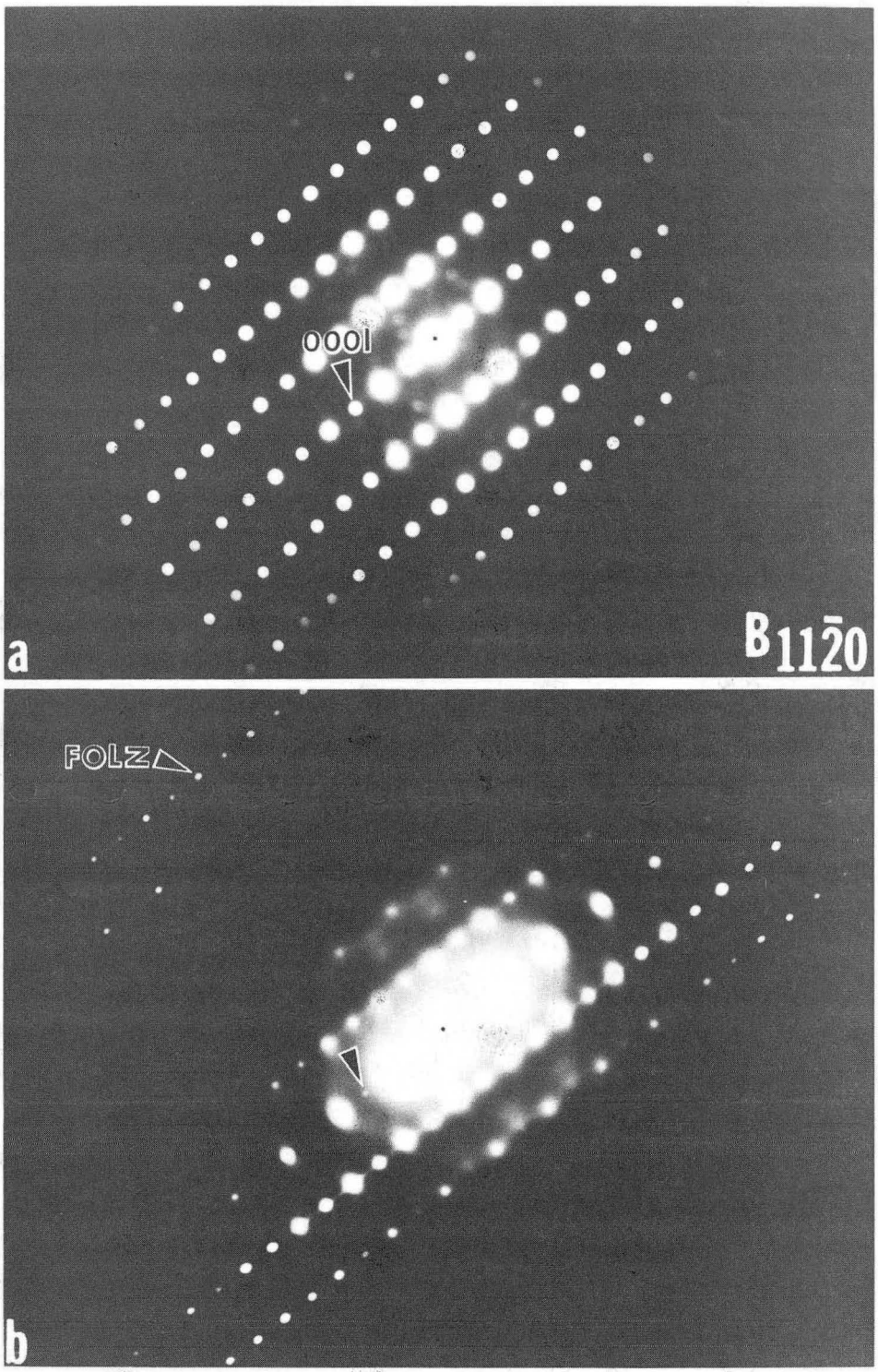

XBB 840-8882

Fig. 80

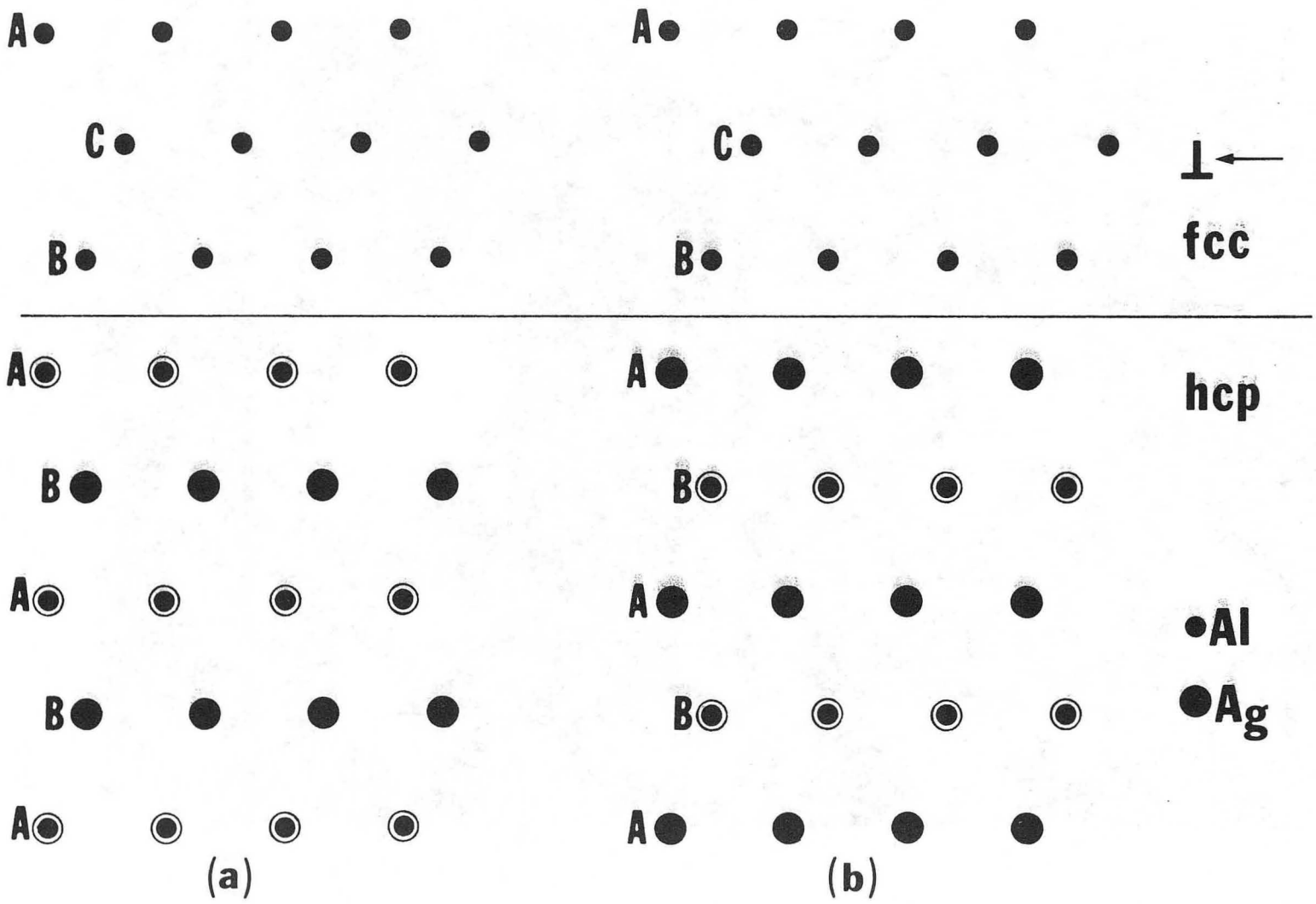

Fig. 81

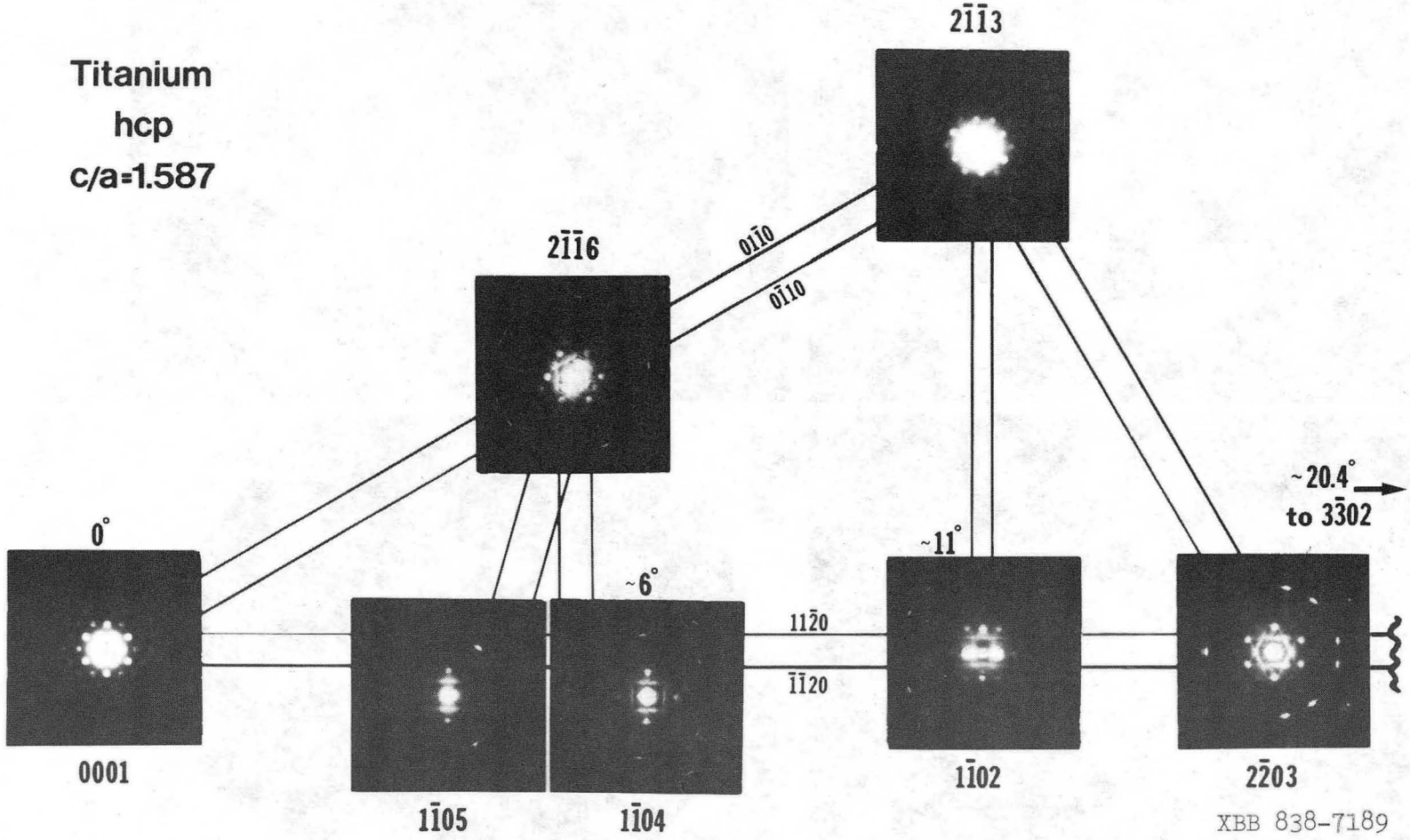
Titanium
hcp
c/a=1.587
2$\bar{1}\bar{1}$3
2$\bar{1}\bar{1}$6
01$\bar{1}$0
0$\bar{1}$10
0°
~6°
~11°
~20.4°
to 33$\bar{0}$2
11$\bar{2}$0
$\bar{1}\bar{1}$20
0001
1$\bar{1}$05
1$\bar{1}$04
1$\bar{1}$02
22$\bar{0}$3
XBB 838-7189

Fig. 82

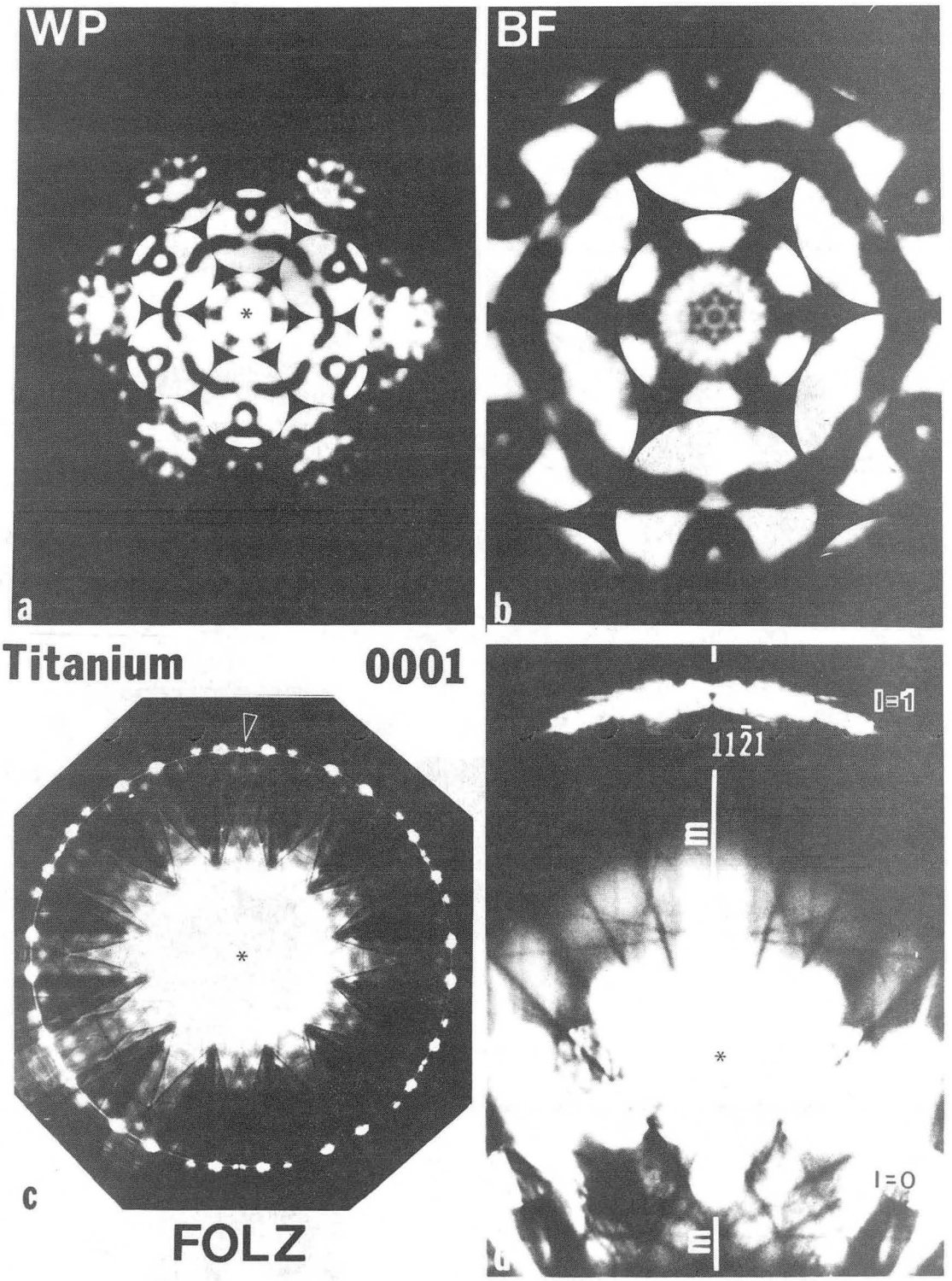

XBB 840-7662

Fig. 83

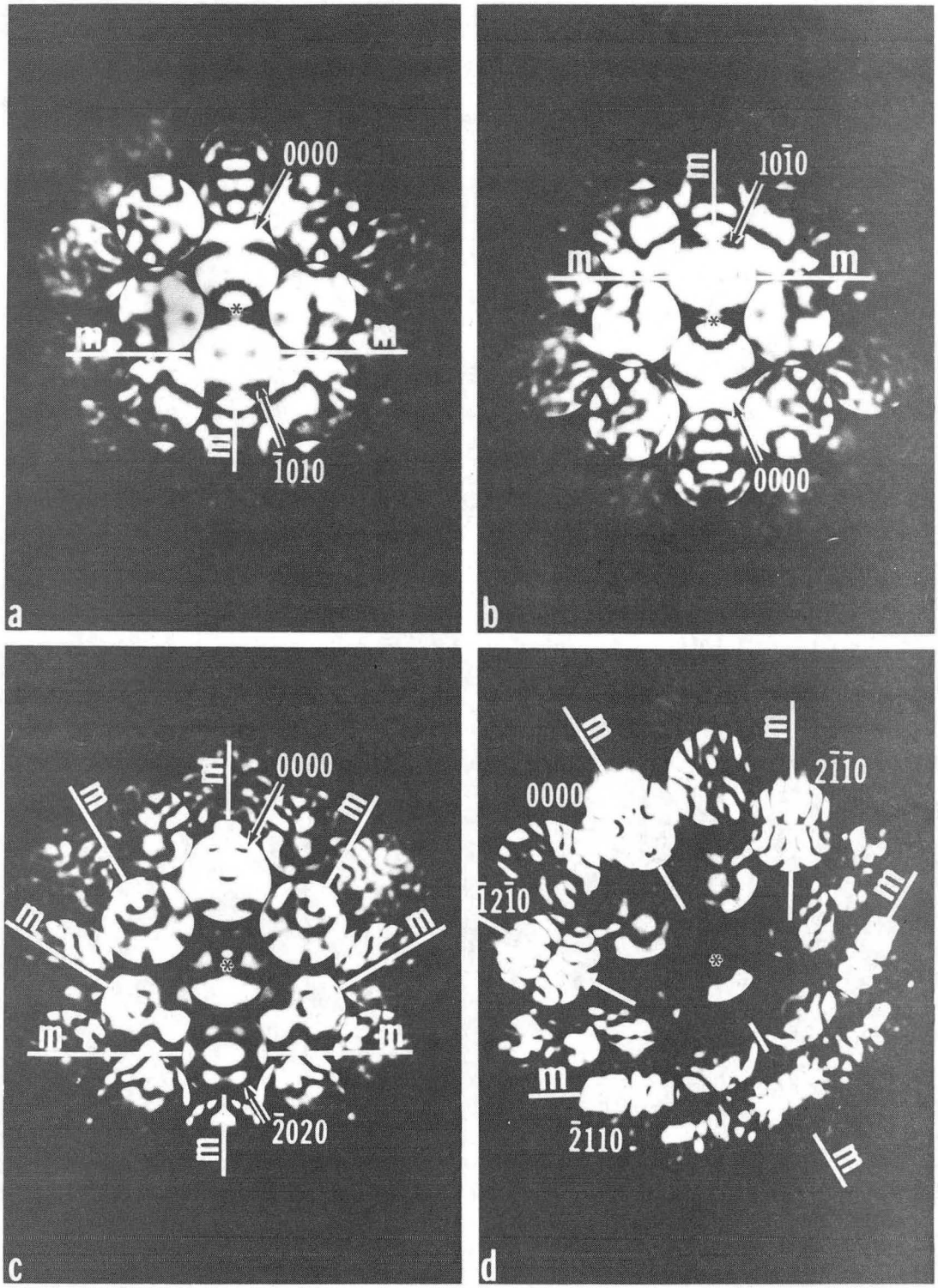

XBB 840-7655

Fig. 84

$P\,6_3/m\,m\,c$ D^4_{6h} $6/m\,m\,m$ Hexagonal

No. 194 $P\,6_3/m\,2/m\,2/c$ Patterson symmetry $P\,6/m\,m\,m$

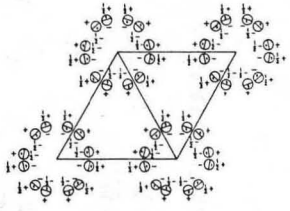

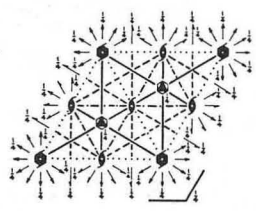

Origin at centre $(\bar{3}m\,1)$ at $\bar{3}\,2/m\,c$

Asymmetric unit $0\le x\le\frac{1}{3}$; $0\le y\le\frac{1}{3}$; $0\le z\le\frac{1}{4}$; $x\le 2y$; $y\le\min(1-x,2x)$

Vertices 0,0,0 $\frac{1}{3},\frac{1}{3},0$ $\frac{1}{3},\frac{1}{3},\frac{1}{4}$
0,0,$\frac{1}{4}$ $\frac{1}{3},\frac{1}{3},\frac{1}{4}$ $\frac{1}{3},\frac{1}{3},\frac{1}{4}$

Symmetry operations

(1) 1	(2) 3^+ 0,0,z	(3) 3^- 0,0,z
(4) $2(0,0,\frac{1}{2})$ 0,0,z	(5) $6^-(0,0,\frac{1}{2})$ 0,0,z	(6) $6^+(0,0,\frac{1}{2})$ 0,0,z
(7) 2 $x,x,0$	(8) 2 $x,0,0$	(9) 2 $0,y,0$
(10) 2 $x,\bar{x},\frac{1}{4}$	(11) 2 $x,2x,\frac{1}{4}$	(12) 2 $2x,x,\frac{1}{4}$
(13) $\bar{1}$ 0,0,0	(14) $\bar{3}^+$ 0,0,z; 0,0,0	(15) $\bar{3}^-$ 0,0,z; 0,0,0
(16) m $x,y,\frac{1}{4}$	(17) $\bar{6}^-$ 0,0,z; 0,0,$\frac{1}{4}$	(18) $\bar{6}^+$ 0,0,z; 0,0,$\frac{1}{4}$
(19) m $x,\bar{x},z$	(20) m $x,2x,z$	(21) m $2x,x,z$
(22) c x,x,z	(23) c $x,0,z$	(24) c $0,y,z$

Maximal non-isomorphic subgroups

I	[2]$P\,6_3\,2\,2$	1; 2; 3; 4; 5; 6; 7; 8; 9; 10; 11; 12
	[2]$P\,6_3/m\,1\,1\,(P\,6_3/m)$	1; 2; 3; 4; 5; 6; 13; 14; 15; 16; 17; 18
	[2]$P\,6_3m\,c$	1; 2; 3; 4; 5; 6; 19; 20; 21; 22; 23; 24
	[2]$P\,\bar{3}\,m\,1$	1; 2; 3; 7; 8; 9; 13; 14; 15; 19; 20; 21
	[2]$P\,\bar{3}\,1\,c$	1; 2; 3; 10; 11; 12; 13; 14; 15; 22; 23; 24
	[2]$P\,\bar{6}\,m\,2$	1; 2; 3; 10; 11; 12; 16; 17; 18; 19; 20; 21
	[2]$P\,\bar{6}\,2\,c$	1; 2; 3; 7; 8; 9; 16; 17; 18; 22; 23; 24
	[3]$P\,m\,m\,c\,(C\,m\,c\,m)$	1; 4; 7; 10; 13; 16; 19; 22
	[3]$P\,m\,m\,c\,(C\,m\,c\,m)$	1; 4; 8; 11; 13; 16; 20; 23
	[3]$P\,m\,m\,c\,(C\,m\,c\,m)$	1; 4; 9; 12; 13; 16; 21; 24

IIa none

IIb [3]$H\,6_3/m\,m\,c\,(\boldsymbol{a}'=3\boldsymbol{a},\boldsymbol{b}'=3\boldsymbol{b})(P\,6_3/m\,c\,m)$

Maximal isomorphic subgroups of lowest index

IIc [3]$P\,6_3/m\,m\,c\,(\boldsymbol{c}'=3\boldsymbol{c})$; [4]$P\,6_3/m\,m\,c\,(\boldsymbol{a}'=2\boldsymbol{a},\boldsymbol{b}'=2\boldsymbol{b})$

Minimal non-isomorphic supergroups

Generators selected (1); $t(1,0,0)$; $t(0,1,0)$; $t(0,0,1)$; (2); (4); (7); (13)

Positions

Multiplicity, Wyckoff letter, Site symmetry		Coordinates			Reflection conditions
					General:
24	l 1	(1) x,y,z	(2) $\bar{y},x-y,z$	(3) $\bar{x}+y,\bar{x},z$	$hh2\bar{h}l$: $l=2n$
		(4) $\bar{x},\bar{y},z+\frac{1}{2}$	(5) $y,\bar{x}+y,z+\frac{1}{2}$	(6) $x-y,x,z+\frac{1}{2}$	$000l$: $l=2n$
		(7) $y,x,\bar{z}$	(8) $x-y,\bar{y},\bar{z}$	(9) $\bar{x},\bar{x}+y,\bar{z}$	
		(10) $\bar{y},\bar{x},\bar{z}+\frac{1}{2}$	(11) $\bar{x}+y,y,\bar{z}+\frac{1}{2}$	(12) $x,x-y,\bar{z}+\frac{1}{2}$	
		(13) $\bar{x},\bar{y},\bar{z}$	(14) $y,\bar{x}+y,\bar{z}$	(15) $x-y,x,\bar{z}$	
		(16) $x,y,\bar{z}+\frac{1}{2}$	(17) $\bar{y},x-y,\bar{z}+\frac{1}{2}$	(18) $\bar{x}+y,\bar{x},\bar{z}+\frac{1}{2}$	
		(19) $\bar{y},\bar{x},z$	(20) $\bar{x}+y,y,z$	(21) $x,x-y,z$	
		(22) $y,x,z+\frac{1}{2}$	(23) $x-y,\bar{y},z+\frac{1}{2}$	(24) $\bar{x},\bar{x}+y,z+\frac{1}{2}$	
					Special: as above, plus
12	k .m.	$x,2x,z$	$2\bar{x},\bar{x},z$	$x,\bar{x},z$	$\bar{x},2\bar{x},z+\frac{1}{2}$	no extra conditions
		$2x,x,z+\frac{1}{2}$	$\bar{x},x,z+\frac{1}{2}$	$2x,x,\bar{z}$	$\bar{x},2\bar{x},\bar{z}$	
		$\bar{x},x,\bar{z}$	$2\bar{x},\bar{x},\bar{z}+\frac{1}{2}$	$x,2x,\bar{z}+\frac{1}{2}$	$x,\bar{x},\bar{z}+\frac{1}{2}$	
12	j m..	$x,y,\frac{1}{4}$	$\bar{y},x-y,\frac{1}{4}$	$\bar{x}+y,\bar{x},\frac{1}{4}$	$\bar{x},\bar{y},\frac{1}{4}$	$y,\bar{x}+y,\frac{1}{4}$	$x-y,x,\frac{1}{4}$	no extra conditions
		$y,x,\frac{1}{4}$	$x-y,\bar{y},\frac{1}{4}$	$\bar{x},\bar{x}+y,\frac{1}{4}$	$\bar{y},\bar{x},\frac{1}{4}$	$\bar{x}+y,y,\frac{1}{4}$	$x,x-y,\frac{1}{4}$	
12	i .2.	$x,0,0$	$0,x,0$	$\bar{x},\bar{x},0$	$\bar{x},0,\frac{1}{2}$	$0,\bar{x},\frac{1}{2}$	$x,x,\frac{1}{2}$	$hkil$: $l=2n$
		$\bar{x},0,0$	$0,\bar{x},0$	$x,x,0$	$x,0,\frac{1}{2}$	$0,x,\frac{1}{2}$	$\bar{x},\bar{x},\frac{1}{2}$	
6	h $mm2$	$x,2x,\frac{1}{4}$	$2\bar{x},\bar{x},\frac{1}{4}$	$x,\bar{x},\frac{1}{4}$	$\bar{x},2\bar{x},\frac{1}{4}$	$2x,x,\frac{1}{4}$	$\bar{x},x,\frac{1}{4}$	no extra conditions
6	g .2/m.	$\frac{1}{2},0,0$	$0,\frac{1}{2},0$	$\frac{1}{2},\frac{1}{2},0$	$\frac{1}{2},0,\frac{1}{2}$	$0,\frac{1}{2},\frac{1}{2}$	$\frac{1}{2},\frac{1}{2},\frac{1}{2}$	$hkil$: $l=2n$
4	f $3m$.	$\frac{1}{3},\frac{2}{3},z$	$\frac{1}{3},\frac{2}{3},z+\frac{1}{2}$	$\frac{2}{3},\frac{1}{3},\bar{z}$	$\frac{2}{3},\frac{1}{3},\bar{z}+\frac{1}{2}$	$hkil$: $l=2n$ or $h-k=3n+1$ or $h-k=3n+2$
4	e $3m$.	$0,0,z$	$0,0,z+\frac{1}{2}$	$0,0,\bar{z}$	$0,0,\bar{z}+\frac{1}{2}$	$hkil$: $l=2n$
2	d $\bar{6}m2$	$\frac{1}{3},\frac{2}{3},\frac{1}{4}$	$\frac{2}{3},\frac{1}{3},\frac{1}{4}$			$hkil$: $l=2n$ or $h-k=3n+1$ or $h-k=3n+2$
2	c $\bar{6}m2$	$\frac{1}{3},\frac{2}{3},\frac{1}{4}$	$\frac{2}{3},\frac{1}{3},\frac{1}{4}$			
2	b $\bar{6}m2$	$0,0,\frac{1}{4}$	$0,0,\frac{1}{4}$			$hkil$: $l=2n$
2	a $\bar{3}m$.	$0,0,0$	$0,0,\frac{1}{2}$			$hkil$: $l=2n$

Symmetry of special projections

Along [001] $p\,6m\,m$ $\boldsymbol{a}'=\boldsymbol{a}$ $\boldsymbol{b}'=\boldsymbol{b}$ Origin at 0,0,z

Along [100] $p\,2g\,m$ $\boldsymbol{a}'=\frac{1}{2}(\boldsymbol{a}+2\boldsymbol{b})$ $\boldsymbol{b}'=\boldsymbol{c}$ Origin at x,0,0

Along [210] $p\,2m\,m$ $\boldsymbol{a}'=\frac{1}{2}\boldsymbol{b}$ $\boldsymbol{b}'=\frac{1}{2}\boldsymbol{c}$ Origin at $x,\frac{1}{2}x$,0

(*Continued on preceding page*)

XBL 852-1381

Fig. 85

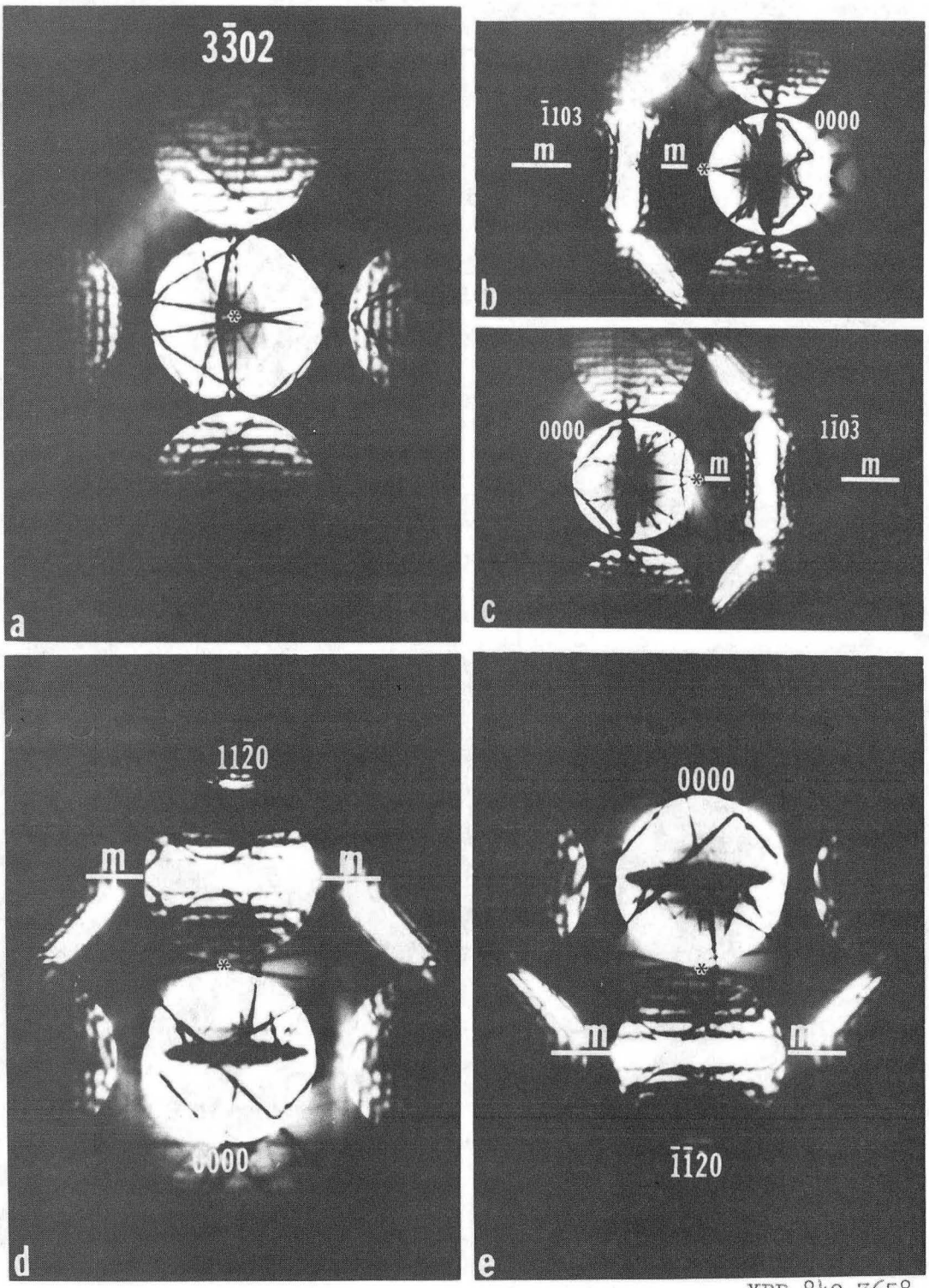

XBB 840-7658

Fig. 86

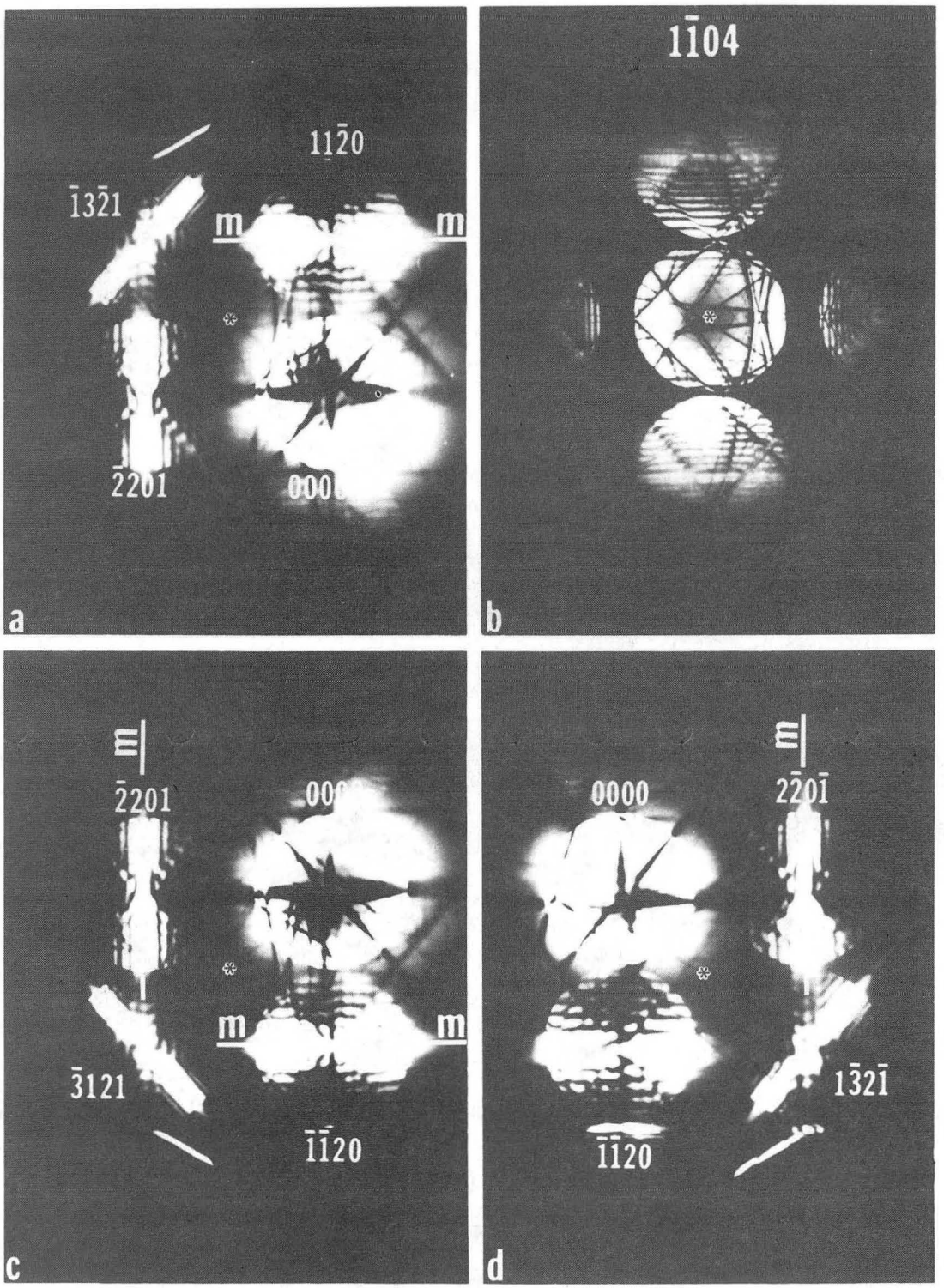

XBB 840-7656

Fig. 87

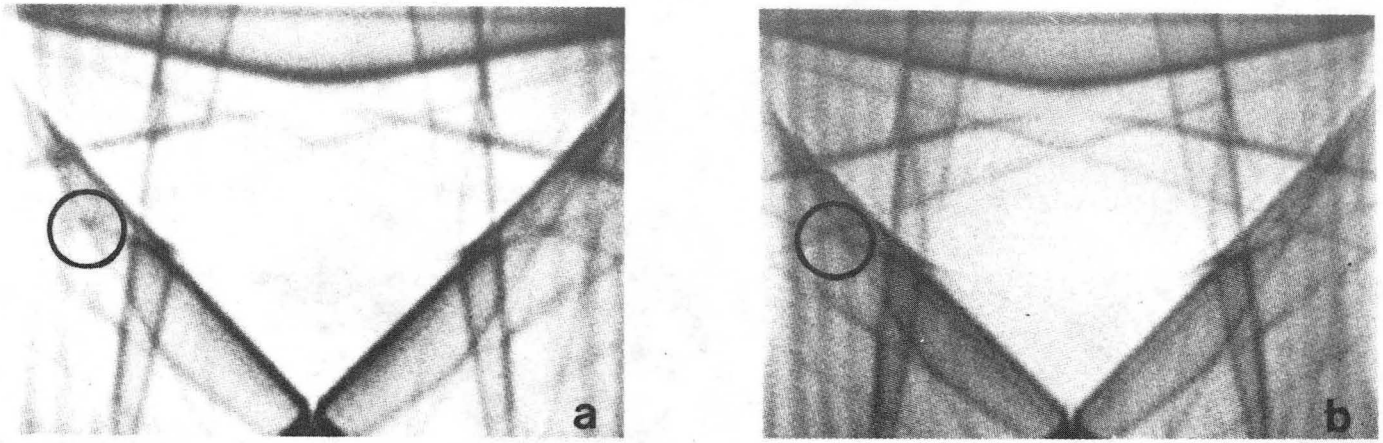

[1$\bar{1}$04] CBED pattern for a. Zn-Al-Mg-Ti; b. Zn-Cu-Al-Mg.

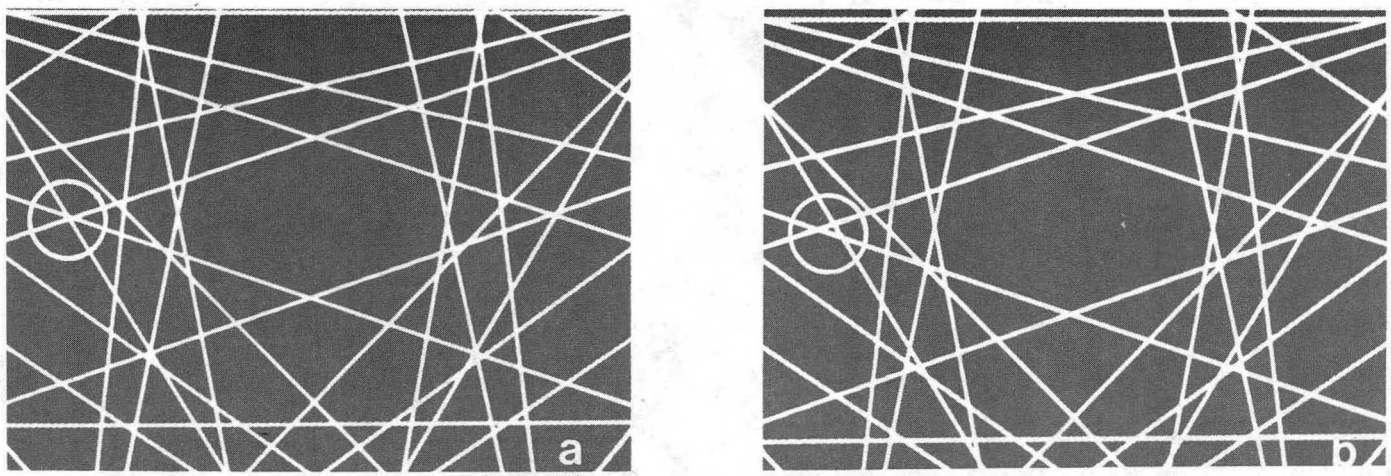

[1$\bar{1}$04] CBED computer simulations for above patterns. XBB 840-7608

Fig. 88

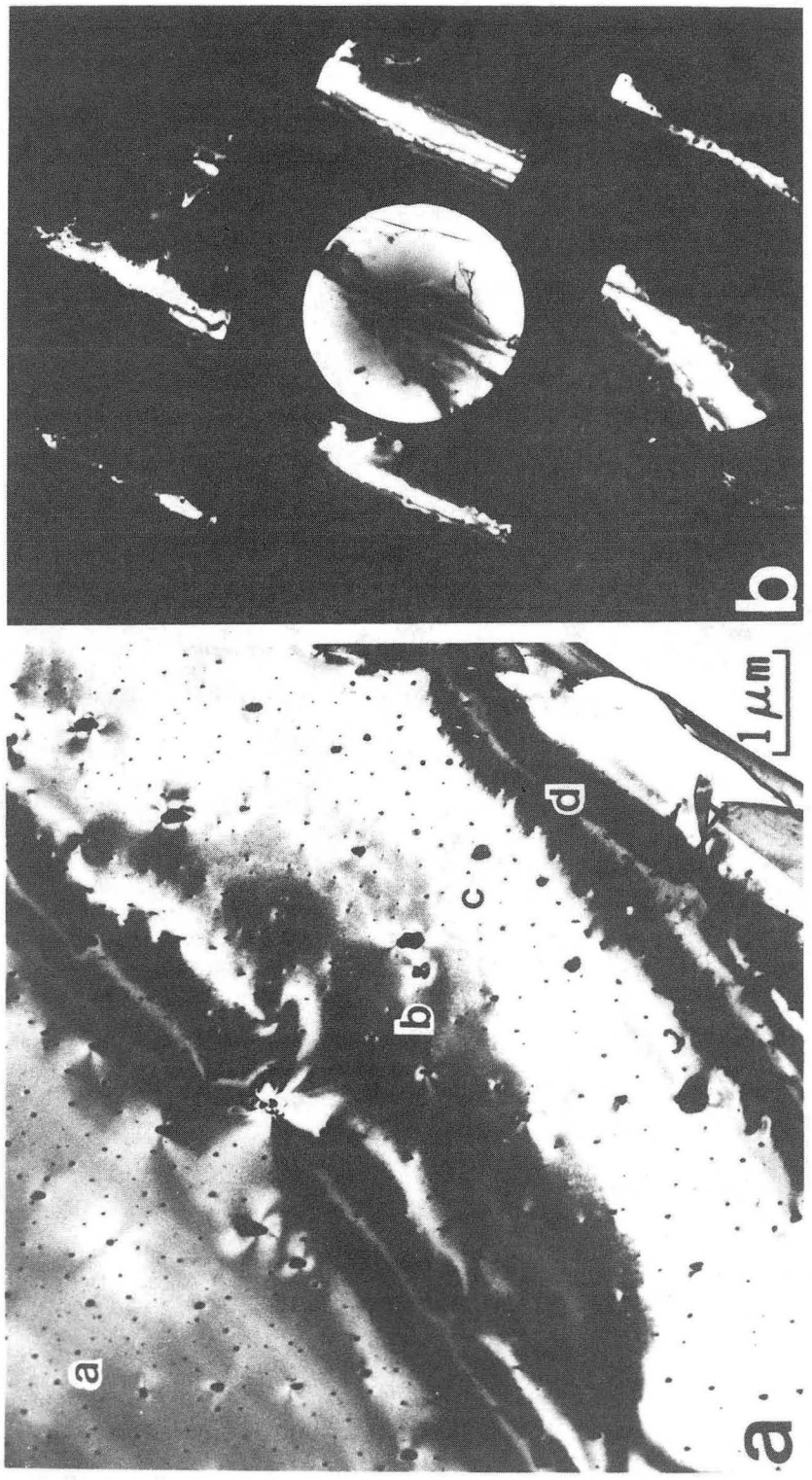

XBB 840-7654

Fig. 89

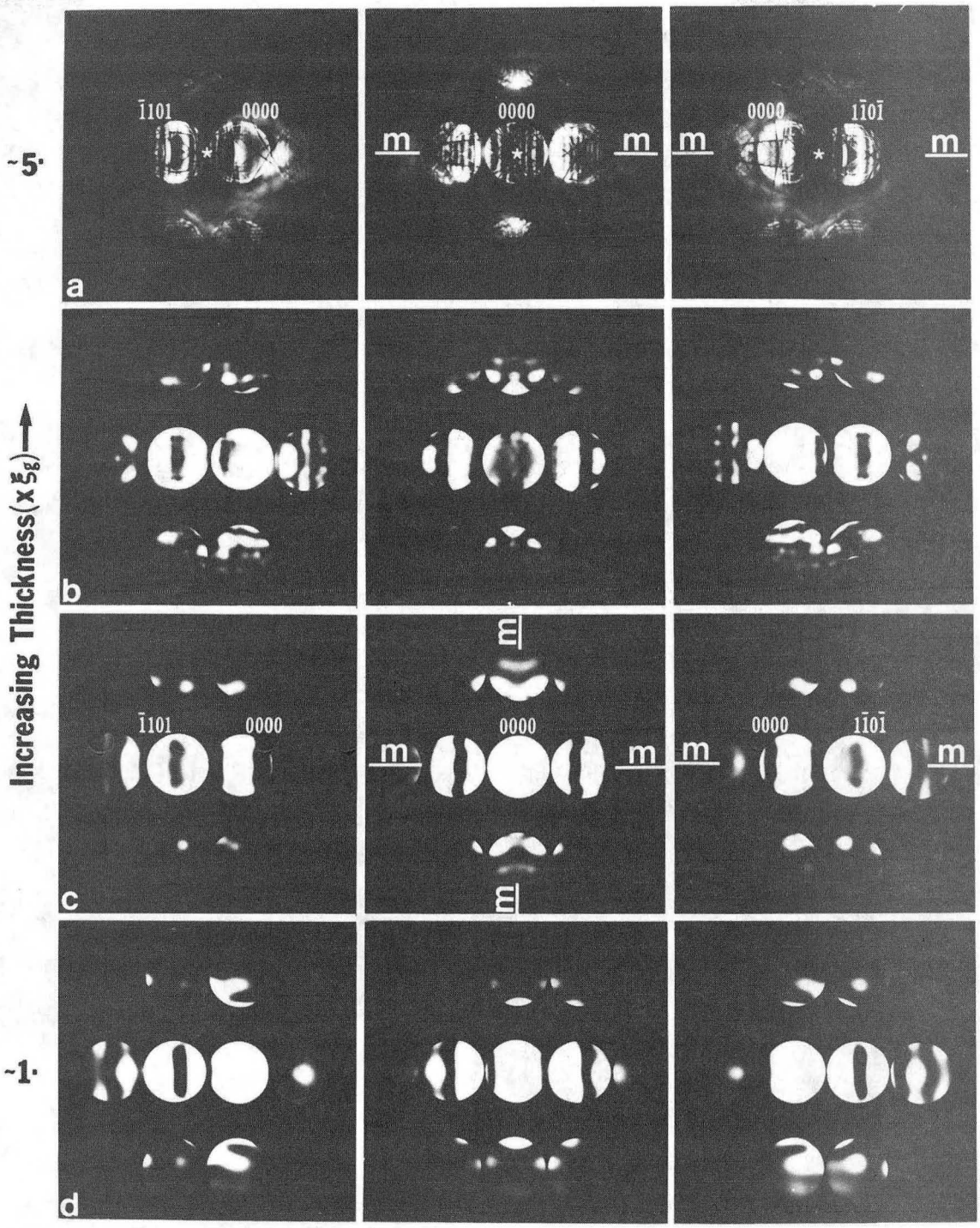

XBB 840-7664

Fig. 90

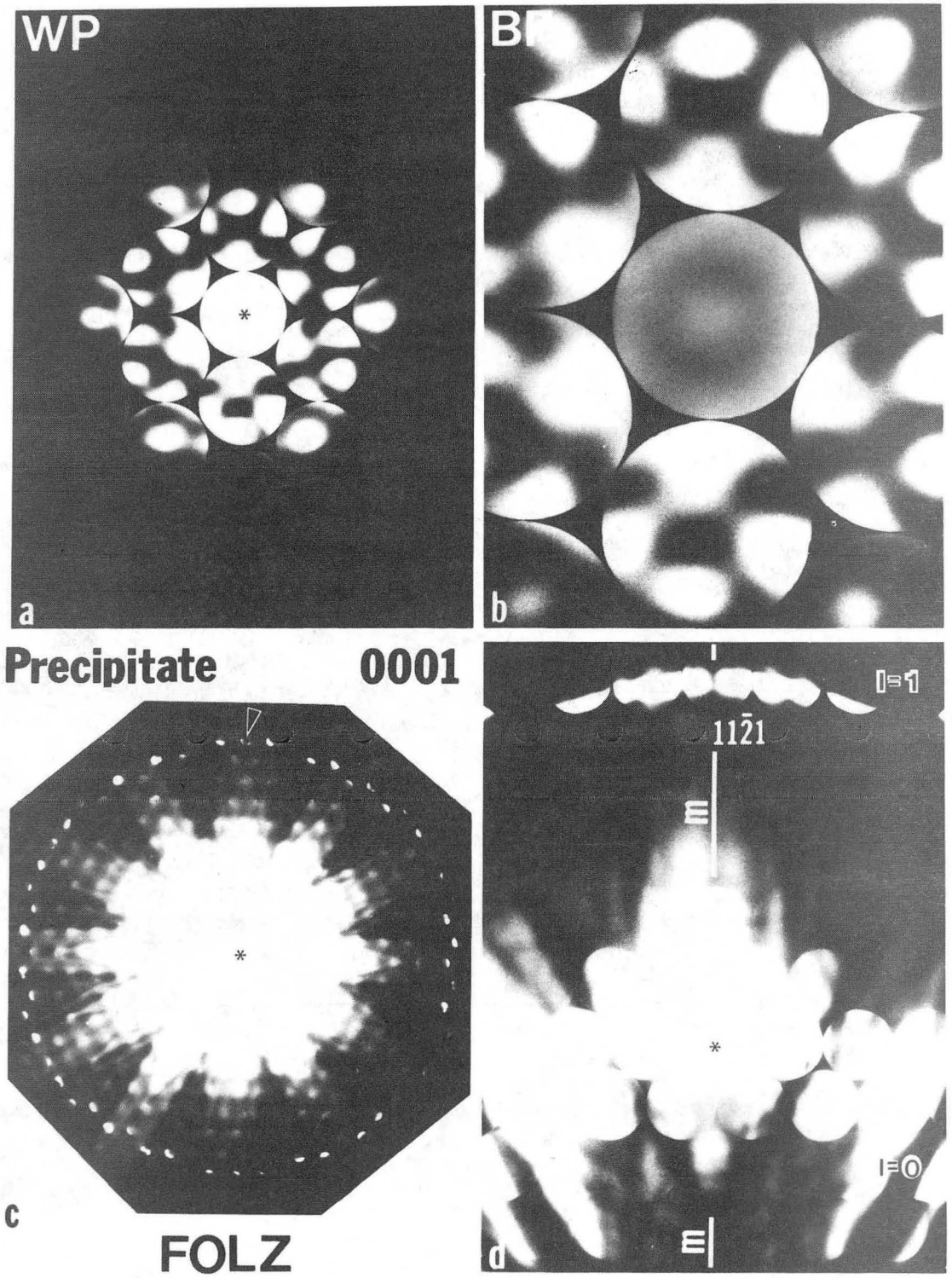

XBB 840-7661

Fig. 91

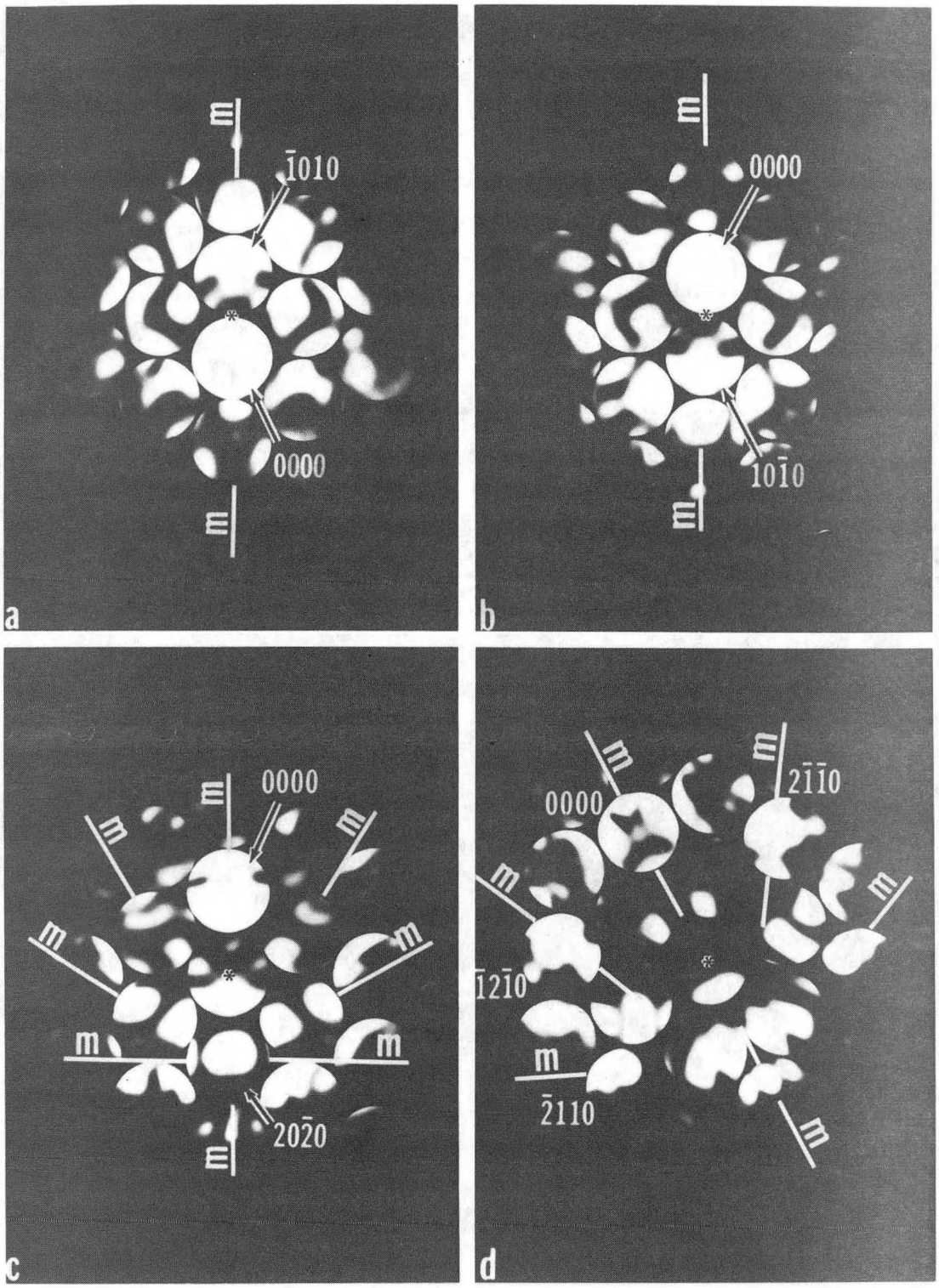

XBB 840-7659

Fig. 92

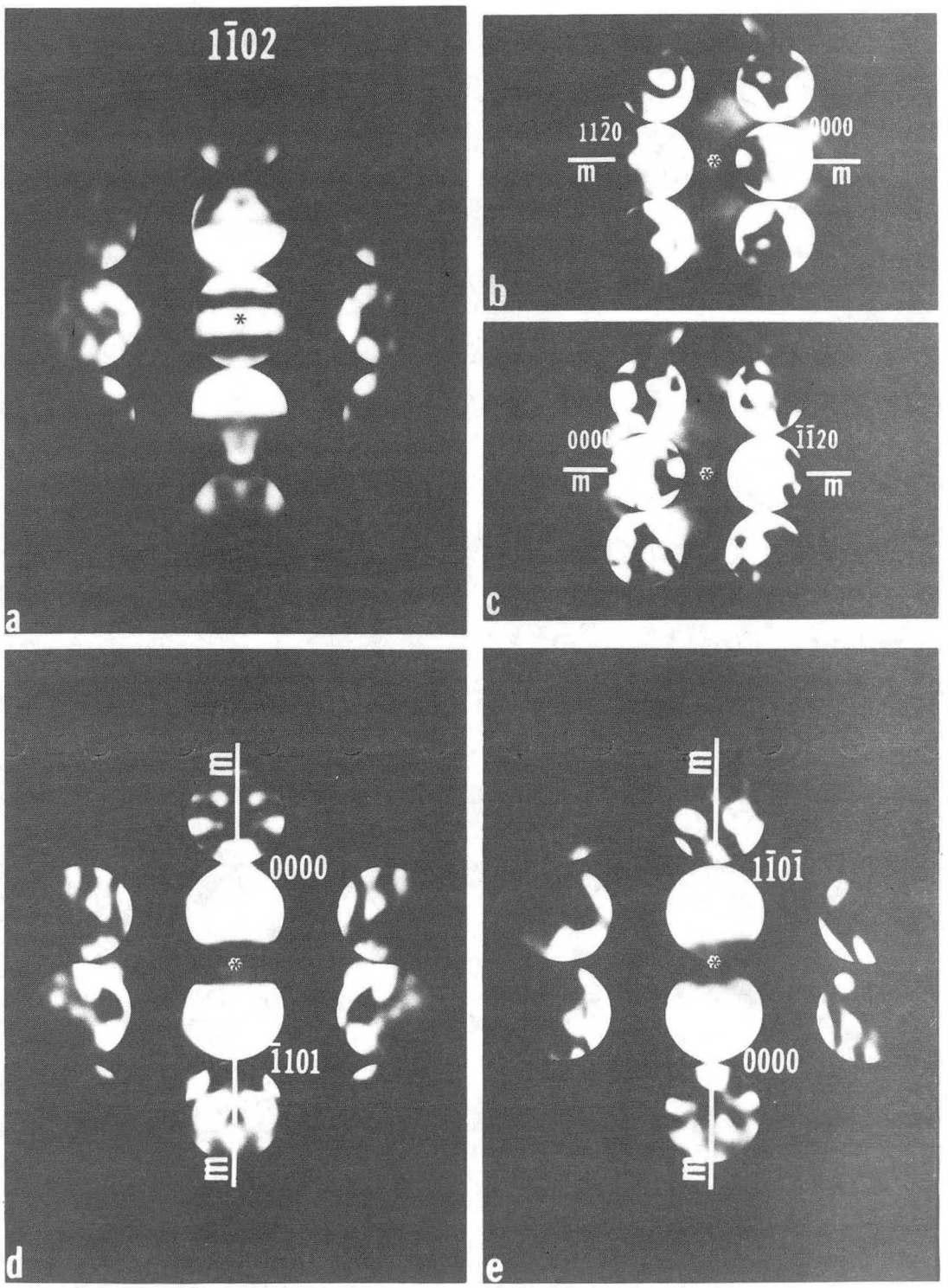

XBB 840-7660

Fig. 93

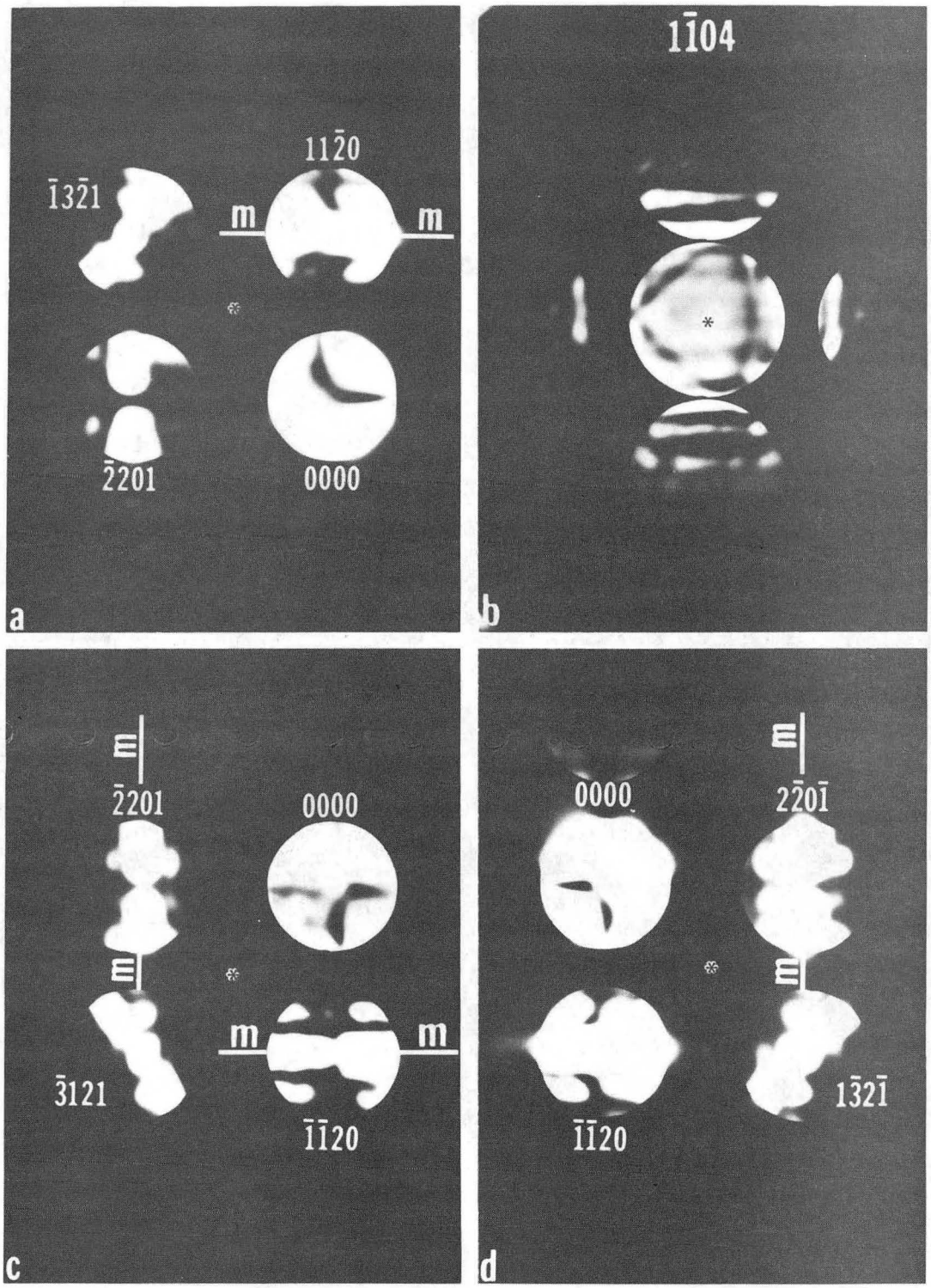

XBB 840-7657

Fig. 94

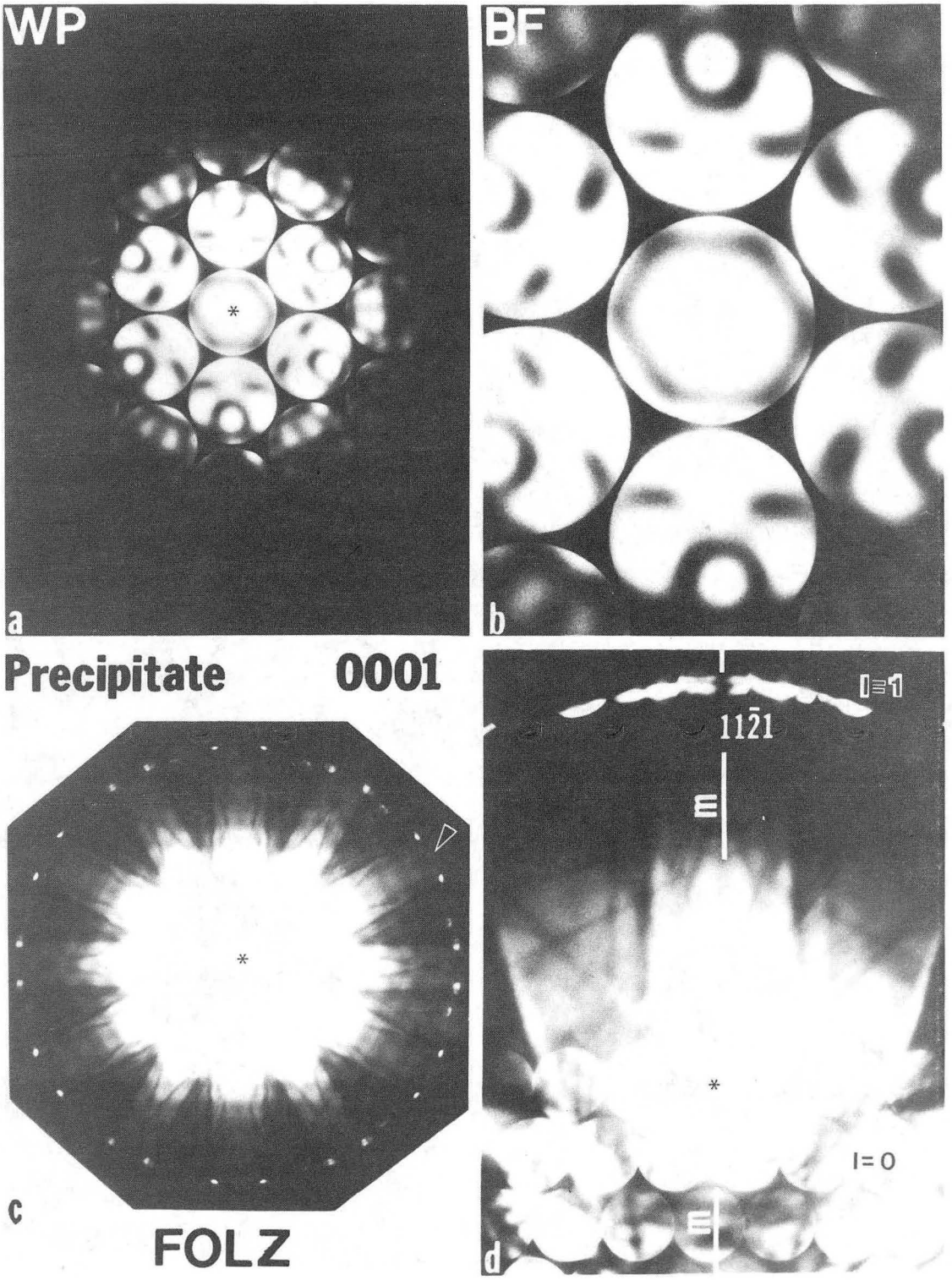

XBB 852-1543

Fig. 95

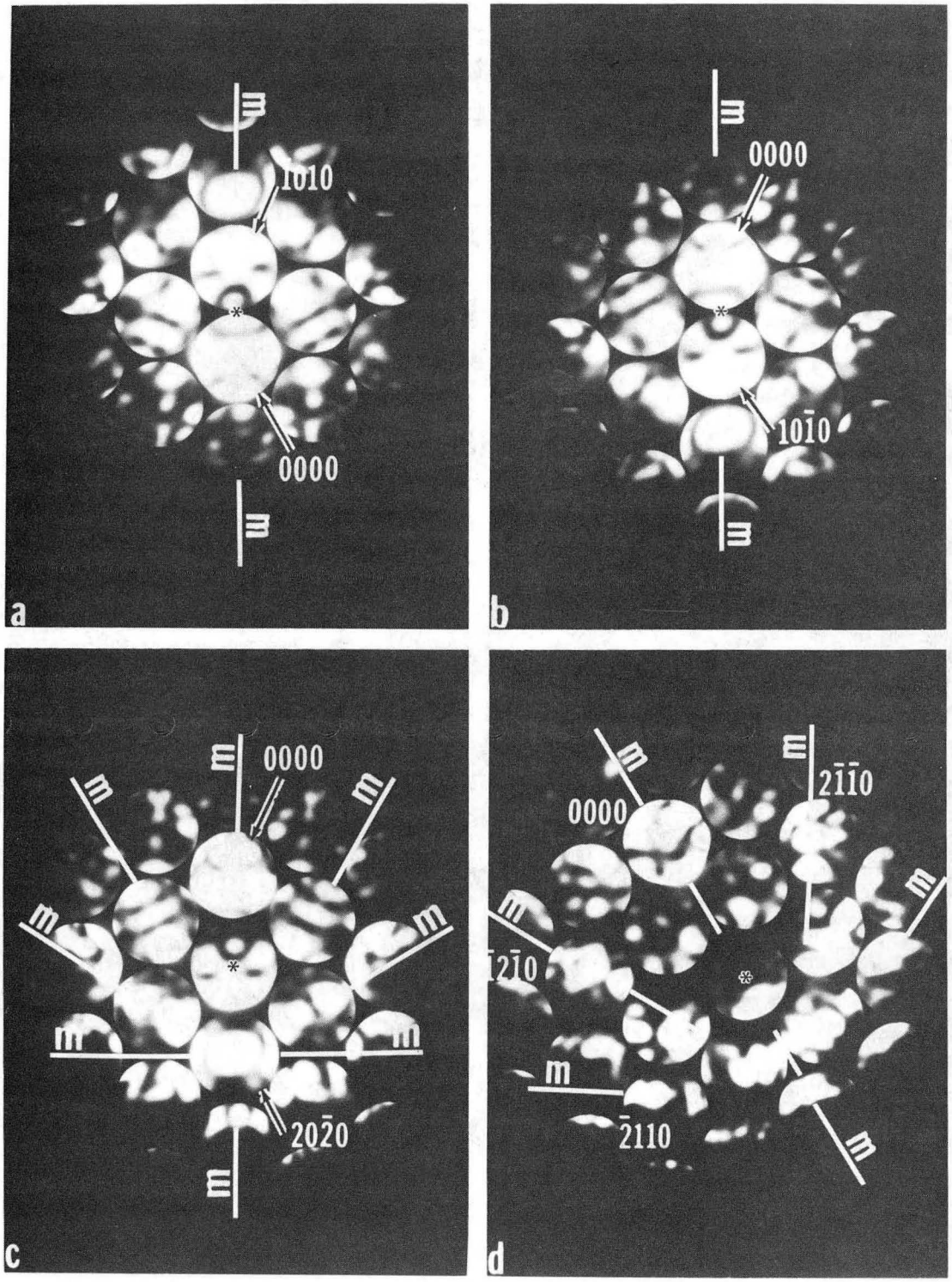

XBB 852-1542

Fig. 96

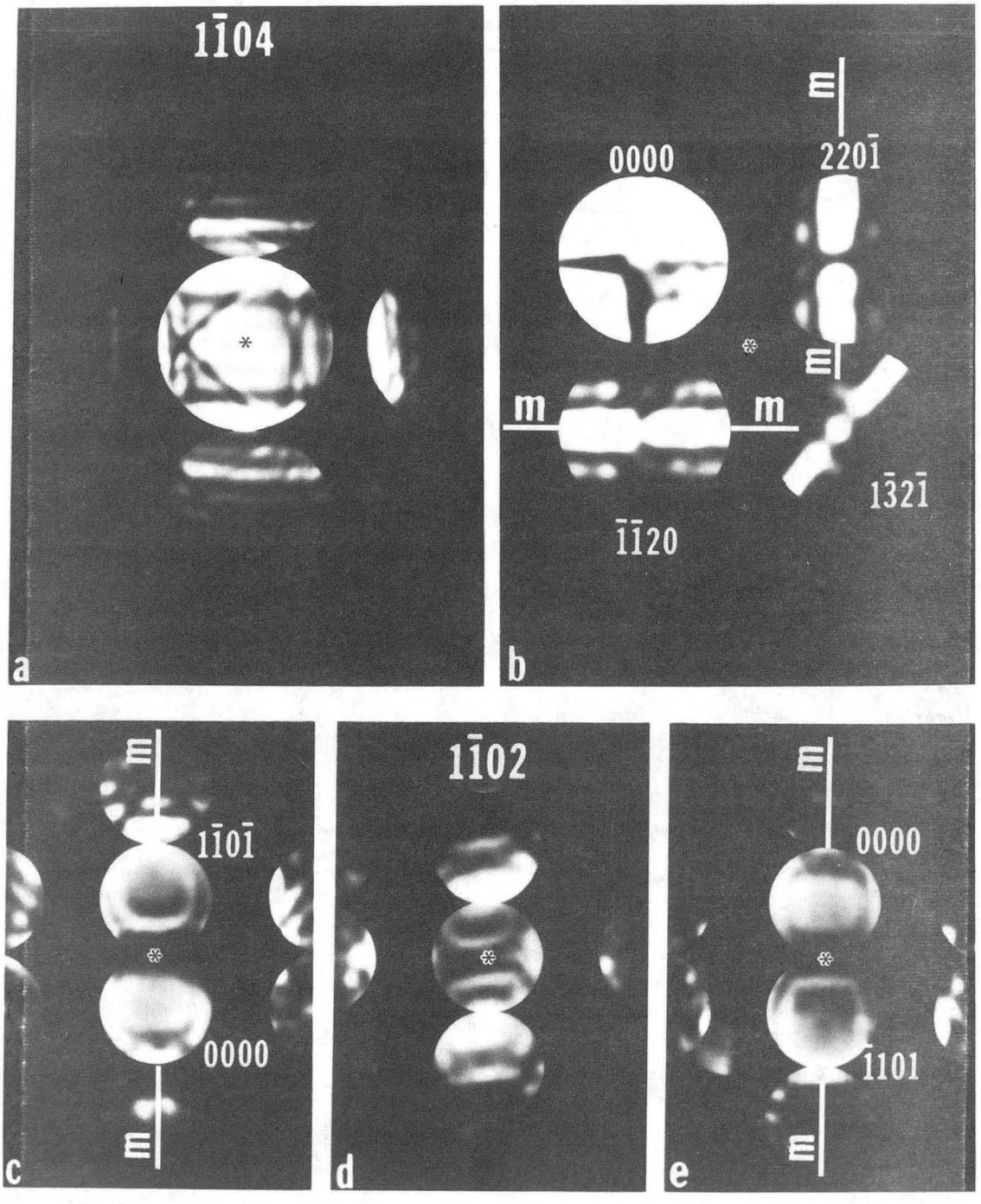

XBB 852-1541

Fig. 97

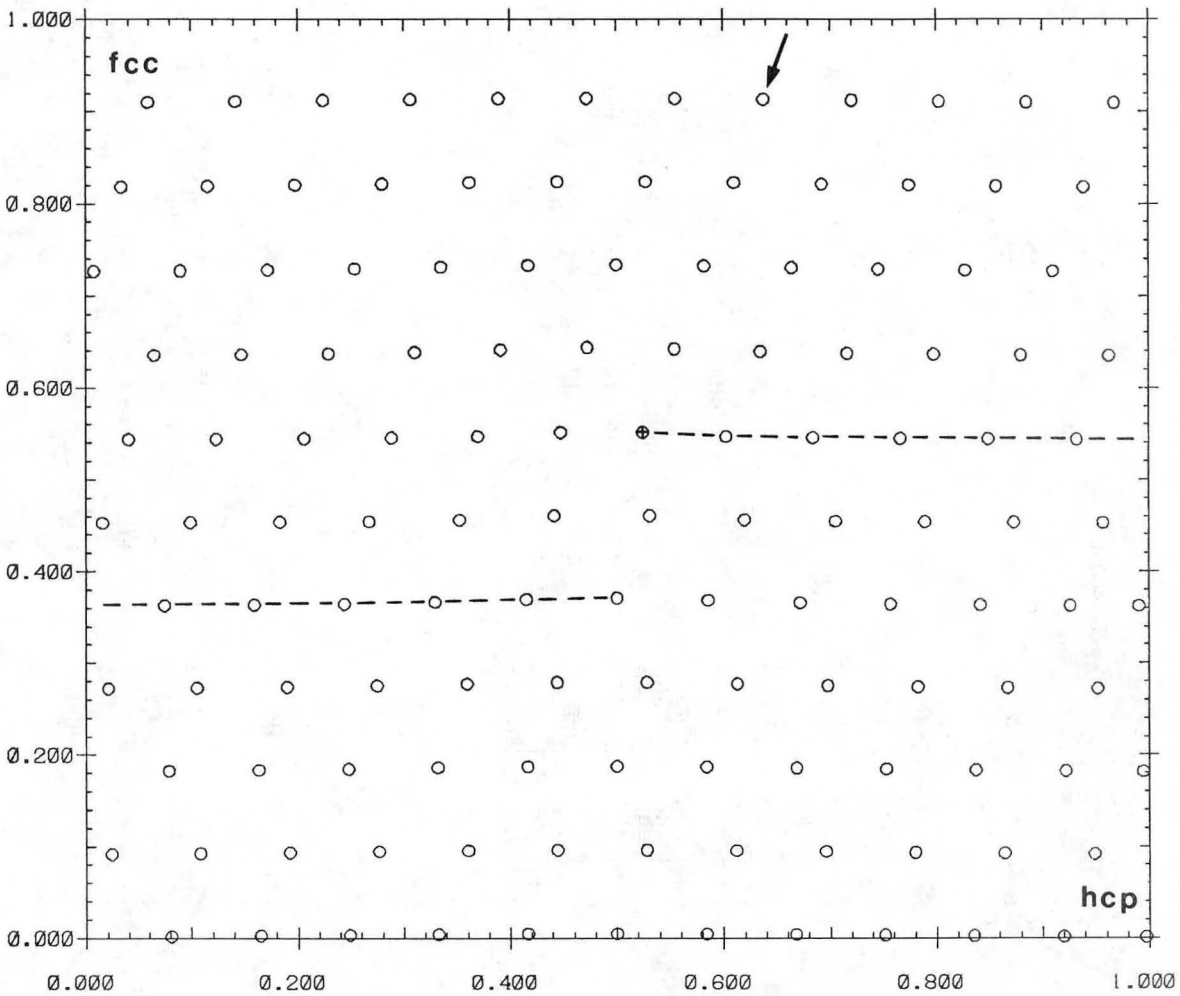

Fig. 98

XBL 853-1517

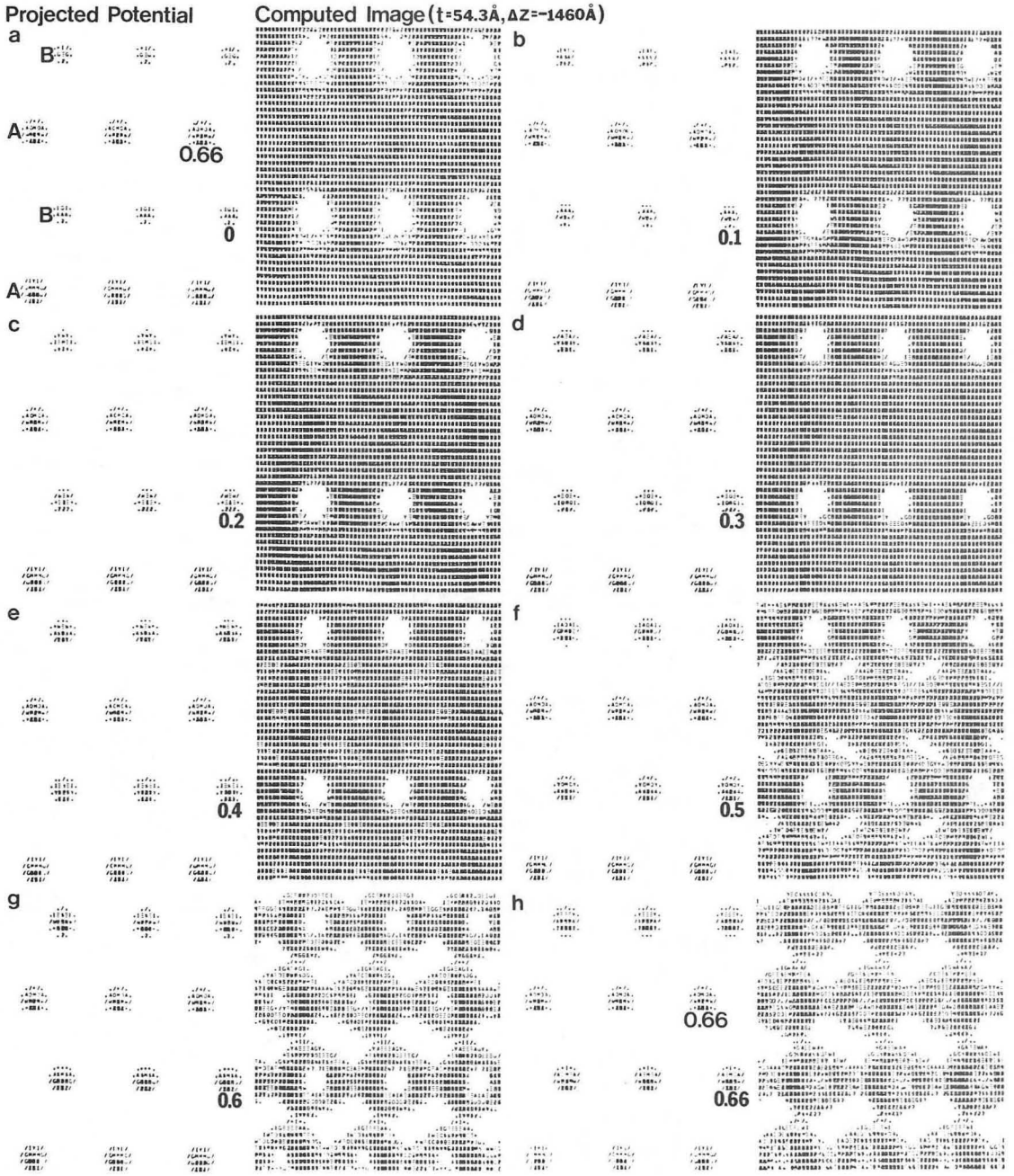

XBL 844-1325

Fig. 99

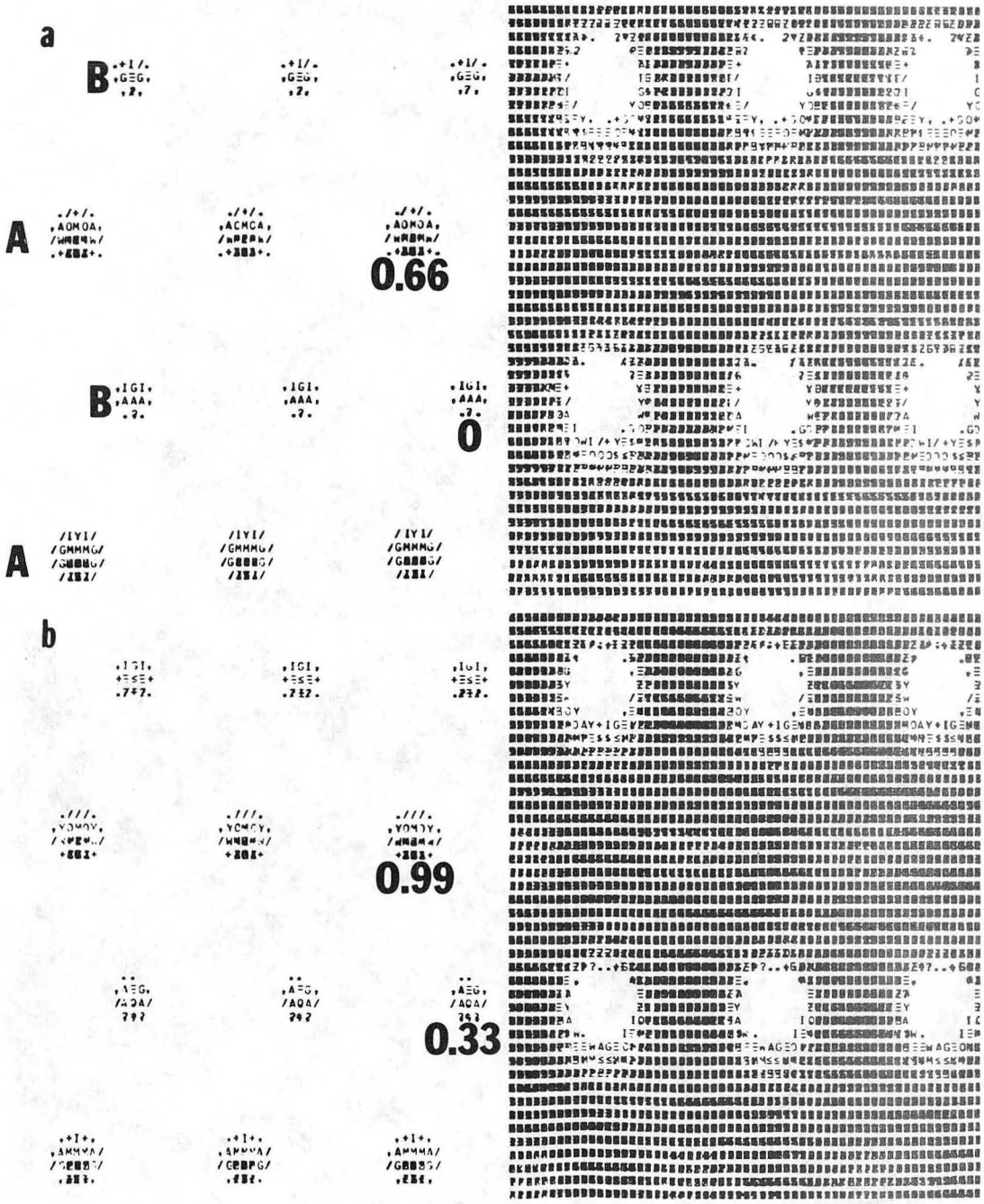

XBL 852-1379

Fig. 100

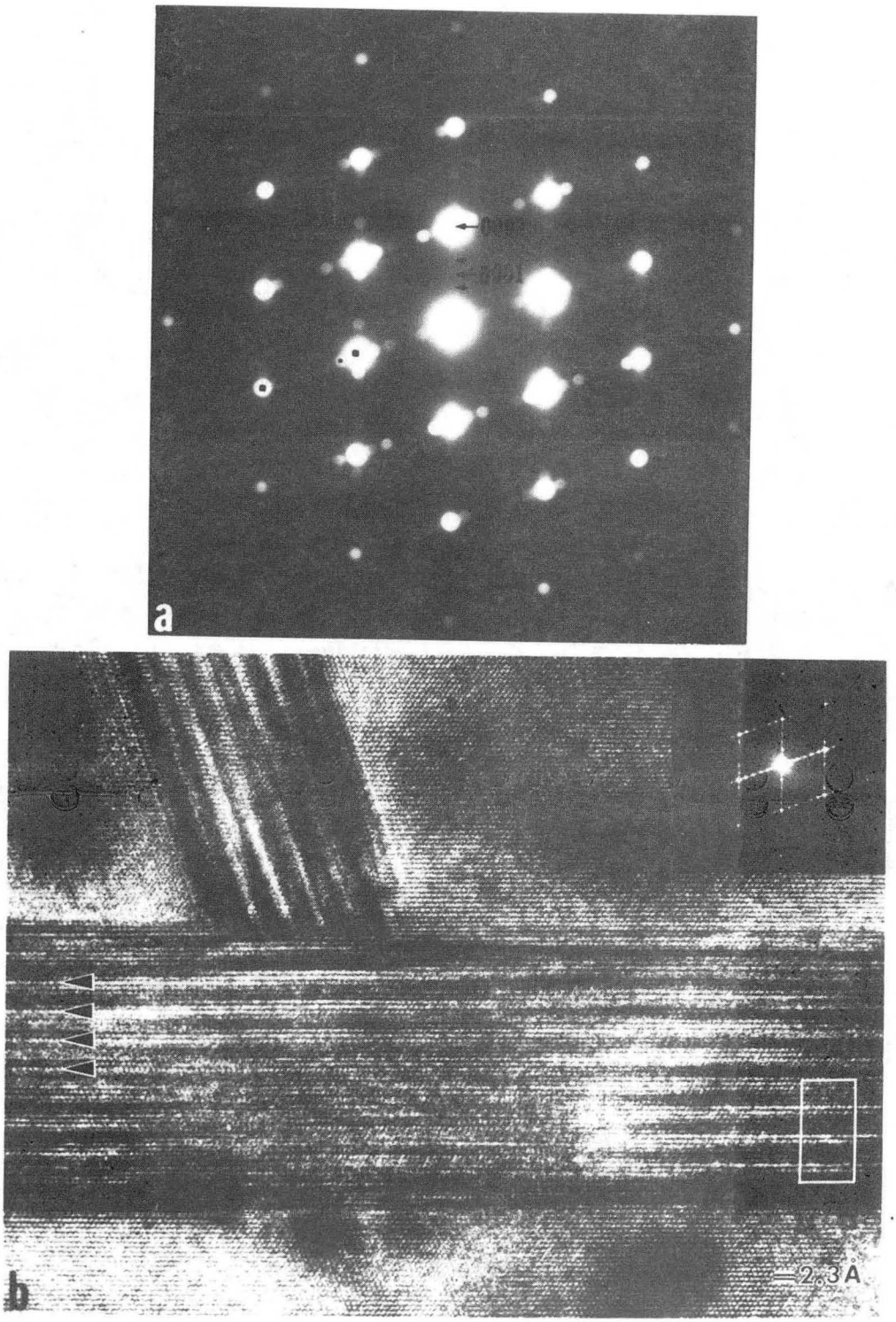

XBB 852-1540

Fig. 101

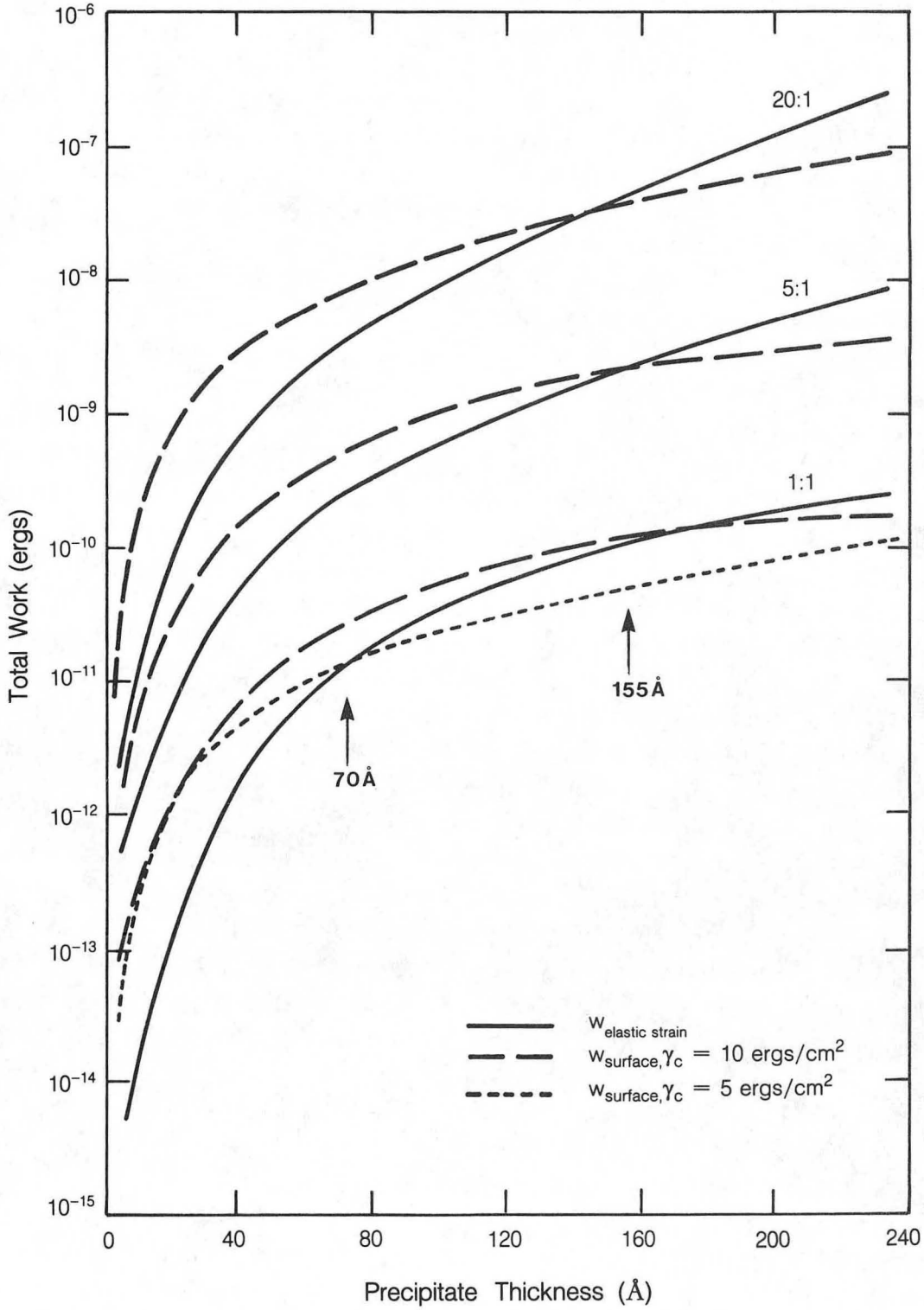

XBL 854-9521

Fig. 102

This report was done with support from the Department of Energy. Any conclusions or opinions expressed in this report represent solely those of the author(s) and not necessarily those of The Regents of the University of California, the Lawrence Berkeley Laboratory or the Department of Energy.

Reference to a company or product name does not imply approval or recommendation of the product by the University of California or the U.S. Department of Energy to the exclusion of others that may be suitable.

TECHNICAL INFORMATION DEPARTMENT
LAWRENCE BERKELEY LABORATORY
UNIVERSITY OF CALIFORNIA
BERKELEY, CALIFORNIA 94720